

Coventry University – Université Grenoble-Alpes

**The dynamics of partly 2D/partly 3D
turbulence: an experimental and theoretical
study in the Low-Rm MHD framework**

by

Nathaniel T. BAKER

December 2016

*A thesis submitted in partial fulfillment of the University's requirements
for the Degree of Doctor of Philosophy*

Abstract

This thesis aims at clarifying the role of the solenoidal component of the Lorentz force in fixing the topological dimensionality, and the ensuing dynamics of low- Rm MHD turbulent flows confined between electrically insulating and no-slip Hartmann walls. The work presented here breaks down into two main parts: an analytical investigation carried out in the weakly inertial limit on the one hand, and an experimental study of fully developed turbulence on the other hand. The analytical investigation was performed on a single, steady and axisymmetric electrically driven vortex confined between no-slip and electrically insulating walls perpendicular to a uniform magnetic field. Thanks to an asymptotic expansion of the Navier-Stokes equations valid for any Hartmann number, we show that the topological dimensionality of the leading order is fully imposed by a single parameter. More precisely, this parameter quantifies the competition between the solenoidal component of the Lorentz force and viscous friction, over the distance separating the two no-slip planes. This study highlights two inertial mechanisms capable of introducing a velocity component in the direction of the field at first order, by means of recirculations in the meridional plane: direct and/or inverse Ekman pumping. An experimental platform has also been designed and built from the ground up during this project, to investigate the dynamics of liquid metal turbulence subject to high magnetic fields (up to 10 T). The statistically steady turbulence sustained in our experiment was forced electrically by imposing a DC current through a square periodic array of electrodes. We show that the statistics of the turbulent fluctuations generated by this setup are homogeneous and axisymmetric to a satisfactory level, despite the forcing mechanism being inhomogeneous and anisotropic. By comparing the energy densities measured along the walls perpendicular to the magnetic field, we confirm that the physical processes at stake in the 3D inertial range of wall-bounded MHD turbulence at low- Rm are the solenoidal component of the Lorentz force on the one hand, and inertia on the other hand. Using a statistical analysis in scale space, we show that the kinematics of the flow driven in our experimental setup follows a universal law, which turns out to be fully described by only two lengthscales: first, the forcing scale in the direction perpendicular to the magnetic field, and second, the range of action of the Lorentz force before it is balanced out by inertial transfers, in the direction parallel to the field. We prove that the ratio of this latter scale to the height of the channel in fact segregates kinematically quasi-2D from kinematically 3D turbulent structures. By computing the actual flux of perpendicular turbulent kinetic energy along horizontal scales, we show that it always flows towards larger turbulent scales regardless of their topology. In other words, the existence of an inverse cascade of perpendicular kinetic energy does not necessarily require horizontal turbulent structures to be topologically quasi-2D in the inertial range.

Résumé

L'objectif de cette thèse est de clarifier le rôle de la composante rotationnelle de la force de Lorentz dans sa capacité à imposer la topologie et la dynamique des écoulements turbulents MHD à bas Rm , confinés par des parois rigides et électriquement isolantes. Le travail présenté ici se scinde en deux parties : d'une part une étude théorique effectuée dans un cadre faiblement inertiel, d'autre part une étude expérimentale portant sur des écoulements turbulents pleinement développés. L'étude théorique porte sur un vortex isolé, stationnaire et axisymétrique, confiné par deux parois rigides et électriquement isolantes, perpendiculaires à un champ magnétique uniforme. Grâce à un développement asymptotique des équations de Navier-Stokes, valable quel que soit le nombre de Hartmann, nous montrons que la dimensionnalité topologique de l'écoulement de base ne dépend que d'un seul paramètre. Ce paramètre en question compare en fait la distance sur laquelle la partie rotationnelle de la force de Lorentz est capable d'agir dans la direction du champ magnétique, avant d'être contrée par les effets visqueux. Cette étude met en lumière deux mécanismes inertIELS capables d'engendrer une composante de la vitesse dans la direction du champ magnétique au premier ordre, en introduisant des recirculations dans le plan méridional : du pompage d'Ekman direct et/ou inverse. Un dispositif expérimental a également été construit durant ce projet, afin d'étudier la dynamique d'écoulements turbulents de métaux liquides soumis à des champs magnétiques intenses. La turbulence stationnaire engendrée par ce dispositif était forcée électriquement en imposant un courant continu à travers une matrice carrée et périodique d'électrodes d'injection. Grâce à ce dispositif, nous avons montré que les statistiques des fluctuations turbulentes étaient raisonnablement homogènes et axisymétriques, malgré un forçage inhomogène et anisotrope. Nous confirmons également, en comparant les densités d'énergie cinétique turbulentes mesurées le long des parois perpendiculaires au champ magnétique, que les processus physiques en jeu dans le domaine inertiel 3D de la turbulence MHD confinée à bas Rm sont bien la composante rotationnelle de la force de Lorentz d'une part, et les transferts inertIELS d'autre part. Grâce à une étude statistique dans l'espace des échelles, nous montrons que la cinématique de la turbulence forcée dans notre expérience suit en fait une loi universelle qui ne dépend que de deux longueurs caractéristiques. Premièrement, l'échelle d'injection, dans la direction perpendiculaire au champ magnétique. Deuxièmement, le rayon d'action de la force de Lorentz avant d'être contrée par les effets inertIELS, dans la direction parallèle au champ. Nous prouvons que le rapport entre cette dernière longueur caractéristique et la hauteur de l'enceinte expérimentale permet de différencier les structures turbulentes cinématiquement quasi-2D de celles qui sont cinématiquement 3D. En calculant directement le flux d'énergie cinétique turbulente perpendiculaire à travers les échelles horizontales, nous montrons que ce dernier est toujours dirigé vers les grandes échelles, et ce quel que soit la dimensionnalité des échelles en question. Autrement dit, une cascade inverse d'énergie perpendiculaire peut exister sans pour autant que les structures turbulentes associées soient quasi-2D.

Acknowledgments

After spending three and a half years on this project, I can safely say that the following PhD resulted from a tenacious team effort. And although I was essentially the one on the front line, the work presented here would simply not exist, had it not been for many invaluable contributions.

To begin with, I must mention my supervisors, who I believe successfully taught me the basics of being a researcher. In particular, I am grateful to Alban for sharing his understanding of MHD and his acute sense of marketing, to Laurent for sharing his knowledge about experimental techniques and for opening my eyes on the inner workings of French academia, not to mention François for his never-failing optimism and pragmatism whenever came the time to actually solve issues. Credit is also due to the examiners Sven Eckert, Richard Hill and Joël Sommeria for the time they have spent reviewing this manuscript, the stimulating discussion we had during the defense, as well as their highly motivating feedback.

I was extremely fortunate to conduct the experimental work in a cutting edge research facility, and undoubtedly benefited from the advice and help of many people working at the LNCMI, Institut Néel and now defunct CRETA laboratories. In particular, I am very much indebted to Jurgen Spitznagel and Claude Mollard for their technical advice and outstanding job in the machining of the new parts found on the updated Flowcube, to Jean-Louis Demarinis who helped me solve electrical engineering related issues, to Pierre-Frédéric Sibeud who taught me how to operate the superconducting magnet and was fully dedicated during its cooling, to Paul Chometon and Emmanuel Verloop who assisted me during the assembling of the Hartmann plates and the mounting of the experiment, and to Olivier Exshaw who helped me solder the connectors onto the back of the PCBs. I also wish to thank André Sulpice, the former director of the CRETA, who was always immediately available to give a hand, and to Ian Bates from Coventry University for the CAD drawings he made, the orders he placed, and all his contributions which helped build and improve the Flowcube.

It would certainly be foolish to think that the pursuit of such a long term effort only takes place inside the lab. From that perspective, I sincerely benefited from Kelig's solidarity during the most difficult times, and enjoyed every laugh we shared while he was staying in Grenoble. Last but not least, I would rather not think about the state in which I would be today if it had not been for Ari's, Gom's, Pepe's, Didi's, Mimi's, and of course Hélène's unconditional friendship, love and support.

Contents

Contents	1
General introduction	5
1 Basics of magnetohydrodynamics	7
1.1 Governing laws	7
1.1.1 Navier-Stokes equations	7
1.1.2 Maxwell's equations	8
1.2 The underlying physics of MHD	9
1.2.1 The low- Rm approximation	9
1.2.2 The effect of the Lorentz force at low- Rm	11
1.2.3 Recapitulation	15
1.3 Wall-bounded flows	16
1.3.1 A fundamental example: the Hartmann channel flow	17
1.3.2 The Hartmann Layer	19
1.3.3 Quasi-2D electrically driven vortices	22
1.3.4 Ekman pumping	24
2 A weakly inertial vortex confined between two no-slip walls	27
2.1 Geometry and governing equations	28
2.2 Calculations	31
2.2.1 Inertialess base flow	31
2.2.2 Corrections due to inertia	33
2.3 Numerical methods	36
2.3.1 Algorithm description	36
2.3.2 Convergence test	37
2.3.3 Validity of the radial boundary condition	38
2.3.4 Sensitivity to the injection profile	39
2.4 Results	41
2.4.1 Results at leading order	41
2.4.2 Results at first order	45

2.4.3	Is two-dimensionality a good source of helicity?	50
2.5	Summary of the main findings	51
3	An experimental apparatus for the study of MHD turbulence	53
3.1	Historical review of past experimental studies	53
3.2	Description of the Flowcube	57
3.2.1	Components	57
3.2.2	The Hartmann plates	59
3.2.3	Electric forcing	61
3.2.4	Magnetic fields	63
3.2.5	Data logging	63
3.2.6	Experimental protocol	64
3.2.7	Recapitulation	67
3.3	Methods of measurement	67
3.3.1	Electric Potential Velocimetry (EPV)	67
3.3.2	Pulsed Ultrasound Doppler Velocimetry (PUDV)	69
3.3.3	EPV / PUDV benchmarking	72
3.4	Validity and reliability of measurements	74
3.4.1	Impact of noise on structure functions	74
3.4.2	Convergence of statistical moments	77
4	Turbulence	81
4.1	Basic phenomenology	81
4.1.1	Observations	81
4.1.2	3D homogeneous and isotropic hydrodynamic turbulence	82
4.1.3	2D homogeneous and isotropic hydrodynamic turbulence	85
4.1.4	Turbulence with mixed 2D and 3D characteristics	88
4.1.5	Particularities of MHD turbulence	90
4.2	Description of turbulence in physical space	94
4.2.1	Local conservation of energy in a fluid	94
4.2.2	The role of enstrophy in turbulence	95
4.2.3	The Reynolds averaged equations	96
4.3	Turbulence in scale space	98
4.3.1	Correlation and structure functions	98
4.3.2	Dynamics of inhomogeneous, anisotropic turbulence: the Kármán-Howarth equation	99
4.3.3	Evaluation of mean turbulent kinetic energy density	102
5	Partly 2D/partly 3D MHD turbulence in a bounded domain	105
5.1	Global features of Flowcube's turbulence	105
5.1.1	Topology of the mean flow and turbulent fluctuations	105
5.1.2	Turbulence homogeneity	108

5.1.3	Turbulence isotropy	111
5.1.4	Turbulence intensity	113
5.1.5	Componentality vs. dimensionality	114
5.2	Transition between 3D and 2D kinematics	117
5.2.1	Turbulent kinetic energy density	117
5.2.2	Experimental confirmation of the threshold for a kinematically 2D inertial range	119
5.3	Statistical analysis in scale space	121
5.3.1	Kinematics	121
5.3.2	Energy transfers	124
5.4	How to evaluate Joule dissipation in scale space?	128
5.5	Summary of the main findings and prospects	132
General conclusion		135
Appendix A: Derivation of the Kármán-Howarth equation		137
Appendix B: Green's function for the Laplacian operator		141
Bibliography		145

General introduction

Magnetohydrodynamic (MHD) turbulence has attracted attention for quite a while now, as it covers a wide and unique range of subjects from down to earth applications for the metallurgical and nuclear industries (for instance stirring, pumping or casting of liquid metals), all the way up to mysteries of the universe (dynamics of the Sun, magneto-convection in the Earth's core). A compelling by-product of MHD is the now well established ability of magnetic fields to reorganize the turbulent flow of electrically conducting fluids. At the laboratory scale, this reorganization translates into the two-dimensionalization of the flow, in the sense that it becomes independent of the spatial coordinate along the magnetic field.

Thanks to this property, MHD became an appealing framework to investigate some more universal and fundamental properties of turbulence, which outreached the subjects mentioned above, one of these aspects being the dynamics of 2D turbulence. Early motivation to study 2D turbulence was perhaps initiated from the assessment that 3D turbulence (i.e. turbulence occurring in all three-dimensions of space) came with daunting inextricable questions, which mostly resulted from its non-linear nature. It was thought that removing one spatial coordinate could help answer long standing questions regarding the latter, however 2D turbulence grew to become an active field of research of its own instead. This situation was even encouraged by the study of natural systems like geophysical flows in oceans and atmospheres, which have been shown to feature 2D motions to some extent.

Real-life systems can however never be exactly 2D, if only for the existence of rigid walls, i.e. boundary layers. The coexistence of these, however small, sources of three-dimensionality with an otherwise 2D bulk suggests that real-life turbulent flows are in fact more likely to stem from a combination of 2D and 3D features, which poses a genuine question as far as their dynamics is concerned. Indeed, 3D turbulence is well known to channel kinetic energy towards small turbulent structures, which then dissipate it into heat through viscous friction. This mechanism is however forbidden as soon as the flow is constrained to two dimensions. In fact, 2D turbulence is known to channel kinetic energy towards large turbulent structures. Although 2D and 3D turbulent flows are better and better understood separately, it is still unclear how their seemingly irreconcilable dynamics relate to each other, whenever 2D and 3D turbulent structures coexist.

The present thesis aims at contributing to the understanding of the interplay between 2D and 3D dynamics. More specifically, the central thread, which will be followed throughout this work can be summarized in the subsequent question: In what direction does turbulent

GENERAL INTRODUCTION

kinetic energy flow, when turbulence simultaneously features 2D and 3D kinematics? This question will be tackled in the MHD framework at the laboratory scale, which gives us the opportunity to control the dimensionality of a flow at will, by imposing an external magnetic field.

The following thesis breaks down into five chapters. We will start by reviewing the main concepts of MHD in chapter 1. Doing so will give insight into the physical processes at play, which lie at the heart of MHD's phenomenology. These concepts will then be used in chapter 2 to derive a model illustrating the two-dimensionalization of a single electrically driven vortex confined between insulating and no-slip walls. This study will take place in the weakly inertial limit, which is an attractive first step before dealing with fully inertial turbulent flows. Chapter 3 will be dedicated to the description of the experimental setup used here to investigate turbulence in liquid metals subject to high magnetic fields. We will review in chapter 4 some fundamental results pertaining to the field of turbulence. In particular, we will focus on presenting the known differences between 2D and 3D hydrodynamic turbulence, and see how they compare against MHD turbulence itself. We will finally present and discuss our experimental results in chapter 5, which have been accumulated throughout the past three years.

Chapter 1

Basics of magnetohydrodynamics

Magnetohydrodynamics (MHD) is an elegant discipline, which describes the flow of an electrically conducting fluid in an electromagnetic field. In that respect, MHD couples the principles of fluid dynamics to those of electromagnetism. When the flow is assumed incompressible (as will be throughout this thesis), the unknowns of a typical MHD problem are the velocity field \mathbf{u} , the pressure field p , the electromagnetic field (\mathbf{E}, \mathbf{B}) and the current density field \mathbf{j} . The purpose of this chapter is to give an overview of how all these variables relate to each other, and illustrate the fundamental results in MHD on which the work presented in this thesis relies.

1.1 Governing laws

1.1.1 Navier-Stokes equations

Let us consider the incompressible flow of an electrically conducting fluid such as a liquid metal, characterized by its density ρ , kinematic viscosity ν and electric conductivity σ . Its behavior is governed by the laws of hydrodynamics, which rely on the following two physical principles: the conservation of mass of the fluid

$$\nabla \cdot \mathbf{u} = 0, \quad (1.1)$$

and the conservation of its momentum

$$\frac{\partial \mathbf{u}}{\partial t} + \mathbf{u} \cdot \nabla \mathbf{u} = -\frac{\nabla p}{\rho} + \frac{\mathbf{j} \times \mathbf{B}}{\rho} + \nu \Delta \mathbf{u}. \quad (1.2)$$

The fundamental difference between hydrodynamics and magnetohydrodynamics stems from the presence of an additional body force $\mathbf{j} \times \mathbf{B}$ in the momentum equation, called the Lorentz force (\mathbf{B} refers to the magnetic field and \mathbf{j} to the current density). The Lorentz force is at the heart of the specific behavior of MHD, hence will receive great attention throughout this thesis. The momentum equation may be re-written in a slightly different way by taking its

1. BASICS OF MAGNETOHYDRODYNAMICS

curl, yielding a governing equation for the vorticity $\boldsymbol{\omega} = \nabla \times \mathbf{u}$, hereafter referred to as the vorticity equation

$$\frac{\partial \boldsymbol{\omega}}{\partial t} = \nabla \times (\mathbf{u} \times \boldsymbol{\omega}) + \frac{1}{\rho} \nabla \times (\mathbf{j} \times \mathbf{B}) + \nu \Delta \boldsymbol{\omega}. \quad (1.3)$$

Vorticity is an interesting quantity to consider when studying turbulence, as it is a quantitative measurement of the velocity gradients existing in a flow. It therefore contains useful information on the dynamics of small scales, and is strongly linked to the dissipation of kinetic energy by viscous friction (Doering & Gibbon, 1995).

1.1.2 Maxwell's equations

In order to completely close an MHD system, additional laws governing the electromagnetic quantities are required. Those are given by Maxwell's equations. Let us consider now an electrically conducting medium of electric charge density ρ_e and electric conductivity σ . The vacuum permittivity and permeability are $\epsilon_0 = 8.854 \times 10^{-12} \text{ F/m}$, and $\mu_0 = 4\pi \times 10^{-7} \text{ H/m}$ respectively. The laws of electromagnetism are given by Maxwell's equations, which can be broken down into Gauss' laws

$$\nabla \cdot \mathbf{B} = 0 \quad (1.4)$$

and

$$\nabla \cdot \mathbf{E} = \frac{\rho_e}{\epsilon_0}, \quad (1.5)$$

Ampère's law¹

$$\nabla \times \mathbf{B} = \mu_0 \mathbf{j}, \quad (1.6)$$

and Faraday's law

$$\nabla \times \mathbf{E} = -\frac{\partial \mathbf{B}}{\partial t}. \quad (1.7)$$

In addition to Maxwell's equations, a phenomenological law linking the current density \mathbf{j} to the electromagnetic field (\mathbf{E}, \mathbf{B}) exists. This final relationship is known as Ohm's law

$$\mathbf{j} = \sigma(\mathbf{E} + \mathbf{u} \times \mathbf{B}). \quad (1.8)$$

According to the momentum equation (1.2), the dynamics of the flow depend on the behavior of \mathbf{B} and \mathbf{j} . Furthermore, owing to Ampère's law (1.6), \mathbf{j} is uniquely defined by \mathbf{B} . In other words, a single vectorial law linking \mathbf{B} to \mathbf{u} is actually enough to completely close the MHD model. Such an equation is derived by combining the curl of (1.6) with the curl of (1.8) and (1.7), which yields a transport equation for the magnetic field known as the induction equation

$$\frac{\partial \mathbf{B}}{\partial t} = \nabla \times (\mathbf{u} \times \mathbf{B}) + \frac{1}{\mu_0 \sigma} \Delta \mathbf{B}. \quad (1.9)$$

¹in which the displacement current $\mu_0 \epsilon_0 \partial_t \mathbf{E}$ may be neglected if the electrically conducting medium happens to be a liquid metal.

1.2 The underlying physics of MHD

1.2.1 The low- Rm approximation

Striking similarities arise when comparing the vorticity and the induction equations, which in both cases are an advection/diffusion transport equation for the vorticity and the magnetic field respectively. More importantly, there appears to be an intricate feedback between these two quantities. In order to illustrate it, let us consider an initially at rest body of fluid, which is immersed in a static and uniform magnetic field \mathbf{B}_0 . The initial state (characterized by $\mathbf{u} = 0$ and $\mathbf{B} = \mathbf{B}_0$), is now perturbed by a small velocity perturbation \mathbf{u}_i . The subsequent state is characterized by $\mathbf{u} = \mathbf{u}_i$ and $\mathbf{B} = \mathbf{B}_0 + \mathbf{b}_i$. For the sake of this discussion, we assume that the fluid remains incompressible throughout this perturbation process, implying that the fluid's density remains constant. We finally neglect momentum diffusion (characterized by ν) over magnetic diffusion (measured by $1/\mu_0 \sigma$). Indeed, the magnetic Prandtl number $Pr_m = \mu_0 \sigma \nu$ for the liquid metal used in our experiment is $Pr_m = 1.7 \times 10^{-6}$, indicating that the former effect is about one million times smaller than the latter. Linearizing the inviscid vorticity equation (1.3) in which has been substituted Ampère's law (1.6), and the induction equation (1.9) yields

$$\frac{\partial \boldsymbol{\omega}_i}{\partial t} = \frac{B_0}{\mu_0 \rho} \frac{\partial(\nabla \times \mathbf{b}_i)}{\partial \mathbf{x}_{\parallel}}, \quad (1.10)$$

and

$$\frac{\partial \mathbf{b}_i}{\partial t} = B_0 \frac{\partial \mathbf{u}_i}{\partial \mathbf{x}_{\parallel}} + \frac{1}{\mu_0 \sigma} \Delta \mathbf{b}_i, \quad (1.11)$$

where we have notated $B_0 = \|\mathbf{B}_0\|$, and $B_0 \partial/\partial \mathbf{x}_{\parallel} = (\mathbf{B}_0 \cdot \nabla)$ the directional derivative along the magnetic field. Injecting (1.11) and the Laplacian of (1.10) into time differentiated (1.10) leads to a governing equation for the vorticity perturbation alone

$$\frac{\partial^2 \boldsymbol{\omega}_i}{\partial t^2} - \frac{1}{\mu_0 \sigma} \Delta \left(\frac{\partial \boldsymbol{\omega}_i}{\partial t} \right) = \frac{B_0^2}{\mu_0 \rho} \frac{\partial^2 \boldsymbol{\omega}_i}{\partial \mathbf{x}_{\parallel}^2}. \quad (1.12)$$

Let us now write equation (1.12) in dimensionless form. To do so, we introduce a typical length scale L and a typical velocity scale U , such that the typical time scale of the flow is given by $\tau_u = L/U$. The non dimensional variables $\tilde{\boldsymbol{\omega}}_i$, $\tilde{\mathbf{x}}_{\parallel}$ and \tilde{t} are subsequently defined as $\tilde{\boldsymbol{\omega}}_i = \boldsymbol{\omega}_i \tau_u$, $\tilde{\mathbf{x}}_{\parallel} = \mathbf{x}_{\parallel}/L$ and $\tilde{t} = t/\tau_u$, while the non dimensional Laplacian operator is defined as $\tilde{\Delta} = L^2 \Delta$. We finally introduce the Joule time $\tau_J = \rho/\sigma B_0^2$, which characterizes the electromagnetic effects, as well as the magnetic diffusion time $\tau_m = \mu_0 \sigma L^2$. All in all, the non dimensional form of equation (1.12) is given by

$$Rm \frac{\partial^2 \tilde{\boldsymbol{\omega}}_i}{\partial \tilde{t}^2} - \tilde{\Delta} \left(\frac{\partial \tilde{\boldsymbol{\omega}}_i}{\partial \tilde{t}} \right) = N \frac{\partial^2 \tilde{\boldsymbol{\omega}}_i}{\partial \tilde{\mathbf{x}}_{\parallel}^2}, \quad (1.13)$$

1. BASICS OF MAGNETOHYDRODYNAMICS

where $Rm = \tau_m/\tau_u$ and $N = \tau_u/\tau_J$ are known as the magnetic Reynolds number and the interaction parameter respectively. Values of the physical parameters found in our experimental setup are for instance $L = 0.15$ m, $\rho = 6400$ kg/m³, $\sigma = 3.4 \times 10^6$ S/m, $B_0 \sim [0.25 - 10]$ T and $U \sim [0.08 - 0.3]$ m/s. As a result, Rm and N lie in the range

$$Rm \sim [0.03 - 0.13] \quad \text{and} \quad N \sim [60 - 30000]. \quad (1.14)$$

Equation (1.13) highlights the feedback resulting from electromagnetism on the flow. Owing to the regimes accessible in our experiment, we shall hereafter restrict ourselves to flows characterized by $N \gg 1$ and $Rm \ll 1$. While the former criterion merely states that we shall focus on regimes where electromagnetic effects are indeed observable, the latter criterion is slightly more cryptic. To get a better understanding of the meaning of Rm , let us take a closer look at the induction equation reproduced below

$$\frac{\partial \mathbf{B}}{\partial t} = \nabla \times (\mathbf{u} \times \mathbf{B}) + \frac{1}{\mu_0 \sigma} \Delta \mathbf{B}. \quad (1.15)$$

With words, equation (1.15) states that the magnetic field may simultaneously be advected by the flow at the velocity \mathbf{u} , while also being diffused within the medium with a magnetic diffusivity $1/\mu_0 \sigma$. The diffusive process is in fact the consequence of the source/field relationship stemming from Ampere's law (1.6). Considering perturbations around the same equilibrium state defined previously, the linearized induction equation at leading order reads

$$\frac{\partial \mathbf{b}_i}{\partial t} = \nabla \times (\mathbf{u}_i \times \mathbf{B}_0) + \frac{1}{\mu_0 \sigma} \Delta \mathbf{b}_i, \quad (1.16)$$

which may also be put in dimensionless form by introducing $\tilde{\mathbf{b}}_i = \mathbf{b}_i/\|\mathbf{b}_i\|$ and $\tilde{\mathbf{B}}_0 = \mathbf{B}_0/\|\mathbf{B}_0\|$ the non-dimensional induced and imposed static magnetic fields respectively. Keeping L , U and τ_u the typical length, velocity and time scales of the system yields

$$\frac{\|\mathbf{b}_i\|}{\|\mathbf{B}_0\|} \frac{\partial \tilde{\mathbf{b}}_i}{\partial \tilde{t}} = \tilde{\nabla} \times (\tilde{\mathbf{u}}_i \times \tilde{\mathbf{B}}_0) + \frac{1}{Rm} \frac{\|\mathbf{b}_i\|}{\|\mathbf{B}_0\|} \tilde{\Delta} \tilde{\mathbf{b}}_i. \quad (1.17)$$

In the limit of small perturbations $\|\mathbf{b}_i\|/\|\mathbf{B}_0\| \ll 1$, the time rate of change of the induced magnetic field may be neglected compared to the other terms. This framework (also known as the quasi-static approximation), refers to a state where the total magnetic field $\mathbf{B} = \mathbf{B}_0 + \mathbf{b}_i$ is instantly homogenized throughout the system thanks to the transportation of \mathbf{b}_i . Within this context, Rm appears to be a measure of the ratio $\|\mathbf{b}_i\|/\|\mathbf{B}_0\|$. Indeed, equation (1.17) implies

$$Rm \sim \frac{\|\mathbf{b}_i\|}{\|\mathbf{B}_0\|}.$$

To summarize, the $Rm \ll 1$ limit, also known as the low- Rm approximation, implies that the magnetic field induced by the flow is negligible compared to the imposed static magnetic field. That is to say

$$\mathbf{B} = \mathbf{B}_0. \quad (1.18)$$

This last result has crucial consequences on how MHD effects will be modeled from now on. Indeed, assuming the imposed magnetic field is static simplifies Faraday's law to

$$\nabla \times \mathbf{E} = 0, \quad (1.19)$$

hence one can define an electrostatic potential ϕ from which \mathbf{E} derives

$$\mathbf{E} = -\nabla\phi. \quad (1.20)$$

Arguments (1.18) and (1.20) drastically simplify the coupling between hydrodynamics and electromagnetism. Indeed, the Lorentz force simply becomes

$$\frac{\mathbf{j} \times \mathbf{B}_0}{\rho}, \quad (1.21)$$

while Ohm's law may be written as

$$\mathbf{j} = \sigma(-\nabla\phi + \mathbf{u} \times \mathbf{B}_0). \quad (1.22)$$

In other words, the low- Rm framework with a static magnetic field implies that the Lorentz force now depends on the current density exclusively, which in turn depends on the velocity field \mathbf{u} and a single scalar function ϕ . From a mathematical point of view, this reduces the number of electromagnetic unknowns from nine in the general case (i.e. one for each component of \mathbf{E} , \mathbf{B} and \mathbf{j}) to four in the low- Rm case: one for each component of \mathbf{j} , plus one for ϕ . The former is given by Ohm's law (1.22), while the latter is given by the conservation of charge, which stems from the divergence of Ampere's law

$$\nabla \cdot \mathbf{j} = 0. \quad (1.23)$$

Equation (1.23) states that the current density field is solenoidal. To conclude, the low- Rm approximation simplifies equation (1.13) by making the term involving the second order time derivatives negligible. Within this framework, the coupling between hydrodynamics and electromagnetism manifests itself as a “pseudo-diffusion” of vorticity along the main magnetic field.

1.2.2 The effect of the Lorentz force at low- Rm

Until now, we have purposely avoided any discussion about the current density, whose effects implicitly appeared in the induction equation through the induced magnetic field \mathbf{b}_i . Although it is mathematically correct to define the current density from the induced magnetic field a posteriori using Ampère's law, this reasoning misses some crucial physics, if only because Ampère's law is a non local integral definition of \mathbf{b}_i . In other words, magnetic fields originate from electric currents, not the other way around. Understanding the behavior of these electric currents is therefore fundamental to get a good grasp of the physics at stake.

1. BASICS OF MAGNETOHYDRODYNAMICS

As such, let us examine the divergence and curl of the current density field, respectively given by the conservation of charge

$$\nabla \cdot \mathbf{j} = 0, \quad (1.24)$$

and the curl of Ohm's law

$$\nabla \times \mathbf{j} = \sigma B_0 \frac{\partial \mathbf{u}}{\partial \mathbf{x}_{\parallel}}. \quad (1.25)$$

Equation (1.25) implies that velocity gradients along the magnetic field are a source of electric current, while the conservation of charge (1.24) requires the current density field to be solenoidal. In other words, electric loops are drawn everywhere velocity gradients along the magnetic field exist. This phenomenon is illustrated on a blob of swirling fluid in figure 1.1 below.

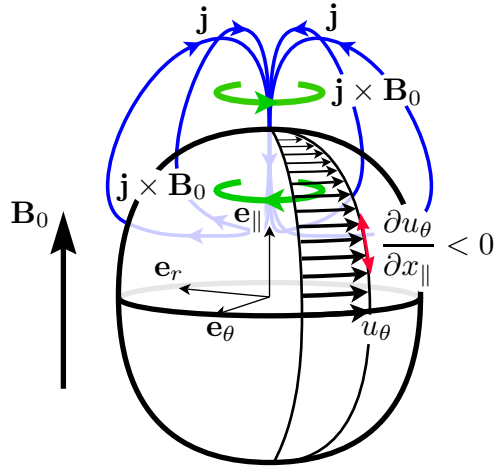


Figure 1.1. The effect of the Lorentz force: velocity gradients along \mathbf{e}_z (red arrow) produce current loops in the $(\mathbf{e}_r, \mathbf{e}_{\parallel})$ meridional plane (blue loops), eventually leading to a restoring force along \mathbf{e}_{θ} (green arrows). The net effect of the Lorentz force is to smooth out the initial velocity gradient in the direction of the magnetic field.

For the following reasoning, we adopt a cylindrical system of coordinates, such that the blob is characterized by a positive azimuthal velocity $\mathbf{u} = u_{\theta} \mathbf{e}_{\theta}$. This structure is assumed to be immersed in a steady and uniform magnetic field $\mathbf{B}_0 = B_0 \mathbf{e}_{\parallel}$. The configuration presented here evidently possesses a gradient of azimuthal velocity along \mathbf{B}_0 , such that according to the azimuthal component of (1.25), eddy currents are drawn in the $(\mathbf{e}_r, \mathbf{e}_{\parallel})$ meridional plane. Following Ohm's law, current is generated according to the electromotive force $\mathbf{u} \times \mathbf{B}_0$, which is merely proportional to \mathbf{u} . The electric current must therefore exit the blob where its azimuthal velocity is the greatest, and loop back where it is the smallest, yielding counter-clockwise current paths in the meridional plane. The current loops run through the core of the blob, where the strong velocity gradients along \mathbf{e}_r are spared. A Lorentz force $\mathbf{j} \times \mathbf{B}_0$ eventually results from the coupling between the current loops and

the magnetic field. Since the direction of the Lorentz force depends on the direction of the current density \mathbf{j} , it will act in opposite directions whether the fluid particles lay inside or outside of the blob. Ultimately, the Lorentz force functions as a restoring force, which tends to smooth out velocity gradients along \mathbf{B}_0 . It does so by accelerating the quiescent fluid particles, while simultaneously decelerating the fluid particles laying in the region of intense swirl. In the process, the eddy currents whose very origins are the velocity gradients are damped and disappear: the Lorentz force acts towards its own destruction.

Using a global approach, Davidson (1995) quantified how the effects illustrated above impacted MHD flows. In particular, he considered an inviscid random flow (viscous friction is momentarily put aside to put the emphasis on the effects of the Lorentz force) immersed in a steady and uniform vertical magnetic field $B_0 \mathbf{e}_{\parallel}$. The flow is further enclosed in a spherical domain \mathcal{V} bounded by perfectly insulating and impermeable walls. To begin with, he considers the conservation of global angular momentum $\mathbf{H} = \int (\mathbf{x} \times \mathbf{u}) dV$, which reads

$$\frac{\partial \mathbf{H}}{\partial t} = \frac{1}{\rho} \int_{\mathcal{V}} [\mathbf{x} \times (\mathbf{j} \times \mathbf{B}_0)] dV. \quad (1.26)$$

He showed that (1.26) may in fact be put in the following equivalent form

$$\frac{\partial \mathbf{H}}{\partial t} = -\frac{\sigma B_0^2}{4\rho} \mathbf{H}_{\perp}, \quad (1.27)$$

which implies, once integrated over time that $H_{\parallel} = \mathbf{H} \cdot \mathbf{e}_{\parallel}$ is constant, while $\mathbf{H}_{\perp} = \mathbf{H} - H_{\parallel} \mathbf{e}_{\parallel}$ decays exponentially. That is to say, vortical structures whose rotation axis is perpendicular to the magnetic field are destroyed preferentially, while those aligned with the magnetic field are left untouched. In addition, he considers the global budget of kinetic energy $E = \int \mathbf{u}^2 / 2 dV$, which is found by integrating the work energy principle for the fluid over the domain \mathcal{V} , yielding

$$\frac{\partial E}{\partial t} = - \int_{\mathcal{V}} \frac{\mathbf{j}^2}{\rho \sigma} dV. \quad (1.28)$$

Equation (1.28) means that while working, the Lorentz force dissipates kinetic energy. Finally, by applying the Schwarz inequality to the definition of H_{\parallel} , Davidson (1995) derived a lower bound for the kinetic energy E

$$E \geq \frac{H_{\parallel}^2}{2} \left[\int_{\mathcal{V}} \mathbf{x}_{\perp}^2 dV \right]^{-1}. \quad (1.29)$$

The result of the Lorentz force on the flow is fully appreciated by considering equations (1.27), (1.28) and (1.29) simultaneously. The Lorentz force tends to destroy the components of angular momentum, which are perpendicular to the magnetic field. This process is accompanied by Joule damping (i.e. the dissipation of kinetic energy into heat), which stems from current loops being generated where velocity gradients exist. Assuming H_{\parallel} is

initially non zero, a lower bound exists for E , meaning that no matter how dissipative the Lorentz force is, it cannot bring the flow of an inviscid fluid to a full stop. What ensues is a flow of minimal kinetic energy, which is characterized by rotating structures all aligned with the magnetic field. Additionally, the flow has become independent of the spatial coordinate along \mathbf{B}_0 , and has thus been two-dimensionalized. Davidson (1995) finally stresses that this whole process conserves momentum globally, since

$$\int_V (\mathbf{j} \times \mathbf{B}_0) \, dV = 0. \quad (1.30)$$

In other words, the acceleration of a fluid particle is concurrent with the deceleration of another one (and vice versa), both contributions canceling each other out such that no net momentum is produced. In that respect, it can be said that the Lorentz force redistributes momentum in space.

Sommeria & Moreau (1982) gave a simple, yet powerful local interpretation of the effects of the Lorentz force, when electromagnetic effects are assumed to act much quicker than inertia (i.e. in the limit $\tau_J \ll \tau_u$). The prototype chosen for this demonstration is an inviscid vortex immersed in a vertical magnetic field $\mathbf{B}_0 = B_0 \mathbf{e}_{\parallel}$. The vortex is assumed to be characterized by a height l_{\parallel} along the magnetic field, and characteristic width l_{\perp} across it. Their argument relies on the Helmholtz decomposition of the Lorentz force (first put forward by Roberts (1967)), which states that any vector field \mathbf{f} may be split into an irrotational and a solenoidal component \mathbf{f}_I and \mathbf{f}_S respectively

$$\mathbf{f} = \mathbf{f}_I + \mathbf{f}_S, \quad (1.31)$$

with

$$\mathbf{f}_I = \nabla [\Delta^{-1}(\nabla \cdot \mathbf{f})] \quad \text{and} \quad \mathbf{f}_S = -\Delta^{-1}[\nabla \times (\nabla \times \mathbf{f})]. \quad (1.32)$$

In the particular case where $\mathbf{f} = B_0 (\mathbf{j} \times \mathbf{e}_{\parallel}) / \rho$, and assuming that the low- Rm approximation holds, one has

$$\mathbf{f}_I = -\frac{\sigma B_0^2}{\rho} \nabla \left[\Delta^{-1} \left(\frac{\partial u_{\parallel}}{\partial x_{\parallel}} \right) \right] \quad \text{and} \quad \mathbf{f}_S = -\frac{\sigma B_0^2}{\rho} \Delta^{-1} \left(\frac{\partial^2 \mathbf{u}}{\partial x_{\parallel}^2} \right), \quad (1.33)$$

where the Δ^{-1} operator refers to the inverse Laplacian. It is an integral operator whose existence implicitly depends on the prescription of boundary conditions. Under the assumption $\tau_J \ll \tau_u$, one can expect $l_{\parallel} > l_{\perp}$, hence the velocity gradients along the magnetic field may be assumed negligible compared to those in the direction perpendicular to it. The Δ^{-1} operator may then be approximated by Δ_{\perp}^{-1} . Still in the inviscid limit, the governing equation for the vorticity component aligned with \mathbf{B}_0 turns out to be

$$\frac{\partial \omega_{\parallel}}{\partial t} = -\frac{\sigma B_0^2}{\rho} \Delta_{\perp}^{-1} \left(\frac{\partial^2 \omega_{\parallel}}{\partial x_{\parallel}^2} \right). \quad (1.34)$$

Sommeria & Moreau (1982) interpreted equation (1.34) as a pseudo-diffusion equation, whose overall effect is to smooth out vorticity gradients in the direction parallel to the magnetic field, therefore bringing the structure towards a 2D configuration (in the sense that it does not depend on x_{\parallel} anymore). This diffusive process has the particularity of acting with the diffusivity $\alpha \sim \sigma B_0^2 l_{\perp}^2 / \rho$ which depends on the transverse scale of the structure l_{\perp} . Writing (1.34) non dimensionally with $\tilde{z} = z/l_{\parallel}$, $\tilde{\Delta}_{\perp}^{-1} = \Delta_{\perp}^{-1}/l_{\perp}^2$ and $\tau_J = \rho/\sigma B_0^2$ yields the characteristic time τ_{2D} representing the time needed by the Lorentz force to diffuse the momentum of a structure of width l_{\perp} over the distance l_{\parallel} along the magnetic field:

$$\tau_{2D} = \tau_J \left(\frac{l_{\parallel}}{l_{\perp}} \right)^2. \quad (1.35)$$

1.2.3 Recapitulation

Let us now summarize the low- Rm MHD model that we will be using hereafter. From now on, the magnetic field will be assumed to be vertical and pointing along \mathbf{e}_z . Viscous friction is also reintroduced. According to our discussion thus far, all the physics of low- Rm MHD are contained in the following set of equations

$$\frac{\partial \mathbf{u}}{\partial t} + \mathbf{u} \cdot \nabla \mathbf{u} = -\frac{\nabla p^*}{\rho} + \nu \Delta \mathbf{u} - \frac{\sigma B_0^2}{\rho} \Delta^{-1} \left(\frac{\partial^2 \mathbf{u}}{\partial z^2} \right), \quad (1.36)$$

$$\nabla \cdot \mathbf{u} = 0, \quad (1.37)$$

where $p^* = p - \sigma B_0^2 \Delta^{-1}(\partial_z u_z)$ represents the sum of magnetic and hydrodynamic pressure. Of course, the set of equations (1.36) - (1.37) must be closed by boundary conditions: no-slip boundaries for the velocity, and electrically insulating walls for the current. Physical boundaries will be introduced in the next section. The impact of walls is a fundamental aspect of the work presented here and will be extensively discussed throughout the thesis.

Let us now take the non dimensional form of the momentum equation (1.36). According to our previous discussion, we can expect the flow to quickly become anisotropic under the influence of the Lorentz force. We therefore introduce two different characteristic lengthscales L_{\perp} and L_z in the directions perpendicular and parallel to the magnetic field respectively. We define the following non dimensional variables $\tilde{z} = z/L_z$, $\tilde{\mathbf{u}} = \mathbf{u}/U$ and $\tilde{p}^* = p^*/\rho U^2$, as well as the non dimensional operator $\tilde{\nabla} = L_{\perp} \nabla$. Let us also keep $\tau_u = L_{\perp}/U$ to characterize inertia, such that $\tilde{t} = t/\tau_u$. According to the previous sections, there are several MHD effects, which must carefully be accounted for. On the one hand, velocity gradients induce eddy currents, which are drawn along the time scale $\tau_J = \rho/\sigma B_0^2$. On the other hand, these eddy currents interact with the magnetic field and generate Lorentz forces, which then tend to diffuse momentum along \mathbf{B}_0 in the time $\tau_{2D} = \tau_J (L_z/L_{\perp})^2$. We finally introduce the characteristic time $\tau_{\nu} = L_{\perp}^2/\nu$, which is associated to viscous friction. All in all, the dimensionless form of (1.36) is given by

$$\frac{\partial \tilde{\mathbf{u}}}{\partial t} + \tilde{\mathbf{u}} \cdot \tilde{\nabla} \tilde{\mathbf{u}} = -\tilde{\nabla} \tilde{p}^* + Re^{-1} \tilde{\Delta} \tilde{\mathbf{u}} - N \left(\frac{L_\perp}{L_z} \right)^2 \tilde{\Delta}^{-1} \left(\frac{\partial^2 \tilde{\mathbf{u}}}{\partial z^2} \right). \quad (1.38)$$

The equation above introduces two non-dimensional parameters, which are the Reynolds number Re and the interaction parameter N respectively defined by

$$Re = \frac{UL_\perp}{\nu} = \frac{\tau_\nu}{\tau_u} \quad \text{and} \quad N = \frac{\sigma B_0^2 L_\perp}{\rho U} = \frac{\tau_u}{\tau_J}. \quad (1.39)$$

From (1.39), it is apparent that Re quantifies the competition between viscous friction and inertia (in particular $Re \gg 1$ suggests that the flow will be turbulent), while N characterizes the amount of electric current that is drawn for a given velocity gradient. More specifically, $N \gg 1$ suggests that a substantial amount of electric current will originate from the flow, hence we can expect that the Lorentz force will play an important part in fixing its dynamics. However, N does not actually measure how the Lorentz force reshapes the flow. Indeed, according to equation (1.38) the diffusive effect of the Lorentz force is in fact of order $N(L_\perp/L_z)^2 = \tau_u/\tau_{2D}$, rather than just N . Sreenivasan & Alboussière (2002) highlighted experimentally this effect on a single vortex, which lead them to define the *true* interaction parameter $N_t = N(L_\perp/L_z)^2$ as the relevant non-dimensional parameter giving the balance between the solenoidal component of the Lorentz force and inertia. From equation (1.38), one may also anticipate the existence of a third non-dimensional parameter which must compare viscous dissipation to electromagnetic effects. This parameter is called the Hartmann number, and is in fact defined as the square of the ratio of these two aforementioned processes

$$Ha = B_0 L_z \sqrt{\frac{\sigma}{\rho\nu}} = \sqrt{\frac{\tau_\nu}{\tau_J}}. \quad (1.40)$$

Ha may in fact be written in terms of Re and N according to

$$Ha^2 = Re N. \quad (1.41)$$

To conclude this part, let us compute the orders of magnitude of the aforementioned numbers in order to get a first idea of the flow regimes encountered in our experiment. The orders of magnitudes of the different parameters are $L_\perp = 0.15$ m, $L_z = 0.1$ m, $U \sim [0.08 - 0.3]$ m/s, $B_0 \sim [0.25 - 10]$ T, $\rho = 6400$ kg/m³, $\nu = 4 \times 10^{-7}$ m²/s and $\sigma = 3.4 \times 10^6$ S/m, which give

$$Re \sim [30000 - 100000], \quad N \sim [60 - 30000] \quad \text{and} \quad Ha \sim [900 - 36000].$$

1.3 Wall-bounded flows

Now that the basic physics at stake have been clarified, and that the equations for the low- Rm approximation with a static magnetic field have been derived, it is time to take a closer look at the effects introduced by boundaries. Sticking to cases close to our experimental setup, we will focus exclusively on no-slip and perfectly electrically insulating walls.

1.3.1 A fundamental example: the Hartmann channel flow

Let us consider the flow studied by Hartmann (1937), which is represented in figure 1.2. The Hartmann flow consists of a 2D flow taking place in the $(\mathbf{e}_x, \mathbf{e}_z)$ plane, confined between two infinite and horizontal walls. These two walls are located a distance $2h$ apart from each other in the \mathbf{e}_z direction, and are assumed to be no-slip and perfectly electrically insulating i.e. $\mathbf{u}(x, z = \pm h) = 0$ and $j_z(x, z = \pm h) = 0$ respectively. The fluid is put in motion by a constant pressure gradient $-\nabla p = -G_x \mathbf{e}_x$. A vertical static and uniform magnetic field $\mathbf{B} = B_0 \mathbf{e}_z$ is applied perpendicularly to the walls, and the low- Rm approximation is assumed to hold.

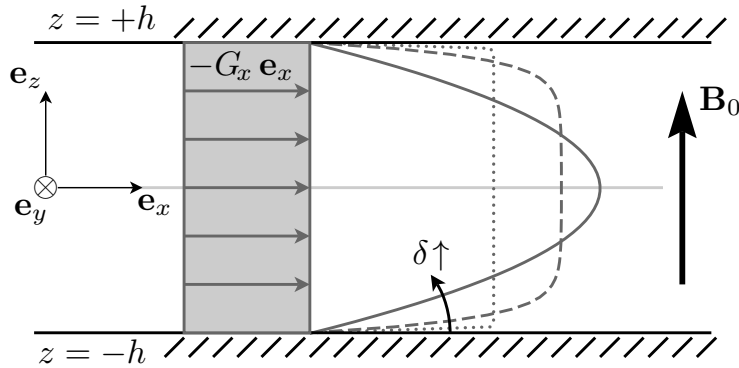


Figure 1.2. Fully established Hartmann flow of an electrically conducting fluid between two electrically insulating horizontal walls. (.....) and (---): Hartmann profiles for increasing values of δ . (—): plane Poiseuille profile recovered for $\delta = \infty$.

Thanks to the symmetry with respect to the channel's center-plane, it is safe to look for a velocity field of the form $\mathbf{u} = u_x(x, z) \mathbf{e}_x$. No assumptions are made on the current density field however, hence $\mathbf{j} = \mathbf{j}(x, z)$. It is finally assumed that the flow is steady and laminar. All in all, the governing equations for this problem boil down to

$$\frac{G_x}{\rho} \mathbf{e}_x = \nu \Delta \mathbf{u} + \frac{B_0}{\rho} \mathbf{j} \times \mathbf{e}_z, \quad (1.42)$$

$$\mathbf{j} = \sigma (-\nabla \phi + B_0 u_x \mathbf{e}_y), \quad (1.43)$$

$$\frac{\partial u_x}{\partial x} = 0, \quad (1.44)$$

$$\frac{\partial j_x}{\partial x} + \frac{\partial j_z}{\partial z} = 0. \quad (1.45)$$

The continuity equation states that $u_x = u_x(z)$. Consequently, the x and y components of the momentum equation require that $j_y = j_y(z)$ and $j_x = 0$ respectively. Combining this

1. BASICS OF MAGNETOHYDRODYNAMICS

latter result with the conservation of charge, and the insulating boundary condition yields $j_z = 0$. The current profile must therefore be of form

$$\mathbf{j} = j_y(z) \mathbf{e}_y. \quad (1.46)$$

The only non-zero component of Ohm's law requires ϕ to be a function of y exclusively. At the same time, taking the divergence of Ohm's law reads

$$\frac{\partial^2 \phi}{\partial y^2} = 0, \quad (1.47)$$

which eventually imposes

$$\nabla \phi = E_0 \mathbf{e}_y, \quad (1.48)$$

with E_0 representing the constant electric field. Taking the x component of the momentum equation, in which has been re-injected Ohm's law, the velocity profile is found to be a solution of

$$\frac{\partial^2 u_x}{\partial z^2} - \frac{u_x}{\delta^2} = \frac{G_x + \sigma E_0 B_0}{\rho \nu}, \quad (1.49)$$

where the parameter δ is defined as $\delta = B_0^{-1} \sqrt{\rho \nu / \sigma}$. The no-slip boundary conditions on the top and bottom walls eventually yield the Hartmann velocity profile

$$u_x(z) = U_H \left[1 - \frac{\cosh(z/\delta)}{\cosh(h/\delta)} \right], \quad (1.50)$$

where the constant $U_H = -\delta^2 (G_x + \sigma E_0 B_0) / \rho \nu$ may be interpreted as the value of the velocity on the channel's centerline. In the limit of non conducting fluids, $\sigma \rightarrow 0$ i.e. $\delta \rightarrow \infty$. Solution (1.50) may then be expanded in a Taylor series of small parameters $z/\delta \ll 1$ and $h/\delta \ll 1$. Keeping the terms of second order at most, and noting $U_P = -G_x h^2 / 2 \rho \nu$, one can recover the parabolic Poiseuille profile

$$u_x(z) = U_P \left[1 - \left(\frac{z}{h} \right)^2 \right]. \quad (1.51)$$

The evolution of the Hartmann profile with δ (or equivalently B_0^{-1}) is sketched in figure 1.2. There are two important features to notice. First of all, the velocity profile in the bulk flattens as δ decreases (i.e. as the magnetic field becomes more and more influential), while the velocity gradients close to the walls become steeper. This behavior reflects the fact that a boundary layer of characteristic thickness δ develops along the perpendicular walls, where viscous friction balances out electromagnetic effects. Second of all, the maximum velocity, which is found on the channel's centerline, increases with δ . To quantify this effect a little further, let us examine the flow rate defined as the integral of $u_x(z)$ over the height of the channel

$$Q = - \frac{2 h \delta^2 (G_x + \sigma E_0 B_0)}{\rho \nu} \left[1 - \frac{\delta}{h} \frac{\sinh(h/\delta)}{\cosh(h/\delta)} \right]. \quad (1.52)$$

According to equation (1.52), there are two ways to drive a flow, either by applying a pressure gradient G_x , or by applying an electric field E_0 (viz. injecting electric current along \mathbf{e}_y). Regardless of the driving mechanism, increasing the magnetic field appears to brake the flow. Electromagnetic effects in the presence of no-slip walls therefore introduce energy dissipation in addition to viscosity. This argument can be seen the other way around: for a given flowrate, the pressure drop is all the more important, as the magnetic field is high.

1.3.2 The Hartmann Layer

As we have seen in the previous example, there is a region close to the walls perpendicular to \mathbf{B}_0 where viscous friction and electromagnetic effects balance each other out. A boundary layer, known as the Hartmann layer results, which has a characteristic thickness $\delta = B_0^{-1} \sqrt{\rho\nu/\sigma}$. The thickness of the Hartmann layer is related to the Hartmann number Ha following

$$\delta = \frac{h}{Ha}, \quad (1.53)$$

where h stands for the typical lengthscale in the direction of the magnetic field. In a laboratory scale experiment, δ is usually quite thin. For instance, with $h = 0.1\text{ m}$ and $Ha \sim [900 - 36000]$ in our experiment, δ typically lies in the range $\delta \sim [3\mu\text{m} - 1\text{mm}]$. It nonetheless has an active feedback on the flow. Figure 1.3 gives a generic close up view of a Hartmann layer, which has developed along a rigid, no-slip and perfectly insulating wall. Owing to mass conservation and the extreme thinness of δ , the bulk right above the Hartmann layer can be approximated by a two component vector field laying within the plane perpendicular to the magnetic field. It is thus characterized by a velocity $\mathbf{u}_\perp^\infty = \|\mathbf{u}_\perp^\infty\| \mathbf{e}_\perp$ and current density \mathbf{j}_\perp^∞ . The velocity profile in the Hartmann layer may therefore be expected to be of the form

$$\mathbf{u}_\perp(x, y, z) = \mathbf{u}_\perp^\infty(x, y) f(z). \quad (1.54)$$

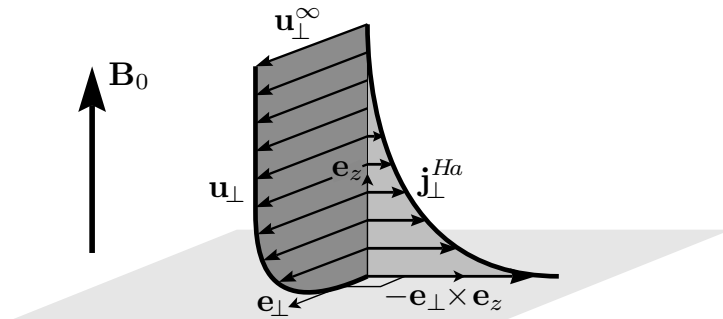


Figure 1.3. Close up view of the Hartmann layer developing along a no-slip and electrically insulating wall perpendicular to the magnetic field. The velocity and current density profiles are exponential.

1. BASICS OF MAGNETOHYDRODYNAMICS

The equation governing the flow inside the Hartmann layer is found by applying the boundary layer approximation to (1.2), for flows laying exclusively in the perpendicular plane. First of all, we restrict ourselves to the asymptotic limit $N \gg 1$, for which inertia is negligible compared to electromagnetic effects. Second of all, we also impose the asymptotic limit $Ha \gg 1$, which makes the thickness of the Hartmann layer much smaller than any other lengthscale. As a result, horizontal derivatives are negligible compared to vertical ones. Ultimately, the governing equation for the Hartmann layer becomes

$$\frac{\partial^2 \mathbf{u}_\perp}{\partial z^2} - \frac{\mathbf{u}_\perp}{\delta^2} = \frac{\mathbf{G}_\perp^\infty(x, y)}{\rho\nu}, \quad (1.55)$$

where $\mathbf{G}_\perp^\infty(x, y)$ refers to the force driving \mathbf{u}_\perp^∞ in the first place. Both are related to each other via $\mathbf{u}_\perp^\infty = -\mathbf{G}_\perp^\infty \delta^2 / \rho\nu$. The driving force $\mathbf{G}_\perp^\infty(x, y)$ acts perpendicularly to the magnetic field, and is taken constant along \mathbf{e}_z . It may for instance, be a pressure gradient or an electric field. Since the Hartmann layer acts as a buffer layer between the no-slip wall and the bulk, its velocity profile must satisfy the following boundary conditions: $\mathbf{u}_\perp(x, y, 0) = 0$ and $\mathbf{u}_\perp(x, y, \infty) = \mathbf{u}_\perp^\infty$. Under these circumstances, the velocity profile inside the bottom Hartmann layer scales as

$$\mathbf{u}_\perp(x, y, z) = \mathbf{u}_\perp^\infty(x, y) [1 - \exp(-z/\delta)]. \quad (1.56)$$

The current density profile \mathbf{j}_\perp may now be determined by injecting (1.56) into Ohm's law. It consequently appears that \mathbf{j}_\perp can be split into two contributions

$$\mathbf{j}_\perp = \mathbf{j}_\perp^\infty + \mathbf{j}_\perp^{Ha}, \quad (1.57)$$

where $\mathbf{j}_\perp^\infty = \sigma(-\nabla\phi + \mathbf{u}_\perp^\infty \times \mathbf{B}_0)$ can be physically interpreted as the electric current resulting from the flow in the bulk, while $\mathbf{j}_\perp^{Ha} = -\sigma \mathbf{u}_\perp^\infty \times \mathbf{B}_0 \exp(-z/\delta)$ refers to the electric content of the Hartmann layer. Integrating \mathbf{j}_\perp^{Ha} along \mathbf{B}_0 yields

$$\int_0^\infty \mathbf{j}_\perp^{Ha} dz = \sigma \delta \mathbf{u}_\perp^\infty \times \mathbf{B}_0. \quad (1.58)$$

Equation (1.58) in fact states that the Hartmann layer's current content is proportional to the velocity field right above it (Heiser & Shercliff, 1965). In other words, the flow of an electrically conducting fluid along a no-slip and insulating wall is necessarily accompanied by electric current being drawn within the boundary layer (as a matter of fact the magnitude of \mathbf{j}_\perp^{Ha} happens to be maximum at the wall). A charge budget across the Hartmann layer yields

$$j_z^\infty - j_z^w = - \int_0^\infty \nabla_\perp \cdot \mathbf{j}_\perp^{Ha} dz, \quad (1.59)$$

where j_z^∞ and j_z^w refer to the vertical current density right outside the Hartmann layer and at the wall respectively. Equation (1.58) may then be re-interpreted in terms of vertical current

j_z and vertical vorticity ω_z by substituting the actual expression for \mathbf{j}_\perp^{Ha} within (1.59), which eventually gives

$$j_z^\infty - j_z^w = \sigma \delta B_0 \omega_z^\infty. \quad (1.60)$$

In the case where a perfectly insulating wall is considered, $j_z^w = 0$. The vorticity component aligned with \mathbf{B}_0 can then be seen as either extracting or introducing electric current (depending on the sign of ω_z^∞) from/into the boundary layer. Indeed, the vorticity measured right outside the Hartmann layer is merely proportional to the electric current crossing the layer vertically. On the other hand, if electric current is injected locally, then $j_z^w \neq 0$. Owing to (1.60), vorticity may then be driven by injecting current in the liquid metal layer sitting above the wall.

According to the z component of Ohm's law, and assuming the wall is perfectly insulating in equation (1.60), the order of magnitude of the vertical voltage drop across the Hartmann layer may be estimated by

$$\left. \frac{\partial \phi}{\partial z} \right|_{Ha} = \frac{j_z^\infty}{\sigma} \sim \delta B_0 \omega_z^\infty. \quad (1.61)$$

At the same time, the horizontal component of Ohm's law yields the order of magnitude of the horizontal voltage difference within the Hartmann layer

$$\|\nabla_\perp \phi\|_{Ha} \sim B_0 \|\mathbf{u}_\perp^\infty\|. \quad (1.62)$$

Combining (1.61) and (1.62) yields the following ratio for the electric potential gradient inside the Hartmann layer

$$\left. \frac{\partial \phi}{\partial z} \right|_{Ha} \sim \frac{\|\nabla_\perp \phi\|_{Ha}}{Ha}. \quad (1.63)$$

The vertical contribution $\partial_z \phi|_{Ha}$ appears to vary Ha times more slowly than the horizontal gradient $\|\nabla_\perp \phi\|_{Ha}$. In the limit $Ha \gg 1$, the electric potential may thus be considered invariant across the Hartmann layer. In other words, measuring the electric potential at the wall is equivalent to measuring the electric potential right outside the Hartmann layer. This fundamental result is at the heart of the velocimetry technique used in Flowcube, which has been analyzed for instance by Kljukin & Thess (1998). More specifically, the conservation of mass written non-dimensionally inside the Hartmann layer yields

$$\frac{\partial \tilde{u}_z}{\partial \tilde{z}} \sim \frac{\tilde{\nabla}_\perp \cdot \tilde{\mathbf{u}}_\perp}{Ha}. \quad (1.64)$$

The vertical velocity component u_z may therefore be neglected compared to the horizontal velocity component $\|\mathbf{u}_\perp\|$ in the vicinity of the Hartmann wall, when in the $Ha \gg 1$ limit. Consequently, the velocity field right above the Hartmann layer can be assumed to lie within the horizontal plane, hence may be defined through the stream function $\psi(x, y)$ following

$$\mathbf{u}_\perp^\infty(x, y) = \nabla \times (\psi \mathbf{e}_z). \quad (1.65)$$

1. BASICS OF MAGNETOHYDRODYNAMICS

The vertical vorticity right outside the Hartmann $\omega_z^\infty(x, y)$ is also defined from the stream function $\psi(x, y)$ according to

$$\omega_z^\infty(x, y) = -\Delta\psi. \quad (1.66)$$

As we have just seen with (1.63), the vertical gradient of electric potential may be neglected inside the Hartmann layer when $Ha \gg 1$, hence the conservation of charge and Ohm's law state that

$$\Delta\phi = \omega_z^\infty B_0, \quad (1.67)$$

right above the Hartmann wall. Since ϕ and ψ satisfy compatible boundary conditions, equations (1.66) and (1.67) yield the local relationship

$$\psi = -\frac{\phi}{B_0}. \quad (1.68)$$

That is to say, the iso-potential contours measured in the vicinity of the Hartmann layer can be readily interpreted as a map of the flow when $Ha \gg 1$. Since the electric potential is invariant across the Hartmann layer, measuring it at the wall is equivalent to measuring the value of the stream function outside the boundary layer. Note however that this result also implicitly requires the asymptotic limit $N \gg 1$ to be valid.

A final comment must be made regarding the stability of the Hartmann layer. This question is all the more legitimate, as we will be dealing exclusively with fully developed, turbulent flows. Yet if the Hartmann layer itself is turbulent, the proportionality between its current content and the velocity in the bulk is lost (Alboussière & Lingwood, 2000). The measuring technique described above may therefore not be assumed to hold. The most recent experimental study on the laminar/turbulent transition of the Hartmann layer was conducted by Moresco & Alboussière (2004). Their experimental setup consisted of an electrically driven flow of mercury taking place inside an annular channel with a square section. Moresco & Alboussière (2004) globally monitored the state of the flow via the friction factor, which quantifies the energy loss inside the duct as a result of viscous and Joule dissipation. In particular, they showed that in the limit $Ha \gg 1$, the friction factor depends consistently on the non dimensional parameter $R_\delta = Re/Ha$, where R_δ can incidentally be interpreted as a Reynolds number based on the thickness of the Hartmann layer δ , and the mean velocity of the flow. The transition of the Hartmann layer from a laminar to a turbulent state was found to occur at the critical value of $R_\delta \sim 380$. Throughout our experimental study, R_δ typically lay in the range $R_\delta \sim [3 - 33]$, which ensured that we always steered well clear of the infamous threshold.

1.3.3 Quasi-2D electrically driven vortices

We shall now discuss known results regarding electrically driven vortices, since they are the backbone of our experiment. The properties of such vortices were first quantitatively studied by Sommeria (1988), and have been successfully used ever since to drive and study

MHD turbulence (Sommeria, 1986), (Paret & Tabeling, 1998), (Klein & Pothérat, 2010). The experimental rig used by Sommeria (1988) consisted of a cylindrical box containing a thin layer of mercury of thickness a . The bottom plate was made out of an electrically insulating material, except at its center where a small copper electrode was inserted flush. The upper surface of the mercury was kept free and monitored, so that its curvature remained negligible throughout. This device was then inserted in a vertical and uniform magnetic field $B_0 \mathbf{e}_z$, and a total electric current I was injected via the center electrode. The electric current exited the device by an annular copper side wall. In these circumstances, a vortex centered on the electrode emerged as a result of the interaction between the radial component of the current and the vertical magnetic field (see figure 1.4).

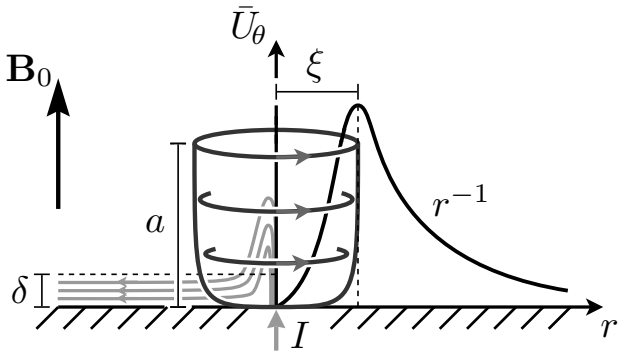


Figure 1.4. Electrically driven quasi-2D vortex in a shallow layer of height a . Free surface at the top (no boundary layer), Hartmann layer at the bottom $\delta = a/Ha$, shear layer along the axis of the vortex $\xi = a/\sqrt{Ha}$. The lines in light grey represent the current paths flowing exclusively in the Hartmann layers. The black curve shows the azimuthal velocity profile in the 2D bulk.

Sommeria (1988)'s model involves distinguishing between a boundary layer region of thickness $\delta = a/Ha$ where velocity gradients along z are prominent and a 2D bulk where velocity gradients along z are null. Following (1.56), the velocity profile in the Hartmann layer is given by

$$\mathbf{u}_\perp = \bar{\mathbf{U}}_\perp [1 - \exp(-z/\delta)], \quad (1.69)$$

where $\bar{\mathbf{U}}_\perp$ refers to the 2D velocity in the bulk. The governing equation for $\bar{\mathbf{U}}_\perp$ is found by averaging the horizontal components of the Navier-Stokes equation over the height of the channel (Sommeria & Moreau, 1982)

$$\frac{d\bar{\mathbf{U}}_\perp}{dt} = -\frac{\nabla_\perp \bar{P}}{\rho} + \nu \Delta_\perp \bar{\mathbf{U}}_\perp - \frac{\nu}{a\delta} \bar{\mathbf{U}}_\perp + \frac{\bar{\mathbf{J}}_\perp \times \mathbf{B}_0}{\rho a}, \quad (1.70)$$

where a vertically averaged quantity \bar{Q} is linked to its local counterpart q via

$$\bar{Q} = \frac{1}{a} \int_0^a q dz. \quad (1.71)$$

1. BASICS OF MAGNETOHYDRODYNAMICS

The second to last term of (1.70) stems from splitting the Laplacian operator into a horizontal and vertical operator Δ_{\perp} and ∂_z^2 respectively. Integrating the latter introduces a new characteristic time $\tau_H = a\delta/\nu = aB_0^{-1}\sqrt{\rho/\sigma\nu}$, also known as the Hartmann friction time. This parameter reflects the fact that although the bulk can be assimilated to a 2D flow, it still experiences the 3D effects of viscosity along the bottom Hartmann layer. It can also be noticed that τ_H is Ha times smaller than the viscous friction time $\tau_\nu = a^2/\nu$. This observation shows that Hartmann layers dissipate more energy than hydrodynamic boundary layers as a result of high electric currents flowing inside them. The last term of (1.70) corresponds to the electromagnetic driving of the vortex, and shows that the interaction between the radial component of the current and the vertical magnetic field is a source of momentum. Since the model assumes a 2D bulk, the electric current must flow in the bottom Hartmann layer exclusively. Indeed, the bottom Hartmann layer is the only location where velocity gradients along z still exist. In other words, the vortex is literally driven by the bottom Hartmann layer. In the inviscid and steady limit, the axisymmetric solution to (1.70) is given by a strict balance between the two aforementioned terms, i.e.

$$\bar{U}_\theta = \frac{\delta B_0}{\rho\nu} \bar{J}_r. \quad (1.72)$$

Integrating (1.72) along the perimeter of a circle of radius r eventually yields

$$\bar{U}_\theta = \frac{\Gamma}{r}, \quad \text{with} \quad \Gamma = \frac{I}{2\pi\sqrt{\sigma\rho\nu}}, \quad (1.73)$$

and $I = 2\pi r \bar{J}_r$ is the total electric current exiting the cylinder of radius r and height a . Owing to the conservation of charge, I happens to also refer to the total injected current. Although the asymptotic solution (1.73) is valid far from the axis of the vortex, Sommeria (1988)'s experimental results suggest that a small region close to the injection electrode exists where viscous friction cannot be neglected. At this location (also referred to as the vortex core) a shear layer develops, which originates from the electric discontinuity arising at the interface between the electrode and the insulating wall. The thickness ξ of this shear layer can be estimated by writing that viscous dissipation in the vortex core (characterized by $\tau_\xi = \xi^2/\nu$) acts on the same timescale as the electromagnetic effects (characterized by $\tau_H = a\delta/\nu$), giving

$$\xi = \frac{a}{\sqrt{Ha}}. \quad (1.74)$$

Comparing (1.53) with (1.74) shows that the Hartmann layer and the vortex core scale very differently. More specifically, the core can be expected to be much larger than the Hartmann layer, especially for large values of Ha . To get an idea, with $a = 0.1$ m and $Ha \sim [900 - 36000]$ in our experiment, ξ typically lies in the range $\xi \sim [0.5 - 3]$ mm.

1.3.4 Ekman pumping

Studying wind driven oceanic circulations, Ekman (1905) showed that the phenomenon resulted from differential rotation experienced by fluid particles laying inside the boundary

layer, which had developed at the surface of the water. The net effect of these boundary circulations was found to bring masses of water to converge, eventually giving rise to down-welling (also known as Ekman pumping), as a result of incompressibility. As it turns out, Ekman pumping is not exclusive to oceanic circulations, and can be observed anytime differential rotation exists. In particular, Ekman pumping exists when a viscous fluid swirls right above a rigid plate, which is also known as the Bödewadt problem, and is illustrated in figure 1.5 below.

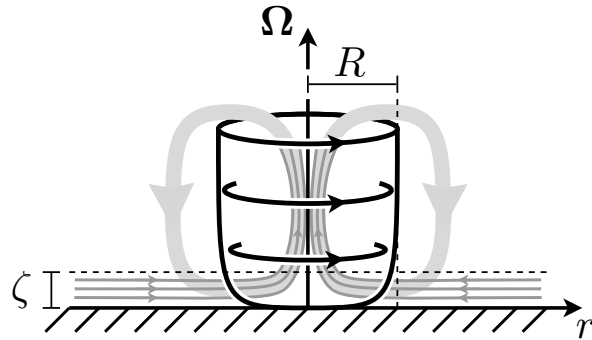


Figure 1.5. Ekman pumping: the vertical gradient in the boundary layer of the main azimuthal flow yields secondary motions in the meridional plane

Without stepping into the details of the solving (which can be found for instance in Schlichting (1979)), one can still get a good understanding of the phenomenon by studying orders of magnitude. As such, let us consider a vortex of width R swirling on top of a rigid plate in a viscous fluid. This vortex is characterized by an angular velocity Ω , hence in cylindrical coordinates, by an azimuthal velocity field $\mathbf{u} = r\Omega \mathbf{e}_\theta$. Due to viscous friction, a boundary layer of thickness $\zeta = \sqrt{\nu/\Omega}$ develops right above the plate. We may therefore distinguish two regions of interest. On the one hand, the far field, which is dominated by inertia, is where fluid particles experience a solid body rotation. On the other hand, the boundary layer, is where the fluid particles experience differential rotation as a result of viscous friction. Since the base flow is supposed to be purely azimuthal, the z component of the Navier-Stokes equations yields

$$\frac{\partial p}{\partial z} = 0, \quad (1.75)$$

meaning that the pressure remains constant along the axis, and especially while crossing the boundary layer. Incidentally, one may infer that the radial pressure gradient is also invariant across the boundary layer, and may therefore be estimated in the far field region where viscous friction is negligible. That is to say

$$\frac{1}{\rho} \frac{\partial p}{\partial r} \sim R\Omega^2, \quad (1.76)$$

which simply illustrates the fact that the centrifugal forces exerting on the bulk of the vortex are balanced by a radial pressure gradient. Concurrently, this radial pressure gradient is

1. BASICS OF MAGNETOHYDRODYNAMICS

balanced by viscous friction in the boundary layer. Since $\zeta \ll R$, the latter is estimated by the velocity gradients along z , and scales as

$$\frac{1}{\rho} \frac{\partial p}{\partial r} \sim \nu \frac{u_r}{\zeta^2}, \quad (1.77)$$

where u_r refers to the radial component of the velocity in the boundary layer. Combining equations (1.76) and (1.77) yields an estimate for the radial component in the boundary layer

$$u_r \sim R\Omega. \quad (1.78)$$

With words, this balance tells us that the radial pressure gradient appearing to oppose the centrifugal forces in the bulk exists everywhere. However, the centrifugal forces u_θ vanish within the boundary layer as a result of the no-slip boundary condition. The radial pressure gradient therefore induces an inwards radial flow inside the boundary layer. As a result of incompressibility, this converging radial flow yields an axial velocity component, which can be evaluated by the continuity equation

$$u_z \sim \sqrt{\nu\Omega}. \quad (1.79)$$

Despite $u_z \ll u_\theta$, the secondary flow induced by the mere presence of the no-slip wall has drastic consequences. Indeed, according to Davidson (2001), Ekman pumping is mainly responsible for the energy decay of a vortex swirling above a no-slip plate by flushing its fluid particles through the boundary layer where velocity gradients (hence viscous dissipation) are significant. It is therefore a fundamental phenomenon to keep in mind when determining energy dissipation of an albeit 2D turbulent flow, confined between no-slip walls.

The picture in laboratory experiments turns out to be slightly more complex. Indeed, despite the many ways available to smooth out velocity gradients in the direction of the swirl (such as shallow confinement, stratification, or even a background magnetic field or rotation), exact rigid body rotation is very seldom imposed. This in turn may have a profound impact on secondary motions, as first witnessed by Akkermans *et al.* (2008), who studied the recirculations taking place in front of a dipolar vortex traveling in a shallow layer of electrolyte. They showed that the remaining three-dimensionality (which emanated from the vertical gradients of velocity or forcing) induced a large counter clockwise recirculation going in the opposite direction to Ekman pumping. A recent study from Pothérat *et al.* (2013), based on numerical simulations and experimental observations showed that this counter-clockwise recirculation is in fact driven by an axial pressure gradient that builds up along the axis of the vortex as a result of the negative gradient of azimuthal velocity in the vertical direction. Since the associated flow recirculates in opposite direction to Ekman pumping, and that both are driven by differential rotation, it was called inverse Ekman pumping by the latter authors. Ultimately, the meridional recirculations can follow either direct or inverse pumping, depending solely on the dimensionality of the bulk.

Chapter 2

A weakly inertial vortex confined between two no-slip walls

As we have just seen at the end of the previous chapter, the velocity gradients resulting from no-slip boundaries can alter a flow by introducing secondary motions. Completely different secondary motions occur, whether these gradients are confined to the small boundary layers close to the walls or exist at the bulk scale. The former is associated to direct Ekman pumping resulting from converging jets in the boundary layers, while the latter is characterized by inverse Ekman pumping originating from a negative pressure gradient along the axis of the swirl. In anticipation of our study on the dynamics of turbulence, understanding the topological dimensionality of fluid layers seems all the more crucial, as it also introduces completely opposite energy dissipation mechanisms. Indeed, whether three-dimensionality is present or not decides whether turbulence transfers energy to large, weakly dissipative structures (2D turbulence) or efficiently dissipates energy at small scales in the bulk of the flow (3D turbulence).

The original work exposed in this chapter and published in Baker *et al.* (2015) aims at characterizing the relationship between the topological dimensionality of a wall-bounded electrically driven vortex, and the resulting secondary flows. We have adopted an analytic approach to this problem in order to circumvent the limitations associated to both numerical and experimental investigations. On the one hand, the main shortcoming of any numerical study comes from accessible computational power. Even though there was a recent breakthrough in solving low-Rm MHD turbulent flows in wall bounded domains (Kornet & Pothérat, 2015), the regimes reachable by DNS are, to date, still far from those encountered experimentally. On the other hand, experiments are limited by the resolution of the measuring devices in use. These issues prevent a thorough investigation of the boundary layers, which happen to be the crucial source of three-dimensionality.

2.1 Geometry and governing equations

Since our experimental apparatus relies on an array of electrically driven vortices, and since vortices are the building blocks to describe turbulence, a natural test bed for this study appears to be the electrically driven isolated vortex. Let us therefore consider the configuration represented in figure 2.1 below.

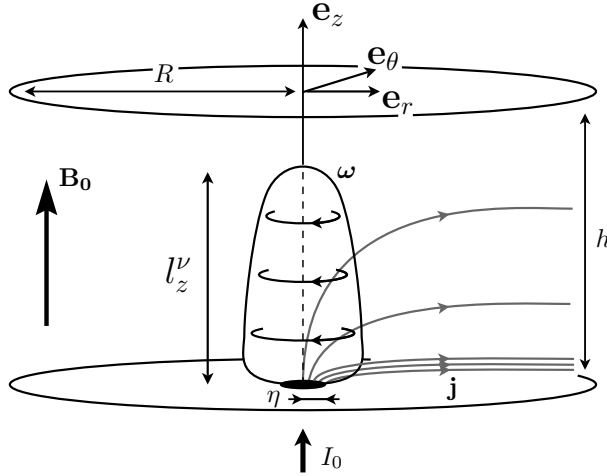


Figure 2.1. Sketch of the problem: an isolated vortex of height $l_z^\nu < h$ confined between two horizontal no-slip and electrically insulating walls separated by a distance h .

The flow, which takes place inside a cylindrical cavity of radius R is supposed to be axisymmetrical. As such, we focus exclusively on solutions which are invariant to rotations about the axis of the channel i.e. $\partial/\partial\theta = 0$. The domain is bounded by two no-slip horizontal walls located at $z = 0$ and $z = h$, and is filled with an electrically conducting fluid (typically a liquid metal such as Galinstan, of electrical conductivity $\sigma = 3.4 \times 10^6$ S/m, density $\rho = 6400$ kg/m³, and viscosity $\nu = 4 \times 10^{-7}$ m²/s). A static and uniform magnetic field $B_0 \mathbf{e}_z$ is applied vertically, and the low- Rm approximation is assumed to hold. A flow is driven by injecting electric current through an electrode of radius η located on the bottom plate. The top and bottom plates are perfectly electrically insulating otherwise, which forces the current to exit the channel through the sides. In anticipation of the upcoming calculations, the profile of injected current is assumed to be a smooth function, such as the Gaussian distribution:

$$j_z^w(r) = \frac{I_0}{\pi\eta^2} \exp \left[-(r/\eta)^2 \right], \quad (2.1)$$

where I_0 is the total current injected inside the domain. Given this configuration, the electric current is known to flow radially, interacting with the vertical magnetic field to induce a patch of vertical vorticity right above the bottom Hartmann layer. As one can notice, the geometry adopted here is quite close to that of Sommeria (1988) presented earlier. It however sets itself apart from the latter study by two crucial aspects:

- (i) The upper surface of the flow is in contact with a no-slip and perfectly electrically insulating wall, instead of staying free.
- (ii) The bulk is in no way assumed 2D. As a matter of fact we will see that the magnitude of the velocity gradients in the bulk is controlled via a single non-dimensional parameter.

In the inertialess limit (Kalis & Kolesnikov, 1980), the development of this patch of vorticity relies on the competition between two effects. On the one hand, the rotational part of the Lorentz force diffuses momentum along the magnetic field (Sommeria & Moreau, 1982), hence leading to a vortex extending in the z direction. On the other hand, viscous friction diffuses momentum isotropically, therefore opposing the growth of the vortex along z . Calling l_z^ν the range of action of the Lorentz force, its diffusive effect takes place over the characteristic time $\tau_{2D} = (\rho/\sigma B_0^2)(l_z^\nu/\eta)^2$. Conversely, viscous dissipation takes place over the time $\tau_\nu = \eta^2/\nu$. Assuming a steady flow, the distance l_z^ν over which the Lorentz force is able to act before being balanced by viscous dissipation is derived by equating both effects, yielding:

$$\frac{l_z^\nu}{h} = \frac{\eta^2}{h^2} Ha, \quad (2.2)$$

where $Ha = B_0 h \sqrt{\sigma/\rho\nu}$ is the Hartmann number based on the height of the channel. Asymptotically speaking, $l_z^\nu/h \ll 1$ means that the diffusive effect of the Lorentz force is balanced by viscous dissipation long before momentum can reach the top wall. In this case, the distance l_z^ν may be physically interpreted as the height of the vortex. On the contrary, $l_z^\nu/h \gg 1$ means that momentum can be diffused far beyond the top wall. This process is however blocked by the presence of the no-slip top wall, which prevents the vortex from extending past it. The ratio l_z^ν/h has been identified by Pothérat & Klein (2014) as the non dimensional parameter defining whether the structure is able to “feel” the presence of the top wall, hence controlling its dimensionality: 3D when $l_z^\nu/h \ll 1$ and quasi-2D when $l_z^\nu/h \gg 1$.

From now on, we will use the dimensionless coordinates $\tilde{r} = r/\eta$ and $\tilde{z} = z/h$, as well as the non dimensional variables $\tilde{u} = u/U$, $\tilde{\omega} = \omega \eta/U$, $\tilde{j} = j/\sigma U B_0$ and $\tilde{\phi} = \phi/U B_0 \eta$. We also introduce the non dimensional operator $\tilde{\nabla}$ defined as

$$\tilde{\nabla} = \left(\frac{\partial}{\partial \tilde{r}}, \frac{1}{\tilde{r}} \frac{\partial}{\partial \theta}, \frac{\eta}{h} \frac{\partial}{\partial \tilde{z}} \right).$$

The scaling for the velocity U is derived from the linear theory of quasi-2D electrically driven vortices put forward by Sommeria (1988). It is estimated from $U = (\Gamma/\eta)\sqrt{l_z^\nu/h}$, where $\Gamma = I_0/2\pi\sqrt{\sigma\rho\nu}$ is the circulation induced right above a point-like electrode through which flows the current I_0 , when viscous friction in the horizontal plane is neglected. This scaling for U is representative of the velocity at the edge of the vortex core, whose radius results from the competition between the Lorentz force and viscous dissipation. Hence the explicit dependence of U on the ratio l_z^ν/h . The governing equations consist of the steady state vorticity equation

$$\frac{1}{N} \left(\tilde{\mathbf{u}} \cdot \tilde{\nabla} \tilde{\boldsymbol{\omega}} - \tilde{\boldsymbol{\omega}} \cdot \tilde{\nabla} \tilde{\mathbf{u}} \right) = \frac{1}{Ha} \left(\frac{l_z^\nu}{h} \right)^{-1} \tilde{\Delta} \tilde{\boldsymbol{\omega}} + \frac{1}{\sqrt{Ha}} \left(\frac{l_z^\nu}{h} \right)^{1/2} \frac{\partial \tilde{\mathbf{j}}}{\partial \tilde{z}}, \quad (2.3)$$

Ohm's law

$$\tilde{\mathbf{j}} = -\tilde{\nabla} \tilde{\phi} + \tilde{\mathbf{u}} \times \mathbf{e}_z, \quad (2.4)$$

the conservation of mass

$$\tilde{\nabla} \cdot \tilde{\mathbf{u}} = 0, \quad (2.5)$$

and charge

$$\tilde{\nabla} \cdot \tilde{\mathbf{j}} = 0. \quad (2.6)$$

The problem at hand appears to be governed by three non dimensional parameters, namely the interaction parameter N based on the width of the injection electrode η , the Hartmann number Ha based on the height of the channel h and the ratio l_z^ν/h :

$$N = \frac{\sigma B_0^2 \eta}{\rho U}, \quad Ha = B_0 h \sqrt{\frac{\sigma}{\rho \nu}} \quad \text{and} \quad \frac{l_z^\nu}{h} = \frac{\eta^2}{h^2} Ha. \quad (2.7)$$

The boundary conditions on the horizontal walls consist of no-slip boundaries

$$\tilde{\mathbf{u}}(\tilde{r}, 0) = \tilde{\mathbf{u}}(\tilde{r}, 1) = 0, \quad (i)$$

an imposed vertical current at the bottom wall

$$\tilde{j}_{\tilde{z}}(\tilde{r}, 0) = \tilde{j}_{\tilde{z}}^w(\tilde{r}), \quad (ii)$$

and a perfectly electrically insulating top wall

$$\tilde{j}_{\tilde{z}}(\tilde{r}, 1) = 0. \quad (iii)$$

In addition, we impose a perfectly conducting and free slip radial boundary

$$\tilde{j}_{\tilde{z}}(\tilde{R}, \tilde{z}) = 0, \quad (iv)$$

and

$$\tilde{\tau}_{\tilde{r}}(\tilde{R}, \tilde{z}) = 0, \quad (v)$$

where $\tilde{\tau}_{\tilde{r}}$ represents the shear stress exerting on the wall whose normal vector is \mathbf{e}_r . The free-slip and perfectly conducting radial boundary can be physically interpreted as a pseudo-wall made of liquid metal, and was preferred over a no-slip boundary condition as it does not introduce parallel layers along the radial boundary, which can disturb the flow. Considering the scaling that was chosen for U , the normalized bottom boundary condition on the current \tilde{j}_z^w is expressed as

$$\tilde{j}_{\tilde{z}}^w(\tilde{r}) = \frac{2}{\sqrt{Ha}} \left(\frac{l_z^\nu}{h} \right)^{-1} \exp(-\tilde{r}^2).$$

In other words, for a given value of Ha and l_z^ν/h , the intensity of the total injected current is adjusted so that the intensity of the resulting flow remains comparable throughout all cases investigated.

We shall now consider a weakly inertial flow in the limit $N \gg 1$, and expand equations (2.3) through (2.6) using the regular perturbation series:

$$\begin{aligned}\tilde{\mathbf{j}} &= \tilde{\mathbf{j}}^0 + N^{-1} \tilde{\mathbf{j}}^1 + N^{-2} \tilde{\mathbf{j}}^2 + O(N^{-3}), \\ \tilde{\mathbf{u}} &= \tilde{\mathbf{u}}^0 + N^{-1} \tilde{\mathbf{u}}^1 + N^{-2} \tilde{\mathbf{u}}^2 + O(N^{-3}), \\ \tilde{\boldsymbol{\omega}} &= \tilde{\boldsymbol{\omega}}^0 + N^{-1} \tilde{\boldsymbol{\omega}}^1 + N^{-2} \tilde{\boldsymbol{\omega}}^2 + O(N^{-3}).\end{aligned}$$

2.2 Calculations

2.2.1 Inertialess base flow

The equations governing the problem at leading order are given by

$$\tilde{\Delta} \tilde{\boldsymbol{\omega}}^0 = -\sqrt{Ha} \left(\frac{l_z^\nu}{h} \right)^{3/2} \frac{\partial \tilde{\mathbf{j}}^0}{\partial \tilde{z}}, \quad (2.8)$$

$$\tilde{\mathbf{j}}^0 = -\tilde{\nabla} \tilde{\phi}^0 + \tilde{\mathbf{u}}^0 \times \mathbf{e}_z, \quad (2.9)$$

$$\tilde{\nabla} \cdot \tilde{\mathbf{u}}^0 = 0, \quad (2.10)$$

$$\tilde{\nabla} \cdot \tilde{\mathbf{j}}^0 = 0. \quad (2.11)$$

Solving $\tilde{\boldsymbol{\omega}}^0$ and $\tilde{\mathbf{j}}^0$ can be done separately by taking the Laplacian of (2.8) on the one hand, and taking the Laplacian of twice the curl of (2.9) on the other hand. Combining both of them yields

$$\tilde{\Delta}^2 \tilde{\boldsymbol{\omega}}^0 = \left(\frac{l_z^\nu}{h} \right)^2 \frac{\partial^2 \tilde{\boldsymbol{\omega}}^0}{\partial \tilde{z}^2}, \quad (2.12)$$

and

$$\tilde{\Delta}^2 \tilde{\mathbf{j}}^0 = \left(\frac{l_z^\nu}{h} \right)^2 \frac{\partial^2 \tilde{\mathbf{j}}^0}{\partial \tilde{z}^2}. \quad (2.13)$$

It is quite remarkable that equations (2.12) and (2.13) can seemingly be solved independently, and depend on the same and unique parameter l_z^ν/h . They remain nonetheless coupled via twice the curl of Ohm's law:

$$\tilde{\Delta} \tilde{\mathbf{j}}^0 = -\frac{1}{\sqrt{Ha}} \left(\frac{l_z^\nu}{h} \right)^{1/2} \frac{\partial \tilde{\boldsymbol{\omega}}^0}{\partial \tilde{z}}. \quad (2.14)$$

Equations (2.12) and (2.13) admit a purely azimuthal solution for $\tilde{\mathbf{u}}^0$ and a purely meridional solution for $\tilde{\mathbf{j}}^0$. Consequently, knowing either component $\tilde{\omega}_{\tilde{z}}^0$ or $\tilde{\omega}_{\tilde{r}}^0$, and $\tilde{j}_{\tilde{r}}^0$ or $\tilde{j}_{\tilde{z}}^0$ is enough

to completely derive the solution at leading order. The boundary conditions associated to the leading order read

$$\tilde{\omega}_{\tilde{z}}^0(\tilde{r}, 0) = \tilde{\omega}_{\tilde{z}}^0(\tilde{r}, 1) = 0, \quad (i^0)$$

$$\tilde{j}_{\tilde{z}}^0(\tilde{r}, 0) = \tilde{j}_{\tilde{z}}^w(\tilde{r}), \quad (ii^0)$$

$$\tilde{j}_{\tilde{z}}^0(\tilde{r}, 1) = 0, \quad (iii^0)$$

$$\tilde{j}_{\tilde{z}}^0(\tilde{R}, \tilde{z}) = 0. \quad (iv^0)$$

In addition, we shall approximate boundary condition (v) by

$$\tilde{\omega}_{\tilde{z}}^0(\tilde{R}, \tilde{z}) = 0. \quad (v^0)$$

Boundary condition (v^0) is not entirely equivalent to the free-slip boundary condition (v) , which strictly speaking is written in terms of $\tilde{\omega}_{\tilde{z}}^0$ as

$$\tilde{\omega}_{\tilde{z}}^0(\tilde{R}, \tilde{z}) = \frac{2}{\tilde{R}} \tilde{u}_\theta^0(\tilde{R}, \tilde{z}). \quad (2.15)$$

It is only in the limit $\tilde{R} \gg 1$ (since \tilde{u}_θ^0 is of order 1), that boundary condition (v) may be approximated by (v^0) . However, (v^0) offers a much simpler numerical implementation. Indeed, not only does it remove any remaining dependency on \tilde{u}_θ^0 , it also naturally introduces an orthogonal basis of functions on which the solution can be projected. From a practical point of view, we ensured that the edge of the channel was sufficiently far from the injection area in order to minimize the impact of this approximation on the flow (see section 2.3).

Solutions of (2.12) and (2.13) with separated variables, which satisfy the coupling (2.14), as well as boundary conditions (iv^0) and (v^0) must be of form

$$\tilde{\omega}_{\tilde{z}}^0 = \sum_{n=1}^{\infty} J_0(\lambda_n \tilde{r}) \sum_{i=1}^4 A_{ni} \exp(s_{ni} \tilde{z}), \quad (2.16)$$

and

$$\tilde{j}_{\tilde{z}}^0 = \sum_{n=1}^{\infty} J_0(\lambda_n \tilde{r}) \sum_{i=1}^4 B_{ni} \exp(s_{ni} \tilde{z}), \quad (2.17)$$

where $J_0(\tilde{r})$ refers to the zeroth order Bessel function of first kind, and λ_n represents its n^{th} root normalized by \tilde{R} . Note that solutions with separated variables which satisfy the coupling (2.14) and boundary condition (v^0) alone automatically satisfy boundary condition (iv^0) , making the latter redundant and therefore unnecessary to close the problem. Conversely, a different set of boundary conditions at $\tilde{r} = \tilde{R}$ may not admit a solution with separated variables. The arguments for the exponentials s_{ni} may be expressed in terms of Ha and l_z^ν/h alone. They take four different values $s_{ni} = \pm s_{n\pm}$, where $s_{n\pm}$ is defined by

$$s_{n\pm} = \frac{Ha}{2} \left[1 \pm \sqrt{1 + \frac{4 \lambda_n^2}{Ha} \left(\frac{l_z^\nu}{h} \right)^{-1}} \right]. \quad (2.18)$$

Restricting ourselves to cases that are relevant to MHD (i.e. cases where Ha is sufficiently large), the parameter $Ha^{-1} (l_z^\nu/h)^{-1}$ is expected to be much less than 1. Under this assumption, the roots $s_{n\pm}$ are expected to scale as

$$s_{n+} \sim \frac{h}{\delta} \quad \text{and} \quad s_{n-} \sim \lambda_n^2 \frac{h}{l_z^\nu}, \quad (2.19)$$

where $\delta = h/Ha$ represents the thickness of the Hartmann boundary layer. That is to say, s_{n+} scales as $1/\delta$, thus describes the boundary layers, while s_{n-} scales as λ_n^2/l_z^ν , which is the diffusion length associated to Bessel mode n . In this sense it represents the dimensionality of the bulk. From (2.14), coefficients A_{ni} and B_{ni} must satisfy

$$B_{ni} = -A_{ni} \frac{s_{ni}}{s_{ni}^2 \kappa - \lambda_n^2 / \kappa}, \quad (2.20)$$

with $\kappa = Ha^{-1/2} (l_z^\nu/h)^{1/2}$. The coefficients A_{ni} are determined by solving the linear system stemming from the boundary conditions

$$\begin{aligned} \sum_{i=1}^4 A_{ni} &= 0, \\ \sum_{i=1}^4 A_{ni} \exp(s_{ni}) &= 0, \\ \sum_{i=1}^4 A_{ni} \frac{s_{ni}}{s_{ni}^2 \kappa - \lambda_n^2 / \kappa} &= -\alpha_n, \\ \sum_{i=1}^4 A_{ni} \frac{s_{ni}}{s_{ni}^2 \kappa - \lambda_n^2 / \kappa} \exp(s_{ni}) &= 0, \end{aligned} \quad (S^0)$$

where α_n results from the projection of $\tilde{j}_z^w(\tilde{r})$ on the basis of Bessel functions:

$$\alpha_n = \frac{2/\tilde{R}^2}{J_1^2(\lambda_n \tilde{R})} \int_0^{\tilde{R}} \xi \tilde{j}_z^w(\xi) J_0(\lambda_n \xi) d\xi. \quad (2.21)$$

At this stage, the supplementary radial components $\tilde{\omega}_r^0$ and \tilde{j}_r^0 , as well as the velocity field $\tilde{\mathbf{u}}^0 = \tilde{u}_\theta^0 \mathbf{e}_\theta$, can be readily determined by integrating $\tilde{\nabla} \cdot \tilde{\boldsymbol{\omega}}^0 = 0$, $\tilde{\nabla} \cdot \tilde{\mathbf{j}}^0 = 0$, and $\tilde{\boldsymbol{\omega}}^0 = \tilde{\nabla} \times \tilde{\mathbf{u}}^0$ respectively.

2.2.2 Corrections due to inertia

The equations governing the problem at first order are given by

$$\tilde{\mathbf{u}}^0 \cdot \tilde{\nabla} \tilde{\boldsymbol{\omega}}^0 - \tilde{\boldsymbol{\omega}}^0 \cdot \tilde{\nabla} \tilde{\mathbf{u}}^0 = \frac{1}{Ha} \left(\frac{l_z^\nu}{h} \right)^{-1} \tilde{\Delta} \tilde{\boldsymbol{\omega}}^1 + \frac{1}{\sqrt{Ha}} \left(\frac{l_z^\nu}{h} \right)^{1/2} \frac{\partial \tilde{\mathbf{j}}^1}{\partial \tilde{z}}, \quad (2.22)$$

$$\tilde{\mathbf{j}}^1 = -\tilde{\nabla}\tilde{\phi}^1 + \tilde{\mathbf{u}}^1 \times \mathbf{e}_z, \quad (2.23)$$

$$\tilde{\nabla} \cdot \tilde{\mathbf{u}}^1 = 0, \quad (2.24)$$

$$\tilde{\nabla} \cdot \tilde{\mathbf{j}}^1 = 0. \quad (2.25)$$

Unlike the leading order (which is forced electrically at the bottom wall), the first order is driven by an azimuthal inertial force stemming from the base flow. In other words, $\tilde{\omega}_{\tilde{z}}^1$ and $\tilde{j}_{\tilde{z}}^1$ must satisfy homogeneous boundary conditions all along the edges of the domain. As a consequence, $\tilde{\omega}_{\tilde{z}}^1$ is strictly null, and $\tilde{\phi}^1$ is uniform across the channel. In order to have a non-divergent solution on the axis of the channel, $\tilde{\omega}_{\tilde{r}}^1$ must also be null throughout the domain, meaning that the inertial correction to the base flow occurs in the meridional plane exclusively. In addition, the electric current becomes purely electromotive, since it is proportional to the velocity via Ohm's law. These arguments simplify the problem greatly by removing all couplings between mechanical and electrical quantities at first order. In the end, the governing equations reduce to

$$\tilde{F}_\theta^0 \mathbf{e}_\theta = \frac{1}{Ha} \left(\frac{l_z^\nu}{h} \right)^{-1} \tilde{\Delta} \tilde{\omega}^1 - \frac{1}{\sqrt{Ha}} \left(\frac{l_z^\nu}{h} \right)^{1/2} \frac{\partial \tilde{u}_{\tilde{r}}^1}{\partial \tilde{z}} \mathbf{e}_\theta, \quad (2.26)$$

where $\tilde{F}_\theta^0 = 2 \tilde{u}_\theta^0 \tilde{\omega}_{\tilde{r}}^0 / \tilde{r}$ is the inertial forcing originating from the non linear terms of the base flow. Owing to the previous arguments, equation (2.26) is non trivial only in the \mathbf{e}_θ direction. It is solved by introducing the stream function $\tilde{\psi}^1 = \psi^1 / U\eta$ such that $\tilde{\mathbf{u}}^1 = \tilde{\nabla} \times (\tilde{\psi}^1 \mathbf{e}_\theta)$ and $\tilde{\omega}^1 = \tilde{\nabla} \times \tilde{\nabla} \times (\tilde{\psi}^1 \mathbf{e}_\theta)$, which yields

$$\frac{l_z^\nu}{h} Ha \tilde{F}_\theta^0 = - \left[\tilde{\Delta} - \frac{1}{\tilde{r}^2} \right]^2 \tilde{\psi}^1 + \left(\frac{l_z^\nu}{h} \right)^2 \frac{\partial^2 \tilde{\psi}^1}{\partial \tilde{z}^2}, \quad (2.27)$$

where $\tilde{\Delta} \cdot$ represents the scalar Laplace operator in cylindrical coordinates. Again, the intensity of the flow depends on the interaction parameter N , while the topology of the first order recirculations depends on Ha and the ratio l_z^ν/h . Since mechanical and electrical quantities are decoupled at first order, the boundary conditions associated to this problem boil down to no-slip and non-penetrating boundaries at the top and bottom walls, and no shear stress at the radial boundary

$$\frac{\partial \tilde{\psi}^1}{\partial \tilde{z}} \Bigg|_{\tilde{r},0} = \frac{\partial(\tilde{r}\tilde{\psi}^1)}{\partial \tilde{r}} \Bigg|_{\tilde{r},0} = 0, \quad (i_0^1)$$

$$\frac{\partial \tilde{\psi}^1}{\partial \tilde{z}} \Bigg|_{\tilde{r},1} = \frac{\partial(\tilde{r}\tilde{\psi}^1)}{\partial \tilde{r}} \Bigg|_{\tilde{r},1} = 0, \quad (i_1^1)$$

$$\frac{\partial}{\partial \tilde{r}} \left(\frac{1}{\tilde{r}} \frac{\partial(\tilde{r}\tilde{\psi}^1)}{\partial \tilde{r}} \right) \Bigg|_{\tilde{R},\tilde{z}} - \frac{\partial^2 \tilde{\psi}^1}{\partial \tilde{z}^2} \Bigg|_{\tilde{R},\tilde{z}} = 0. \quad (v^1)$$

Solutions of equation (2.27) are sought for as the sum of a homogeneous solution $\tilde{\psi}_h^1(\tilde{r}, \tilde{z})$, and a particular solution of the problem with inertial forcing $\tilde{\psi}_f^1(\tilde{r}, \tilde{z})$. The homogeneous problem is very similar to the one solved earlier and reads

$$\tilde{\psi}_h^1(\tilde{r}, \tilde{z}) = \sum_{n=1}^{\infty} J_1(\mu_n \tilde{r}) \sum_{i=1}^4 C_{ni} \exp(p_{ni} \tilde{z}), \quad (2.28)$$

where $J_1(\tilde{r})$ is the first order Bessel function of first kind, and μ_n represents its n^{th} root normalized by \tilde{R} . As for the leading order, the roots p_{ni} are defined as

$$p_{n\pm} = \frac{Ha}{2} \left[1 \pm \sqrt{1 + \frac{4\mu_n^2}{Ha} \left(\frac{l_z^\nu}{h} \right)^{-1}} \right]. \quad (2.29)$$

The particular solution $\tilde{\psi}_f^1$ is found by expanding \tilde{F}_θ^0 as a Fourier-Bessel series of $J_1(\mu_n \tilde{r})$

$$\tilde{F}_\theta^0(\tilde{r}, \tilde{z}) = \sum_{n=1}^{\infty} J_1(\mu_n \tilde{r}) \varphi_n(\tilde{z}), \quad (2.30)$$

with

$$\varphi_n(\tilde{z}) = -2\kappa \sum_{i,j=1}^{\infty} \sum_{k,l=1}^4 \beta_{nij} \frac{A_{ik} A_{jl} s_{jl}}{\lambda_i \lambda_j} \exp[(s_{ik} + s_{jl}) \tilde{z}], \quad (2.31)$$

where

$$\beta_{nij} = \frac{2/\tilde{R}^2}{J_2^2(\mu_n \tilde{R})} \int_0^{\tilde{R}} \xi J_1(\lambda_i \xi) J_1(\lambda_j \xi) J_1(\mu_n \xi) d\xi. \quad (2.32)$$

The response of the flow to the forcing is therefore

$$\tilde{\psi}_f^1(\tilde{r}, \tilde{z}) = \sum_{n=1}^{\infty} J_1(\mu_n \tilde{r}) \sum_{i,j,k,l} K_{nijkl} \exp[(s_{ik} + s_{jl}) \tilde{z}], \quad (2.33)$$

where

$$K_{nijkl} = \frac{\frac{2\beta_{nij}}{\kappa} \left(\frac{l_z^\nu}{h} \right)^2 \frac{A_{ik} A_{jl} s_{jl}}{\lambda_i \lambda_j}}{\mu_n^4 - \left[\left(\frac{l_z^\nu}{h} \right)^2 + 2(\mu_n \kappa)^2 \right] (s_{ik} + s_{jl})^2 + [\kappa(s_{ik} + s_{jl})]^4}. \quad (2.34)$$

At this stage, the value of K_{nijkl} is fully determined, since it only depends on quantities resulting from the base flow. Finally,

$$\tilde{\psi}^1 = \sum_{n=1}^{\infty} J_1(\mu_n \tilde{r}) \left\{ \sum_{i=1}^4 C_{ni} \exp(p_{ni} \tilde{z}) + \sum_{i,j,k,l} K_{nijkl} \exp[(s_{ik} + s_{jl}) \tilde{z}] \right\}, \quad (2.35)$$

where the integration constants C_{ni} are determined from the boundary conditions

$$\begin{aligned} \sum_{i=1}^4 C_{ni} &= - \sum_{i,j,k,l} K_{nijkl}, \\ \sum_{i=1}^4 C_{ni} p_{ni} &= - \sum_{i,j,k,l} K_{nijkl} (s_{ik} + s_{jl}), \\ \sum_{i=1}^4 C_{ni} \exp(p_{ni}) &= - \sum_{i,j,k,l} K_{nijkl} \exp(s_{ik} + s_{jl}), \\ \sum_{i=1}^4 C_{ni} p_{ni} \exp(p_{ni}) &= - \sum_{i,j,k,l} K_{nijkl} (s_{ik} + s_{jl}) \exp(s_{ik} + s_{jl}). \end{aligned} \quad (S^1)$$

To summarize, equations (2.16), (2.17) and (2.35) provide a complete solution for the flow at order $O(N^{-1})$ in the limit $N \gg 1$, and for any arbitrary value of Ha or l_z^ν/h . This solution is shown to be exclusively governed by three non dimensional parameters: N , which determines the intensity of the flow (as in the theory of Pothérat *et al.* (2000)); Ha , which controls the thickness of the boundary layers (as in the classical theory); and l_z^ν/h , which defines the dimensionality of the flow. With such a formulation of the problem, one can clearly see that the geometrical aspect ratio η/h is not the most adequate parameter to precisely describe the dimensionality of the base flow. However l_z^ν/h is. This may explain why the height-to-width aspect ratio of the vortex can be seen as a “confusing parameter” (Satijn *et al.*, 2001). It is also worth noting that the even orders correspond to the azimuthal component of the flow, while the odd orders give corrections in the meridional plane. This behavior was also found in the analogous configuration described by Davoust *et al.* (2015), which consists of an annular channel with a rotating bottom. We shall now numerically evaluate this solution to find how the topological dimensionality of the base flow impacts the secondary recirculations.

2.3 Numerical methods

2.3.1 Algorithm description

Let us now briefly go over some technical aspects involved in the solving. An in-house FORTRAN95 code was developed to evaluate numerically $\tilde{\omega}_z^0(\tilde{r}, \tilde{z})$, $\tilde{j}_z^0(\tilde{r}, \tilde{z})$ and $\tilde{\psi}^1(\tilde{r}, \tilde{z})$. The solver was designed to solve systems (S^0) and (S^1) , and to reconstruct the solution via equations (2.16), (2.17) and (2.35) respectively. The FMLIB 1.3 multi-precision package (Smith, 1991) was used to ensure sufficient accuracy of the solution for any value of Ha . The input parameters for our code were Ha , l_z^ν/h , and the number of modes N_{mode} . The structure of the algorithm is as follows:

- (1) Set the working precision based on Ha
- (2) Generate the zeros of Bessel functions J_0 and J_1 .

- (3) Compute α_n and β_{nij} according to (2.21) and (2.32) respectively, by evaluating the integrals using a Gauss-Legendre quadrature rule of order 100.
- (4) Compute $s_{n\pm}$ and $p_{n\pm}$ according to (2.18) and (2.29) respectively.
- (5) Compute K_{nijkl} according to (2.34).
- (6) Find A_{ni} and C_{ni} by solving (S^0) and (S^1) with a Gauss-Jordan elimination method
- (7) Discretize domain, build the solution according to (2.16), (2.17) and (2.35), and convert output to double precision.

2.3.2 Convergence test

Let us now evaluate the number of terms necessary to accurately represent infinite sums. To this end, we introduce ϵ^n , the relative error at order n respectively defined by

$$\epsilon^0(N_{mode}) = \frac{\|\tilde{u}_\theta^0(N_{mode}) - \tilde{u}_\theta^0(N_{max})\|_2}{\|\tilde{u}_\theta^0(N_{max})\|_2}, \quad (2.36)$$

and

$$\epsilon^1(N_{mode}) = \frac{\|\tilde{\psi}^1(N_{mode}) - \tilde{\psi}^1(N_{max})\|_2}{\|\tilde{\psi}^1(N_{max})\|_2}, \quad (2.37)$$

where $\|\cdot\|_2$ represents the classically defined \mathcal{L}^2 -norm. ϵ^n compares the difference between a run computed with the number of modes N_{mode} , with respect to the reference case computed with the highest number of modes N_{max} . For all cases, N_{max} was set to 80. The convergence tests were conducted for three different channel radii $\tilde{R} = 5, 10$ and 20 , since this parameter was expected to impact the accuracy of the solution. According to figure 2.2, the number of modes required to achieve a given relative error unsurprisingly increases with \tilde{R} . Indeed, the vortex becomes thinner with respect to the total width of the channel, meaning that modes of smaller wavelengths are required to capture it precisely.

At leading order, increasing the number of modes with $\tilde{R} = 10$ and $\tilde{R} = 20$ steadily improves the accuracy of the solution until ϵ^0 eventually reaches double precision. The behavior of ϵ^0 for $\tilde{R} = 5$ is completely different: fast convergence is observed at first, followed by a region where accuracy hardly improves with N_{mode} . This effect is first evidence that the radial wall is too intrusive for $\tilde{R} = 5$. At first order, ϵ^1 follows a similar behavior regardless of the position of the radial wall: increasing the number of modes improves the residual error before it levels off. This behavior comes from the discrepancy that exists between the *real* inertial forcing F_θ^0 (which is only approximately null at the edge due to the simplified boundary condition) and its Fourier-Bessel expansion, which is strictly null by definition of $J_1(\mu_n \tilde{R})$. This discrepancy introduces Gibbs phenomena close to the edge of the channel. It is however important to note that the oscillations are confined to a region close to the edge. Additionally, they become less and less an issue as R is increased, since F_θ^0 naturally vanishes away from the core of the vortex.

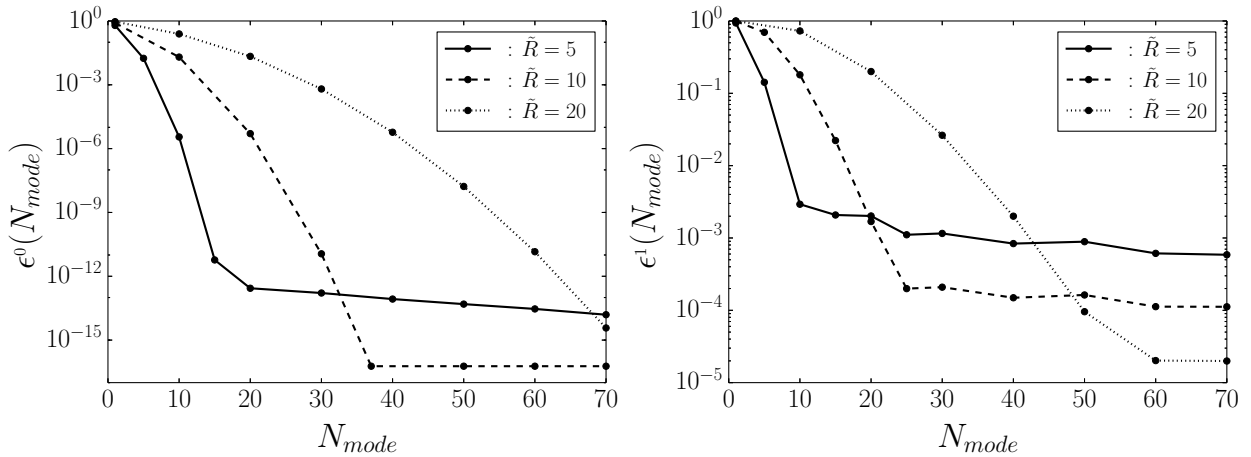


Figure 2.2. Convergence test. Left: leading order, right: first order.

The conclusion of this convergence analysis is that \tilde{R} must be as large as possible to prevent numerical artifacts. The operating point chosen was $\tilde{R} = 20$ and $N_{\text{mode}} = 50$, which gave us a good compromise between accuracy and computational time (proportional to N_{mode}^3). With these settings, the solution at leading order is reliable up to eight significant digits, and the relative accuracy of the first order is better than 0.01%

2.3.3 Validity of the radial boundary condition

Figure 2.3 shows the radial profiles of azimuthal velocity evaluated at mid-height of the channel, for different radial wall distances. In the case at hand, $l_z^\nu/h = 1000$, meaning that the base flow is already quasi-2D. According to figure 2.3, the azimuthal velocity follows a $1/\tilde{r}$ decay law outside the core of the vortex. This behavior is in agreement with the quasi-2D theory developed by Sommeria (1988) for a vortex driven by injecting current through a pointlike electrode. This suggests that the radial distribution of injected current plays a minor role in determining the actual shape of the vortex, and that a gaussian distribution provides a very good representation of a thin current injection electrode (at least when the flow is quasi two-dimensional). This point will be further studied in the following section.

Table 2.1 gives an estimation of the leading order shear stress at the edge of the domain

$$\tilde{\tau}_{r\theta}^0 = \tilde{r} \frac{\partial}{\partial \tilde{r}} \left(\frac{\tilde{u}_\theta^0}{\tilde{r}} \right) \Bigg|_{\tilde{R}, \tilde{z}}, \quad (2.38)$$

for different positions of the radial wall. It gives an a posteriori confirmation that the simplified radial boundary condition (v^0) tends towards a free slip boundary condition when \tilde{R} is increased. Furthermore, we find that $\tilde{\tau}_{r\theta}^0$ scales as $1/\tilde{R}^2$ to a very good precision. This brings supplementary evidence that the solution is reliable, since $\tilde{u}_\theta^0(\tilde{R})$ is expected to scale as $1/\tilde{R}$ for quasi-2D structures. In 3D flows, $\tilde{u}_\theta^0(\tilde{R})$ is expected to be lower, and so should be $\tilde{\tau}_{r\theta}^0$. For $\tilde{R} = 20$, the order of magnitude of the shear stress at the wall is of 10^{-3} .

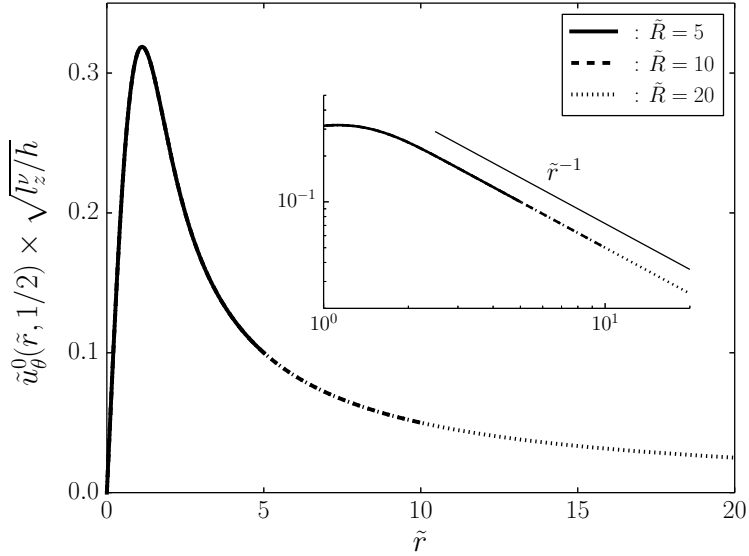


Figure 2.3. Velocity profile at the middle of the channel, obtained for $Ha = 456$ and $l_z^\nu/h = 1000$. The insert highlights how the azimuthal velocity decays as $1/\tilde{r}$ away from the core of the vortex.

	$\tilde{R} = 5$	$\tilde{R} = 10$	$\tilde{R} = 20$
$\tilde{\tau}_{r\theta}^0$	3.99×10^{-2}	1.00×10^{-2}	2.50×10^{-3}

Table 2.1. Shear stress at the radial boundary

2.3.4 Sensitivity to the injection profile

The sensitivity of the base flow to the bottom electric boundary condition is an all the more legitimate question, as the very existence of the flow relies upon it. The spatial distribution of current density could thus be expected to shape the resulting flow. In order to quantify the relevance of our model to describe electrically driven vortices, we shall compare the flow induced by two different injection profiles:

$$j_z^w(r) = \frac{I_0}{\pi\eta^2} \exp [-(r/\eta)^2],$$

and

$$j_z^w(r) = \frac{I_0}{\pi\eta^2} [H(r) - H(r - \eta)],$$

where $H(r)$ refers to the Heaviside step function. These two particular profiles were chosen so that the typical width of the electrode remained η , and that the total amount of electric current injected in the domain was I_0 . For both cases Ha and l_z^ν/h were set to $Ha = 456$ and

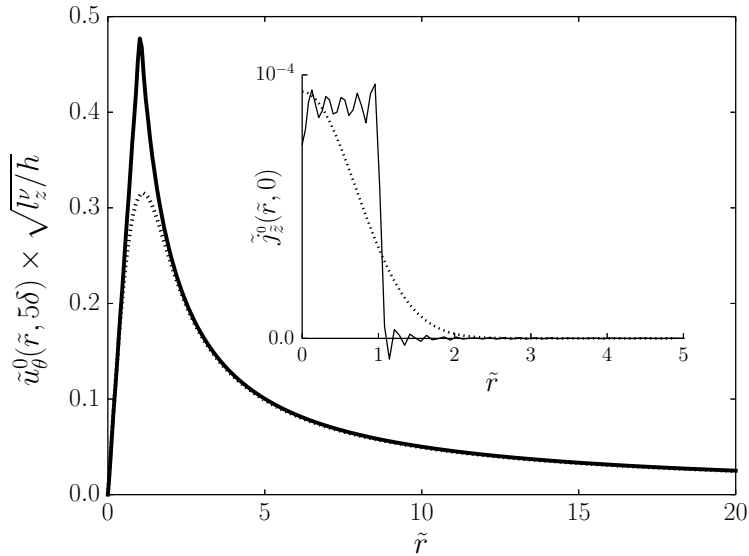


Figure 2.4. Velocity profile right above the Hartmann layer induced by two different radial distributions of electric current. (.....): flow resulting from a Gaussian distribution of current. (—): flow resulting from a step distribution of current. The insert shows the respective current profiles at the bottom wall $\tilde{j}_z^0(\tilde{r}, 0)$.

$l_z^\nu/h = 1000$ respectively. Furthermore, the number of modes used to expand the Gaussian distribution was $N_{mode} = 50$ (in agreement with section 2.3.2), while $N_{mode} = 200$ was imposed to expand the step distribution. A much higher number of modes is obviously necessary for the latter profile since it is singular at $\tilde{r} = 1$.

Figure 2.4 shows the leading order azimuthal velocity along \tilde{r} , right above the bottom Hartmann layer ($\tilde{z} = 5/Ha$) for both current distributions. The associated current profiles are displayed in the insert. The first striking feature of figure 2.4 is that both velocity profiles follow the same asymptotic behavior whether close to the axis of the vortex or away from its core. This behavior comes from the fact that the lateral diffusion of momentum is driven by viscous dissipation, and is therefore independent of the injected electric current. As already discussed in section 2.3.3, both vortices follow a $1/\tilde{r}$ decay law away from their core, which is expected for quasi-2D structures. The velocity peak is found at $\tilde{r} = 1$ in both cases, which corresponds to the outer edge of the electrode. The main difference between both profiles however, is the value of the peak which is approximately twice as large for the step distribution. As a result, we can expect the Gaussian distribution to slightly underestimate the magnitude of the inertial terms. However, since the shape of the flow is identical in both cases, the mechanisms driving the first order recirculations will be unchanged (recall that the inertial forcing stems from mechanical quantities only).

It is also worth noting that although high frequency oscillations exist in the expansion of the step distribution (such oscillations are unavoidable regardless of the number of modes taken into account, as a result of its singular nature), they do not appear in the induced

flow. This effect comes from the analytical approach that was used, and more specifically from the systematic use of dot products to build the solution. This brings supplementary evidence that our model is reliable and robust, since it is insensitive to numerical artifacts.

As in experiments on electrically driven flows, the intensity of the vortex is controlled by the total imposed current through the electrode (Sommeria, 1988), (Messadek & Moreau, 2002), (Klein & Pothérat, 2010), (Pothérat & Klein, 2014). Nevertheless, it is also possible to impose a fixed voltage between electrodes, or between the injection electrode and the side wall. (Kalis & Kolesnikov, 1980) showed that imposing a uniform current density or uniform voltage at the electrode was essentially equivalent as far as the topology of the base flow was concerned. We can therefore assert that our model is a faithful representation of electrically driven vortices in experiments, even if a Gaussian distribution of current is imposed at the bottom.

2.4 Results

Numerical experiments were run for four different values of the Hartmann number: $Ha = 456, 911, 1822$ and 3644 . Let us stress in passing that these values of Ha are typically found in liquid metal experiments, and correspond in our case to magnetic fields laying in the 1 T range. For all values of Ha , the ratio l_z^ν/h was set within the range 10^{-2} to 10^5 . From now on, we will refer to the low- Ha case as $Ha = 456$, while the high- Ha case will refer to $Ha = 3644$.

2.4.1 Results at leading order

Figure 2.5 depicts the base flow for $Ha = 3644$, and for increasing values of l_z^ν/h : $0.01, 1$ and 10000 respectively. Lower Ha cases are not presented here, since they look identical. As a matter of fact, the only influence of Ha at leading order is in determining the thickness of the boundary layers. Owing to the high values we have chosen for Ha , the thickness of these boundary layers is negligible compared to the height of the channel. Consequently they are virtually invisible when looking at the macroscopic properties of the flow.

The dimensionality of the flow can be estimated by comparing the intensity of the velocity field along the top and bottom walls. For $l_z^\nu/h = 0.01$, the flow is mostly concentrated at the bottom of the channel (i.e. where the electric forcing takes place), while there is absolutely no flow at the top. The base flow is said to be weakly 3D (in the sense of Klein & Pothérat (2010)), meaning that although the topological patterns remain the same across the channel (that is to say, the vortex stays columnar), their intensity still depends on \tilde{z} . This behavior is a consequence of the Lorentz force not being strong enough to compete with viscous dissipation beyond l_z^ν , which is in this case a hundred times smaller than h . In other words, weak three-dimensionality characterizes a flow where two adjacently stacked layers of horizontal velocity experience differential rotation, as a result of vertical gradients. As l_z^ν/h increases, the range of action of the Lorentz force becomes longer, and momentum is diffused

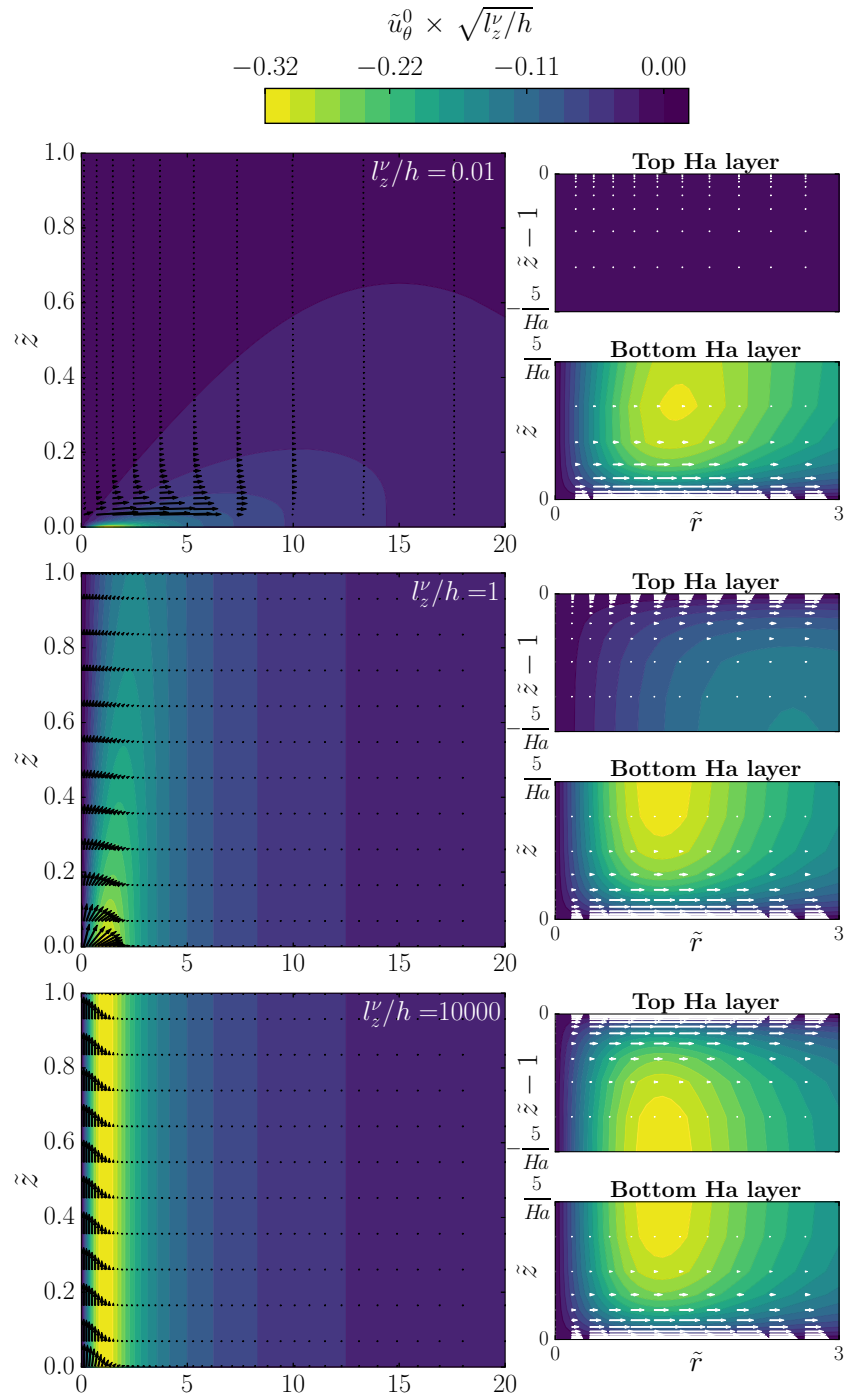


Figure 2.5. Solution at leading order for $Ha = 3644$, and for $l_z^v/h = 0.01, 1$ and 10000 respectively. The magnitude of $\tilde{u}_\theta^0 \times \sqrt{l_z^v/h}$ is indicated by filled contours. The electric current density is represented by black and white vectors (color choice is just a matter of contrast). Scaling of vectors has been adapted to compensate the much higher current densities in the boundary layers. Inserts: close up view of the top and bottom Hartmann layers featuring the usual exponential profile for the electric current.

further up the channel. For $l_z^\nu/h = 10000$, the flow is quasi-2D in the sense that all velocity gradients along \tilde{z} have been smoothed out outside of the boundary layers (a \tilde{z} -dependence always exists in the top and bottom Hartmann layers due to the no-slip walls). The vortex spans across the channel and is therefore able to feel the effect of the top wall.

Figure 2.5 also displays current densities. As expected, they are highest where strong velocity gradients exist, i.e. in the boundary layers and in the core of the vortex. For all cases, we have verified that up to numerical precision, exactly half of the total current injected in the channel flows within the bottom Hartmann layer, while the other half flows vertically. This result confirms the heuristic prediction of Pothérat & Klein (2014). For low values of l_z^ν/h (0.01 and 1), the velocity gradient along \tilde{z} introduced by three-dimensionality progressively extracts the vertical current into the bulk, channeling it towards the edge of the domain. For $l_z^\nu/h = 10000$ however, quasi two-dimensionality has smoothed out all velocity gradients along \tilde{z} in the bulk: the vertical current flows exclusively within the core of the vortex and the top and bottom Hartmann layers. Close up views of the Hartmann layers are given in the inserts of figure 2.5. It is clear from these figures that the electric content of all bottom Hartmann layers is quite similar, but that the electric content of the top Hartmann layer depends on how far the Lorentz force is able to diffuse momentum along \tilde{z} . As expected, the electric current decreases away from the walls following an exponential profile in all cases.

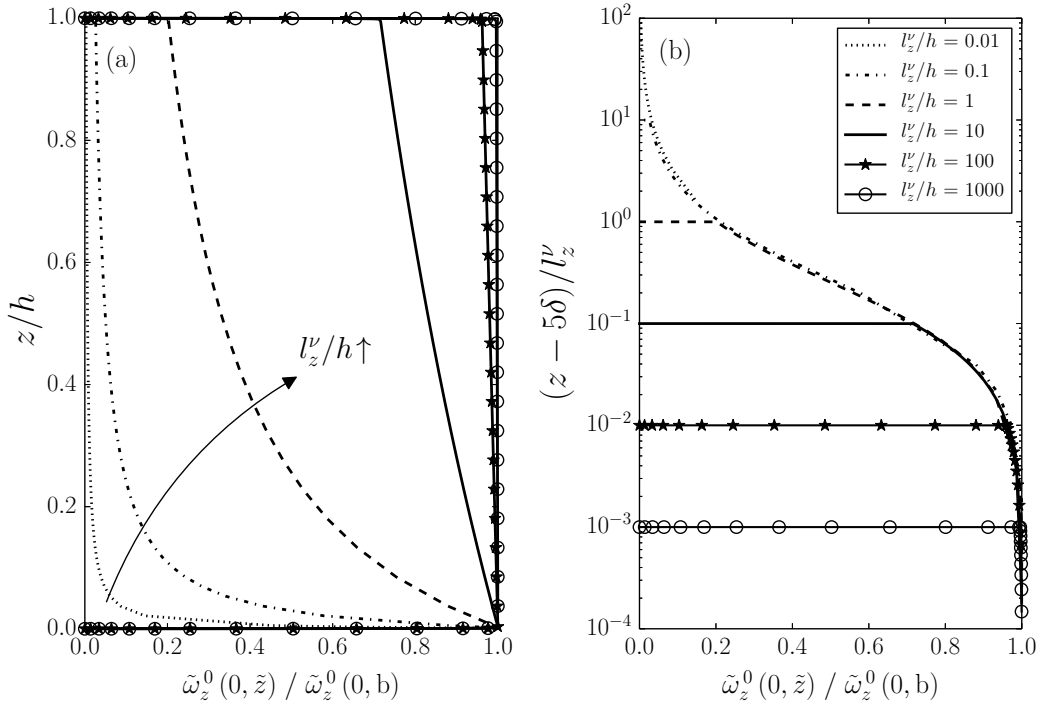


Figure 2.6. Axial vorticity $\tilde{\omega}_z^0(0, \tilde{z})$ normalized by the vorticity right outside the bottom Hartmann layer $\tilde{\omega}_z^0(0, b)$ for $Ha = 3644$. Left: z is normalized by the height of the channel h . Right: z is normalized by the Lorentz force diffusion length l_z^ν .

The dimensionality of the base flow is better quantified with figure 2.6. From now on, $\tilde{\omega}_z^0(\tilde{r}, t)$ and $\tilde{\omega}_z^0(\tilde{r}, b)$ refer to the vorticity right outside the top and bottom Hartmann layers respectively (see for instance Pothérat *et al.* (2002) for a mathematically rigorous definition of this concept). Figure 2.6 portrays the profile of vertical vorticity $\tilde{\omega}_z^0(0, \tilde{z})$ normalized by $\tilde{\omega}_z^0(0, b)$ along the axis of the channel. In figure 2.6.a, all structures evolve in a channel of fixed height (\tilde{z} is normalized by h). This representation highlights the effect of the ratio l_z^ν/h on the dimensionality of the base flow: as l_z^ν/h increases, the momentum induced right above the injection electrode is diffused farther and farther by the Lorentz force, hence progressively smoothing out velocity gradients along \tilde{z} . In figure 2.6.b, all curves are shifted down by 5δ to account for the varying thickness of the Hartmann layer, and then normalized by l_z^ν . The collapse of all curves in these variables clearly indicates that all vortices follow a universal profile, which is solely defined by the competition between the Lorentz force and viscous dissipation. In other words, the effect of the vertical confinement is local, and only consists in ending the universal profile by introducing a no-slip boundary (the presence of the top wall is felt over a distance whose order of magnitude is no larger than the thickness of the Hartmann layer).

Figure 2.7 compares the vorticity on the axis of the channel right below the top Hartmann layer to the vorticity right above the bottom one. This figure highlights how all the information about the dimensionality of the base flow is exclusively contained within the single parameter l_z^ν/h , regardless of the value of the Hartmann number. Furthermore, the transition from 3D to quasi-2D base flows appears to be a gradual process that occurs around $l_z^\nu/h \sim 100$. This effect was also noted by Klein & Pothérat (2010) in turbulent flows.

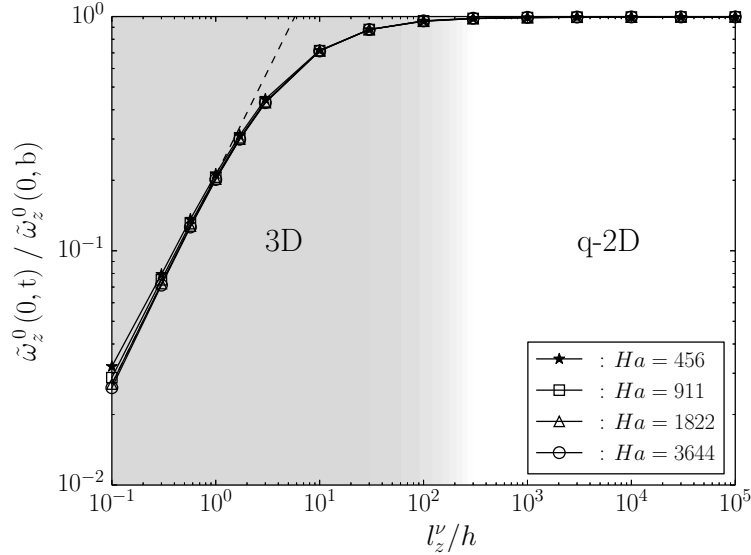


Figure 2.7. Dimensionality of the base flow: 3D when $\tilde{\omega}_z^0(0, t)/\tilde{\omega}_z^0(0, b) < 1$, quasi-2D when $\tilde{\omega}_z^0(0, t)/\tilde{\omega}_z^0(0, b) \rightarrow 1$. A color gradient is used to highlight the smooth transition from a 3D to a quasi-2D base flow as the parameter l_z^ν/h increases.

2.4.2 Results at first order

Figures 2.8 and 2.9 give a complete view of the velocity field for the low- and high- Ha cases. When the base flow is 3D ($l_z^\nu/h < 100$), a large counter-clockwise recirculation dominates in the (\tilde{r}, \tilde{z}) plane. This phenomenon corresponds in fact to inverse Ekman pumping, which results from the buildup of an axial pressure gradient along the axis of the vortex as a result of the negative gradient of azimuthal velocity along \mathbf{e}_z . As the base flow becomes increasingly quasi-2D ($l_z^\nu/h > 100$), a clockwise recirculation becomes visible at the bottom of the domain, and grows steadily with l_z^ν/h . The secondary flow is then composed of two counter-rotating structures, which correspond to direct Ekman pumping, or what is also called the “tea-cup effect”. As we have seen earlier, direct pumping is driven by a radial pressure gradient inside the boundary layers, which develops in the bulk to oppose centrifugal forces.

To further elucidate the role of pressure gradients on the topology of secondary flows, let us reconstruct numerically from the Navier-Stokes equation projected along \mathbf{e}_z the vertical pressure gradient along the axis of the vortex, which is given by

$$\frac{\partial \tilde{p}^0}{\partial \tilde{z}} = \frac{2}{Ha} \left(\frac{l_z^\nu}{h} \right)^{-1} \frac{\partial^2 \tilde{u}_{\tilde{z}}^1}{\partial \tilde{r}^2} \Big|_{0,\tilde{z}} + \frac{1}{Ha^2} \frac{\partial^2 \tilde{u}_{\tilde{z}}^1}{\partial \tilde{z}^2} \Big|_{0,\tilde{z}}. \quad (2.39)$$

The profiles of pressure gradient along the axis of the vortex are represented in figure 2.10 in order to illustrate the previous argument. When the flow is 3D, a positive pressure gradient exists in the bulk, whose effect is to drive a jet down along the axis of the vortex. Because this phenomenon is entirely governed by velocity gradients in the core, it is no surprise that the intensity of the inverse pumping is driven by l_z^ν/h . As a result of quasi-two dimensionality, the dependence of the pressure (or any other quantity for that matter) on \tilde{z} in the bulk disappears. However, a very strong vertical pressure gradient exists at both ends of the axis as a result of a converging radial flow within the boundary layers.

Interestingly, a negative pressure gradient always exists in the bottom Hartmann layer regardless of whether the base flow is 3D or quasi-2D. This means that a recirculation always exists at the bottom of the channel (though it is not always visible), which results from direct pumping. By contrast, a positive pressure gradient does not exist in the top Hartmann layer for $l_z^\nu/h = 1$, meaning that in this particular case, the top recirculation is exclusively driven by inverse pumping due to the vertical pressure gradient in the lower half of the channel. As a matter of fact, figure 2.10 showcases the progressive shift in the mechanism driving the top recirculation, which is not obvious a priori, as it does not transpire in its topology. To summarize, direct and inverse pumping co-exist in all cases investigated.

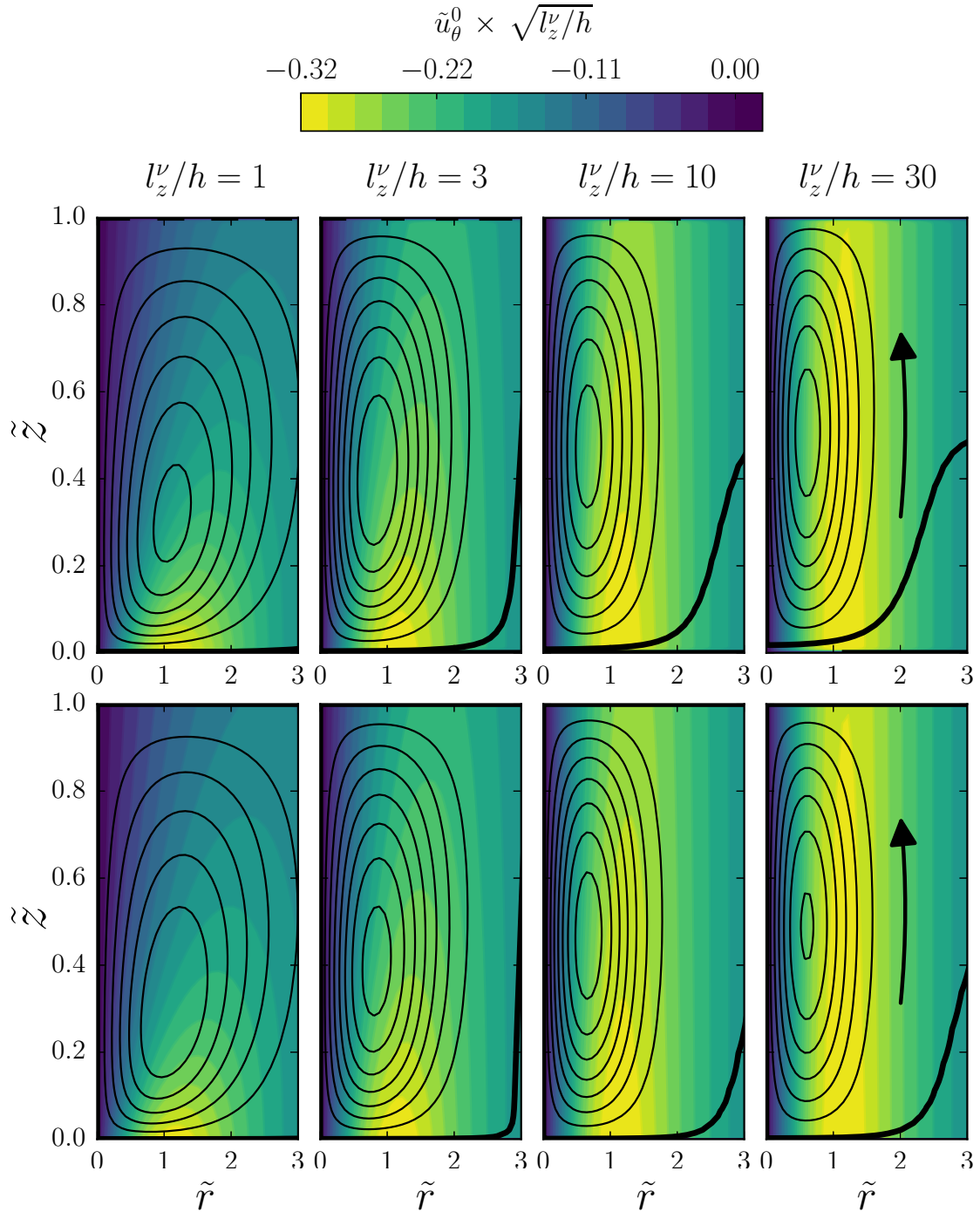


Figure 2.8. Complete velocity field for 3D base flows (i.e. low values of l_z^ν/h). Top: $Ha = 456$, bottom: $Ha = 3644$. The magnitude of \tilde{u}_θ^0 is indicated by filled contours. Streamlines correspond to iso-values of ψ^1 . (—): counter-clockwise recirculation ($\psi^1 < 0$), (—): $\psi^1 = 0$.

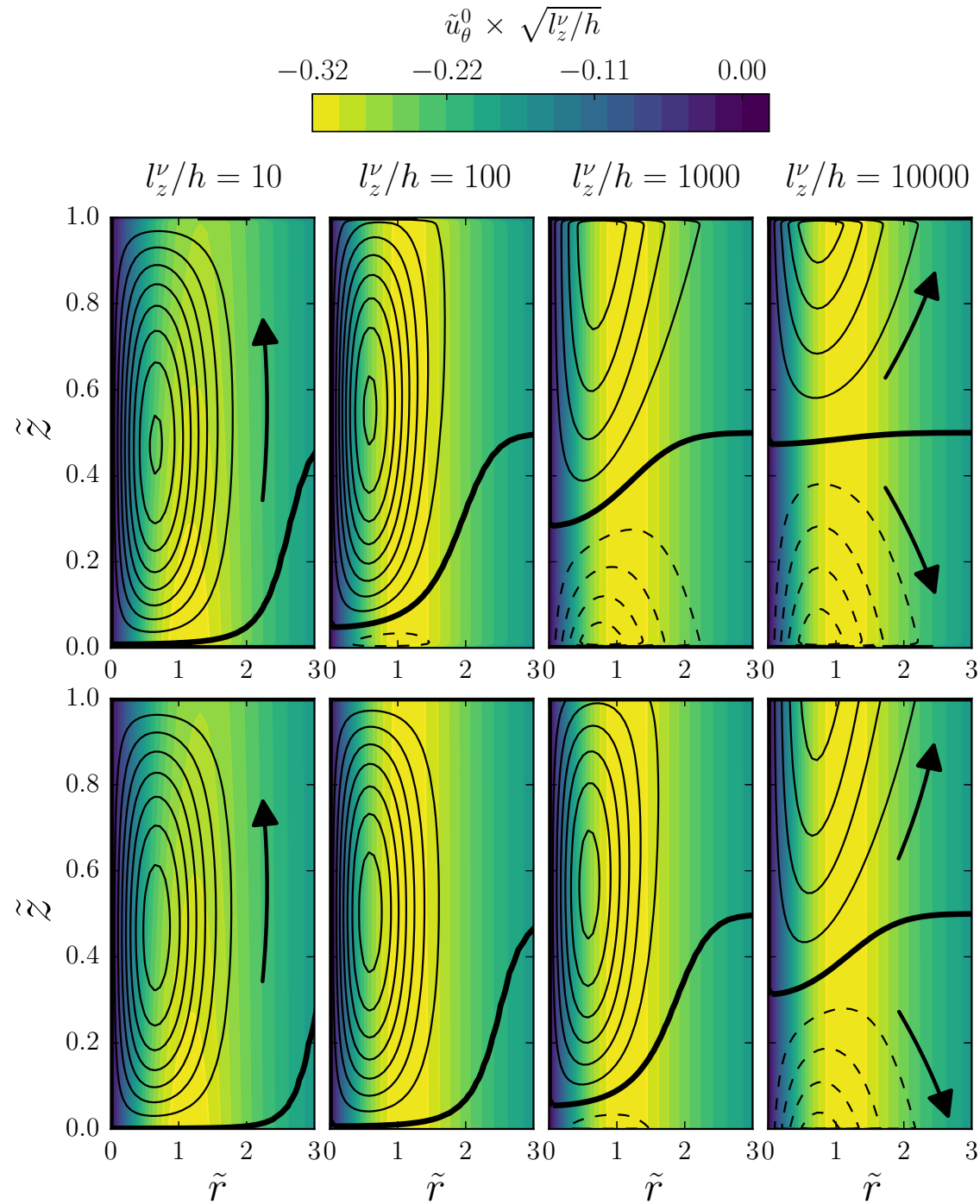


Figure 2.9. Complete velocity field for increasingly quasi-2D base flows (i.e. high values of l_z^v/h). Top: $Ha = 456$, bottom: $Ha = 3644$. The magnitude of \tilde{u}_θ^0 is indicated by filled contours. Streamlines correspond to iso-values of ψ^1 . (---): clock-wise recirculation ($\psi^1 > 0$), (—): counter-clockwise recirculation ($\psi^1 < 0$), (—): $\psi^1 = 0$.

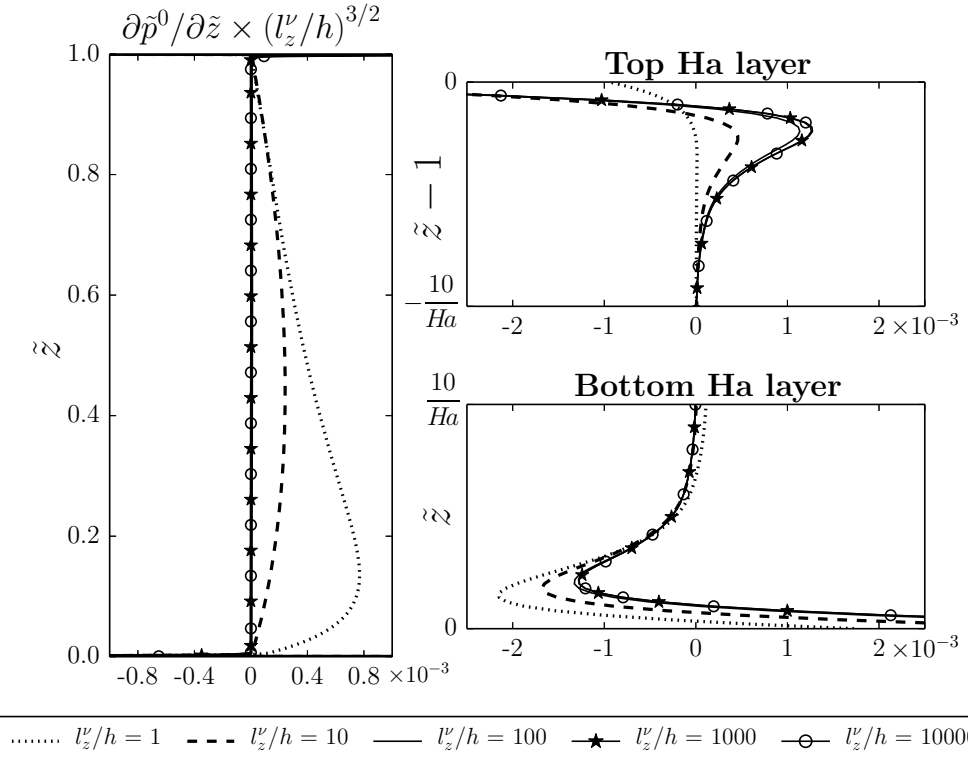


Figure 2.10. Pressure gradient along the axis of the vortex. 3D base flows (i.e. low values of l_z^ν/h) introduce a positive pressure gradient along \mathbf{e}_z in the bulk, which drives a jet down the axis of the channel. In the Hartmann layers, the negative pressure gradient at the bottom pushes the fluid up the axis, while the positive pressure gradient at the top pulls it down.

Figure 2.11 gives a close up view of the bottom Hartmann layers for the smaller values of l_z^ν/h . This figure confirms the existence of a weak clockwise recirculation in the Hartmann layers, although this direct recirculation is too weak to balance the downwards axial jet. The confinement of this weak direct pumping to the thin boundary layers makes it very difficult to fully capture whether experimentally or numerically. Yet, it is a clear feature of the analytical solution. In addition, figure 2.11 demonstrates that the Hartmann number does not actually impact the mechanisms driving the meridional flow, but modifies its topology instead by squeezing the streamlines closer to the walls.

In order to further quantify the secondary flows, we introduce the poloidal flowrate $q_{\tilde{z}}^1(\tilde{z})$ defined by

$$q_{\tilde{z}}^1(\tilde{z}) = \frac{1}{2} \int_0^{2\pi} \int_0^{\tilde{R}} |\tilde{u}_{\tilde{z}}^1(\tilde{r}, \tilde{z})| \tilde{r} d\tilde{r} d\theta. \quad (2.40)$$

We also introduce $\tilde{h}_c = h_c/h$, where h_c represents the height of the bottom recirculation. \tilde{h}_c is found as the first local minimum of $q_{\tilde{z}}^1(\tilde{z})$. Figure 2.12 represents the height of the bottom

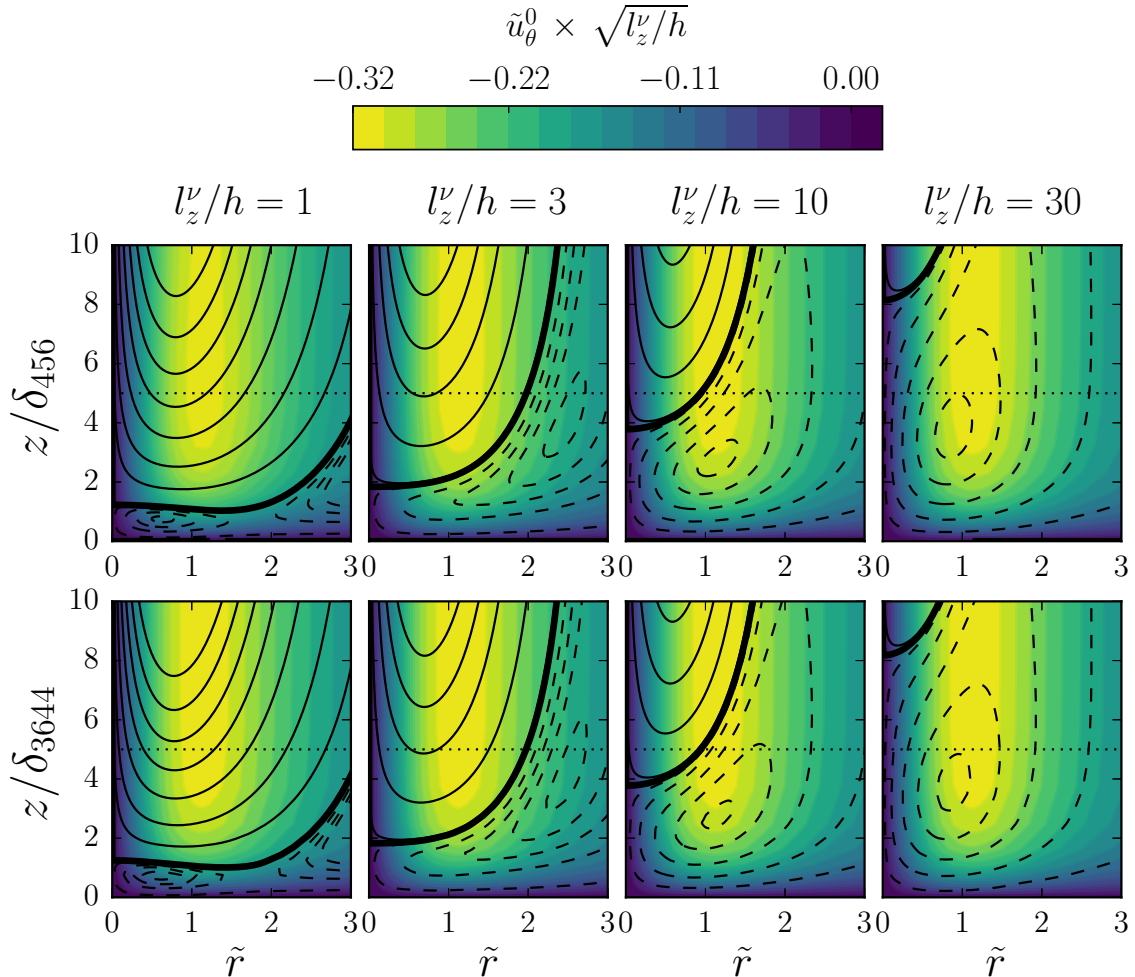


Figure 2.11. Close up view of the velocity field in the bottom Hartmann layer for 3D base flows. Top: $Ha = 456$, bottom: $Ha = 3644$. The magnitude of \tilde{u}_θ^0 is indicated by filled contours. Streamlines correspond to iso-values of ψ^1 . (---): clock-wise recirculation ($\psi^1 > 0$), (—): counter-clockwise recirculation ($\psi^1 < 0$), (—): $\psi^1 = 0$. (.....): plausible positioning of the outer edge of the Hartmann layer located at $z/\delta_{Ha} = 5$, where $\delta_{Ha} = h/Ha$ for $Ha = 456$ and $Ha = 3644$ respectively.

recirculation against the variable $l_z^v/h \times Ha^{-1}$, which can also be interpreted as the ratio $(\eta/h)^2$ by virtue of (2.2). When the base flow is quasi two-dimensional ($l_z^v/h > 100$), the quantity η/h may naturally be confused with the aspect ratio of the vortex. It appears from figure 2.12 that when the leading order flow is close to being quasi-2D, the topology of the meridional flow is fully determined by the parameter η/h . More specifically, narrow aspect ratios correspond to inverse Ekman pumping, while wide aspect ratios lead to an asymptotic state where two counter rotating structures of equal size split the channel in half. The shift

from inverse to direct pumping concurs with a ratio $(\eta/h)^2$ that is of order unity. Note that for a perfectly quasi-2D flow ($l_z^\nu/h \rightarrow \infty$) only *direct* Ekman pumping subsists for any finite value of η/h .

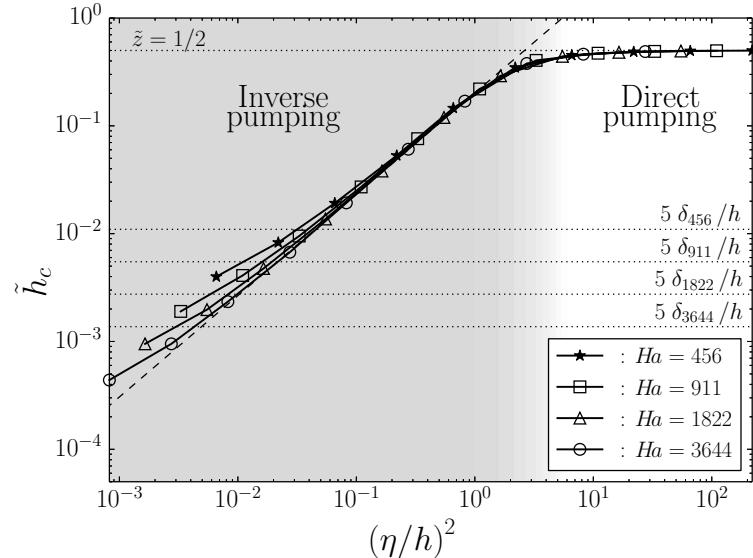


Figure 2.12. Height of the bottom recirculation against $(\eta/h)^2$. The middle of the channel is located by $\tilde{z} = 1/2$. An estimation of the thickness of the bottom Hartmann layer is given by $\tilde{z} = 5 \delta_{Ha} / h$, where $\delta_{Ha} = h/Ha$ for $Ha = 456, 911, 1822$ and 3644 respectively.

2.4.3 Is two-dimensionality a good source of helicity?

Having now characterized both the azimuthal and meridional flows, we are in a position to determine their potential to generate helicity. Figure 2.13 displays the helicity $\tilde{H}(\tilde{z})$ integrated over a cross-section of height \tilde{z} :

$$\tilde{H}(\tilde{z}) = 2\pi \int_0^{\tilde{R}} \tilde{\mathbf{u}} \cdot \tilde{\boldsymbol{\omega}} \tilde{r} d\tilde{r}, \quad (2.41)$$

which happens to be significant only at first order i.e. $\tilde{H}(\tilde{z}) = N^{-1} \tilde{H}^1 + O(N^{-3})$, with

$$\tilde{H}^1(\tilde{z}) = 2\pi \int_0^{\tilde{R}} (\tilde{u}_\theta^0 \tilde{\omega}_\theta^1 + \tilde{u}_r^1 \tilde{\omega}_r^0 + \tilde{u}_z^1 \tilde{\omega}_z^0) \tilde{r} d\tilde{r}. \quad (2.42)$$

Figure 2.13 suggests that helicity exists in the bulk when the base flow is 3D, while quasi two-dimensionality confines helicity to the boundary layers. Furthermore, $\tilde{H}^1(\tilde{z})$ is

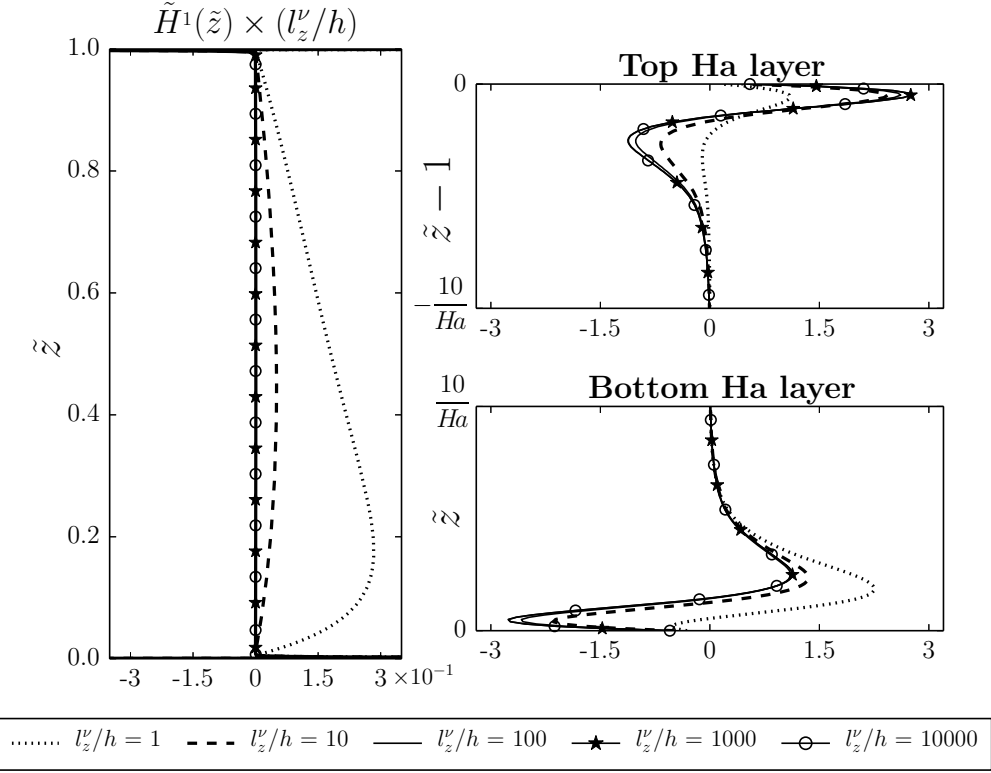


Figure 2.13. Local helicity integrated over horizontal cross sections $H^1(\tilde{z})$.

non symmetrical only for 3D base flows, meaning that the global production of helicity will be non zero only in this case. Consequently, Ekman pumping does not appear to be the most favorable source of global helicity in MHD vortices, which may seem surprising at first. It can however be attributed to several factors. First, secondary flows are a lot stronger when inverse pumping dominates. Second, Ekman pumping introduces symmetrical structures of opposite sign, which compensate each other globally. Helicity generated by inverse pumping on the other hand conserves its sign across the entire layer.

Finally, direct and inverse pumping appear to produce helicity in different ways. While inverse Ekman pumping collocates the axial velocity and vorticity in the bulk, direct pumping produces helicity mainly by combining centripetal jets and shear within the boundary layers.

2.5 Summary of the main findings

We showed in this chapter that the topology of an electrically driven vortex confined between two no-slip walls in the low- Rm approximation and weakly inertial limit can be fully described with two parameters. On the one hand, the dimensionality of the leading order is uniquely characterized by the ratio l_z^v/h , which compares the range of action of the Lorentz force to the height of the channel. On the other hand, the topology of the secondary

2. A WEAKLY INERTIAL VORTEX CONFINED BETWEEN TWO NO-SLIP WALLS

recirculations is fully described by the parameter η/h , which compares the width of the injection electrode to the height of the channel. In the quasi two-dimensional limit, η/h may be interpreted as the aspect ratio of the vortex.

Using an analytical approach, we were able to completely resolve the finest properties of the flow and in particular the Hartmann boundary layers, which are an inherent source of three-dimensionality. The Hartmann numbers used in this study were comparable to those found experimentally. Thanks to this approach, we were able to distinguish two different inertial mechanisms able to drive the first order recirculations: inverse and direct Ekman pumping. We found that both co-existed in all cases investigated (although direct pumping is confined to the bottom boundary layer when the base flow is three-dimensional), and that the shift from one mechanism to the other occurred smoothly. This result could not have been obtained either numerically or experimentally due to a lack of resolution of either approaches at high Ha .

A phase diagram summarizing all the different configurations is reported in figure 2.14. More specifically, it underlines the fact that inverse pumping can still exist when the base flow is close to being 2D, if the vortex is of sufficiently small aspect ratio η/h . This comes from the very nature of direct pumping, which originates within the boundary layers and is therefore strongest there. In thin vortices, its influence on the bulk is limited, whereas a small pressure gradient in the bulk suffices to drive inverse pumping.

Finally, it was found that global helicity is expected to be prominent only in three-dimensional configurations. In a geophysical context, this result might help clarify the question of whether Ekman pumping is a relevant source of helicity to sustain planetary dynamos. As noted by Davidson (2014), Ekman pumping may not be a very efficient source of helicity in planetary cores because quasi-2D vortices extending across the liquid core of the Earth for example are unlikely to exist. They can therefore be expected to be three-dimensional, hence favoring alternative mechanisms such as inverse pumping or the propagation of inertial waves.

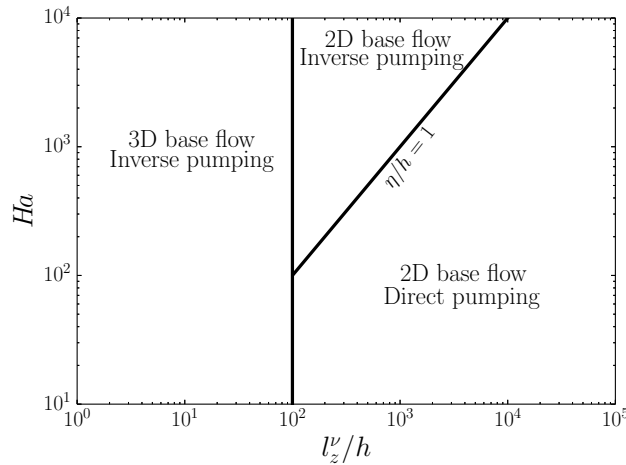


Figure 2.14. Phase diagram summarizing all features of wall bounded low- Rm MHD vortices.

Chapter 3

An experimental apparatus for the study of MHD turbulence

Some effects resulting from inertia have been highlighted in the previous chapter using a very simple flow, namely an isolated vortex. The calculations were carried out in the weakly inertial limit, which simplified the model's equations enough for us to actually compute a solution. As far as the study of fully inertial turbulent flows is concerned, calculating exact solutions is illusional (at least in a reasonable amount of time, and for regimes which are actually observed in the laboratory). The purpose of this chapter is to present the experimental apparatus which we have used to investigate MHD turbulence confined between no-slip and insulating walls.

3.1 Historical review of past experimental studies

Experimentalists have demonstrated a lot of ingenuity in trying to observe and validate theoretical predictions concerning the dynamics of 2D turbulence. Among the diverse ways that exist to create quasi-2D turbulence in the laboratory, MHD is a candidate which received great attention very early on. As an introduction to this chapter, we propose a review of past experimental apparatus dedicated to the study of low- Rm MHD turbulence. Doing so, we will give insight into the knowledge and know-how accumulated by the community over the years, in the continuity of which our own experiment takes place. It will also highlight some aspects of low- Rm MHD turbulence that still need clarification and which this thesis aims at answering.

Early experimental work by Kit & Tsinober (1971) focused on demonstrating that MHD turbulence in high magnetic fields was indeed a relevant candidate to emulate and study 2D turbulence. To confirm the latter observations, Kolesnikov & Tsinober (1972) investigated the spatial structure of turbulence occurring in the wake of a cylinder aligned with the magnetic field. Their setup consisted of a mercury loop whose working section was an electrically insulating rectangular duct of cross section $20 \times 60 \text{ mm}^2$ and length 1.2 m. The

3. AN EXPERIMENTAL APPARATUS FOR THE STUDY OF MHD TURBULENCE

duct was placed inside the gap of an electromagnet delivering up to 0.8 T, while a flow of mercury was imposed perpendicularly to the magnetic field with a constant mean velocity of 20 cm/s. An electrically insulating cylinder was present at the entrance of the duct, which generated 2D turbulent perturbation (in the sense that they were spatially invariant along the axis of the cylinder). The intensity of the turbulence thus generated (defined as the ratio of the magnitude of the turbulent fluctuations to that of the mean flow) was in the 10 to 15% range. The streamwise component of the flow was measured using hot wire anemometry, while the cross wise components of the electric field were diagnosed using electric potential velocimetry. By computing one dimensional Fourier spectra at different locations downstream of the cylinder, Kolesnikov & Tsinober (1972) showed that the turbulent structures shed in these circumstances lived longer when the magnetic field was on. This observation confirmed the fact that electromagnetic effects indeed tend to balance out 3D inertial instabilities. Furthermore, these energy spectra gave first quantitative results on the properties of MHD turbulence. More specifically, when no field was applied, the energy spectrum featured a very clear $k_{\perp}^{-5/3}$ slope over about a decade for frequencies larger than the vortex shedding frequency (k_{\perp} referring to wave vectors perpendicular to the magnetic field). This observation agrees quite well with Kolmogorov's picture of a direct energy cascade where energy transits from the injection scale to the small dissipative scales (cf. section 4.1.2). In the presence of the magnetic field however, fewer scales appeared in the large frequency domain, and featured a steep k_{\perp}^{-3} . By contrast, the lower part of the spectrum appeared to display a $k_{\perp}^{-5/3}$ slope. Both these observations seem to fit the 2D turbulence predictions put forward by Kraichnan, according to which an inverse energy cascade from the injection scale to large scales of the system is accompanied by a direct enstrophy cascade (cf. section 4.1.3).

A groundbreaking experiment was perhaps that of Alemany *et al.* (1979), which definitely illustrated the effects of magnetic fields on initially isotropic turbulence evolving in a virtually unbounded domain. In this experiment, turbulence was generated by towing a grid through a 2.7 m high tank filled with mercury. The grid could travel as fast as 80 cm/s, while the applied magnetic field ranged between 0 and 0.25 T. The velocity component parallel to the magnetic field (and incidentally the direction of the grid) was measured using hot wire probes. The initial interaction parameter N_0 based on the initial properties of turbulence (i.e. rms of the fluctuations right behind the grid, and size of the mesh) was around $N_0 \sim 1$, meaning that electromagnetic effects and inertia were initially of the same order of magnitude. However, since the turbulence was decaying, magnetic effects started to creep up, and Joule dissipation became more and more prominent. As a result, Alemany *et al.* (1979) were able to observe the transition between initially 3D turbulence dominated by inertia, and the development of anisotropy as a result of Joule dissipation. The former flow was found to have an inertial range scaling as $k_{\parallel}^{-5/3}$ (k_{\parallel} representing wave vectors parallel to the magnetic field), while the latter regime was found to follow a k_{\parallel}^{-3} law. These spectra were interpreted as resulting from a balance between inertial energy transfers and Joule dissipation during the anisotropic phase. Although quite tempting to compare these slopes to the predictions for 2D dynamics, Alemany *et al.* (1979) stress that the anisotropy of the flow is not strong enough for these

3.1. Historical review of past experimental studies

spectra to be in any way related to an inverse energy cascade. Indeed, owing to the tank's high aspect ratio and the relatively low magnetic fields, the long anisotropic structures were prone to hydrodynamic instabilities which would quickly break them back to 3D structures.

The first observation of the inverse energy cascade in forced, statistically steady and quasi-2D MHD turbulence is attributed to Sommeria (1986). The experimental setup he used consisted of a 12 cm wide square box filled with a 2 cm deep layer of mercury. The bottom surface was electrically insulating and no-slip, while the upper surface was electrically conducting and either free-slip (inert nitrogen atmosphere) or rigid (formation of mercury oxides). The whole apparatus was set in a magnetic field, and the layer put in motion by injecting DC current through an array of 36 injection electrodes. The magnetic field was of the order of 1 T, while the maximum amount of injected current could reach 20 A. The flow was diagnosed by measuring the electric potential at the bottom wall. Under these circumstances, Sommeria (1986) showed that the bulk was quasi-2D, and that the main source of energy dissipation came from Hartmann friction along the bottom wall. Although the homogeneity and axisymmetry of the flow were difficult to assess, the inhomogeneous and periodic square forcing did not seem to transpire in the results. In spectral space, the one dimensional kinetic energy density displayed a clear $k_{\perp}^{-5/3}$ in the large scales, which could undoubtedly be associated to an inverse cascade. Indeed, the injection scale which was fixed by the spacing between injection electrodes laid below these larger inertial scales. The small scale region of the spectrum was however inaccessible as a result of spatial resolution not being high enough.

Paret & Tabeling (1998) refined the observation of the inverse energy cascade in forced and statistically steady turbulence further. The experimental apparatus they used was similar to the one used by Sommeria (1986), and consisted of a 15 cm wide square container containing a shallow (5.5 cm deep) and stratified layer of NaCl solution. Permanent magnets were arranged in an array and fixed underneath the container, with the magnetic field lines pointing vertically and delivering up to 0.3 T. A time series of electric pulses of constant amplitude and random sign were applied across the cell in order to drive turbulence with no net mean flow. Thanks to the transparent electrolyte they used, Paret & Tabeling (1998) had access to both velocity components in the horizontal plane by using PIV measurements. Recording the transient flow occurring right after the forcing was switched on, they showed that the energy, which initially concentrated around the forcing scale was progressively transferred towards larger scales as time went by. In the steady state, the energy spectrum featured a clear $k_{\perp}^{-5/3}$ power law over a bit less than a decade. The computation of the spectral energy flux undoubtedly showed that this inertial range was indeed associated to an inverse energy cascade.

One peculiar aspect of MHD is of course Joule dissipation, which is an important issue as far as the dynamics of turbulence is concerned. Indeed, in the classical theory of hydrodynamic turbulence, energy can only be dissipated by viscous friction either at large (2D turbulence) or small (3D turbulence) scales. The presence of Ohmic losses introduces however an additional dissipation mechanism affecting all scales. It therefore has a strong impact on the dynamics of MHD turbulence, which should not be overlooked. To that end,

3. AN EXPERIMENTAL APPARATUS FOR THE STUDY OF MHD TURBULENCE

the study lead by Messadek & Moreau (2002) shed some light on how Joule dissipation affects the dynamics of quasi-2D MHD turbulence, thus quantified the extent to which MHD turbulence mimics quasi-2D hydrodynamic turbulence. Their experimental setup consisted of shear turbulence driven electrically in an annular channel filled with mercury. The channel was shallow (1 cm deep), and the magnetic field high enough (ranging from 0.5 to 6 T), so that the flow was always quasi-2D. Depending on the operating parameters, Messadek & Moreau (2002) were able to fine tune the intensity of the Hartmann braking resulting from electric current flowing through the Hartmann boundary layers. More specifically, for low magnetic fields (i.e. cases where the Hartmann braking was relatively weak), they were able to observe *hydrodynamic* turbulence (in the sense that inertial energy transfers took place much quicker than Joule dissipation in the boundary layer), featuring a $k_{\perp}^{-5/3}$ inertial range in Fourier space. On the contrary, for large magnetic field, they observed a k_{\perp}^{-3} energy spectrum much like Alemany *et al.* (1979). Unlike the latter however, Messadek & Moreau (2002) interpreted this spectrum as a competition between non linear energy transfers and energy dissipation in the Hartmann layers as a result of Hartmann friction.

More recent experiments became concerned with the remaining three dimensionality found in MHD turbulence. For instance, Klein & Pothérat (2010) showed that the topological dimensionality of wall-bounded MHD turbulence resulted exclusively from the competition between the diffusive effect of the Lorentz force and inertia, as measured by the true interaction parameter $N_t = \tau_u/\tau_{2D}$. The experimental setup they used consisted of a 10 cm wide cubic container filled with galinstan. The container was immersed in a vertical magnetic field (up to 5 T), and turbulence was electrically driven using a network of 100 injection electrodes alternately connected to a regulated DC power supply. The flow was forced along the bottom wall and left to develop vertically under the action of the Lorentz force. The flow was diagnosed using electric potential measurements along the top and bottom walls, which were perpendicular to the magnetic field. By correlating the top and bottom potential signals, Klein & Pothérat (2010) monitored the similarity in the flow patterns away and close to the forcing area. They observed that as the Lorentz force became quicker in diffusing momentum, the flow patterns along the top and bottom walls gradually shifted from initially decorrelated to fully identical. They further quantified the topological state of the turbulence as being either strongly 3D (flow patterns are completely decorrelated), weakly 3D (flow patterns are correlated in shape but not in intensity), or quasi-2D (flow patterns are fully correlated). Later on, Pothérat & Klein (2014) refined the picture even further by introducing the non-dimensional ratio l_z/h , which compares the range of action of the Lorentz force with the height of their channel. It turns out that l_z/h is a neat and succinct way of quantifying the dimensionality of the turbulence. Indeed $l_z/h \ll 1$ means that the Lorentz force is not strong enough to diffuse momentum before three-dimensional effects (such as inertia or viscosity) kick in, hence leading to a 3D flow. Alternately, $l_z/h \gg 1$ implies that the Lorentz force is capable of diffusing momentum much further than the distance separating the two horizontal walls, hence yielding a quasi-2D flow.

3.2 Description of the Flowcube

3.2.1 Components

The Flowcube is an experimental rig originally designed by Klein (2010), which was rebuilt from the ground up during this thesis in order to extend the accessible inertial range as much as possible, and enable a high resolution measurement of it. The improved and enlarged version of the Flowcube is shown in figure 3.1. The centerpiece of this experiment is a closed vessel filled with galinstan (a eutectic alloy of gallium, indium and tin, liquid at room temperature), characterized by a density $\rho = 6400 \text{ kg/m}^3$, kinematic viscosity $\nu = 4 \times 10^{-7} \text{ m}^2/\text{s}$ and electric conductivity $\sigma = 3.4 \times 10^6 \text{ S/m}$. Statistically steady turbulence is driven electrically by inducing Lorentz forces, which appear while simultaneously applying a vertical static and uniform magnetic field and forcing DC current through the bottom wall.

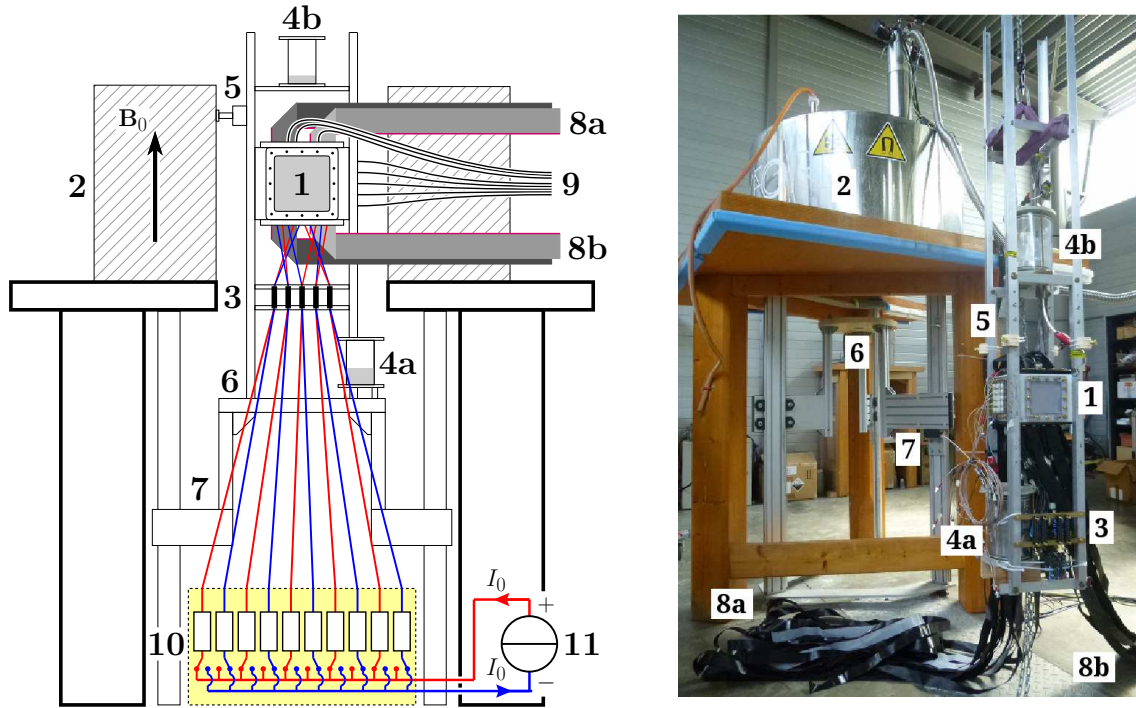


Figure 3.1. Left: sketch of the experiment mounted inside the superconducting magnet. Right: experiment posing in front of the superconducting magnet. (1) vessel filled with galinstan; (2) superconducting magnet; (3) current injection panel (physically connected to the back of the injection electrodes); (4a) fill tank; (4b) overflow tank; (5) alignment adjustment spacers; (6) support platform; (7) elevator; (8a) analog output for the top potential probes; (8b) analog output for the bottom potential probes; (9) analog output for the ultrasound transducers; (10) injection table; (11) power supply.

3. AN EXPERIMENTAL APPARATUS FOR THE STUDY OF MHD TURBULENCE

The vessel consists of a rectangular parallelepiped frame made of polyacetal, which possesses a 150 mm wide square base and a height $h = 100$ mm. The frame is closed by electrically insulating side plates, whose surface is either made of ceramic or polycarbonate (cf. figure 3.2.left). Probes are embedded flush in each one of these plates to either drive the flow or analyze its properties.

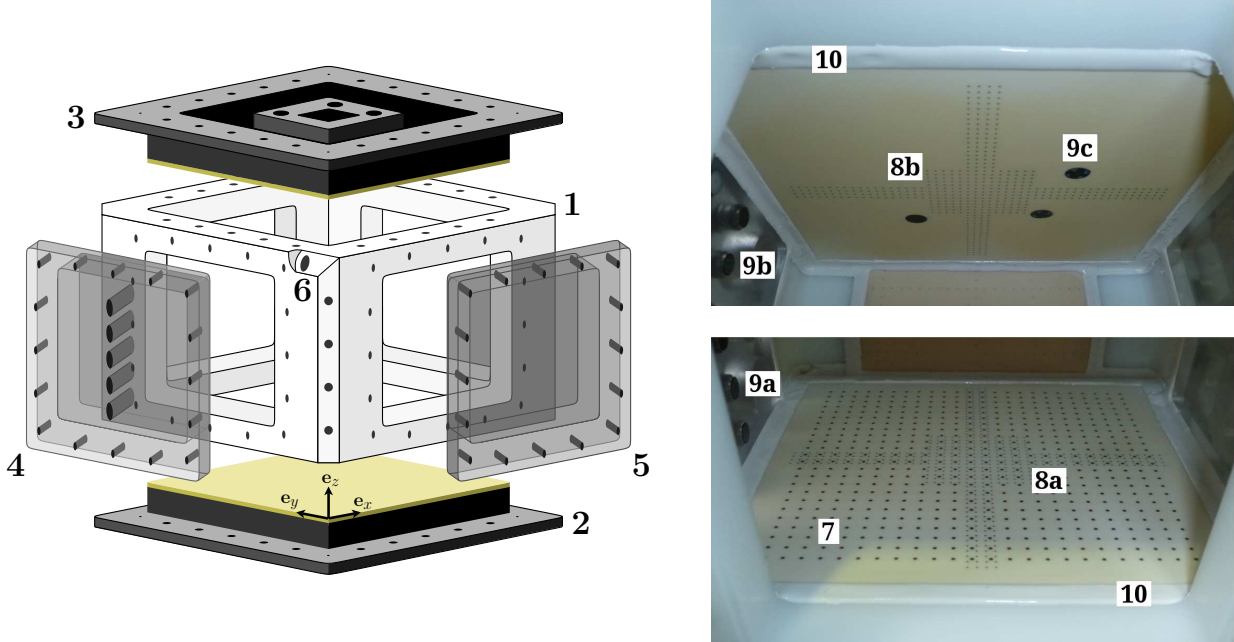


Figure 3.2. Left: exploded view of the vessel. Right: close up views of the vessel's interior. (1) polyacetal frame; (2) injection plate; (3) top plate; (4) ultrasound plate; (5) window; (6) galinstan outlet (inlet is located in the diagonally opposite bottom corner); (7) injection electrodes; (8a/b) potential probes; (9a/b/c) ultrasound transducers; (10) silicone seals.

The core of the experiment are the top and bottom Hartmann plates (cf. figure 3.2.right), which consist of 148 mm \times 148 mm wide printed circuit boards (PCBs) mounted on polyamide coated brass frames. Both plates are fitted with 484 potential probes arranged in a cross pattern, which are used to measure the electric potential along these walls. The patterns found on the top and bottom plates are mirror symmetrical, such that each potential probe found on the bottom plate has an exactly overhanging counterpart. Three 8.2 mm diameter holes were drilled through the top plate to accommodate the presence of ultrasound transducers. The bottom plate (also referred to as the injection plate) is equipped with a 24×24 array of 1 mm diameter copper electrodes, through which the DC electric current was forced in and out of the experiment. Before the top and bottom plates were fitted inside the frame, all probes and electrodes were gold plated so as to improve electrical contact between them and the galinstan. The side walls consist of polycarbonate windows, one of which can accommodate the presence of five ultrasound transducers stacked on top of each

other. Taking the altitude reference $z = 0$ mm at the surface of the bottom plate, the five ultrasound transducers are located at heights $z = 12, 31, 50, 69$ and 88 mm respectively.

Airtightness of the vessel is ensured by O-rings on the outer side of the frame, complemented by internal silicone seals cast within the gaps between plates. Liquid metal was supplied to the main chamber from a fill tank connected to one of the bottom corners. A similar tank connected to the diagonally opposite top corner received the metal overflow. Before liquid metal was allowed in, a thorough cleansing of the whole experiment was performed. More specifically, it was vacuumed and flushed with Argon five times to remove as much oxygen as possible. This step is mandatory to delay galinstan oxidization, as gallium oxides tend to yield very poor electric contacts. The experiment was then gently filled from the bottom up by relying on gravity exclusively. Doing so helped keep the free surface clean and steady, thus maximizing the chances of a good electric contact with the top plate once the metal eventually reached it. Throughout the filling process, the experiment was tilted 45° sideways such that the entry and exit points for the liquid metal were the lowest and highest points of the vessel respectively. Doing so guaranteed that galinstan thoroughly wet the top wall before any overflow took place, again maximizing chances of electric contact at the top. The filling took place under an inert Argon atmosphere, whose pressure was about 1 bar. Once completely filled, the experiment was inserted inside the magnet. The vertical positioning of the experiment was done with a dedicated elevator, while the lateral alignment was fine tuned using adjustable spacers.

3.2.2 The Hartmann plates

The design and building of the Hartmann plates deserves to be mentioned, as it certainly was the most painstaking and time-consuming task of this entire project. Indeed, although the technological implementation of electric potential velocimetry has been tried and tested for a long time, its implementation in the improved version of Flowcube bore some interesting challenges, which mainly arose from high probe density. To be more specific, each Hartmann plate was equipped with 484 potential probes, each separated by 2.5 mm. In addition to these potential probes, the bottom plate was also equipped with 576 injection electrodes each separated by 5 mm to drive the flow. This large number of probes and electrodes was chosen to drive and measure turbulence over the widest range of scales as possible, and to make sure we measured it with sufficient spatial resolution.

The heart of the Hartmann plates are three-layered PCBs manufactured by PCB electronics SA, composed of a 1.6 mm thick outer layer of ROGERS 4003C (a high performance hydrocarbon ceramic) and standard FR4 epoxy inner layers. The outer ROGERS layer is to be in direct contact with galinstan, while the inner FR4 layers have electric tracks etched in them to extract the potential signals. The purpose of these tracks is to bundle together the potential signals and channel them to connectors located all around the edges of the PCBs (cf. figure 3.3.right). These connectors were eventually linked via ribbon cables to the acquisition system to measure the potential signals. The potential probes actually consist of

3. AN EXPERIMENTAL APPARATUS FOR THE STUDY OF MHD TURBULENCE

0.25 mm diameter copper plated vias filled with 0.20 mm diameter copper wires. Each wire was individually soldered on to its track.

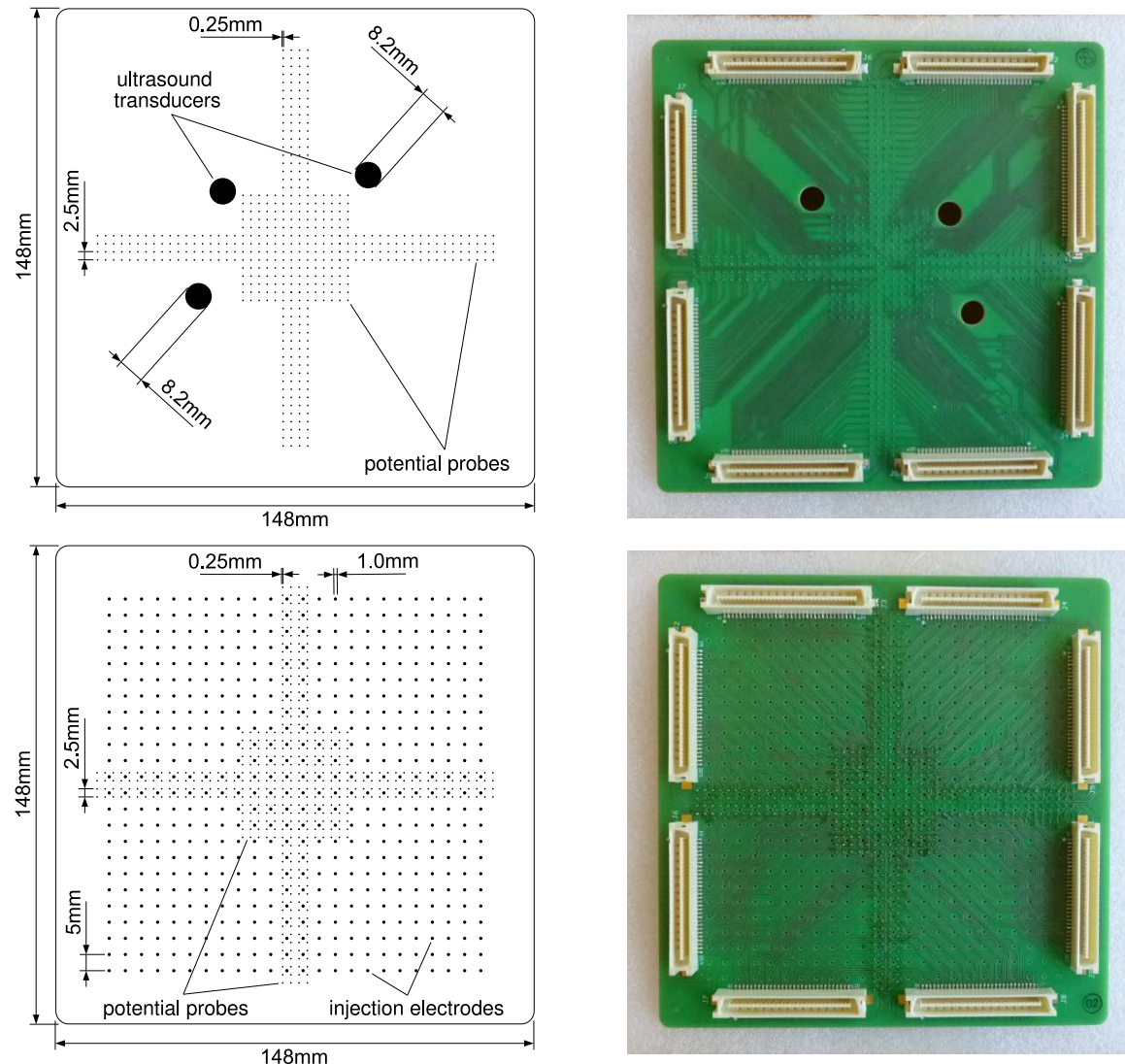


Figure 3.3. Left: front view of the top and bottom Hartmann plates, each featuring 484 potential probes. The bottom plate (also known as the injection plate) features spots for 576 injection electrodes, while the top plate can accommodate for 3 ultrasound transducers. Right: rear view of the PCBs after all connectors and probes were soldered in place. The tracks enabled the extraction of potential signals to the connectors located all around.

Once all soldering onto the PCBs was complete, mating connectors were glued in place and sealed with silicone sealant. The PCBs were then fastened onto a polyamid coated brass frame using epoxy resin. Prior to the final potting of the plates with polyurethane

resin, injection electrodes were glued in position on the bottom PCB (figure 3.5). After the plates had completely set, the outer surfaces were polished. Injection electrodes and potential probes were then gold plated so as to get a good electric contact between them and galinstan.

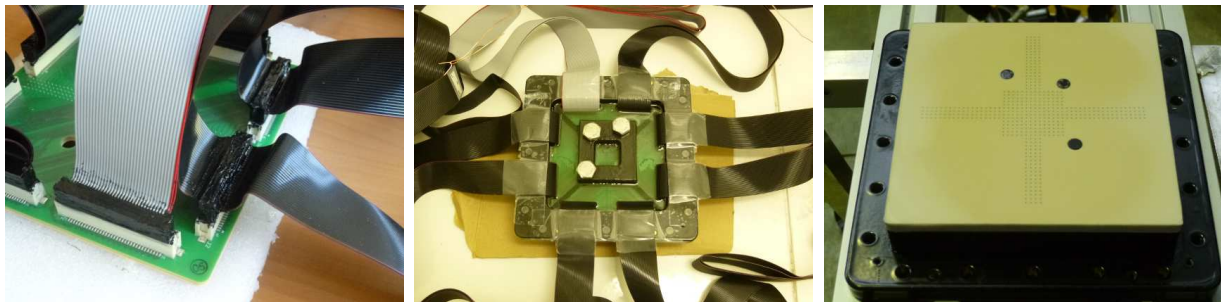


Figure 3.4. Building of the top Hartmann plate. From left to right: sealing the mating connectors; potting the plate with polyurethane resin; top plate ready to be mounted (polished, gold plated and fitted with the ultrasound transducers).



Figure 3.5. Building of the bottom Hartmann plate. From left to right: gluing of the injection electrodes; profile view before trimming and sanding the injection electrodes and potential probes; polished bottom plate.

3.2.3 Electric forcing

Electric current enters and leaves the vessel through the bottom injection electrodes, which can individually be connected to either poles of a DC power supply via the current injection table (cf. figure 3.6). The injection electrodes are physically connected to the injection table via the injection panel, which simply refers to a series of connectors soldered at the back of the electrodes. An EA-PSI 9080-300 DC power supply manufactured by Elektro-Automatik GmbH & Co.KG was used to supply electric current to the Flowcube (up to 300 A in total, ca. 7.5 kW). The interfacing between the power supply and the vessel was provided by the injection table, consisting of a series of $2\Omega \pm 0.25\%$ resistors

3. AN EXPERIMENTAL APPARATUS FOR THE STUDY OF MHD TURBULENCE

mounted in parallel. These high precision resistors ensured that the total incoming current was evenly split among the electrodes, thus preventing any forcing dissymmetry during the experiments. Indeed, the contact resistance between copper and galinstan is so low, that any perturbation (such as the temporary presence of gallium oxide) may completely off balance the overall current distribution. Each resistor was individually connected to the positive or negative pole of the power supply using a switchboard at one end, and to an injection electrode at the other end. The typical path for the electric current forced through a pair of electrodes is sketched in figure 3.6, where I_0 is the total current delivered by the power supply and $i_e = 2I_0/N_e$ is the amount of current per electrode. Here, N_e is the total number of connected electrodes, regardless of their polarity. The injection table used throughout this project was inherited from Klein (2010), and enabled the simultaneous connection of up to 100 injection electrodes. The resistors' power rating was 100 W, which limited the amount of current per electrode to 7 A, and required cooling.

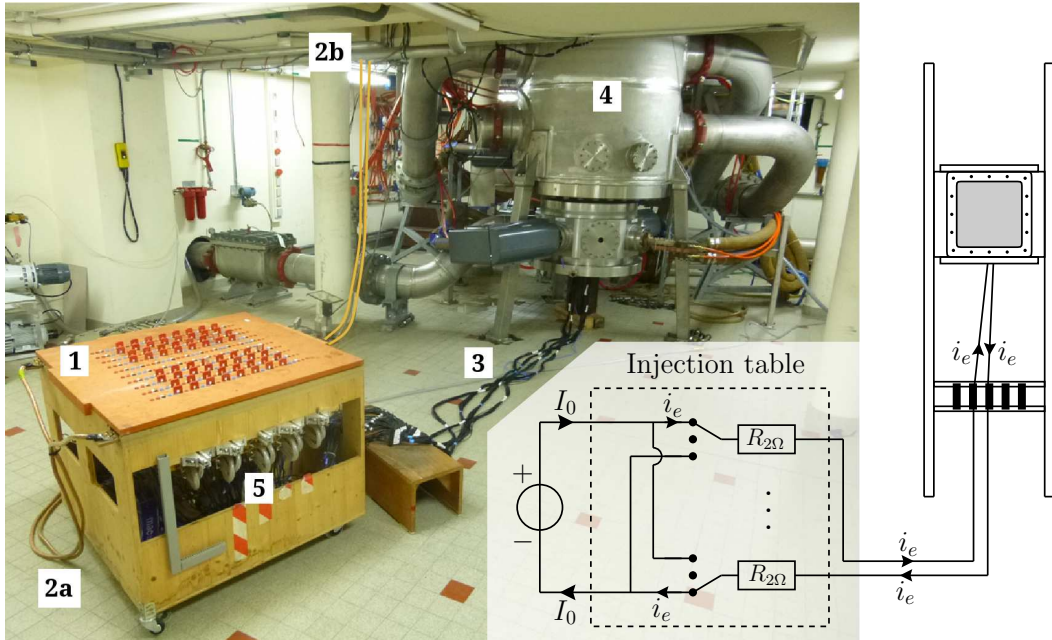


Figure 3.6. Overview of the current injection system. (1) injection table with U-shaped connectors to distribute current to the injection electrodes; (2a) leads for total injection current, injection table end; (2b) leads for total injection current, power supply end (power supply located on the upper floor); (3) leads to injection panel (each black cable is linked to one single injection electrode); (4) resistive magnet; (5) aluminum cooling system for the resistors.

Electric current plays a somewhat ambiguous role in our experiment. Indeed, on the one hand electric current is injected in the vessel to put the fluid in motion. On the other hand, these very motions induce electromotive forces which draw eddy currents. We shall therefore be extremely cautious in distinguishing between both contributions, as they have completely

opposite effects on the dynamics of the flow: injected current is a source of kinetic energy, while eddy currents induce strong energy dissipation via Joule heating.

3.2.4 Magnetic fields

The experiment was hosted by the high fields laboratory in Grenoble (LNCMI-G), which granted access to two of their magnets to conduct the ensuing experiments. A superconducting magnet with a bore of inner diameter 450 mm was used to deliver magnetic fields up to 4 T (showcased in figure 3.1), while higher fields (from 5 to 10 T) were accessible thanks to a resistive magnet of inner diameter 376 mm (visible in figure 3.6).

These two magnets use radically different technologies, both having their pros and cons. For instance, the superconducting magnet gives access to high magnetic field at a relatively low electric cost, since the coil has no electric resistivity. To get an idea, the electric current required to get 4 T in the superconducting magnet is 90 A, vs. 12000 A in the resistive magnet. As a result, the latter requires substantial water cooling, which can in turn introduce noise. The reduced electric cost necessary to operate a superconducting magnet is however balanced by its heavy consumption of cryogenic fluids to keep the temperature of the coil below 4 K. To get an idea, 100 L of liquid helium had to be injected into the magnet every 10 days to keep the coil cold (there is a dedicated facility at the lab providing liquid helium year round). These two magnets also differed in their operation. In particular, the ramp-up of the superconducting magnet is much slower, since the input power must be limited (~ 300 W) to ensure the coil remains superconducting throughout its charge. Going from 0 to 4 T in the superconducting magnet takes about 4 hours, while going from 0 to 10 T with the resistive magnet takes only about 10 min thanks to the 12 MW power supply attached to it. In both cases, magnetic field inhomogeneities at the vessel's level were of the order of 5% in both magnets.

As far as accessibility is concerned, the superconducting magnet was virtually always available, and its use was not time limited. Access to the resistive magnet was however more competitive, and subject to prior review and approval of a proposal. During this project, we were fortunate to get access to the resistive magnet twice (about 80 hours of actual magnet time in total).

3.2.5 Data logging

Electric potential signals were amplified by an operational amplifier pack built by neuroConn GmbH. This pack enabled the simultaneous measurement of 767 analog channels, which were directly connected to the potential probes. For all experiments, the sampling frequency was set to $f_s = 250$ Hz, and the data was recorded with 24 bit precision. The highest gain was used, which gave a ± 170 mV dynamic range (depending on the operating conditions, the amplitude of the electric potential at the Hartmann walls was typically in the range $50 \mu\text{V}$ to $5 \times 10^4 \mu\text{V}$). The amplifiers were left to warm up for at least 10 min before any measurement was performed in order to get drift-free signals. The hardware was

3. AN EXPERIMENTAL APPARATUS FOR THE STUDY OF MHD TURBULENCE

run by a MATLAB Simulink® script. At the beginning and end of each run, the noise level was recorded so as to monitor the ambient noise level. As it turns out, the amplitude of the input noise in the superconducting magnet (i.e. at lower fields) was constant and of the order of $3 \mu\text{V}$, while the input noise in the resistive magnet (i.e. at higher fields) depended on the setpoint but was typically of the order of $300 \mu\text{V}$ (more on the consequences of noise on the processing in section 3.4.1).



Figure 3.7. Recording devices. Left: amplifier pack, right: DOP4000.

The ultrasound signals were generated and recorded using the DOP4000 manufactured by Signal-Processing SA, to which four channels may be connected at once. The sampling frequency of the DOP is much lower than that of the amplifiers. Depending on the required dynamic range (i.e. on the amplitude of the velocity to measure), the sampling frequency typically ranged between 0.5 Hz for the lowest velocities (found along the vertical direction) and 10 Hz for the highest horizontal velocities. Ultrasound measurements require the flow to be seeded with tracing particles to reflect acoustic waves. Using galinstan has this one advantage that it inevitably introduces gallium oxides, which are effective acoustic reflectors (Brito *et al.*, 2001). The DOP4000 was run by a custom software provided by Signal-Processing SA.

3.2.6 Experimental protocol

The Flowcube offers three different operating parameters: the injection scale l_i defined as the distance separating two adjacently connected injection electrodes, the total amount of current injected in the vessel I_0 , and the intensity of the magnetic field B_0 . Some parameters were however easier to change than others. Indeed, while changing the injection scale required to physically connect (i.e. solder) each concerned electrode to the injection panel, the total injected current or the intensity of the magnetic field could be adjusted at one's fingertips. In addition, there were a few physical constraints on the system: the injection table limited the number of simultaneously connected injection electrodes to 100; a maximum threshold of 7 A per electrode was enforced so as to prevent any damaging of the injection table's resistors; the power supply at hand provided up to $I_0 = 300$ A in total.

The data presented hereafter was gathered by scanning the space of parameters (I_0, B_0) for two different injection patterns. To be more specific, the case $l_i = 5$ mm refers to a

50 mm wide injection patch formed by an array of 10×10 injection electrodes each distant by $l_i = 5$ mm (figure 3.8.left), while the case $l_i = 15$ mm refers to a 110 mm wide injection patch formed by an array of 8×8 injection electrodes each distant by $l_i = 15$ mm (figure 3.8.right). The aspect ratio of the injection scale to the size of the patch is 0.10 with the small injection scale and 0.14 with the large one.

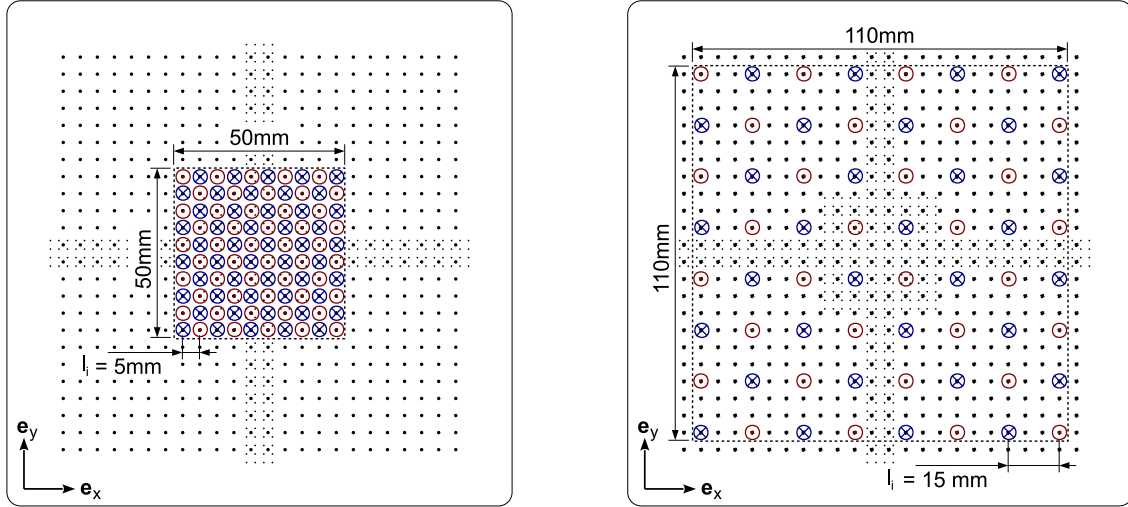


Figure 3.8. Sketch of the two different injection patterns used during this project. Left: array of 10×10 injection electrodes used in the configuration $l_i = 5$ mm. Right: array of 8×8 injection electrodes used in the configuration $l_i = 15$ mm. The dashed contours delimit the forcing patch, i.e. the region of space where turbulence is actually sustained. The polarity of the electrodes is indicated by symbols: \odot for a positive pole, \otimes for a negative pole.

I_0 (A)	B_0 (T)							B_0 (T)								
	0.5	1	2	3	5	7	10	0.25	0.5	1	2	3	4	5	7	10
56	56	56	56	56	56	56	56	64	64	64	64	64	64	64	64	64
100	100	100	100	100	100	100	100	96	96	96	96	96	96	96	96	96
150	150	150	150	150	150	150	150	128	128	128	128	128	128	128	128	128
200	200	200	200	200	200	200	200	160	160	160	160	160	160	160	160	160
250	250	250	250	250	250	250	250	192	192	192	192	192	192	190	192	192
300	300	300	300	300	300	300	300	224	224	224	224	224	224	224	224	224

(a) Case $l_i = 5$ mm, $N_e = 100$

(b) Case $l_i = 15$ mm, $N_e = 64$

Table 3.1. Combinations of operating parameters investigated in this work.

Table 3.1 summarizes all the different combinations of operating parameters investigated. As one can notice, about 100 different combinations were explored, which yielded an exhaustive description of the different regimes observable in the Flowcube.

3. AN EXPERIMENTAL APPARATUS FOR THE STUDY OF MHD TURBULENCE

B_0 [T]	1	3	5	7	10
u'_{bot} [m/s]	0.140	0.198	0.222	0.252	0.278
τ_u [s]	$1.08 \cdot 10^{-1}$	$7.57 \cdot 10^{-2}$	$6.76 \cdot 10^{-2}$	$5.96 \cdot 10^{-2}$	$5.40 \cdot 10^{-2}$
τ_J [s]	$1.88 \cdot 10^{-3}$	$2.09 \cdot 10^{-4}$	$7.53 \cdot 10^{-5}$	$3.84 \cdot 10^{-5}$	$1.88 \cdot 10^{-5}$
τ_{2D} [s]	$8.37 \cdot 10^{-2}$	$9.30 \cdot 10^{-3}$	$3.35 \cdot 10^{-3}$	$1.71 \cdot 10^{-3}$	$8.37 \cdot 10^{-4}$
τ_H [s]	6.86	2.29	1.37	0.980	0.686
τ_ν [s]	$2.50 \cdot 10^4$				
$N = \tau_u/\tau_J$	57	362	898	1550	2870
$N_t = \tau_u/\tau_{2D}$	1.29	8.14	20.2	34.9	64.5
$Re = \tau_\nu/\tau_u$	23200	33000	37000	42000	46300
$Ha = \sqrt{\tau_\nu/\tau_J}$	3600	11000	18000	26000	36000

Table 3.2. Typical range of timescales and non dimensional parameters for $l_i = 15$ mm and $I_0 = 224$ A (7 A per electrode).

Typical values of the different timescales and non-dimensional parameters defined in section 1.2.3 are computed for the case $l_i = 15$ mm and $I_0 = 224$ A. Values are reported in table 3.2. The reference velocity scale used for the calculation u'_{bot} is defined as the rms value of the turbulent fluctuation found along the injection plate, thus is representative of the turbulent kinetic energy injected in the system. In addition, the reference lengthscale perpendicular to the field was taken as the injection scale l_i , while the reference lengthscale in the direction of the field was chosen as the height of the channel h . We recall that $\tau_u = l_i/u'_{\text{bot}}$ is the eddy turnover time of a structure of size l_i , $\tau_J = \rho/\sigma B_0^2$ is the Joule time, $\tau_{2D} = \tau_J (h/l_i)^2$ is the time associated to the two-dimensionalization of a structure of width l_i over the distance h , $\tau_H = hB_0^{-1}\sqrt{\rho/\sigma\nu}$ is the Hartmann friction time and $\tau_\nu = l_i^2/\nu$ is the time associated to viscous friction.

The present study focuses on the dynamics of forced turbulence. The main objective was to log sufficiently long data series in order to get meaningful statistics, which required turbulence to be steadily forced. Throughout the recording, the total injected current was carefully monitored to ensure no electrical asymmetries existed. A typical experimental run consisted of the following steps:

- (1) Apply the magnetic field B_0 ; wait for the magnetic field to be stabilized (a few seconds)
- (2) Record electric potential offsets for 3 min
- (3) Turn power supply on at set point I_0 ; wait for the flow to stabilize (several τ_u)
- (4) Launch acquisition of electric potentials: 18 min long series in total, split in 6 distinct files of 3 min each
- (5) Turn power supply off; wait for the flow to decay (several τ_H)
- (6) Record electric potential offsets for 3 min and find faulty channels (if any) by comparing to offsets measured at the beginning

3.2.7 Recapitulation

The overall working principle of the Flowcube is given in figure 3.9. For the purpose of the illustration, we have represented a fictitious injection pattern consisting of a 4×4 array of injection electrodes. Half of these electrodes are connected to the positive pole of the power supply (represented in red), while the other half is connected to the negative pole of the power supply (represented in blue). In this fictitious case, the total current per electrode is therefore given by $i_e = I_0/8$. The injected electric current splits as soon as it enters the vessel: the horizontal component of the current density field \mathbf{j} interacts with the vertical magnetic field \mathbf{B}_0 , hence driving vortices centered on top of each injection electrode (only two represented in the present sketch). The solenoidal component of the Lorentz force then diffuses the momentum of these structures vertically. In the quasi-2D limit, these vortices extend across the height of the experiment. The top and bottom electric potential signals (EPV signals) are picked up by ribbon cables and channeled to the amplifiers pack, while the ultrasound signals (PUDV signal) are sent to the DOP4000 for recording.

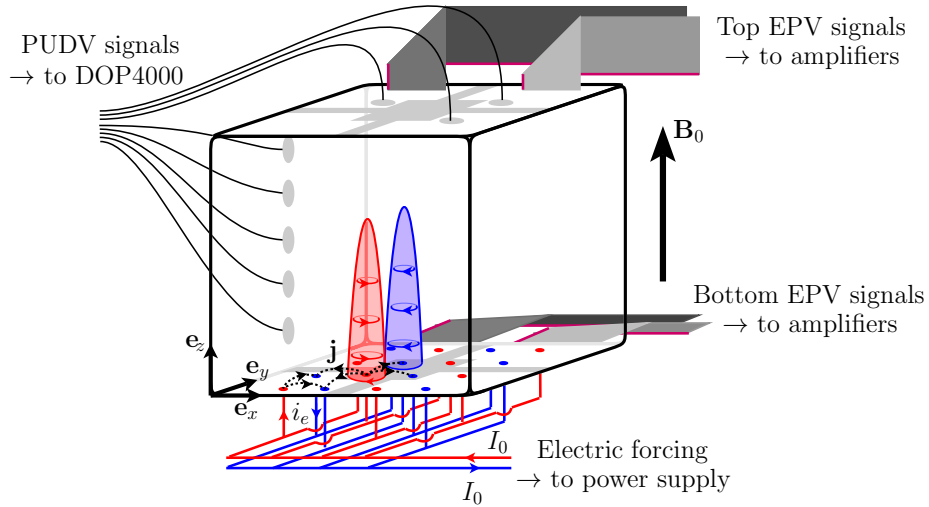


Figure 3.9. Working principle of the Flowcube

3.3 Methods of measurement

3.3.1 Electric Potential Velocimetry (EPV)

Most of the quantitative results presented in this thesis stem from the measurement of electric potential, a robust technique that has been extensively used throughout the years in liquid metal experiments. As a matter of fact, many of the experiments reviewed at the beginning of this chapter successfully relied on this velocimetry technique. In the present

3. AN EXPERIMENTAL APPARATUS FOR THE STUDY OF MHD TURBULENCE

section we will quickly go through the theory used to link values of electric potential at the wall to mechanical quantities of interest such as \mathbf{u}_\perp . According to section 1.3.2, the theory of the Hartmann layer implies that in the limit $Ha \gg 1$ and $N \gg 1$, measuring the electric potential at the wall is equivalent to measuring the stream function right outside the Hartmann layer. These two quantities being linked according to the relation

$$\psi = -\frac{\phi}{B_0}. \quad (3.1)$$

Assuming the velocity field right outside the Hartmann layers lays within the (x,y) horizontal plane, \mathbf{u}_\perp is readily linked to the stream function ψ following

$$\mathbf{u}_\perp = \nabla \times [\psi(x, y) \mathbf{e}_z]. \quad (3.2)$$

More explicitly, this yields

$$\mathbf{u}_\perp = \frac{\partial \psi}{\partial y} \mathbf{e}_x - \frac{\partial \psi}{\partial x} \mathbf{e}_y, \quad (3.3)$$

that is to say

$$\mathbf{u}_\perp = -\frac{1}{B_0} \left(\frac{\partial \phi}{\partial y} \mathbf{e}_x - \frac{\partial \phi}{\partial x} \mathbf{e}_y \right). \quad (3.4)$$

The crux of the matter therefore appears to be the numerical evaluation of the derivatives found in (3.4). Let us therefore consider a square formed by four adjacent potential probes M, N, P and Q (cf. figure 3.10), at which the electric potential is known. The coordinates of these points are given by the vectors \mathbf{x}_M , \mathbf{x}_N , \mathbf{x}_P and \mathbf{x}_Q respectively, in the frame of reference

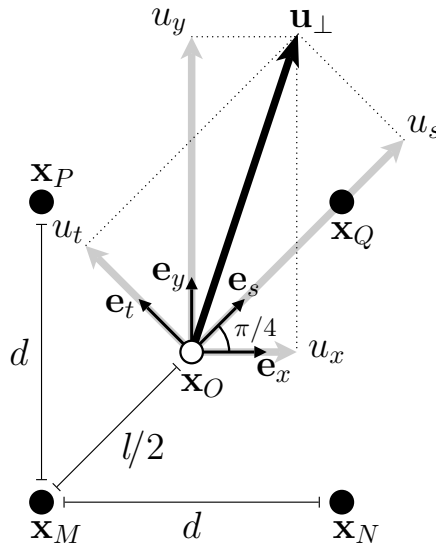


Figure 3.10. Linking the electric potential ϕ to the velocity field \mathbf{u}_\perp at fictitious point O using four adjacent potential probes.

defined by the unit vectors $(\mathbf{e}_x, \mathbf{e}_y)$. The center of the square delimited by these four probes is called O, whose coordinates are given by the vector $\mathbf{x}_O = (\mathbf{x}_P + \mathbf{x}_N)/2 = (\mathbf{x}_Q + \mathbf{x}_M)/2$. The potential probes are uniformly spaced by $d = 2.5$ mm, which relates to the square's diagonal l according to $l = \sqrt{2}d = 3.54$ mm. We finally introduce the frame of reference defined by the unit vectors $(\mathbf{e}_s, \mathbf{e}_t)$, which merely are $\pi/4$ rotation of $(\mathbf{e}_x, \mathbf{e}_y)$ about the axis \mathbf{e}_z (pointing towards the reader). The change from reference $(\mathbf{e}_x, \mathbf{e}_y)$ to reference $(\mathbf{e}_s, \mathbf{e}_t)$ is done through the following variable substitutions:

$$\begin{cases} \mathbf{e}_s = & \mathbf{e}_x/\sqrt{2} + \mathbf{e}_y/\sqrt{2} \\ \mathbf{e}_t = - & \mathbf{e}_x/\sqrt{2} + \mathbf{e}_y/\sqrt{2} \end{cases} \Leftrightarrow \begin{cases} \mathbf{e}_x = & \mathbf{e}_s/\sqrt{2} - \mathbf{e}_t/\sqrt{2} \\ \mathbf{e}_y = & \mathbf{e}_s/\sqrt{2} + \mathbf{e}_t/\sqrt{2} \end{cases}. \quad (3.5)$$

The two components of the velocity field $u_s = \mathbf{u}_\perp \cdot \mathbf{e}_s$ and $u_t = \mathbf{u}_\perp \cdot \mathbf{e}_t$ can be immediately evaluated at the single point O. Owing to (3.4), they are given by

$$u_s(O) = \frac{\phi(N) - \phi(P)}{B_0 l} + o(l^2) \quad \text{and} \quad u_t(O) = \frac{\phi(M) - \phi(Q)}{B_0 l} + o(l^2). \quad (3.6)$$

Following the change of variables given by (3.5), the velocity vector at point O in the frame of reference associated to the vectors $(\mathbf{e}_x, \mathbf{e}_y)$, is thus

$$u_x(O) = \frac{\phi(N) - \phi(M) - \phi(P) - \phi(Q)}{\sqrt{2} B_0 l} + o(l^2) \quad (3.7)$$

and

$$u_y(O) = \frac{\phi(N) + \phi(M) - \phi(P) - \phi(Q)}{\sqrt{2} B_0 l} + o(l^2). \quad (3.8)$$

Equations (3.7) and (3.8) show that \mathbf{u}_\perp is determined experimentally using second order finite difference schemes. The approximation for \mathbf{u}_\perp is therefore all the more accurate, as the distance between adjacent potential probes is small. In practice, the spacing between adjacent probes cannot be too close however, otherwise the voltage difference between them would be too low and fall within noise level. It must finally be kept in mind that EPV relies on the physical assumption that the horizontal component of the current density \mathbf{j}_\perp is negligible in the bulk.

3.3.2 Pulsed Ultrasound Doppler Velocimetry (PUDV)

Pulsed Ultrasound Doppler Velocimetry (PUDV) is a measuring method originating from the medical field, where non-invasive measurements of blood flows are required. PUDV is based on the principle of echography, which analyses the echoes resulting from the reflection of sound waves upon seeding particles. While medicine utilizes the presence of red blood cells to trace blood flows, we relied on the gallium oxides naturally present in galinstan (Brito *et al.*, 2001). The Flowcube is equipped with 8 identical ultrasound probes consisting of electrically insulating and non-magnetic epoxy piezoelectric crystals of diameter $d = 8$ mm,

and emitting frequency $f_e = 8\text{MHz}$. The entire data acquisition chain for PUDV was handled by the DOP4000 unit based on the original design by Willemetz (1990). Although we will not look into the technical details of how the DOP4000's hardware actually works, it is always a good idea to understand the physics and processing involved so as to make reliable measurements.

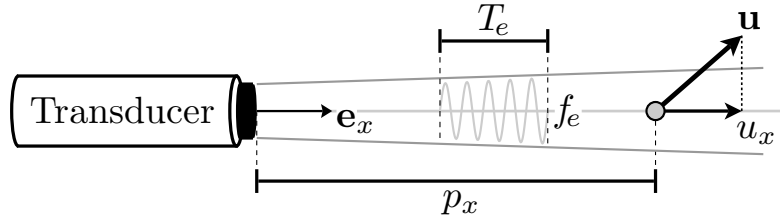


Figure 3.11. Illustrating the principle of PUDV on a flow seeded with a single particle, whose position relative to the probe p_x , and velocity along the axis of the transducer u_x are to be determined.

Let us consider the basic configuration presented in figure 3.11, where an ultrasound transducer whose beam is aligned with \mathbf{e}_x is immersed in a flow seeded with one tracing particle. The position of the particle p_x relative to the transducer, as well as its velocity component along the transducer $u_x = \mathbf{u} \cdot \mathbf{e}_x$ are to be determined. In PUDV, the transducer first acts as an emitter by generating a short wave packet, then as a receiver by recording the echo resulting from the wave reflecting upon the particle. The wave packets are emitted at the frequency f_e over the duration T_e . The time spacing between two consecutive pulses is T_{prf} , also known as the pulse repetition frequency. Knowing the speed of sound in galinstan ($c = 2680 \text{ m/s}$), the position of the particle is readily calculated from the time τ needed for the wave packet to travel back and forth between the transducer and the particle, and is given by

$$p_x = \frac{c\tau}{2}. \quad (3.9)$$

The velocity of the particle is found by evaluating the variation of its position between consecutive ultrasound bursts. As the particle moves relatively to the transducer, it reflects the emitted wave sooner or later than during the previous emission, thus phase shifting the resulting echo by $\varphi(t) = \pm 2\pi f_e \tau(t)$, or equivalently in terms of depth

$$\varphi(t) = \pm \frac{4\pi f_e p_x(t)}{c}. \quad (3.10)$$

The sign of $\varphi(t)$ depends on the direction of the particle relative to the transducer. In the example illustrated in figure 3.12, the particle moves towards the probe; $\varphi(t)$ is therefore negative. $\varphi(t)$ describes a wave form, whose instantaneous frequency f_d is given by $f_d = (d\varphi/dt)/2\pi$, that is to say

$$f_d = \pm \frac{2f_e}{c} \frac{dp_x(t)}{dt} = \pm \frac{2f_e u_x}{c}. \quad (3.11)$$

Equation (3.11) shows that the velocity component of the particle in the direction of the ultrasound beam is directly related to the Doppler frequency f_d , with the convention that u_x is negative when it is pointing towards the probe. In practice, f_d is found by analyzing the Fourier spectrum of $\varphi(t)$ reconstructed using a set of consecutive echoes. As illustrated in figure 3.12, $\varphi(t)$ is constructed experimentally by monitoring the amplitude of the echoes resulting from consecutive emissions at the fixed reference time T_{ref} (where $T_{\text{ref}} < T_{\text{prf}}$). Assuming the particle moves at a constant velocity and remains inside the ultrasonic beam throughout the measurement process, $\varphi(t)$ takes the form of a sinusoidal signal sampled at the time rate T_{prf} .

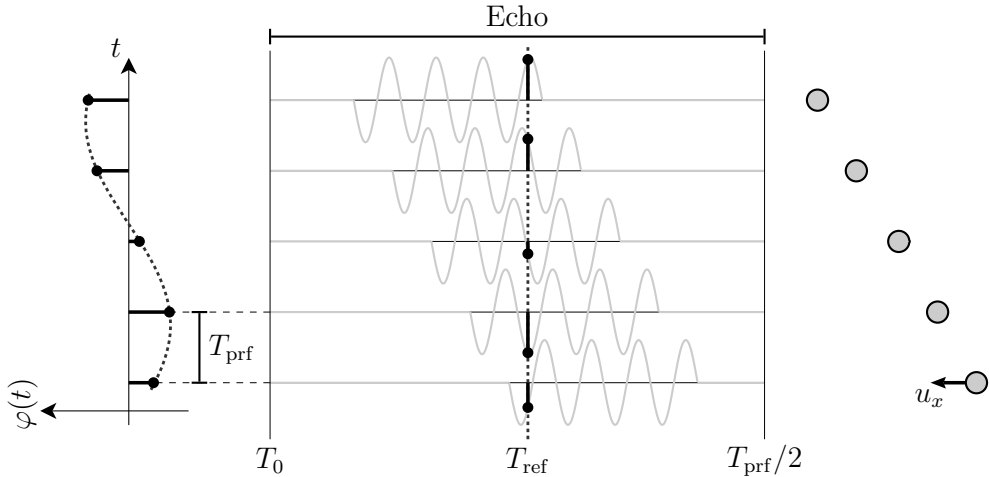


Figure 3.12. Determining the Doppler frequency using five consecutive echoes. The phase shift introduced by the particle's motion is observable by comparing the amplitude of the echoes at the given reference time T_{ref} . T_0 and $T_{\text{prf}}/2$ represent the beginning and end of the echo respectively ($T_{\text{prf}}/2$ is associated to the maximum exlorable depth p_x^{\max}).

The different operating settings available to run PUDV happen to be intricately coupled and antagonistic. Indeed, as we have just seen, determining u_x boils down to finding the frequency of $\varphi(t)$, whose values are available every T_{prf} . According to Shannon's sampling theorem, the maximum Doppler frequency evaluable without ambiguity is thus $f^{\max} = 1/2T_{\text{prf}}$. This maximum Doppler frequency translates in turn into a maximum measurable velocity free from aliasing

$$u_x^{\max} = \frac{c}{4 f_e T_{\text{prf}}}. \quad (3.12)$$

Conversely, T_{prf} also defines the maximum explorable depth according to

$$p_x^{\max} = \frac{c T_{\text{prf}}}{2}, \quad (3.13)$$

which simply corresponds to the furthest location the sound wave can travel to and back before the subsequent ultrasonic burst is emitted. Other constraints exist in terms of precision of the measurement, which result from a compromise between spatial and spectral

resolutions. On the one hand, the spatial accuracy of p_x is determined by the distance the particle has traveled during the time needed for the incident wave to fully reflect upon it. In other words the shorter T_e is, the more accurate p_x will be. On the other hand, the precision of u_x depends on the quality of the estimate for f_d , which is all the better as more samples of $\varphi(t)$ are available. This is only possible if T_e is long enough.

In practice, a Doppler echo results from the reflection of the ultrasonic burst on many particles randomly scattered throughout the beam. In order to reconstruct the full spatial profile from a set of echoes, the latter are first sampled into N_g different gates each labeled by a reference time T^i , or equivalently a reference depth p^i ($i = 1, \dots, N_g$). For each gate, the Doppler frequency is found by reconstructing the signal $\varphi^i(t)$ evaluated at each reference time T^i , as illustrated earlier. In real life however, the wave form $\varphi^i(t)$ is not purely sinusoidal. Its Fourier representation thus possesses a continuous range of frequencies. Noting $S(f)$ the spectral density of the Doppler signal, the DOP4000 defines the Doppler frequency f_d^i evaluated at gate p_x^i through the average

$$f_d^i = \frac{\int_{-\infty}^{\infty} f S(f) df}{\int_{-\infty}^{\infty} S(f) df}. \quad (3.14)$$

Knowing the Doppler frequency at each gate p_x^i eventually yields the velocity profile $u_x^i(p^i)$ by virtue of (3.11).

3.3.3 EPV / PUDV benchmarking

Let us now compare the readings given by EPV and PUDV. Since EPV and PUDV are not available at the exact same location in the experiment, the following benchmarking was performed by considering the ultrasound probes closest to the top and bottom walls, and comparing them to the EPV signals measured along the top and bottom walls respectively.

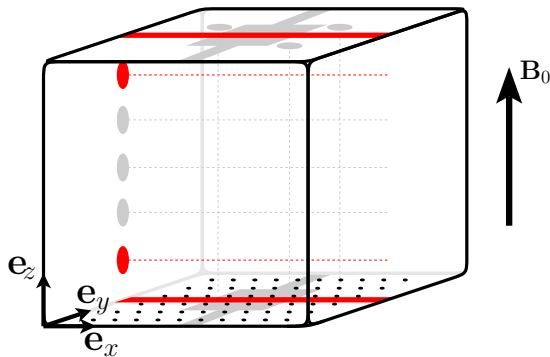


Figure 3.13. Measuring devices used for the benchmarking (highlighted in red).

3.3. Methods of measurement

In all cases, the measurements were made along the same horizontal line (highlighted in red in figure 3.13) running through the middle of the injection patch. The heights of the top and bottom ultrasound probes are $z = 88$ mm and $z = 12$ mm respectively. Since the Hartmann layers are extremely thin compared to the height of the channel, we will identify their locations with those of the top and bottom walls located at $z = 100$ mm and $z = 0$ mm respectively. This convention was adopted for clarity, but should not hide the fact that the velocity at the walls are evidently null as a result of the no-slip boundary condition, and that EPV in fact gives a measure of the velocity field right outside the Hartmann layers. From now on, the EPV and PUDV signals measured at heights 100 mm and 88 mm respectively will be referred to as the top signals, while the EPV and PUDV signals measured at 0 mm and 12 mm respectively will be referred to as the bottom signals.

The operating parameters chosen for this benchmarking are $l_i = 5$ mm, $I_0 = 200$ A, $B_0 = 10$ T. These settings were chosen for two reasons. First of all, the smaller injection scale was used to highlight the superior spatial sampling rate of the PUDV method, equal to 0.8 mm in this particular case. Indeed, turbulent structures of size $l_i = 5$ mm lay at the bottom limit of EPV's detection range, since the distance separating two adjacent potential probes is 2.5 mm. Second of all, $I_0 = 200$ A, $B_0 = 10$ T yields the most quasi-2D turbulent flow available with the smaller injection scale. As a matter of fact, the dimensionality of the forcing scale l_i is typically of the order $l_z/h \sim 1.7$ in this particular case, meaning that the turbulent statistics should be relatively invariant across z (cf. chapter 5). As a result, the velocity profiles measured in the top or bottom portion of the experiment should be directly comparable.

Owing to the large discrepancy in time sampling between the amplifiers and the DOP4000, the set of data they produce are obviously not synchronous. As far as the study of turbulence is concerned, this lack of synchronicity is not a significant issue, as we are mainly interested in statistical quantities. Figure 3.14.left gives the spatial distribution of the mean velocity component $\bar{U}_x(x) = \langle u_x(x, t) \rangle_t$, where the operator $\langle \cdot \rangle_t$ denotes a time average. The first obvious feature of this graph is the presence of 5 positive and negative peaks whose locations, and wavelength coincide with those of the injection electrodes in use. The presence of these peaks are therefore markers of the electric forcing. It can be observed that the bottom signals compare quite well with each other. As a matter of fact, the bottom signals would most certainly coincide exactly if it weren't for the slightly worse spatial sampling of EPV. The top signals also agree quite well, and capture the same flow features. Figure 3.14.left shows that despite the extreme magnetic field, there is still some obvious three dimensionality left in the mean flow, which is evident by comparing the top and bottom profiles and noticing that the amplitude of the former is 4 to 5 times weaker than that of the latter. Figure 3.14.right shows the rms profile of the turbulent fluctuations defined as $u'_x(x, t) = u_x(x, t) - \bar{U}_x(x)$. As with the mean flow, the turbulent fluctuations captured by the EPV and PUDV method at the bottom compare very well, while slight differences in amplitude appear between the top signals. This behavior is consistent with the flow not being fully quasi-2D. To conclude, EPV and PUDV appear to be reliable methods of measurement, which yield comparable results when used in the same operating conditions.

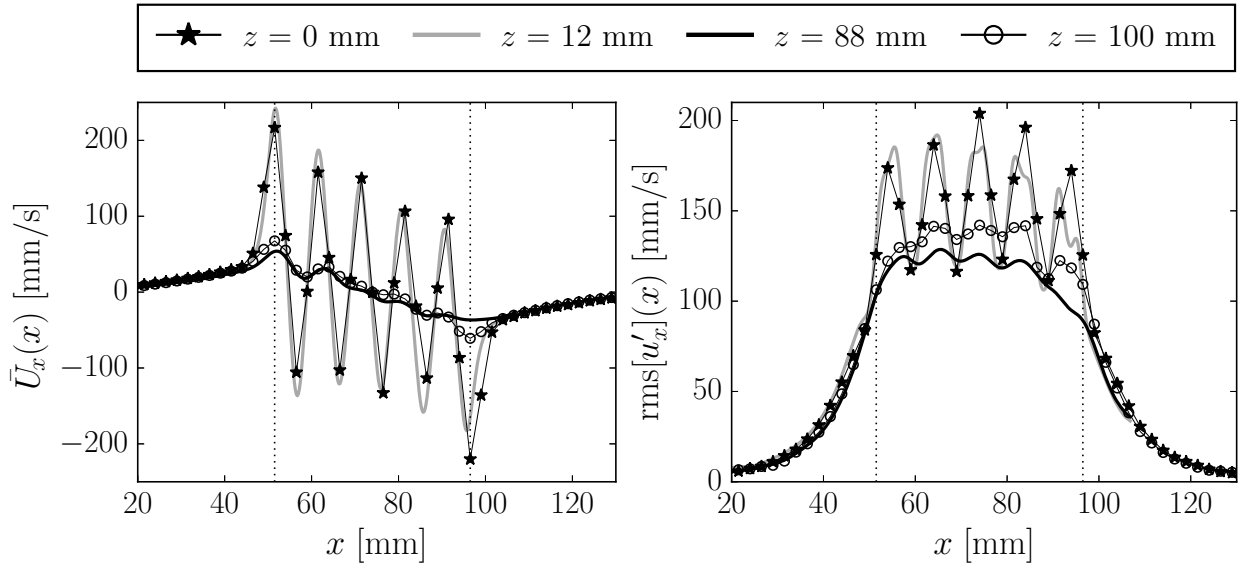


Figure 3.14. EPV (\star , \circ) vs. PUDV ($—$, $—$) at the top and bottom of the cube for $B_0 = 10 \text{ T}$, $I_0 = 200 \text{ A}$. Left: profile of the mean velocity component $\bar{U}_x(x) = \langle u_x(x, t) \rangle_t$. Right: profile of the turbulent fluctuations $\text{rms}[u'_x]$. The vertical dotted lines demarcate the forcing area of the case at hand.

Figure 3.14 also gives us a first flavor of the spatial structures of the turbulence we will be studying hereafter. To do so, we have reported the boundaries of the forcing area by dotted lines. Recall that in the case $l_i = 5 \text{ mm}$, the injection area consists of a 50 mm wide square patch located at the center of the bottom plate, whose boundaries are located in the aforementioned plot for $50 \text{ mm} < x < 100 \text{ mm}$ (cf. figure 3.8.left). Figure 3.14 shows that although a weak mean flow persists outside of the forcing patch, the magnitude of the turbulent fluctuations are very quickly damped when there are not sustained, and become negligible only a few millimeters away from the border. Furthermore, one can see that the turbulent intensity defined as the amplitude of the turbulent fluctuations to the mean flow is extremely high, with turbulent fluctuations at the top being twice as strong as the respective mean flow.

3.4 Validity and reliability of measurements

3.4.1 Impact of noise on structure functions

Experimental studies only yield an approximation of the physical quantity of interest by adding an inherent level of noise to the measurements. This matter is all the more important in the case of EPV, which relies on accurate measurements of weak electric potentials. Let $\phi^m(t)$ be the measured time series associated to the physical quantity ϕ . $\phi^m(t)$ is only an

3.4. Validity and reliability of measurements

approximation to ϕ as the recording has been corrupted by a background noise $\theta(t)$, such that $\phi^m(t) = \phi(t) + \theta(t)$. Assuming the noise is white and uncorrelated to the signal implies that $\langle \theta \rangle_t = 0$ and $\langle \phi \theta \rangle_t = \langle \phi \rangle_t \langle \theta \rangle_t = 0$ respectively. Let us now consider $\delta\phi = \phi_B - \phi_A$, the exact increment of ϕ measured between points A and B. Owing to the previous remarks, $\delta\phi$ relates to the measured increment $\delta\phi_m = \phi_B^m - \phi_A^m$ according to $\delta\phi = \delta\phi_m + (\theta_A - \theta_B)$.

We now focus on the experimental computation of the second order structure function $\langle \delta\phi^2 \rangle_t$. Keeping in mind that $\phi(t)$ and $\theta(t)$ are uncorrelated, the exact second order structure function can be re-written as

$$\langle \delta\phi^2 \rangle = \langle \delta\phi_m^2 \rangle \left[1 - 2 \frac{\langle \Theta^2 \rangle}{\langle \delta\phi_m^2 \rangle} + \frac{\langle \theta_A \theta_B \rangle}{\langle \delta\phi_m^2 \rangle} \right], \quad (3.15)$$

where we have notated $\langle \Theta^2 \rangle = \langle \theta_A^2 \rangle = \langle \theta_B^2 \rangle$ the variance of the noise at a given channel, which should largely be the same regardless of the location it is measured at. The ratio $\langle \Theta^2 \rangle / \langle \delta\phi^2 \rangle$ is the inverse of the Signal to Noise Ratio (SNR), which compares the power of the signal to that of the background noise. The ratio $\langle \theta_A \theta_B \rangle / \langle \delta\phi^2 \rangle$ quantifies how much cross channel noise affects the second order structure function. Whether the noise has an electronic or mechanical origin, there are no apparent justification for this term to be negligible. Equation (3.15) clearly demonstrates that the measured second order structure function is equal to the genuine one by the signal to noise ratio. Although (3.15) was derived primarily with the second order structure function of turbulent velocity increments in mind, it is worth noting that it also applies to the experimental evaluation of the mean kinetic energy $\langle \mathbf{u}_\perp^2 \rangle$. Indeed, owing to section 3.3.1, \mathbf{u}_\perp may be seen as a linear combinations of electric potential increments.

As far as the Flowcube is concerned, the signal to noise ratio is directly linked to the operating parameters. Indeed, the value of the electric potential is all the higher as the flow is intense, while the flow's intensity is an increasing function of both the magnetic field B_0 and the electric forcing I_0 . Assuming a background noise of constant amplitude, the signal to noise ratio should thus be all the more favorable, as B_0 and I_0 are large. Although the constant background noise assumption (ca. $3 \mu\text{V}$) is verified in the superconducting magnet (B_0 up to 4 T), it is simply not true in the resistive magnet (B_0 from 5 upwards). As a matter of fact, it was found that when the experiment was placed in the latter, strong noise was present (10 to 100 times higher than in the superconducting magnet), whose amplitude was directly linked to the magnetic field set point. To date, there is no convincing explanation for such noise, possible culprits ranging from electromagnetic disturbances to low frequency oscillation of the building itself through vibrations induced by the magnet's water cooling system. To quantify these effects further, we introduce the signal to noise ratios SNR_{Var} and SNR_{Cov} expressed in dB, which are respectively defined as

$$\text{SNR}_{\text{Var}} = \left\langle 10 \log_{10} \left[\frac{\langle \delta\phi_m^2 \rangle_t}{\langle \Theta^2 \rangle_t} \right] \right\rangle_{A,B} \quad \text{and} \quad \text{SNR}_{\text{Cov}} = \left\langle 10 \log_{10} \left| \frac{\langle \delta\phi_m^2 \rangle_t}{\langle \theta_A \theta_B \rangle_t} \right| \right\rangle_{A,B}. \quad (3.16)$$

In the expressions above, $\langle \cdot \rangle_{A,B}$ should be understood as a spatial average over all possible pairs of points A and B present in the experiment. SNR_{Var} and SNR_{Cov} based on electric

potential time series have been computed for different sets of operating conditions. For their computation, $\langle \Theta^2 \rangle$ and $\langle \theta_A \theta_B \rangle$ were estimated using the time series recorded while the liquid metal was sitting still in the magnetic field, before any electric current was injected. The values are reported in table 3.3 below.

		B_0 (T)			B_0 (T)		
		0.5	1	3	5	7	10
I_0 (A)	96	33	42	52	30	28	28
	128	34	43	54	32	29	30
	160	38	44	55	33	31	31
	192	36	45	56	34	31	32
	224	37	46	57	35	33	33
		(a) SNR_{Var}			(b) SNR_{Cov}		

Table 3.3. Signal to noise ratio for different operating parameters. Left: SNR relative to single channel noise. Right: SNR relative to cross channel noise. The double line distinguishes experimental runs performed in the superconducting ($B_0 = 0.5, 1$ and 3 T), to those performed in the resistive magnet ($B_0 = 5, 7$ and 10 T).

Table 3.3 shows that for a given magnetic field, both SNR_{Var} and SNR_{Cov} improve with the intensity of the flow. Furthermore, cross channel noise turns out to be negligible, since for any given set of parameters (I_0, B_0), SNR_{Cov} is always around 10 dB higher than the respective value of SNR_{Var} . In other words, $\langle \theta_A \theta_B \rangle / \langle \delta \phi_m^2 \rangle$ is systematically one order of magnitude smaller than $\langle \Theta^2 \rangle / \langle \delta \phi_m^2 \rangle$. Finally, for the worst signal to noise ratio ($B_0 = 10$ T and $I_0 = 96$ A), the noise to signal amplitude ratio $\langle \Theta^2 \rangle / \langle \delta \phi_m^2 \rangle$ is of 4%, while for the best signal to noise ratio ($B_0 = 3$ T and $I_0 = 224$ A) the noise to signal amplitude ratio $\langle \Theta^2 \rangle / \langle \delta \phi_m^2 \rangle$ is of 0.1%. The signals recorded in the resistive magnet are thus still reliable despite the much stronger noise observed there.

The relationship between the exact third order structure function $\langle \delta \phi^3 \rangle$ and its estimation based off measurements $\langle \delta \phi_m^3 \rangle$ is by far much simpler. Indeed, using the same reasoning as before, these two quantities are linked to each other by

$$\langle \delta \phi^3 \rangle = \langle \delta \phi_m^3 \rangle - 3 \langle \delta \phi^2 (\theta_B - \theta_A) \rangle - 3 \langle \delta \phi (\theta_B - \theta_A)^2 \rangle - \langle (\theta_B - \theta_A)^3 \rangle. \quad (3.17)$$

Keeping in mind that ϕ and θ are independent variables, and that both are centered, the second and third terms to the right of (3.17) are identically null. The last term to the right of (3.17) vanishes as well, owing to the fact that θ is a centered variable. All in all, one has

$$\langle \delta \phi^3 \rangle = \langle \delta \phi_m^3 \rangle, \quad (3.18)$$

meaning that noise does not corrupt the third order structure function associated to turbulent fluctuations. As we will shortly see however, determining $\langle \delta \phi^3 \rangle$ experimentally bears its own set of headaches.

3.4.2 Convergence of statistical moments

One approach to studying the dynamics of turbulence relies on analyzing the statistical quantities associated to the turbulent velocity increment $\delta\mathbf{u}'$. In particular, the second and third order moments are of great interest as they are closely related to the energy distribution in scale space and the scale to scale energy transfers respectively. While the second order moment is not known for posing convergence problems, computation of the third order turns out to be trickier. Mathematically speaking, this behavior comes from the fact that the probability density function (PDF) of the random variable $\delta\mathbf{u}'$ is centered around 0. As such, any odd moment (such as the third) is a signed quantity prone to cancellations during the averaging operation. The calculation process therefore requires a huge amount of samples before reaching an accurate and reliable estimate. In practice, obstacles quickly arise when trying to assess the third order moment, which are mostly due to the inherent unpredictability of experiments. As a result, the planning of the experimental campaign had to be an optimal compromise of the following constraints:

- (1) It is not known ahead of time how long the experimental setup will hold for
- (2) Access time to the resistive magnet is limited and strictly allocated
- (3) The widest range of operating parameters should be scanned, yet statistics for all points must be reliable
- (4) Post processing is too long for live monitoring of convergence levels to be an option

Fortunately, Podesta *et al.* (2009) introduced a procedure which quantifies, given a number of independent observations, how accurate the estimate for the n^{th} moment is. Conversely, this procedure can also be used to predict, from a limited population of samples, how many observations are required to achieve a given accuracy. We will briefly review the procedure below using a generic random variable X . By definition, the n^{th} order moment of the random variable X is given by

$$\langle X^n \rangle = \int_{-\infty}^{\infty} X^n f(X) dX, \quad (3.19)$$

where $f(X)$ is the probability density function associated to the random variable X , and $\langle \cdot \rangle$ should be understood as an ensemble average. Equation (3.19) defines in fact the expected value of the random variable X^n , that is to say the value one would await after averaging over an infinite number of occurrences of X^n . In practice, $\langle X^n \rangle$ is approximated experimentally by the estimate M_n , which is found by averaging over a finite number of realizations. By definition,

$$M_n(N_s) = \frac{1}{N_s} \sum_{i=1}^{N_s} X_i^n, \quad (3.20)$$

where N_s refers to the number of independent observations of X^n and X_i^n refers to the i^{th} occurrence of X^n . It is only in the limit $N_s \rightarrow \infty$ that equations (3.19) and (3.20) are

3. AN EXPERIMENTAL APPARATUS FOR THE STUDY OF MHD TURBULENCE

rigorously equal. M_n is itself a random variable, which can thus be characterized by a mean $\mu_n(N_s)$ and a standard deviation $\sigma_n(N_s)$, where

$$\mu_n(N_s) = \langle M_n(N_s) \rangle \quad \text{and} \quad \sigma_n(N_s) = \sqrt{\langle M_n(N_s)^2 \rangle - \mu_n(N_s)^2}. \quad (3.21)$$

μ_n and σ_n are related to the random variable X according to

$$\mu_n = \langle X^n \rangle \quad \text{and} \quad \sigma_n = \sqrt{\langle X^{2n} \rangle - \langle X^n \rangle^2} / \sqrt{N_s}, \quad (3.22)$$

such that the ratio $|\sigma_n/\mu_n|$ is given by

$$\left| \frac{\sigma_n}{\mu_n} \right| = \frac{1}{\sqrt{N_s}} \left| \frac{\langle X^{2n} \rangle}{\langle X^n \rangle^2} - 1 \right|^{1/2}. \quad (3.23)$$

As a matter of fact, μ_n is the quantity that is sought for in the first place. However, each observation of M_n is, on average, within the distance σ_n from μ_n . In order to have a reliable measurement of $\langle X^n \rangle$, the PDF associated to M_n must sharply peak around μ_n , that is to say M_n is required to take the value μ_n as certainly as possible. A measure of this property is precisely given by the ratio $|\sigma_n/\mu_n|$ found in equation (3.23). More specifically, μ_n is a reliable estimate of $\langle X^n \rangle$ when $|\sigma_n/\mu_n| \ll 1$. From (3.23), this can only be achieved if the number of independent samples N_s is large enough to balance out the quantity $\sqrt{|\langle X^{2n} \rangle / \langle X^n \rangle^2 - 1|}$, which is unknown a priori. Equation (3.23) demonstrates quite clearly the underlying issue with statistical convergence: reducing the ratio $|\sigma_n/\mu_n|$ by one order of magnitude implies increasing the number of independent samples by two, which poses some obvious experimental challenges. This behavior is true independently of the order considered. The value of the constant $\sqrt{|\langle X^{2n} \rangle / \langle X^n \rangle^2 - 1|}$ on the other hand is all the larger as n is high. Low order moments therefore need fewer independent samples than high order ones to reach the same accuracy. In order to get a prediction for the required recording's length, we followed Podesta *et al.* (2009)'s observation according to which (3.23) may be re-written in the form

$$\left| \frac{\sigma_n}{\mu_n} \right| = a N_s^{-1/2}. \quad (3.24)$$

a is a positive coefficient, which can be found empirically by fitting a $N_s^{-1/2}$ power law to a plot made of the quantity $|\sigma_n/\mu_n|$ computed for different sample sizes N_s . Once a has been found, extrapolating the curve to any imposed value of $|\sigma_n/\mu_n|$ yields an estimate for the number of samples required to reach the aforementioned accuracy. In practice we aimed for $|\sigma_n/\mu_n| < 0.1$. After setting new operating conditions, an 18 min long data set was recorded, on which the procedure described above was applied. We found out that the ratio $|\sigma_n/\mu_n|$ for $n = 2$ and $n = 3$ seemed to depend neither on the magnitude of the magnetic field, nor on the intensity of the forcing. There however seemed to be a general trend according to which small velocity increments usually required one order of magnitude more samples than large velocity increments to reach the same accuracy level. This didn't turn out to be an issue, since over sampling was possible for small increments as a result of spatial averaging.

3.4. Validity and reliability of measurements

The procedure is illustrated in figure 3.15, which compares the a priori estimate for N_s found using (3.24) to the a posteriori monitoring of the convergence level of M_3 associated to the random variable $\langle \|\delta\mathbf{u}'\|^2 \delta u'_x \rangle$ (cf. section 4.3.2 for the full meaning of this quantity). The relative error associated to the convergence of M_3 was defined as

$$\epsilon_3 = \left| \frac{M_3(N_s) - M_3(N_{\max})}{M_3(N_{\max})} \right|, \quad (3.25)$$

which compares $M_3(N_s)$ to its most accurate estimation computed using the maximum number of independent samples available N_{\max} . The scale chosen for this illustration is $r_\perp = 15$ mm. Furthermore, the operating settings were $B_0 = 3$ T and $I_0 = 160$ A, which are quite standard for Flowcube, thus are representative overall. As figure 3.15 shows, one must roughly have $N_s \geq 10^7$ for $|\sigma_3/\mu_3|$ to be less than 0.1. Computing M_3 with 3.4×10^7 independent samples makes the relative error on the estimate to be less than 1%. This behavior was quite consistent throughout our data. Note also that the $N_s^{-1/2}$ decay of ϵ_3 is in full agreement with the theory.

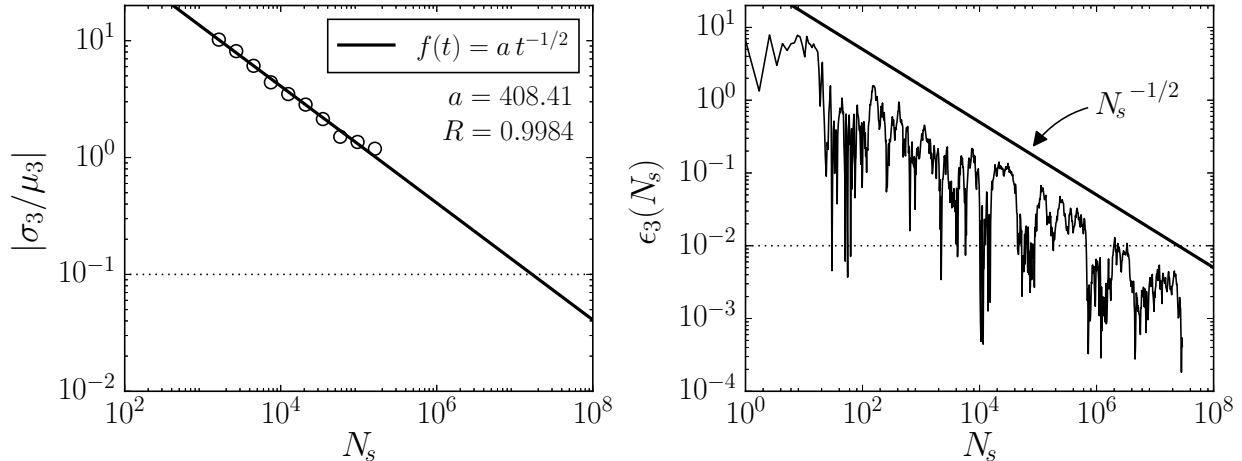


Figure 3.15. Statistical convergence of $\langle \|\delta\mathbf{u}'\|^2 \delta u'_x \rangle$ for $r_\perp = 15$ mm, $B_0 = 3$ T and $I_0 = 160$ A. Left: a priori estimation of $|\sigma_3/\mu_3|$ as a function of the number of samples. The calculation is based on Podesta *et al.* (2009) procedure using an 18 min long recording (ca. 2.1×10^6 samples); (.....): $|\sigma_3/\mu_3| = 0.1$ threshold. Right: a posteriori monitoring of the relative error ϵ_3 based on 288 min worth of data (ca. 3.4×10^7 samples); (.....): 1% relative error mark achieved when $N_s \geq 10^7$.

By comparison, figure 3.16 shows the relative error for the convergence of the second order moment M_2 associated to the random variable $\langle \|\delta\mathbf{u}'\|^2 \rangle$. The convergence of M_2 is computed using the first 2×10^6 data points of the time series referred to earlier. Figure 3.16 illustrates why second order moments converge faster. Despite ϵ_2 still following a $\sqrt{N_s}$ convergence rate, the relative error ϵ_2 starts off at a much lower level than ϵ_3 . As a matter of fact, after averaging over the first hundred samples, ϵ_2 is one order of magnitude lower

3. AN EXPERIMENTAL APPARATUS FOR THE STUDY OF MHD TURBULENCE

than ϵ_3 . As a consequence, the 1% error mark is attained two orders of magnitude quicker for ϵ_2 than for ϵ_3 (more specifically $N_s \geq 10^5$ for the former vs. $N_s \geq 10^7$ for the latter).

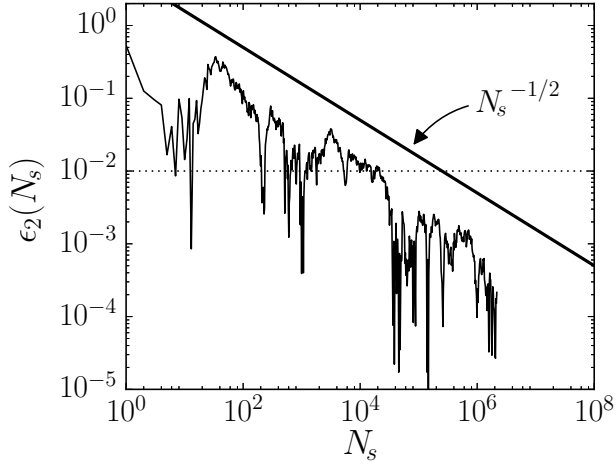


Figure 3.16. Relative error on the estimate for $\langle \|\delta\mathbf{u}'\|^2 \rangle$ for $r_\perp = 15$ mm, using an 18 min long recording (ca. 2.1×10^6 samples), $B_0 = 3$ T and $I_0 = 160$ A. (.....): 1% relative error mark achieved for $N_s \geq 10^5$.

Chapter 4

Turbulence

It is now time to take the plunge and start examining turbulence per se. The intent of the present chapter is to review and discuss some elementary results known about turbulence. In particular, we will mention the basic phenomenology of 3D and 2D hydrodynamic turbulence and see how it differs from MHD turbulence confined between electrically insulating and no-slip walls. Key mathematical concepts will also be introduced here, which we will use to interpret our experimental results presented in chapter 5.

4.1 Basic phenomenology

4.1.1 Observations

Most of the flows encountered in our everyday life are naturally turbulent. It is thus relatively easy to get a qualitative feel for what turbulence involves, namely agitation, instability and seemingly chaotic behavior. Despite this intuitive understanding, turbulent flows are inherently difficult to describe quantitatively, which is a direct consequence of their non-linear character. Mathematically speaking, non-linearity is at the heart of two fundamental features of turbulence. On the one hand, turbulence is unpredictable at human level (non-linearity makes the flow extremely sensitive to however small perturbations). A statistical description of turbulence is thus more than natural. On the other hand, turbulence acts over a wide and continuous range of scales of motion (throughout a non-linear process, interactions between given scales may excite completely unrelated scales). Scales of motion are the cornerstone concept of any quantitative description of turbulence. They are usually referred to as turbulent eddies or structures, and are understood as blobs of swirling fluid outlined from the flow, to which a typical lengthscale and amount of momentum can incidentally be associated. The intensity of turbulent motions is customarily measured by their kinetic energy.

In fluid mechanics, non-linearity stems from inertial forces. As a matter of fact, it is known since Reynolds (1883)'s historical experiments that turbulence appears whenever in-

4. TURBULENCE

ertia outweighs viscous friction. Having said that, inertial forces acting on an incompressible fluid are conservative, meaning that they act neither as a source nor a sink of motion. Turbulence is thus a phenomenon that needs to be triggered and sustained by an external process to even exist in the first place. Experimentally speaking, it can be observed that when turbulence occurs, it inevitably appears close to obstacles first, where strong velocity gradients exist; Turbulence originates from spatial inhomogeneities, which result from no-slip and impermeable boundaries. The typical lengthscale of these spatial inhomogeneities is associated to motion at large scales, and will interchangeably be referred to as the integral, injection or forcing scale. Quantitatively speaking, a flow is said to be turbulent when the Reynolds number Re based on the integral scale and the characteristic velocity of the system is much greater than unity.

Given the above, turbulence necessarily requires the flow to be inhomogeneous and anisotropic at some level to exist. Yet, there is a consensus, backed by abundant experimental evidence, that fully developed turbulence usually features a range of scales for which turbulent motions are relatively homogeneous and isotropic. The former characteristic must be understood as an insensitivity of the flow's statistics to the point of reference (i.e. the location of the measuring device), while the latter should be understood as an insensitivity of the statistics to the orientation of the reference coordinate system (i.e. the orientation of the measuring device). Homogeneity and isotropy are commonly made assumptions in the field of turbulence, which yielded many groundbreaking results, thanks to the great simplifications they imply.

Turbulent flows fall under two general categories: (i) forced statistically steady, and (ii) freely decaying. Both frameworks have their strengths and weaknesses in trying to capture and understand some aspects of turbulence. Indeed, time independence of the former category is certainly an interesting simplification, which tends to suppress the influence of the initial conditions on the flow. It however comes at the cost of having to deal with some inherent level of inhomogeneity and anisotropy originating from the boundaries to sustain the flow. Conversely, the latter category need not bother with a forcing term (which is usually difficult to fully understand, yet accurately model), thus making the homogeneous and isotropic assumptions perhaps more suitable. It is however more time consuming to get reliable statistics in decaying turbulence, since it requires accumulating realizations of turbulence decays. Additionally, there is no saying how the initial conditions impact the statistics of such a flow. This thesis is exclusively concerned with statistically steady turbulence.

4.1.2 3D homogeneous and isotropic hydrodynamic turbulence

Let us start by discussing some important results concerning 3D homogeneous and isotropic *hydrodynamic* turbulence. As of today, our understanding of this phenomenon is still widely influenced by Richardson's concept of the energy cascade (neatly reviewed for instance in Davidson (2015)). The bedrock of this theory comes from the observation that the energy dissipation rate in fully developed turbulence always seems to tend towards a finite value, despite viscous friction being a priori negligible compared to inertia. Richardson's

idea was to describe turbulence scale wise by inferring the two following arguments. On the one hand, turbulent motions originate from inertial processes occurring at the boundaries of a system due to inhomogeneities at large scale, say ℓ . On the other hand, kinetic energy is dissipated into heat by viscous friction, which must be most efficient at particulate level (in the sense of a fluid particle), and thus at small scale, say η . Richardson then introduced a continuous range of intermediate scales of size r , known as the inertial range, whose purpose is to tie together the energy containing and energy dissipating scales, which presumably lay far apart from each other. In this inertial range, viscosity is suggested to play a negligible role, thus implying that it is dominated by inertial mechanisms exclusively. The concept of the energy cascade, in turn, refers to the process following which the kinetic energy produced at large scale is being conservatively passed down to smaller and smaller scales before eventually being converted into heat by viscous dissipation at the smallest possible scale. The energy cascade is thought to be a multistage process (in the statistical sense) meaning that, on average, kinetic energy transits through all existing scales before being dissipated. In particular, energy is (still on average) less likely to jump directly from a large energetic scale directly to a dissipating one. The energy cascade is also said to be local, in the sense that scales laying in the inertial range will preferentially yield their energy to a neighbor in size over their lifetime, rather than to a scale whose size is very different.

Let us now investigate some of the implications of Richardson's reasoning on a statistically steady homogeneous and isotropic hydrodynamic turbulent flow characterized by the energy production rate \mathcal{P} and the energy dissipation rate ϵ . As far as the energy transfer rate at scale r is concerned, let it be $\Pi(r)$. Kinetic energy is assumed to cascade down to the dissipating scales η , where it is converted into heat by viscosity. Calling u_η the typical velocity of the dissipating scales and $\tau_{\nu_\eta} = \eta^2/\nu$ the typical viscous time, one may expect the energy dissipation rate per unit mass to be convincingly described by u_η^2/τ_{ν_η} , that is to say

$$\epsilon \sim \nu \left(\frac{u_\eta}{\eta} \right)^2. \quad (4.1)$$

The energy cascade is expected to stop when the inertia of the small scales becomes comparable to viscous friction at their level, that is to say when

$$\frac{u_\eta \eta}{\nu} \sim 1. \quad (4.2)$$

Combining (4.1) and (4.2) eventually yields estimates for the size and velocity of the dissipating scales (Kolmogorov, 1941*b*), namely

$$\eta \sim (\nu^3/\epsilon)^{1/4} \quad \text{and} \quad u_\eta \sim (\nu \epsilon)^{1/4}. \quad (4.3)$$

Since the flow is assumed to be statistically steady, kinetic energy may not accumulate in any of the scales. As a result, energy dissipation must balance out energy input, which incidentally must also match the rate at which energy is being passed down at each level. In other words

$$\mathcal{P} = \epsilon = \Pi(r). \quad (4.4)$$

Since the energy production mechanism is assumed to be exclusively inertial, it must be best characterized by the eddy turnover time of the large scales $\tau_{u_\ell} = \ell/u_\ell$, where u_ℓ is the typical velocity of the structure of size ℓ . In particular, one may legitimately expect the kinetic energy production rate to be given by $\mathcal{P} \sim u_\ell^2/\tau_{u_\ell}$, that is to say

$$\mathcal{P} \sim \frac{u_\ell^3}{\ell}. \quad (4.5)$$

Combining (4.1) through (4.5) eventually yields the following prediction for the extent of the inertial range

$$\frac{\ell}{\eta} \sim Re_\ell^{3/4}, \quad \text{with} \quad Re_\ell = \frac{u_\ell \ell}{\nu}. \quad (4.6)$$

With words, (4.6) implies that the injection and dissipating scales are all the farther apart, as the large scale structures are turbulent. This result may now explain how energy can be dissipated at a finite rate in a fully developed turbulent flow (i.e. $Re_\ell \gg 1$). Indeed, (4.6) suggests that the size of small scales adjusts itself to the large scale flow in order to dissipate whatever amount energy is injected. The inertial range may then be defined in light of (4.6) as the set of turbulent structures whose sizes r satisfy

$$\eta \ll r \ll \ell, \quad (4.7)$$

Richardson's picture of the energy cascade was later refined by Kolmogorov, who predicted universal properties for the statistics of the scales laying beneath the integral scale. These predictions are known as Kolmogorov's two *similarity hypotheses* (Kolmogorov, 1941b). The first hypothesis states that for fully developed turbulence ($Re_\ell \gg 1$), turbulent scales verifying $r \ll \ell$ are locally isotropic and at statistical equilibrium. As a result, their statistical properties depend on ϵ , r and ν only. This first claim suggests that the small scales do not directly feel the inhomogeneities and unsteadiness of the large scales. This claim also implies that their size is small enough not to experience the spatial gradients taking place over the integral scale, while their lifetime is short enough for them not to feel large scale fluctuation. The second similarity hypothesis, states that in fully developed turbulence, the statistical properties of the scales laying in the inertial range (i.e. the scales r satisfying $\eta \ll r \ll \ell$) are a function of ϵ and r alone. This second hypothesis is a formal expression of the fact that the energy cascade is an inertial process, and is therefore not influenced by viscosity. The implications of Kolmogorov's similarity hypotheses were investigated in Kolmogorov (1941a), and are summarized below. Let us start by defining the statistical quantity $S_2(r) = \langle u_r^2 \rangle$, where u_r refers to the velocity of turbulent scales of size r . According to Kolmogorov's first hypothesis

$$S_2(r) = f(\epsilon, r, \nu), \quad r \ll \ell. \quad (4.8)$$

Taking η as the reference lengthscale, and building a typical timescale upon u_η , the above relationship may be written in dimensionless form as

$$S_2(r) = u_\eta^2 \tilde{f}(r/\eta), \quad r \ll \ell, \quad (4.9)$$

with \tilde{f} a dimensionless function. According to Kolmogorov's second hypothesis, $S_2(r)$ must be independent of ν in the inertial range $\eta \ll r \ll \ell$ (viscosity implicitly occurs in (4.9) through η and u_η). Applying a dimensional argument to (4.9) thus implies

$$S_2(r) = C_2 \epsilon^{2/3} r^{2/3}, \quad \eta \ll r \ll \ell, \quad (4.10)$$

where C_2 is a constant of order unity. The same reasoning may be conducted for the statistical quantity $S_3(r) = \langle u_r^3 \rangle$, which yields

$$S_3(r) = C_3 \epsilon r, \quad \eta \ll r \ll \ell, \quad (4.11)$$

where C_3 is also a constant of order unity. S_2 may be physically interpreted as a qualitative measure of the kinetic energy found at scale r . As such, (4.9) suggests that the energy content of the inertial range has a universal shape when plotted against the reduced variable r/η . Furthermore, $S_3(r)/r$ may be physically interpreted as a qualitative measure of the energy flux flowing through the scale of size r . In particular, relationship (4.11) shows that kinetic energy flows in a single direction (fixed by the sign of C_3), at a constant rate (fixed by the value of ϵ), and independently of the size of the scale r . Note that (4.11) was found using a heuristic argument, but can in fact be formally derived using the Navier-Stokes equations (cf. section 4.3.2). It turns out that for homogeneous and isotropic turbulence $C_3 = -4/5$, which coincides with a flux of energy from large to small scales.

It is now well established that the inertial mechanism responsible for the dynamics of 3D turbulence (i.e. the energy cascade) is the interaction between vorticity and the strain rate field (Tsinober, 1998). In two dimensions however, strain and vorticity occur in non-intersecting domains of space. Restraining a flow to two dimensions therefore automatically inhibits the mechanism allowing kinetic energy to flow down from large to small scales. It also happens that for 2D hydrodynamic turbulence, enstrophy (i.e. squared vorticity) remains bounded. In other words, the velocity gradients (which are responsible for dissipation of kinetic energy) cannot adjust to dissipate whatever amount of kinetic energy is injected into the flow. These observations rule out from the start an energy cascade scenario à la Richardson/Kolmogorov, and tend to suggest that different mechanisms must prevail in 2D turbulence.

4.1.3 2D homogeneous and isotropic hydrodynamic turbulence

Formally speaking, 2D turbulence can be defined as “high-Reynolds number solutions of the Navier-Stokes equation, which depend only on two Cartesian coordinates” (Frisch, 1995). The dynamics of forced 2D homogeneous and isotropic *hydrodynamic* turbulence were theoretically investigated by Kraichnan (1967). He imagined a scenario in which the inertial range extended above and below the forcing scale ℓ , at which kinetic energy and enstrophy were injected into the flow. The upper part of the inertial range is characterized by the set of scales r satisfying $\ell \ll r \ll \mathcal{L}$ (where \mathcal{L} represents for now a typical large scale). On this side of the inertial range, Kraichnan predicted that kinetic energy flowed upscale

from the injection scale to the largest existing scales following what is now known as the inverse energy cascade. Conversely, the lower part of the inertial range is characterized by the set of scales r satisfying $\eta \ll r \ll \ell$ (where η is the small dissipating scales driven by viscosity). There, Kraichnan anticipated a direct enstrophy cascade, where enstrophy flowed downscale from the injection to the small scales. The two mutually exclusive and opposite cascades in 2D turbulence may be illustrated using the following argument (Boffetta & Ecke, 2012). Let \mathcal{P} and Ω be the mean energy and enstrophy injection rates, which take place at the intermediate scale ℓ . Let also $\epsilon_{\mathcal{L}}$ and $\varrho_{\mathcal{L}}$ be the energy and enstrophy dissipation rates at large scale \mathcal{L} , while ϵ_{η} and ϱ_{η} be the energy and enstrophy dissipation rates at small scale η . Assuming a steady state (we will see shortly after when this assumption is applicable), the energy and enstrophy inputs are balanced out, on average, by viscous dissipation. That is to say

$$\mathcal{P} = \epsilon_{\mathcal{L}} + \epsilon_{\eta} \quad \text{and} \quad \Omega = \varrho_{\mathcal{L}} + \varrho_{\eta}. \quad (4.12)$$

The typical lengthscales \mathcal{L} , ℓ and η may then be estimated from the aforementioned processes by $\mathcal{L}^2 \sim \epsilon_{\mathcal{L}}/\varrho_{\mathcal{L}}$, $\eta^2 \sim \epsilon_{\eta}/\varrho_{\eta}$ and $\ell^2 \sim \mathcal{P}/\Omega$, such that

$$\frac{\epsilon_{\eta}}{\epsilon_{\mathcal{L}}} \sim \left(\frac{\eta}{\ell}\right)^2 \left(\frac{\ell}{\mathcal{L}}\right)^2 \frac{(\mathcal{L}/\ell)^2 - 1}{1 - (\eta/\ell)^2}, \quad (4.13)$$

and

$$\frac{\varrho_{\mathcal{L}}}{\varrho_{\eta}} \sim \frac{1 - (\eta/\ell)^2}{(\mathcal{L}/\ell)^2 - 1}. \quad (4.14)$$

Assuming a fully developed turbulent flow in which the direct enstrophy and inverse energy cascades span a wide range of scales, one has $\eta \ll \ell$ and $\ell \ll \mathcal{L}$ respectively. Following (4.13), this yields $\epsilon_{\eta}/\epsilon_{\mathcal{L}} \rightarrow 0$ and $\varrho_{\mathcal{L}}/\varrho_{\eta} \rightarrow 0$, or equivalently

$$\mathcal{P} \sim \epsilon_{\mathcal{L}} \quad \text{and} \quad \Omega \sim \varrho_{\eta}. \quad (4.15)$$

In other words, the kinetic energy injected at scale ℓ is preferentially dissipated at the large scale \mathcal{L} (which requires the kinetic energy to indeed flow upscale), while the enstrophy injected at scale ℓ is preferentially dissipated at the small scale η (which indeed imposes enstrophy to flow downscale).

As a result of the inverse cascade, kinetic energy must be dissipated by the large structures, for the flow to be statistically steady. In pure hydrodynamics, this dissipation mechanism customarily involves large scale viscous friction onto the bounding walls, which is usually far from being enough to dissipate the incoming flux of energy (the eddy turnover time of structures of size \mathcal{L} is much quicker than their viscous time). Kraichnan (1967) thus foresaw that in the general case, the inverse cascade in a bounded domain is unlikely to be statistically steady, since kinetic energy is expected to gradually pile up in the largest structures, before being accumulated into smaller and smaller scales. Fortunately, alternative damping mechanisms exist in MHD, which may prevent this pile up of kinetic energy at large scales (this issue is further discussed in section 4.1.5). It is also worth pointing out

that although kinetic energy does flow upscale, large structures need not become visible. As a matter of fact, a forced 2D turbulent flow is dominated by turbulent structures whose sizes are close to the injection scale. This results from the inertial forcing taking place at intermediate scale being strong enough to break up the larger structures emerging from the inverse cascade (Tabeling, 2002). This aspect is specific to forced 2D turbulence, and contrasts sharply with decaying 2D turbulence in which large long lived structures indeed end up dominating the flow.

Following Kolmogorov's steps, Kraichnan also invoked self-similarity hypotheses in the inertial range, which drove him to the following predictions regarding the overall shape of the scale by scale energy distribution. Dimensional arguments about $S_2(r) = \langle u_r^2 \rangle$ in the inverse cascade range lead Kraichnan to

$$S_2(r) = D_2 \mathcal{P}^{2/3} r^{2/3}, \quad \ell \ll r \ll \mathcal{L}. \quad (4.16)$$

At the same time, assuming that the squared vorticity spectrum $S_2(r)/r^2$ depended only on Ω and r yielded

$$S_2(r) = D'_2 \Omega^{2/3} r^2, \quad \eta \ll r \ll \ell, \quad (4.17)$$

where D_2 and D'_2 are two constants. As far as the quantity $S_3 = \langle u_r^3 \rangle$ is concerned, Lindborg (1999) showed that in homogeneous and isotropic 2D turbulence, a constant energy flux in a statistically steady inverse cascade regime implied

$$S_3(r) = D_3 \mathcal{P} r, \quad \ell \ll r \ll \mathcal{L}, \quad (4.18)$$

where again, D_3 is a constant, which happens to be $D_3 = +3/2$. Comparing (4.16) and (4.18) to their 3D counterparts (4.10) and (4.11) yields interesting similarities. Indeed, it can first be noticed that though weighted by different prefactors, the energy distribution among scales (measured through $S_2(r)$) have the exact same shape whether the energy cascade is direct (as in 3D turbulence) or inverse (as in 2D turbulence). As a result, looking at the energy distribution among scales is not an adequate tool to diagnose the direction of the energy cascade. In order to unambiguously do so, one must rely on a direct measure of the scale by scale energy fluxes (estimated here by $S_3(r)/r$). In particular, (4.11) and (4.18) show that the direct and inverse energy cascades are independent of the scale size r and flow at a constant rate given by \mathcal{P} (or equivalently ϵ for 3D turbulence). The one difference between the two however, comes from the sign of the prefactor, which is negative in three dimensions and positive in two dimensions. As such, if we accept that a negative constant implies a direct energy cascade for 3D turbulence, then a positive constant must in turn imply an inverse energy cascade for 2D turbulence.

Verifying Kraichnan's theory experimentally demanded special setups, which could prevent the flow from being perturbed by some inherent level of three-dimensionality found in the laboratory. The obvious path undertaken to restrain a system to two dimensions was of course to eliminate one spatial coordinate by imposing a geometrical constraint. In that respect, Rutgers (1998)'s study might be the pinnacle of this method. Indeed, his study relied

on an apparatus which could drive a turbulent flow in a soap film of typical thickness $5\ \mu\text{m}$. Turbulence was sustained by vortex shedding behind a comb of needles of width 0.3 mm, which were located on either sides of the film. By computing 1D energy spectra, Rutgers (1998) captured both parts of the inertial range, where the scalings for the inverse energy and direct enstrophy cascade regimes given by (4.16) and (4.17) respectively were convincingly recovered over about 1 decade in each domain. Later on, Belmonte *et al.* (1999) complemented the latter study by examining the third order structure function of 2D grid turbulence shed behind a comb in a soap film. Although their turbulence was strictly speaking decaying, they measured the third order structure function at a fixed distance from the comb. By invoking a locally steady 2D flow and accounting for the energy lost by the turbulence during its travel to the position of the measurement, Belmonte *et al.* (1999) were able to link the third order structure function to the local scale by scale flux of kinetic energy. Here, the term “local” must be understood in the sense of a position downstream from the comb. Indeed, the scale by scale energy flux incidentally decays, as the turbulence is advected downstream. With this setup, they found that the third order structure function was positive at large scales, which hinted at an upscale flux of turbulent kinetic energy. Alternate experimental approaches to investigate 2D turbulence consist in taking advantage of external body forces to impose two-dimensionality to geometries that are not necessarily shallow. For instance, the Coriolis and Lorentz forces but also buoyancy are good candidates, as their overall effect is to smooth out gradients in a given preferential direction.

4.1.4 Turbulence with mixed 2D and 3D characteristics

There seems to be some ambiguity as to what the term “dimensionality” actually refers to in the literature. Until now, we mostly understood dimensionality as a synonym for velocity gradients in the bulk. Owing to this definition, three-dimensionality is associated to the spatial dependence of physical quantities with respect to any given spatial coordinate. The two-dimensional limit then referring to a situation where the bulk is fully correlated over a preferential direction (such as the direction of an imposed magnetic field for instance). Dimensionality may however also be understood as the number of non-zero components of the velocity field. We shall call this latter type of dimensionality “componentality”, in order to distinguish it from the former. It could be that the ambiguity between dimensionality and componentality comes from the existence of apparently 2D flows bounded by no-slip walls. Indeed, wall-bounded systems inevitably carry some intrinsic level of three-dimensionality in the form of boundary layers. Though usually confined close to no-slip walls, these boundary layers can dramatically alter the dimensionality of a flow in two different ways. On the one hand, they introduce velocity gradients in a direction where the bulk is otherwise 2D. As a result, they may act as a source of vorticity filaments, which then ultimately affect the dynamics of the 2D bulk (Van Heijst *et al.*, 2006). On the other hand, these boundary layers can also introduce a third velocity component to a flow which originally had only two, by means of recirculations. We saw in chapter 2 that this third velocity component could

occur as a result of direct Ekman pumping for instance. Note that when using soap films, dimensionality and componentality generally coincide with one another.

When dealing with turbulence per se, it is customary to think of the flow on a scale-wise basis. Speaking about the dimensionality of turbulence can then become even more ambiguous, since some turbulent flows are found to simultaneously feature what could a priori be called 2D and 3D scales. With this point of view, dimensionality then becomes a function of the size of the structure considered. As a matter of fact, it is possible to observe in nature or laboratory experiments so-called coherent vortices, that is to say long-lived and large-scale vortices, which stand out from a background of otherwise random motions. In shallow configurations, these coherent vortices may be topologically 2D (i.e. spatially invariant along their axis of rotation), and emerge as a result of 2D dynamics (i.e. an inverse energy cascade). And yet, these coherent structures may concurrently exist with topologically and dynamically 3D structures in the background. Following these observations, a whole class of experimental and numerical studies emerged, which dealt with flows combining wide ranges of interacting 2D and 3D turbulent scales, characterized by velocity fields possessing either two or three components. The intent of these studies was to investigate the relationship between dimensionality and componentality, and see how the dynamics of such flows was impacted. The present thesis obviously belongs to this category.

For instance, Celani *et al.* (2010) numerically investigated how altering the dimensionality of the domain in which a turbulent flow takes place, can modify its dynamics. Their setup consisted of a periodic domain in which turbulence was sustained by a Gaussian forcing acting at the scale l_i . The forcing acted on horizontal velocity fluctuations exclusively. In that sense, their turbulence possessed two-components. The aspect ratio of their computational domain was varied by changing its height h , keeping the horizontal lengths unchanged. They thus associated the dimensionality of the flow to the value of the aspect ratio h/l_i . Given this definition, $h/l_i = 0$ and $h/l_i = 1$ refer to the 2D and 3D turbulence limit respectively. With this setup, they found that for $h/l_i > 0.5$, all the kinetic energy injected at the scale l_i flowed down towards small scales, suggesting a direct energy cascade. However, as h/l_i was decreased below 0.5, the energy injected at l_i started to split and flow both towards large and small scales. Furthermore, the relative amount of kinetic energy flowing upscale appeared to be all the more important, as h/l_i was small. Celani *et al.* (2010)'s results thus suggest that hybrid situations may exist where neither Richardson's nor Kraichnan's cascade scenarios seem to apply. Their use of periodic boundary conditions does however not elucidate the role of boundaries on this shift of dynamics.

Later on, Xia *et al.* (2011) studied experimentally the interplay between dimensionality and componentality. Their experimental setup consisted of a thick layer of electrolyte solution put in motion by electromagnetic forces, very much like Paret & Tabeling (1998)'s rig. They focused on cases where the aspect ratio of the forcing scale l_i to the height of the box h was larger than 0.5. In other words, they focused on 3D flows by Celani *et al.* (2010)'s definition. Despite forcing three-dimensional and three-component turbulence, Xia *et al.* (2011) observed that after forcing the flow for a sufficiently long time, a large coherent vortex of the size of their domain emerged, and coincided with the disappearance of the ver-

tical velocity component. The existence of this vortex could only result from residual fluxes of kinetic energy towards large scales, which was confirmed by calculating the third order structure function of the background flow (obtained after subtracting the contribution from the coherent vortex to the overall flow). Interestingly, while the third order structure function of the background flow was positive (suggesting a flux of energy towards large scales), the third order structure function of the entire flow (including the contribution from the coherent vortex) was negative.

To drive the subject home, a recent experimental study by Campagne *et al.* (2014) investigated these matters from the perspective of rotating turbulence. Their experimental apparatus consisted of a rotating 50 cm deep container, in which turbulence was forced by traveling vortex dipoles generated along the sides of the vessel and colliding with each other at its center. Under the action of the Coriolis force, velocity gradients were smoothed out in the direction of the rotation, and was thus 2D. Their velocity field possessed nonetheless three components, though the velocity component in the direction of the rotation was weaker than those in the direction perpendicular to it. In this configuration, Campagne *et al.* (2014) showed that when their flow was 2D, the kinetic energy computed from the velocity components perpendicular to the axis of rotation flowed towards larger scales. They further showed that it was accompanied by a downscale flux of kinetic energy associated to the parallel component of the velocity field. In other words, different contributions to the total kinetic energy may cascade in opposite directions.

The studies presented here undoubtedly demonstrate that the interplay between dimensionality, componentality and dynamics yield extremely rich and exciting phenomena.

4.1.5 Particularities of MHD turbulence

MHD turbulence immersed in a static and uniform magnetic field at low- Rm undoubtedly sets itself apart from hydrodynamic turbulence thanks to the presence of the Lorentz force. This additional force brings two dramatic consequences. On the one hand, when the flow is confined between insulating and no-slip walls, the solenoidal component of the Lorentz force tends to two dimensionlize the flow in the direction of the magnetic field. On the other hand, the Lorentz force introduces Joule dissipation, which in effect is a new mechanism able to dissipate kinetic energy. The dynamics of MHD turbulence are therefore very likely to differ from those we have explored so far; We shall now examine to what extent.

The Joule cone

For once, the influence of the Lorentz force on a turbulent flow is perhaps easier to apprehend in Fourier space. According to the discussion in section 1.2.2, the solenoidal part of the Lorentz force is given by

$$\mathbf{f}_S = -\frac{\sigma}{\rho} \Delta^{-1} [(\mathbf{B}_0 \cdot \nabla)^2 \mathbf{u}] . \quad (4.19)$$

Taking the Fourier transform of the former equation, $(\mathbf{B}_0 \cdot \nabla)$ becomes under the usual transformation rules $i(\mathbf{B}_0 \cdot \mathbf{k})$, while Δ^{-1} becomes $-1/k^2$. Equation (4.19) eventually yields

$$\hat{\mathbf{f}}_S(\mathbf{k}) = -\frac{\sigma B_0^2}{\rho} \cos^2[\alpha(\mathbf{k})] \hat{\mathbf{u}}(\mathbf{k}), \quad (4.20)$$

where $\hat{\mathbf{f}}_S$ and $\hat{\mathbf{u}}$ are the Fourier transforms of \mathbf{f}_S and \mathbf{u} respectively, and $\alpha(\mathbf{k}) = (\mathbf{e}_{\parallel}, \mathbf{k})$ is the angle between the wave-vector \mathbf{k} and the axis of the magnetic field. Equation (4.20) showcases two important features of the Lorentz force. On the one hand, its power is negative, which is found by multiplying (4.20) with the complex conjugate of $\hat{\mathbf{u}}$. That is to say, its net effect is to dissipate kinetic energy. On the other hand, energy dissipation by the Lorentz force does not involve the wave-number $k = \|\mathbf{k}\|$, meaning that Joule dissipation is scale independent. This behavior contrasts strikingly with viscous dissipation, which is important only at large k (i.e. small scales). Joule dissipation depends however on the orientation of the wave-vector with respect to \mathbf{B}_0 . In particular, Joule dissipation occurs preferentially at small α , that is to say for wave-vectors aligned with the magnetic field. On the contrary, structures laying in the plane perpendicular to the magnetic field experience no Joule dissipation.

The impact of these effects was studied analytically by Moffatt (1967) within the context of decaying and unbounded MHD turbulence. His thought experiment was the following. Consider an electrically conducting fluid in a fully developed turbulent state, which is initially homogeneous and isotropic. Assume now that at time $t = 0$, a static and homogeneous magnetic field is instantaneously applied, and that the flow is left to decay. Further assuming that N is initially much larger than 1 (i.e. electromagnetic effects are quicker than inertia), how does the flow evolve? This question was investigated during the linear regime of the decay, where inertia is negligible compared to electromagnetic damping. Restraining himself to this stage enabled him to highlight the effect of the Lorentz force, before any other process (namely inertia) could oppose it. As it turns out, the aspect of the flow at the end of the early decay depends drastically on the initial distribution of energy in spectral space. In particular, anisotropy may appear only if the bulk of the kinetic energy lays initially in wave numbers smaller than a critical dissipative wave-number k_d , which quantifies the mechanism responsible for the propagation of the induced field in the medium. In the low- Rm framework, the main contribution to the kinetic energy comes from the region of wave vectors perpendicular to the magnetic field, and the kinetic energy decays as

$$\frac{\partial \langle |\hat{\mathbf{u}}|^2 \rangle(\mathbf{k})}{\partial t} = -\frac{2}{\tau_J} \cos^2(\alpha) \langle |\hat{\mathbf{u}}|^2 \rangle(\mathbf{k}). \quad (4.21)$$

As a result, anisotropy quickly develops, making the flow less and less dependent on the spatial coordinate along the magnetic field, i.e. making the flow 2D. This does not however mean that the velocity component along the magnetic field vanishes, on the contrary. Moffatt (1967) further showed that the end result was to somewhat channel kinetic energy towards the parallel velocity component, where ultimately $u_{\parallel}^2 = 2u_{\perp}^2$ (true as long as the flow

is unbounded in the direction perpendicular to the field). This phenomenology is classically illustrated using the Joule cone, which distinguishes the energy containing and energy depleted regions in Fourier space. It is sketched in figure 4.1. As the linear decay unfolds, the Joule cone opens up, eventually concentrating the remaining energy into the wave vectors which are exactly perpendicular to the magnetic field.

In statistically steady turbulence however, a balance exists between Joule dissipation and inertia. As a matter of fact, such a balance is also expected to emerge subsequently to the linear decay phase, provided the flow still contains a reasonable amount of turbulence. The latter case was investigated numerically by Alemany *et al.* (1979). In particular, they showed that as the non-linear decay unfolded, kinetic energy was, on average, removed from large perpendicular wave-numbers for the benefit of smaller ones. At the same time, they demonstrated that angular energy transfers across the border of the Joule cone also existed, where the energy of small latitude wave-vectors was supplied to larger latitude ones. Inertia therefore appears to work towards restoring isotropy by shifting kinetic energy around spectral space. More specifically, it does so by introducing angular energy transfers across the border of the Joule cone. Interestingly, according to Alemany *et al.* (1979)'s calculations, the radial scale by scale energy transfers (i.e. what is commonly understood as the energy cascade) appeared to be about two orders of magnitude smaller than the polar angular transfers at the integral wave-number. Although this study perfectly illustrates how the Lorentz force alters the dynamics of anisotropic MHD turbulence, it is perhaps a bit premature at this point to speak of an energy cascade per se. Indeed, the latter does not exist, strictly speaking, in freely decaying 2D turbulence. Nevertheless, the dynamics of MHD turbulence appear to have an additional ingredient compared to classical hydrodynamics.

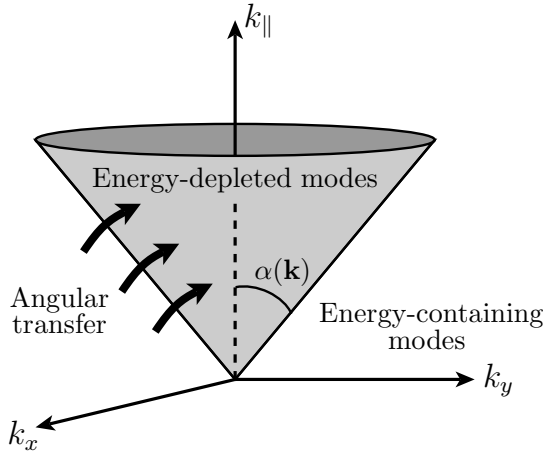


Figure 4.1. The Joule cone distinguishes between energy-containing and energy-depleted regions of Fourier space (mirror symmetry with respect to the (k_x, k_y) plane). In the 2D limit, the Lorentz force concentrates kinetic energy into modes exactly perpendicular to the magnetic field.

Confinement by perpendicular no-slip and electrically insulating walls

Equation (4.20) is in fact to Fourier space, what Sommeria & Moreau (1982)'s interpretation of the Lorentz force as a pseudo-diffusive process is to physical space. Recalling what was discussed in section 1.2.2, the solenoidal part of the Lorentz force acting on a turbulent structure of characteristic width l_\perp , height l_\parallel and velocity u_\perp , is characterized by

$$\tau_{2D} = \frac{\rho}{\sigma B_0^2} \left(\frac{l_\parallel}{l_\perp} \right)^2. \quad (4.22)$$

Further assuming that this turbulent structure lies in the inertial range of a fully developed and statistically steady turbulent flow, the other relevant mechanism competing against the Lorentz force are non-linear inertial transfers, characterized by the eddy turnover time

$$\tau_u = \frac{l_\perp}{u_\perp}. \quad (4.23)$$

An equilibrium between these two mechanisms hence yields a measure of the anisotropy of the turbulent scale

$$\frac{l_\perp}{l_\parallel} = \left[\frac{\rho u_\perp}{\sigma B_0^2 l_\parallel} \right]^{1/3}. \quad (4.24)$$

Should the turbulent eddy be now confined between two perpendicular walls distant by h , the Lorentz force cannot diffuse momentum along the magnetic field further than this distance. Imposing $l_\parallel > h$ in turn introduces a lower bound on the transverse lengthscale l_\perp^c for an MHD turbulent structure to be kinematically 2D (Sommeria & Moreau, 1982), namely

$$\frac{l_\perp^c}{h} > N_c (h, u_\perp)^{-1/3}, \quad (4.25)$$

where $N_c = \sigma B_0^2 h / \rho u_\perp$ can be seen as an interaction parameter based on the height of the channel. In fact, (4.25) tells us that when $l_\perp < l_\perp^c$, the structure is kinematically 3D, in the sense that it experiences velocity gradients and hence Joule dissipation. Conversely, $l_\perp > l_\perp^c$ implies that the scale is kinematically 2D, in the sense that it extends throughout the channel, hence the flow is fully correlated across the distance h . The one aspect of the Lorentz force that stands out here, is that it preferentially two-dimensionalizes large perpendicular scales. MHD therefore appears as an interesting tool to segregate between scales and impose in a controllable way the amount of 2D and 3D scales we wish to have (for a channel of a given height, N_c is a tunable parameter depending on B_0 and u_\perp , which can be set at will by imposing the magnitude of the magnetic field and the intensity of the electric forcing).

As far as the dynamics of these kinematically 2D MHD scales are concerned, it is important to stress that angular energy transfers are forbidden. This argument can be easily understood by recalling that Joule dissipation only appears as a result of velocity gradients along the magnetic field (cf. equation (1.25)). 2D scales are by definition not subject to

such velocity gradients in the bulk, hence Joule dissipation must vanish for them. This however does not mean that they necessarily experience an inverse energy cascade. Indeed, the presence of no-slip boundaries imposes that three-dimensionality remains in the form of Hartmann layers, in which energy dissipation always exists. The net effect of this energy dissipation at the tips of these (in fact quasi-2D) vortices comes from Hartmann braking. As a result, Sommeria & Moreau (1982) also introduced an upper limit for kinematically quasi-2D structures to experience 2D dynamics. This limit comes from considering that energy transfers are quicker than energy dissipation in the Hartmann layers i.e. $\tau_u < \tau_H$, where τ_H refers to the Hartmann friction time defined in section 1.3.3. This in turn yields a lower bound for kinematically 2D turbulent scales to follow an inverse energy cascade

$$l_\perp < \frac{u_\perp h}{2B_0} \sqrt{\frac{\rho}{\sigma\nu}}. \quad (4.26)$$

Equation (4.26) in fact allows MHD turbulence to have an energy sink at large scales. As a result, a steady inverse energy cascade following Kraichnan's scenario may be observed in our experiment.

4.2 Description of turbulence in physical space

4.2.1 Local conservation of energy in a fluid

Besides scale size, the other cornerstone quantity in studies of turbulence is kinetic energy. Let us therefore start by recalling the local governing equations for the kinetic energy in low- Rm MHD in order to understand the phenomenology at stake. The flow is assumed to be pervaded by a vertical magnetic field \mathbf{B}_0 , and subject to the Lorentz force $\mathbf{j} \times \mathbf{B}_0/\rho$, which splits into an irrotational pressure term (encompassed in p^*) and the solenoidal term $\mathbf{f}_S = -(\sigma B_0^2/\rho)\Delta^{-1}(\partial^2 \mathbf{u}/\partial x_\parallel^2)$. We recall that the governing equations are given by

$$\frac{d\mathbf{u}}{dt} = \nabla \cdot \left[-\frac{p^*}{\rho} \mathbb{I} + 2\nu \mathbb{S} \right] + \mathbf{f}_S, \quad (4.27)$$

and

$$\nabla \cdot \mathbf{u} = 0, \quad (4.28)$$

where $d* / dt = \partial* / \partial t + \nabla \cdot [\mathbf{u} \otimes \mathbf{u}]$ is the material derivative (for an incompressible fluid), and $\mathbb{S} = [(\nabla \mathbf{u}) + (\nabla \mathbf{u})^T]/2$ is the strain rate tensor. The work-energy principle is derived by taking the dot product of (4.27) with \mathbf{u} and using (4.28), yielding

$$\frac{1}{2} \frac{d\mathbf{u}^2}{dt} = \nabla \cdot \left[-\frac{p^*}{\rho} \mathbf{u} + 2\nu \mathbb{S} \cdot \mathbf{u} \right] + \mathbf{f}_S \cdot \mathbf{u} - 2\nu \mathbb{S} : \mathbb{S}. \quad (4.29)$$

Equation (4.29) is the governing equation for the kinetic energy per unit mass $\mathbf{u}^2/2$, and merely states that the time rate of change of kinetic energy in real space results either

from its conservative transport (thanks to advection by the flow, the work of the pressure forces and viscous friction) or to sink/source terms (internal dissipation by viscous friction $-2\nu \mathbb{S} : \mathbb{S} < 0$ and work of the Lorentz force). In the case of a forced flow, energy must constantly be fed into the system to balance out energy dissipation. This may be realized through the boundary conditions, which have not yet been specified. In order to fully close the picture, let us examine the conservation law for the total energy. According to the first principle of thermodynamics, the time rate of change of the system's total energy (which splits between internal energy e and kinetic energy $\mathbf{u}^2/2$) results from the work done on the fluid, as well as heat exchanges. In other words

$$\frac{de}{dt} + \frac{1}{2} \frac{d\mathbf{u}^2}{dt} = \nabla \cdot \left[-\frac{p^*}{\rho} \mathbf{u} + 2\nu \mathbb{S} : \mathbf{u} \right] + \mathbf{f}_S \cdot \mathbf{u} - \nabla \cdot \frac{\mathbf{q}}{\rho} + \frac{\mathbf{j} \cdot \mathbf{E}}{\rho}, \quad (4.30)$$

where \mathbf{q} represents the local heat flux density exchanged between fluid particles (typically modeled using Fourier's law), and $\mathbf{j} \cdot \mathbf{E}$ represents a body heat source due to the motion of electrical charges through the electrically conducting fluid. Subtracting (4.29) to (4.30), and substituting Ohm's law to the electric field \mathbf{E} leads to the equation for the internal energy

$$\frac{\partial e}{\partial t} = \nabla \cdot \left[-e \mathbf{u} - \frac{\mathbf{q}}{\rho} \right] + 2\nu \mathbb{S} : \mathbb{S} + \frac{\mathbf{j} \cdot \mathbf{j}}{\rho \sigma} + \frac{\mathbf{j} \times \mathbf{B}_0}{\rho} \cdot \mathbf{u}. \quad (4.31)$$

Equation (4.31) proves the well known result that viscous dissipation converts kinetic energy into heat ($\mathbb{S} : \mathbb{S} > 0$). There are however two additional heat sources specific to MHD, which result from rearranging the terms introduced by Ohm's law: the flow of electric charges through the conducting medium ($\mathbf{j} \cdot \mathbf{j} > 0$), and the work of the total Lorentz force $(\mathbf{j} \times \mathbf{B}_0) \cdot \mathbf{u}/\rho$.

4.2.2 The role of enstrophy in turbulence

Let us adopt an alternate point of view to get another perspective about the differences between 2D and 3D MHD turbulence. To this end, the work-energy principle may be re-written in a slightly different form by introducing the vorticity $\boldsymbol{\omega} = \nabla \times \mathbf{u}$. The alternate form of equation (4.29) being (Davidson, 2015)

$$\frac{1}{2} \frac{d\mathbf{u}^2}{dt} = \nabla \cdot \left[-\frac{p^*}{\rho} \mathbf{u} + \nu \mathbf{u} \times \boldsymbol{\omega} \right] + \mathbf{f}_S \cdot \mathbf{u} - \nu \boldsymbol{\omega} \cdot \boldsymbol{\omega}. \quad (4.32)$$

Relation (4.32) shows that viscous dissipation of kinetic energy is related to the enstrophy $\boldsymbol{\omega}^2 = \boldsymbol{\omega} \cdot \boldsymbol{\omega}$. The governing equation for the enstrophy is derived by taking the dot product of the vorticity equation

$$\frac{d\boldsymbol{\omega}}{dt} = \mathbb{S} \cdot \boldsymbol{\omega} + \nu \nabla \cdot [\nabla \boldsymbol{\omega}] + \nabla \times \mathbf{f}_S \quad (4.33)$$

with ω . The overall result reads

$$\frac{d\omega^2}{dt} = \mathbb{S} : (\omega \otimes \omega) + \nu \nabla \cdot [\nabla \omega \cdot \omega] + (\nabla \times \mathbf{f}_S) \cdot \omega - \nu \nabla \omega : \nabla \omega. \quad (4.34)$$

In the limit of exactly 2D unconfined MHD turbulence, the terms $\mathbb{S} : (\omega \otimes \omega)$ and $(\nabla \times \mathbf{f}_S) \cdot \omega$ are identically zero. The former comes from two-dimensionality imposing vorticity and strain rate to occur in disjointed domains of space, while the latter stems from velocity gradients along the magnetic field (hence \mathbf{f}_S) vanishing in the 2D limit. As a result, in the absence of an external forcing, the enstrophy of 2D unconfined MHD turbulence is bounded by its initial value and can only decay under the action of viscous dissipation (quantified by the term $-\nu \nabla \omega : \nabla \omega$). Amazingly, combining this argument with (4.32) shows how the viscous dissipation of enstrophy in fact works towards the conservation of kinetic energy when the flow is 2D.

In the more true to life limit of quasi-2D MHD turbulence (that is to say a flow bounded by no-slip and insulating walls), the terms $\mathbb{S} : (\omega \otimes \omega)$ and $(\nabla \times \mathbf{f}_S) \cdot \omega$ remain null in the bulk, but are non negligible near solid boundaries, where strong velocity gradients exist. Combining this observation with (4.32) shows how the Lorentz force may still dissipate kinetic energy within boundary layers, despite the bulk being 2D. In particular, Hartmann friction hides in the term $(\nabla \times \mathbf{f}_S) \cdot \omega$ evaluated along no-slip walls perpendicular to the magnetic field.

Incidentally (4.32) and (4.34) also shows how inertia can channel kinetic energy into its dissipation by viscosity in 3D hydrodynamic turbulence (we suppose in this paragraph $p^* = p$ and $\mathbf{f}_S = 0$). Indeed, the hydrodynamic version of (4.32) requires that strong velocity gradients exist to dissipate kinetic energy. At the same time, the hydrodynamic version of (4.32) implies that the only way for these gradients to be promoted is for vorticity lines to interact with the surrounding strain rate field through the term $\mathbb{S} : (\omega \otimes \omega)$. This term in fact contains the inertial mechanisms responsible for Richardson's energy cascade.

4.2.3 The Reynolds averaged equations

The most intuitive way to introduce turbulent motions in the model equations is perhaps by adopting Reynolds' approach, which consists in decomposing the velocity field as $\mathbf{u}(\mathbf{x}, t) = \bar{\mathbf{U}}(\mathbf{x}) + \mathbf{u}'(\mathbf{x}, t)$, where $\bar{\mathbf{U}}(\mathbf{x}) = \langle \mathbf{u}(\mathbf{x}, t) \rangle$ represents the mean flow and $\mathbf{u}'(\mathbf{x}, t) = \mathbf{u}(\mathbf{x}, t) - \bar{\mathbf{U}}(\mathbf{x})$ refers to the turbulent fluctuation. The operator $\langle \cdot \rangle$ must be understood as an ensemble average at location \mathbf{x} , which coincides with a temporal average, under the assumption of ergodicity (which we will consider from now on). Taking the Reynolds decomposition of all the variables, we have $\mathbf{u} = \bar{\mathbf{U}} + \mathbf{u}'$, $p^* = \bar{P}^* + p^{*\prime}$, and $\mathbf{f}_S = \bar{\mathbf{F}}_S + \mathbf{f}'_S$. In addition, we decompose the strain rate tensor as $\mathbb{S} = \bar{\mathbb{S}} + \mathbb{S}'$, where $\bar{\mathbb{S}} = [(\nabla \bar{\mathbf{U}}) + (\nabla \bar{\mathbf{U}})^T]/2$ is the mean strain rate tensor, while $\mathbb{S}' = [(\nabla \mathbf{u}') + (\nabla \mathbf{u}')^T]/2$ is the strain rate tensor based on velocity fluctuations. Inserting these new variables in (4.27) and taking its ensemble average (by

definition $\langle \mathbf{u}' \rangle(\mathbf{x}) = 0$ leads to equation governing the mean flow

$$\frac{\partial \bar{\mathbf{U}}}{\partial t} + \nabla \cdot [\bar{\mathbf{U}} \otimes \bar{\mathbf{U}} + \langle \mathbf{u}' \otimes \mathbf{u}' \rangle] = \nabla \cdot \left[-\frac{\bar{P}^*}{\rho} \mathbb{I} + 2\nu \bar{\mathbb{S}} \right] + \bar{\mathbf{F}}_S. \quad (4.35)$$

The governing equation for the mean kinetic energy immediately follows from taking the dot product of (4.35) with $\bar{\mathbf{U}}$ and accounting for incompressibility

$$\begin{aligned} \frac{1}{2} \frac{\partial \bar{\mathbf{U}}^2}{\partial t} + \nabla \cdot \left[\frac{\bar{\mathbf{U}}^2}{2} \bar{\mathbf{U}} + \langle \mathbf{u}' \otimes \mathbf{u}' \rangle \cdot \bar{\mathbf{U}} \right] &= \nabla \cdot \left[-\frac{\bar{P}^* \bar{\mathbf{U}}}{\rho} + 2\nu \bar{\mathbb{S}} \cdot \bar{\mathbf{U}} \right] + \bar{\mathbf{F}}_S \cdot \bar{\mathbf{U}} \\ &\quad + \langle \mathbf{u}' \otimes \mathbf{u}' \rangle : \nabla \bar{\mathbf{U}} - 2\nu \bar{\mathbb{S}} : \bar{\mathbb{S}}. \end{aligned} \quad (4.36)$$

Doing the same for the work-energy equation (4.29), and subtracting (4.36) eventually yields the governing equation for the turbulent kinetic energy

$$\begin{aligned} \frac{1}{2} \frac{\partial \langle \mathbf{u}'^2 \rangle}{\partial t} + \frac{1}{2} \nabla \cdot [\langle \mathbf{u}'^2 \rangle \bar{\mathbf{U}} + \langle \mathbf{u}'^2 \mathbf{u}' \rangle] &= \nabla \cdot \left[-\frac{\langle p'^* \mathbf{u}' \rangle}{\rho} + 2\nu \langle \mathbb{S}' \cdot \mathbf{u}' \rangle \right] + \langle \mathbf{f}'_S \cdot \mathbf{u}' \rangle \\ &\quad - \langle \mathbf{u}' \otimes \mathbf{u}' \rangle : \nabla \bar{\mathbf{U}} - 2\nu \langle \mathbb{S}' : \mathbb{S}' \rangle. \end{aligned} \quad (4.37)$$

The governing equation for the mean internal energy $\bar{E} = \langle e \rangle$ is also obtained by taking the ensemble average of (4.31) in which the Reynolds variables have been substituted. It reads

$$\frac{\partial \bar{E}}{\partial t} + \nabla \cdot [\bar{E} \bar{\mathbf{U}} + \langle e' \mathbf{u}' \rangle + \bar{\mathbf{Q}}] = 2\nu \bar{\mathbb{S}} : \bar{\mathbb{S}} + 2\nu \langle \mathbb{S}' : \mathbb{S}' \rangle + \chi, \quad (4.38)$$

where

$$\chi = \frac{1}{\rho\sigma} [\bar{\mathbf{J}} \cdot \bar{\mathbf{J}} + \langle \mathbf{j}' \cdot \mathbf{j}' \rangle] + \frac{1}{\rho} [(\bar{\mathbf{J}} \times \mathbf{B}_0) \cdot \bar{\mathbf{U}} + \langle \mathbf{j}' \times \mathbf{B}_0 \cdot \mathbf{u}' \rangle] \quad (4.39)$$

compiles the mean and turbulent electromagnetic heat sources. The global action of turbulence can now be understood in the light of equations (4.36), (4.37) and (4.38), which are transport equations for different types of energy: mean kinetic, turbulent kinetic and mean internal respectively. In particular, they all feature flux terms written in terms of divergences, which express that energy may be conservatively shifted through physical space by different means, as a result of spatial inhomogeneities. Most importantly, these equations share common sink/source terms with each other, meaning that energy can be converted from one kind to another.

To be more specific, the equations for the mean and turbulent kinetic energy are linked to each other via the term $\langle \mathbf{u}' \otimes \mathbf{u}' \rangle : \nabla \bar{\mathbf{U}}$. This term appears however with opposite signs whether in (4.36) or (4.37), meaning that a sink of mean kinetic energy is in fact a source of turbulent kinetic energy (or vice versa). It usually turns out that $\langle \mathbf{u}' \otimes \mathbf{u}' \rangle : \nabla \bar{\mathbf{U}} < 0$. In other words, turbulent kinetic energy is produced out of mean velocity gradients. Similarly, one may also notice that (4.36) and (4.37) feature sinks of kinetic energy resulting from viscous friction ($-2\nu \bar{\mathbb{S}} : \bar{\mathbb{S}}$ and $-2\nu \langle \mathbb{S}' : \mathbb{S}' \rangle$ are indeed negative), which appear in (4.38) as sources of internal energy.

4.3 Turbulence in scale space

Thanks to Reynolds' decomposition in physical space, it is possible to get a first quantitative idea of the journey taken by the kinetic energy of a turbulent flow. We are however missing some crucial information on the scale distribution of the turbulent kinetic energy. Indeed, Reynolds' decomposition in physical space only distinguishes between mean and turbulent structures, regardless of their sizes. The goal of the present section is to introduce some of the tools customarily used to describe turbulence on a scale-wise basis, which will be extensively used hereafter.

4.3.1 Correlation and structure functions

Information on turbulent scales is introduced by means of two point statistics. Let us say they are evaluated at points A and B whose coordinates in space are given by $\mathbf{x}_A = \mathbf{x}$ and $\mathbf{x}_B = \mathbf{x} + \mathbf{r}$ respectively, where \mathbf{r} is the separation or increment vector. The basis for turbulence analyses in scale space is the correlation tensor $\mathbb{Q}(\mathbf{r}) = \langle \mathbf{u}'(\mathbf{x}) \otimes \mathbf{u}'(\mathbf{x} + \mathbf{r}) \rangle$, which gives a measure of how turbulent fluctuations occurring at two points distant from \mathbf{r} apart relate to each other. For now, we take $\langle \cdot \rangle$ to indistinctly represent an ensemble and a spatial average (we will discuss this point in further details in section 4.3.2). The definition of \mathbb{Q} is consistent with the description of turbulence in real space seen earlier: when points A and B coincide (i.e. when $\mathbf{r} = 0$), $\mathbb{Q}(0)$ yields the Reynolds tensor $\langle \mathbf{u}' \otimes \mathbf{u}' \rangle$, while the flow's mean turbulent kinetic energy $E_k = \langle \mathbf{u}'^2 \rangle / 2$ is given by the trace of \mathbb{Q} according to $\text{tr}[\mathbb{Q}(0)] = 2 E_k$. The correlation tensor is a second order tensor, which relates the three components of $\mathbf{u}(\mathbf{x}_A)$ to the three components of $\mathbf{u}(\mathbf{x}_B)$. Generally speaking, \mathbb{Q} can be decomposed onto the nine tensors $Q_{\alpha\beta}(\mathbf{r}) \mathbf{e}_\alpha \otimes \mathbf{e}_\beta$, where α and β respectively represent any of the three directions of space (no summation implied), and $Q_{\alpha\beta}(\mathbf{r}) = \langle u'_\alpha(\mathbf{x}) u'_\beta(\mathbf{x} + \mathbf{r}) \rangle$ are scalar functions of \mathbf{r} . In the general case, the nine components $Q_{\alpha\beta}$, are independent from each other.

Another valuable quantity used to describe turbulence in scale space is the velocity increment $\delta\mathbf{u}'(\mathbf{x}, \mathbf{r}) = \mathbf{u}'(\mathbf{x} + \mathbf{r}) - \mathbf{u}'(\mathbf{x})$, which may be understood as a measure of the velocity of turbulent scales of size $r = \|\mathbf{r}\|$ and less. Indeed, an eddy smaller than r will contribute to $\delta\mathbf{u}'$ either in A or B, hence will introduce a large velocity discrepancy between the two points. On the other hand, a scale much larger than r will contribute approximately in the same way to points A and B, thus both contributions will cancel each other out. The second order structure function $\langle \delta\mathbf{u}'^2 \rangle$ may then be interpreted, in a first approximation, as a measure of the cumulative kinetic energy held in scales of size r and less (Davidson & Krogstad (2008) argue however that this interpretation may lead to misreadings about $\langle \delta\mathbf{u}'^2 \rangle$ and needs to be refined).

As discussed many times already, the Lorentz force is known to quickly bring the flow of an electrically conducting fluid towards an anisotropic state by diffusing momentum in the direction of the magnetic field. As a result, MHD turbulence may possibly be described in terms of homogeneous and axisymmetric turbulence. Let us therefore adopt the cylindrical system of coordinates $(\mathbf{e}_\rho, \mathbf{e}_\theta, \mathbf{e}_z)$, where \mathbf{e}_z is the unit vector in the direction of the field.

We also define $\mathbf{r} = \rho \mathbf{e}_\rho + z \mathbf{e}_z$ the separation vector. Invoking homogeneity implies that the correlation tensor \mathbb{Q} is independent of the point of reference \mathbf{x} , and further possesses index symmetry, that is to say

$$Q_{\alpha\beta}(\mathbf{r}) = Q_{\beta\alpha}(-\mathbf{r}), \quad (4.40)$$

where the vector variable \mathbf{r} should of course be understood as a shorthand for the set of scalar variables (ρ, z) by virtue of axisymmetry. Equation (4.40) provides a good way to test homogeneity in our experiment, namely by looking at how $\mathbb{Q}(\mathbf{x}, \mathbf{r})$ computed at different locations and for increments with opposite directions compare against each other. The second order structure function $\langle \delta \mathbf{u}'^2 \rangle$ is related to the trace of the correlation function $\mathbb{Q}(\mathbf{r})$ via

$$\langle \delta \mathbf{u}'^2 \rangle(\mathbf{r}) = 4E_0 \left[1 - \frac{Q_{zz}(\mathbf{r}) + Q_{\rho\rho}(\mathbf{r}) + Q_{\theta\theta}(\mathbf{r})}{2E_0} \right], \quad (4.41)$$

where $E_0 = \langle \mathbf{u}_A^2 + \mathbf{u}_B^2 \rangle / 4$ is the two point mean kinetic energy computed from points A and B. Equation (4.41) shows that the second order structure function depends on three different functions, which are even in ρ and z . Further simplifications may however arise if we assume that the velocity component along the magnetic field is much smaller than the velocity components perpendicular to it. As we will see in chapter 5, this argument is not too far fetched in our experimental setup. Indeed, the combined effect of gradients smoothing along the magnetic field and impermeable horizontal walls team up to suppress the vertical velocity component. Noting u'_z and \mathbf{u}'_\perp the velocity fluctuations in the directions parallel and perpendicular to field respectively, one may assume $|u'_z| < \|\mathbf{u}'_\perp\|$, which in turn implies $\langle u'_z^2 \rangle \ll \langle \mathbf{u}'_\perp^2 \rangle$, and hence $\langle \mathbf{u}'^2 \rangle \simeq \langle \mathbf{u}'_\perp^2 \rangle$. Since $Q_{zz}(\mathbf{r}) = \langle u'_z(\mathbf{x}) u'_z(\mathbf{x} + \mathbf{r}) \rangle$ must scale as $\langle u'_z^2 \rangle$, while $Q_{\rho\rho}(\mathbf{r}) = \langle u'_\rho(\mathbf{x}) u'_\rho(\mathbf{x} + \mathbf{r}) \rangle$ and $Q_{\theta\theta}(\mathbf{r}) = \langle u'_\theta(\mathbf{x}) u'_\theta(\mathbf{x} + \mathbf{r}) \rangle$ must both scale as $\langle \mathbf{u}'_\perp^2 \rangle$, one may neglect the contribution of vertical kinetic energy to the second order structure function. Writing $R_l(\mathbf{r}) = Q_{\rho\rho}(\mathbf{r})/4E_0$ and $R_t(\mathbf{r}) = Q_{\theta\theta}(\mathbf{r})/4E_0$, (4.41) may therefore be approximated by

$$\langle \delta \mathbf{u}'^2 \rangle(\mathbf{r}) \simeq 4E_0 [1 - R_l(\mathbf{r}) - R_t(\mathbf{r})]. \quad (4.42)$$

Equation (4.42) is a useful relationship to calculate the second order structure function from correlation functions based on the velocity components perpendicular to the magnetic field, which are directly measurable in our experiment.

4.3.2 Dynamics of inhomogeneous, anisotropic turbulence: the Kármán-Howarth equation

The equation governing the dynamics of turbulence in scale space was first derived by Kármán & Howarth (1938) for homogeneous and isotropic turbulence. In this section, we propose to focus on the formalism put forward more recently by Hill (2002), in which an exact dynamical equation for the second order structure function is derived, regardless of whether homogeneity or isotropy are satisfied. This formalism is all the more attractive, as it has already been successfully used by Campagne *et al.* (2014) to describe the dynamics of

4. TURBULENCE

turbulence under rapid rotation. The derivation relies on the two point statistics introduced earlier, evaluated at points A and B whose respective coordinates in space are $\mathbf{x}_A = \mathbf{X} - \mathbf{r}/2$ and $\mathbf{x}_B = \mathbf{X} + \mathbf{r}/2$, where $\mathbf{X} = (\mathbf{x}_A + \mathbf{x}_B)/2$ is the midpoint position between points A and B, and $\mathbf{r} = \mathbf{x}_B - \mathbf{x}_A$ is the separation vector between them. For the sake of clarity, we will use from now on subscript P to denote any quantity (typically \mathbf{u} , p^* etc.) evaluated at point \mathbf{x}_P . Similarly, ∇_A , ∇_B , $\nabla_{\mathbf{r}}$ and $\nabla_{\mathbf{X}}$ indicate that the ∇ operator differentiates along the variables \mathbf{x}_A , \mathbf{x}_B , \mathbf{r} and \mathbf{X} respectively. Keeping in mind that the variables \mathbf{x}_A , \mathbf{x}_B on the one hand, and \mathbf{r} , \mathbf{X} on the other hand are independent from each other, the change of variables considered above implies the following differentiation rules

$$\nabla_A = -\nabla_{\mathbf{r}} + \frac{1}{2}\nabla_{\mathbf{X}} \quad \text{and} \quad \nabla_B = \nabla_{\mathbf{r}} + \frac{1}{2}\nabla_{\mathbf{X}}.$$

The Kármán-Howarth equation for the second order structure function is derived by subtracting the momentum equation (4.27) evaluated at point A to the momentum equation (4.27) evaluated at point B , and by taking the dot product of the difference with $\delta\mathbf{u} = \mathbf{u}_B - \mathbf{u}_A$. Doing so eventually yields (cf. appendix A for the details of the derivation):

$$\begin{aligned} \frac{\partial \delta\mathbf{u}^2}{\partial t} + \nabla_{\mathbf{r}} \cdot [\delta\mathbf{u}^2 \delta\mathbf{u}] + \nabla_{\mathbf{X}} \cdot [\delta\mathbf{u}^2 \mathbf{u}_m] &= 2\delta\mathbf{f}_S \cdot \delta\mathbf{u} - 4\epsilon_m \\ &+ 2\nu \nabla_{\mathbf{r}} \cdot [\nabla_{\mathbf{r}} \delta\mathbf{u}^2] + 2\nabla_{\mathbf{X}} \cdot \left[-\frac{\delta p^* \delta\mathbf{u}}{\rho} + \frac{\nu}{4} \nabla_{\mathbf{X}} (\delta\mathbf{u}^2 - 8p_m^*) \right]. \end{aligned} \quad (4.43)$$

In the above, subscript m refers to the mean quantity evaluated from points A and B, i.e. $\mathbf{u}_m = (\mathbf{u}_A + \mathbf{u}_B)/2$, $p_m^* = (p_A^* + p_B^*)/2$ and $\epsilon_m = (\epsilon_A + \epsilon_B)/2$, with $\epsilon_P = 2\nu \mathbb{S}_P : \mathbb{S}_P$. In addition, $\delta\mathbf{u}^2$ (and subsequently $\delta\bar{\mathbf{U}}^2$ and $\delta\mathbf{u}'^2$) should be understood as shorthands for $\|\delta\mathbf{u}\|^2$, $\|\delta\bar{\mathbf{U}}\|^2$ and $\|\delta\mathbf{u}'\|^2$ respectively. Equation (4.43) is to scale space, what (4.29) is to physical space, in the sense that both equations are *exact* (averaging is yet to be defined) and apply to the *total* velocity field (the Reynolds decomposition is yet to be performed). As we did earlier with (4.37), it is possible to derive an equation for the turbulent second order structure function $\langle \delta\mathbf{u}'^2 \rangle$ by introducing the Reynolds decomposition of (4.43) and by taking a time average now denoted by $\langle \cdot \rangle_t$. The first step consists in deriving the governing equation for the mean second order structure function

$$\begin{aligned} \frac{\partial \delta\bar{\mathbf{U}}^2}{\partial t} + \nabla_{\mathbf{r}} \cdot [\delta\bar{\mathbf{U}}^2 \delta\bar{\mathbf{U}} + \langle \delta\mathbf{u}' \otimes \delta\mathbf{u}' \rangle_t \cdot \delta\bar{\mathbf{U}}] + \nabla_{\mathbf{X}} \cdot [\delta\bar{\mathbf{U}}^2 \bar{\mathbf{U}}_m + \langle \delta\mathbf{u}' \otimes \mathbf{u}'_m \rangle_t \cdot \delta\bar{\mathbf{U}}] \\ = 2\nu \nabla_{\mathbf{r}} \cdot [\nabla_{\mathbf{r}} \delta\bar{\mathbf{U}}^2] + 2\nabla_{\mathbf{X}} \cdot \left[-\frac{\delta\bar{P}^* \delta\bar{\mathbf{U}}}{\rho} + \frac{\nu}{4} \nabla_{\mathbf{X}} (\delta\bar{\mathbf{U}}^2 - 8\bar{P}_m^*) \right] \\ + 2\delta\bar{\mathbf{F}}_S \cdot \delta\bar{\mathbf{U}} + \langle \delta\mathbf{u}' \otimes \delta\mathbf{u}' \rangle_t : \nabla_{\mathbf{r}} \delta\bar{\mathbf{U}} + \langle \delta\mathbf{u}' \otimes \mathbf{u}'_m \rangle_t : \nabla_{\mathbf{X}} \delta\bar{\mathbf{U}} - 4\bar{\epsilon}_m, \end{aligned} \quad (4.44)$$

from which the governing equation for the turbulent kinetic energy may then be derived

$$\begin{aligned} & \frac{\partial \langle \delta \mathbf{u}'^2 \rangle_t}{\partial t} + \nabla_{\mathbf{r}} \cdot \left[\langle \delta \mathbf{u}'^2 \delta \mathbf{u}' \rangle_t + \langle \delta \mathbf{u}'^2 \rangle_t \delta \bar{\mathbf{U}} \right] + \nabla_{\mathbf{X}} \cdot \left[\langle \delta \mathbf{u}'^2 \mathbf{u}'_m \rangle_t + \langle \delta \mathbf{u}'^2 \rangle_t \bar{\mathbf{U}}_m \right] \\ &= 2\nu \nabla_{\mathbf{r}} \cdot \left[\nabla_{\mathbf{r}} \langle \delta \mathbf{u}'^2 \rangle_t \right] + 2\nabla_{\mathbf{X}} \cdot \left[-\frac{\langle \delta p^{*'} \delta \mathbf{u}' \rangle_t}{\rho} + \frac{\nu}{4} \nabla_{\mathbf{X}} \left(\langle \delta \mathbf{u}'^2 \rangle_t - 8p^{*'} \right) \right] \quad (4.45) \\ &+ 2\langle \delta \mathbf{f}'_S \cdot \delta \mathbf{u}' \rangle_t - \langle \delta \mathbf{u}' \otimes \delta \mathbf{u}' \rangle_t : \nabla_{\mathbf{r}} \delta \bar{\mathbf{U}} - \langle \delta \mathbf{u}' \otimes \mathbf{u}'_m \rangle_t : \nabla_{\mathbf{X}} \delta \bar{\mathbf{U}} - 4\langle \epsilon'_m \rangle_t. \end{aligned}$$

Equation (4.45) is quite complex, as it features *all* the terms contributing to the dynamics of turbulence in scale space. As a matter of fact, neither homogeneity, nor isotropy have been assumed yet. The only underlying assumption enabling us to write (4.45) from (4.43) and (4.44) is that of ergodicity, meaning that at all the quantities measured at mid-point \mathbf{X} , and at a given time t are in fact one realization of the random variables associated to these quantities. Let us now simplify (4.45) a little bit. First of all, we invoke statistical steadiness, which allows us to drop the time derivative. Second of all, we restrict ourselves to scales much greater than the viscous dissipation range. To get an idea, the Reynolds number based on the injection scale lays typically in the range $Re_\ell \sim [3000 - 10000]$. Owing to (4.6), the viscous dissipating scales should thus roughly be of the order $\eta \sim [15 - 37]\mu\text{m}$. As such, the terms involving diffusion of kinetic energy by viscous friction whether in scale or physical space may also be dropped. Finally, we are left with the long standing problem of pressure velocity correlations, which result from the non local feedback of the pressure field on the flow. Although it is null in perfectly homogeneous and isotropic turbulence, the pressure field is still capable of inducing long range interactions through the propagation of sound waves in the general case (see for instance Okamoto *et al.* (2010) for a more thorough discussion of this matter in the context of decaying MHD turbulence). We choose not to venture further on this subject, but nonetheless keep this term in the equations to stay cautious when interpreting our results over large separations. In the end (4.45) simplifies to

$$\begin{aligned} & \nabla_{\mathbf{r}} \cdot \left[\langle \delta \mathbf{u}'^2 \delta \mathbf{u}' \rangle_t + \langle \delta \mathbf{u}'^2 \rangle_t \delta \bar{\mathbf{U}} \right] + \nabla_{\mathbf{X}} \cdot \left[\langle \delta \mathbf{u}'^2 \mathbf{u}'_m \rangle_t + \langle \delta \mathbf{u}'^2 \rangle_t \bar{\mathbf{U}}_m \right] \\ &= -\langle \delta \mathbf{u}' \otimes \delta \mathbf{u}' \rangle_t : \nabla_{\mathbf{r}} \delta \bar{\mathbf{U}} - \langle \delta \mathbf{u}' \otimes \mathbf{u}'_m \rangle_t : \nabla_{\mathbf{X}} \delta \bar{\mathbf{U}} - \frac{2}{\rho} \nabla_{\mathbf{X}} \cdot \langle \delta p^{*'} \delta \mathbf{u}' \rangle_t \quad (4.46) \\ &+ 2\langle \delta \mathbf{f}'_S \cdot \delta \mathbf{u}' \rangle_t - 4\langle \epsilon'_m \rangle_t. \end{aligned}$$

Let us now perform a spatial average. As noted before, (4.46) is still dependent on the point of reference \mathbf{X} . We define the spatial average $\langle \cdot \rangle_{\mathbf{X}}$ as

$$\langle \cdot \rangle_{\mathbf{X}} = \frac{1}{V} \int_V \cdot d^3 \mathbf{X}, \quad (4.47)$$

where V is the control volume (i.e. the experiment's container). It can be seen that the averaging operator $\langle \cdot \rangle_{\mathbf{X}}$ commutes with differentiation in scale space. However, it turns

the divergence operator in physical space into a surface integral over the boundaries of the control volume. In the end,

$$\begin{aligned}
 & \nabla_{\mathbf{r}} \cdot \left[\langle \delta \mathbf{u}'^2 \delta \mathbf{u}' \rangle_{t,\mathbf{X}} + \left\langle \langle \delta \mathbf{u}'^2 \rangle_t \delta \bar{\mathbf{U}} \right\rangle_{\mathbf{X}} \right] + \frac{1}{V} \oint_{\partial V} \left[\langle \delta \mathbf{u}'^2 \mathbf{u}'_m \rangle_t + \langle \delta \mathbf{u}'^2 \rangle_t \bar{\mathbf{U}}_m \right] d^2 \mathbf{X} \\
 &= - \left\langle \langle \delta \mathbf{u}' \otimes \delta \mathbf{u}' \rangle_t : \nabla_{\mathbf{r}} \delta \bar{\mathbf{U}} \right\rangle_{\mathbf{X}} - \left\langle \langle \delta \mathbf{u}' \otimes \mathbf{u}'_m \rangle_t : \nabla_{\mathbf{X}} \delta \bar{\mathbf{U}} \right\rangle_{\mathbf{X}} - \frac{2}{\rho V} \oint_{\partial V} \langle \delta p^{*'} \delta \mathbf{u}' \rangle_t d^2 \mathbf{X} \quad (4.48) \\
 &\quad + 2 \langle \delta \mathbf{f}'_S \cdot \delta \mathbf{u}' \rangle_{t,\mathbf{X}} - 4 \langle \epsilon'_m \rangle_{t,\mathbf{X}}.
 \end{aligned}$$

Equation (4.48) is the governing equation for the mean turbulent kinetic energy in scale space. In particular, based on what we have already seen in section 4.2.3, the inertial terms (on the left hand side of (4.48)) can be interpreted as transfers of turbulent kinetic energy in scale and physical space (denoted by $\nabla_{\mathbf{r}} \cdot$ and $\nabla_{\mathbf{X}} \cdot$ respectively). As such, turbulent kinetic energy is shifted from eddies to eddies in scale space, as well as from point to point in physical space. Mean turbulent kinetic energy may be produced from gradients of the mean flow (first two terms on the right hand side of (4.48)). These two gradient terms are in effect very likely to be the energy sources which sustain the flow in a statistically steady state, the boundary conditions in fact transpiring through $\delta \bar{\mathbf{U}}$. Finally, viscous dissipation acts as a sink of kinetic energy through the term $4 \langle \epsilon'_m \rangle_{t,\mathbf{X}}$, while the Lorentz force may act as a source or sink of turbulent kinetic energy (depending on the sign of $\langle \delta \mathbf{f}'_S \cdot \delta \mathbf{u}' \rangle_{t,\mathbf{X}}$). From (4.48) alone, it is unclear how the Lorentz force actually contributes to the dynamics, although from what we have seen until now, it is very likely to dissipate turbulent kinetic energy. The explicit derivation of this term in scale space is delayed to section 5.4.

4.3.3 Evaluation of mean turbulent kinetic energy density

Despite the second order structure function providing useful information on the spatial distribution of kinetic energy in scale space, it lacks one crucial feature: interpretation in terms of scale energy density. Indeed, $\langle \delta \mathbf{u}'^2 \rangle$ represents at best the cumulative energy density found at all scales of size $\|\mathbf{r}\|$ and smaller. Even then, the second order structure function must still be interpreted with a lot of caution, as it entangles information on the energy of small scales with information on the enstrophy at large scales (Davidson & Krogstad, 2008).

One approach to measure the mean turbulent kinetic energy density could be to step into Fourier space and calculate the full 3D energy spectrum. There are however some issues, which makes this approach hazardous, especially in an experimental context. The first limitation of course comes from the fact that computing the full 3D energy spectrum (i.e. the only function in Fourier space which can possibly be interpreted in terms of energy density) requires measuring the velocity correlation function among all three directions of space. Such an amount of data is unfortunately far from being accessible in our experiment, although things might be improved to some extent by invoking symmetry and scaling arguments.

In addition, computing the energy spectrum from a discrete and finite signal is subject to Shannon's sampling theorem. Should it not be satisfied, a quantitative reading of the latter (either in terms of scale or energy density) becomes questionable as a result of aliasing. This is an important concern in our experiment, as the spatial sampling is imposed by the spacing between adjacent potential probes. We therefore have no means of enforcing Shannon's sampling theorem spatially, as the data is in fact sampled in time by the acquisition system. The question then becomes, how can we know for certain that we are not missing the contribution of turbulent structures smaller than twice the distance between adjacent potential probes (which is 5 mm)? This question is especially pertinent for the small injection case ($l_i = 5$ mm), where the injection scale steers barely clear of Shannon's sampling threshold. Last but not least, analyzing turbulence by stepping into Fourier space also poses questions of a somewhat philosophical nature. Indeed, although a wave of wavelength k is perhaps best associated to a turbulent eddy of size $l = \pi/k$ (Davidson, 2015), the association between the two is far from being trivial. In particular, a doubt always subsists about the exact correspondence between wave-number and eddy size, which prevents a reliable, quantitative reading in terms of lengthscale.

Another approach might then to stick to scale space. Some studies (Davidson & Pearson, 2005), (Hamba, 2015) went down that road by introducing real space substitutes to the Fourier energy spectrum. In particular, we propose to focus here on the 2D extension of the signature function proposed by the former author. In 2D homogeneous and isotropic turbulence, the signature function $V(r)$ is defined as (Davidson, 2015)

$$V(r) = -\frac{r^2}{4} \frac{\partial}{\partial r} \frac{1}{r} \frac{\partial \langle \delta u'_l{}^2 \rangle_{t,x}}{\partial r}, \quad (4.49)$$

where $\delta u'_l = u'_r(\mathbf{x} + r \mathbf{e}_r) - u'_r(\mathbf{x})$ is the longitudinal velocity increment. By construction $V(r)$ is defined such that it satisfies the following three properties:

- (i) $\int_0^r V(r) dr \geq 0$, that is to say, $V(r)$ is positive at small scale, which lie in the inertial range. As a matter of fact, the stronger property $V(r) \geq 0$ turns out to hold anytime the longitudinal correlation function $\langle u_r(\mathbf{x}) u_r(\mathbf{x} + r \mathbf{e}_r) \rangle$ decays monotonically with r .
- (ii) $\int_0^\infty V(r) dr = \langle \mathbf{u}'^2 \rangle_{t,x}/2$, in other words $V(r)$ integrates over all scales to give the mean turbulent kinetic energy.
- (iii) The signature function associated to a flow composed of randomly distributed circular eddies of size l_0 sharply peaks at $r = \sqrt{2} l_0$.

All these properties make the signature function physically sound to indeed interpret $V(r)$ as a kinetic energy density. As a result, the turbulent kinetic energy held in eddies of size l_0 is given by

$$\frac{u'^2(l_0)}{2} = V(l_0) l_0. \quad (4.50)$$

4. TURBULENCE

We intend to compute $V(r)$ along the top and bottom walls. Doing so is believed to yield a relatively good picture of the scale distribution of kinetic energy across the horizontal turbulent structures, which are expected to be the most energetic as they are the least impacted by the Lorentz force. As we will see, the flow along the horizontal walls is, to a good degree, homogeneous and isotropic (in the 2D sense), thereby justifying the method.

Chapter 5

Partly 2D/partly 3D MHD turbulence in a bounded domain

This final chapter is dedicated to presenting and discussing our experimental results, which have been gathered using the Flowcube. We will start our discussion by characterizing some global features of the turbulence driven in our experiment in real space, before conducting a scale by scale analysis. From now on, the intensity of the magnetic field will be assessed by the Hartmann number

$$Ha = B_0 h \sqrt{\frac{\sigma}{\rho\nu}}, \quad (5.1)$$

where $h = 0.1\text{ m}$ is the height of the channel. In addition, the electric forcing will be characterized by the Reynolds number

$$Re^0 = \frac{\Gamma}{\nu}, \quad \text{where} \quad \Gamma = \frac{i_e}{2\pi\nu\sqrt{\sigma\rho\nu}} \quad (5.2)$$

measures the circulation induced right above a single injection electrode through which runs the current i_e (cf. for instance relationship (1.73) derived for a single electrically driven quasi-2D vortex). Equation (5.2) is readily linked to the total electric forcing I_0 by recalling that $i_e = 2I_0/N_e$, where N_e is the total number of connected electrodes. As a matter of fact, (5.2) summarizes that for a given magnetic field, the flow is all the more intense, as the total amount of electric current injected is high.

5.1 Global features of Flowcube's turbulence

5.1.1 Topology of the mean flow and turbulent fluctuations

Figure 5.1 and 5.2 display iso-contours of electric potential measured in the high probe density area located at the center of both top and bottom Hartmann plates. The area covered

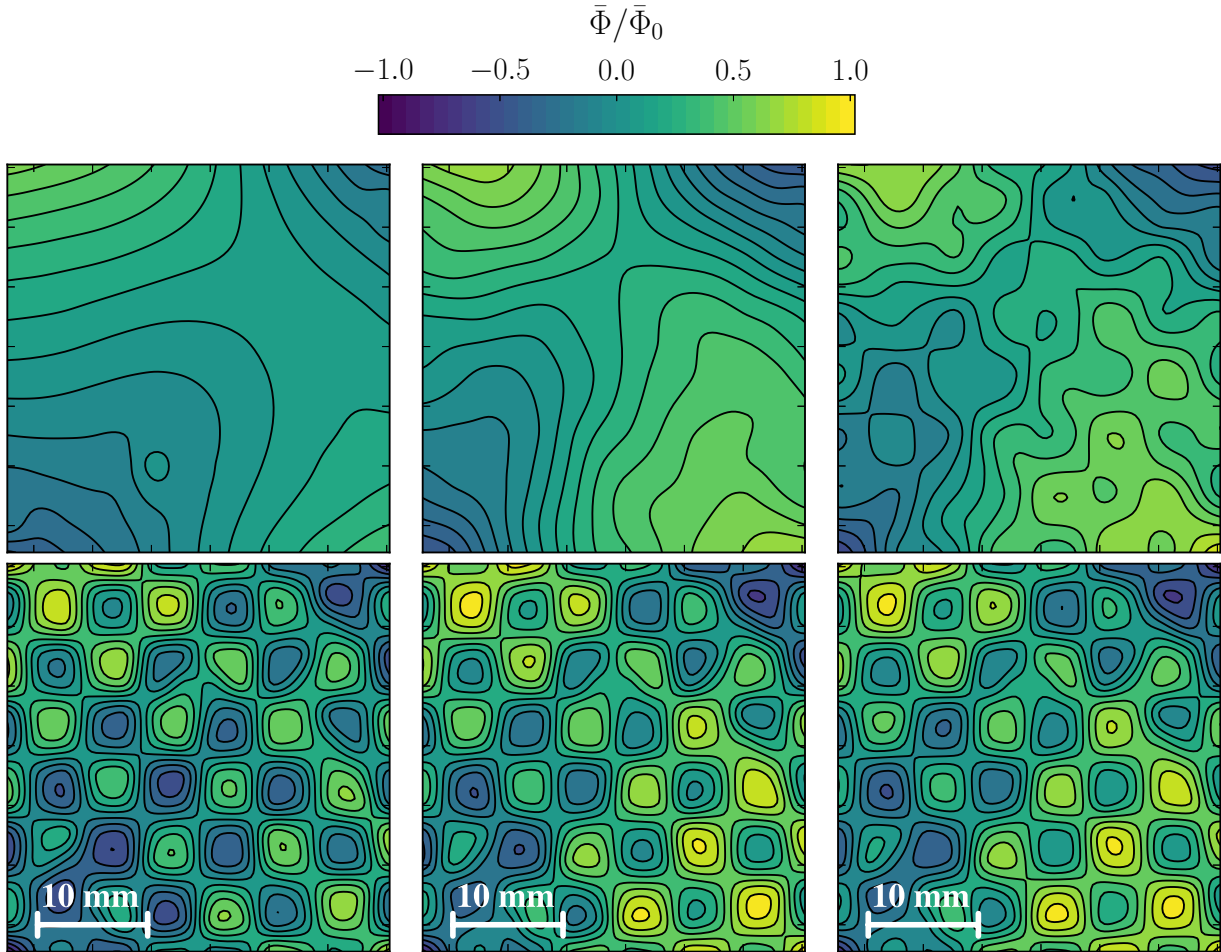


Figure 5.1. Iso-contours of the normalized mean electric potential. Top: electric potential along the top wall $\bar{\Phi}_{\text{top}}/\bar{\Phi}_0$. Bottom: electric potential along the bottom wall $\bar{\Phi}_{\text{bot}}/\bar{\Phi}_0$. The local mean electric potential $\bar{\Phi}(\mathbf{x}) = \langle \phi(\mathbf{x}, t) \rangle_t$ was computed by averaging the signal measured at each individual probe over time. The reference potential $\bar{\Phi}_0 = \max(|\bar{\Phi}_{\text{bot}}|)$ is computed for each set of operating conditions. Operating conditions displayed here consist of the 10×10 injection array ($N_e = 100$) with the injection scale $l_i = 5$ mm, and $Re^0 = 4800$ ($I_0 = 56$ A). From left to right: $Ha = 3600, 18000$ and 36000 ($B_0 = 1, 5$ and 10 T respectively).

by these probes is 32.5×32.5 mm 2 , as highlighted in figure 5.3.right. The experimental configuration showcased in both figures is the same, and consists of a flow forced by the array of 10×10 injection electrodes separated by $l_i = 5$ mm (cf. figure 3.8.left). In figures 5.1 and 5.2, the electric forcing was kept constant at $Re^0 = 4800$ ($I_0 = 56$ A and $N_e = 100$). This relatively modest forcing (by Flowcube's standards) was chosen to first highlight the two-dimensionalization of the flow by the Lorentz force. In particular, the aspect of the flow

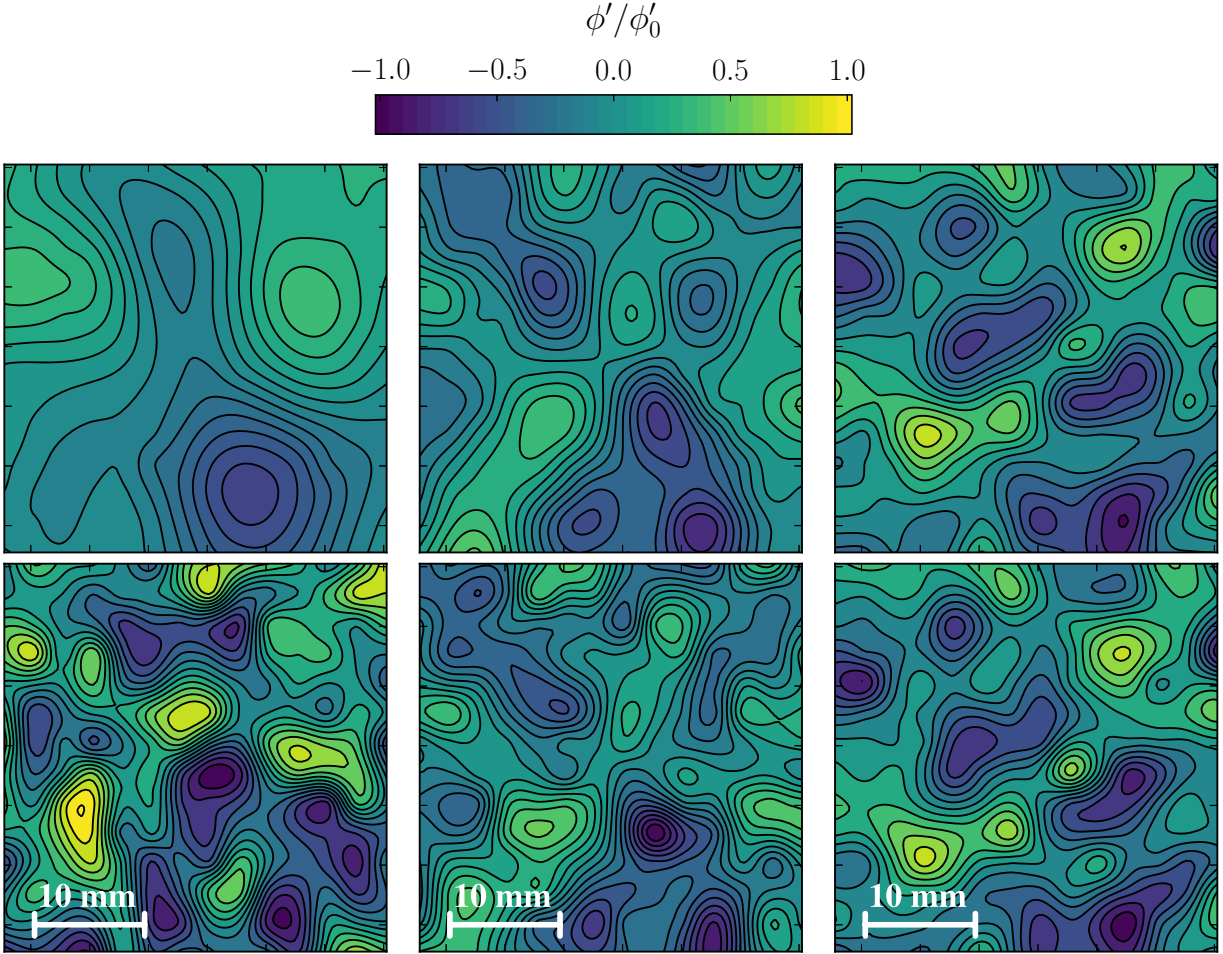


Figure 5.2. Iso-contour snapshots of the normalized fluctuations of electric potential $\phi'(\mathbf{x}, t) = \phi(\mathbf{x}, t) - \bar{\Phi}(\mathbf{x})$. Top: electric potential along the top plate ϕ'_top/ϕ'_0 . Bottom: electric potential along the bottom plate ϕ'_bot/ϕ'_0 , with $\phi'_0 = \max(|\phi'_\text{bot}|)$. Operating conditions consist of the 10×10 injection array ($N_e = 100$) with the injection scale $l_i = 5$ mm, and $Re^0 = 4800$ ($I_0 = 56$ A). From left to right: $Ha = 3600, 18000$ and 36000 ($B_0 = 1, 5$ and 10 T respectively).

is given for varying magnetic fields given by $Ha = 3600, 18000$ and 36000 ($B_0 = 1, 5$ and 10 T respectively).

Figure 5.1 shows the iso-contours of mean electric potential $\bar{\Phi}(\mathbf{x}) = \langle \phi(\mathbf{x}, t) \rangle_t$. $\bar{\Phi}_\text{top}$ refers to the mean electric potential along the top wall (upper part of the figure), while $\bar{\Phi}_\text{bot}$ refers to the mean electric potential along the bottom wall (lower part of the figure). Both top and bottom signals are normalized by $\bar{\Phi}_0 = \max(|\bar{\Phi}_\text{bot}|)$ for each set-point respectively. Owing to equation (1.68), the iso-contours of mean electric potential may directly be interpreted in terms of streamlines of the mean flow. According to the lower part of figure 5.1, the topology

of the mean flow along the bottom wall (i.e. where the forcing takes place) is insensitive to the magnetic field, and consists of counter rotating vortices each centered on one injection electrode. In other words, the mean flow at this location is dominated by the topology of the forcing. As far as the mean flow along the top wall is concerned, the shape of the streamlines depends drastically on the value of the magnetic field. In particular, for a given electric forcing, increasing B_0 makes smaller and smaller structures become visible at the top of the experiment. This observation may be understood in the light of Sommeria & Moreau (1982)'s interpretation of the solenoidal component of the Lorentz force as a pseudo-diffusive process characterized by the diffusivity $\alpha \sim \sigma B_0^2 l_\perp^2 / \rho$. In the latter expression, l_\perp is the width of the structure at hand. This argument shows that for a given magnetic field, the Lorentz force will diffuse the momentum of larger structures quicker than smaller ones. This argument may also be seen the other way around: for a given electric forcing, increasing the magnetic field enables the Lorentz force to diffuse the momentum of smaller and smaller scales.

Figure 5.2 shows snapshots of electric potential fluctuations $\phi'(\mathbf{x}, t) = \phi(\mathbf{x}, t) - \bar{\Phi}(\mathbf{x})$ synchronously measured along the top and bottoms walls. ϕ'_{top} refers to turbulent fluctuations of electric potential along the top wall (upper part of the figure), while ϕ'_{bot} refers to turbulent fluctuations of electric potential along the bottom wall (lower part of the figure). Both top and bottom signals are normalized by $\phi'_0 = \max(|\phi'_{\text{bot}}|)$ for each set-point respectively. The contours presented in figure 5.2 may be seen as instantaneous pictures of the turbulent fluctuations generated in the experiment. Similarly to the mean flow studied earlier, small turbulent structures unsurprisingly become more and more 2D, as the magnetic field is increased. This behavior is evidenced qualitatively by noticing that the top and bottom signals become increasingly mirror symmetrical at high magnetic fields. Interestingly, the two-dimensionalizing effect of the Lorentz force for a given set of parameters seems to act differently on the base flow and the turbulent fluctuations. In particular, for $Ha = 36000$ and $Re^0 = 4800$ (which are the most favorable settings to observe quasi-2D structures when $l_i = 5 \text{ mm}$), the turbulent fluctuations present a higher degree of top/bottom similarity than the mean flow. In other words, the dimensionality of turbulence is not exactly parented to the dimensionality of the base flow. This observation is consistent with the findings of Pothérat & Klein (2014), who concluded that it was in fact possible to generate quasi-2D fluctuations out of 3D mean flows.

5.1.2 Turbulence homogeneity

Given the previous observations, it seems worthwhile to quantify the homogeneity and isotropy level of the turbulence driven in our experiment. This question is all the more legitimate, as there are two apparent sources of inhomogeneity and anisotropy. On the one hand, the forcing mechanism, which consists of a square array of vortices obviously lacks rotational symmetry. It is thus unclear a priori how this Cartesian periodic array of injection electrodes may affect the statistics of turbulent fluctuations. On the other hand,

the magnitude of the velocity gradients in the bulk directly depends on the intensity of the magnetic field, and is expected to be all the stronger, as the flow is 3D.

Let us start by investigating homogeneity. Throughout this thesis, the latter is understood as insensitivity of the turbulent statistics to random translations of the point of reference. Having said that, one can intuitively predict that the behavior of the statistics are likely to differ, whether this point of reference is moved in a direction perpendicular or parallel to the magnetic field. Figure 5.3.left is a scatter plot of the level of horizontal inhomogeneity defined as the relative standard deviation of the perpendicular turbulent kinetic energy

$$\gamma = \frac{\sqrt{\langle [E_{\perp}(\mathbf{x}) - \bar{E}_{\perp}]^2 \rangle_{\mathbf{x}_{\perp}}}}{\bar{E}_{\perp}}, \quad (5.3)$$

where $E_{\perp}(\mathbf{x}) = \langle \mathbf{u}'^2(\mathbf{x}, t) \rangle_t$ is the local perpendicular turbulent kinetic energy (time averaged), and $\bar{E}_{\perp} = \langle E_{\perp}(\mathbf{x}) \rangle_{\mathbf{x}_{\perp}}$ is the total perpendicular turbulent kinetic energy (time and spatially averaged in a horizontal plane). The domains used for spatial averaging are the same central patches of probes along the top and bottom plates as earlier (highlighted in red in figure 5.3.right). Figure 5.3 shows the inhomogeneity levels of all the experimental runs conducted, regardless of the injection pattern used, the magnitude of the magnetic field applied or the intensity of the electric forcing imposed. The results are quite consistent and seem to rely weakly on the actual value of the operating conditions (provided these settings

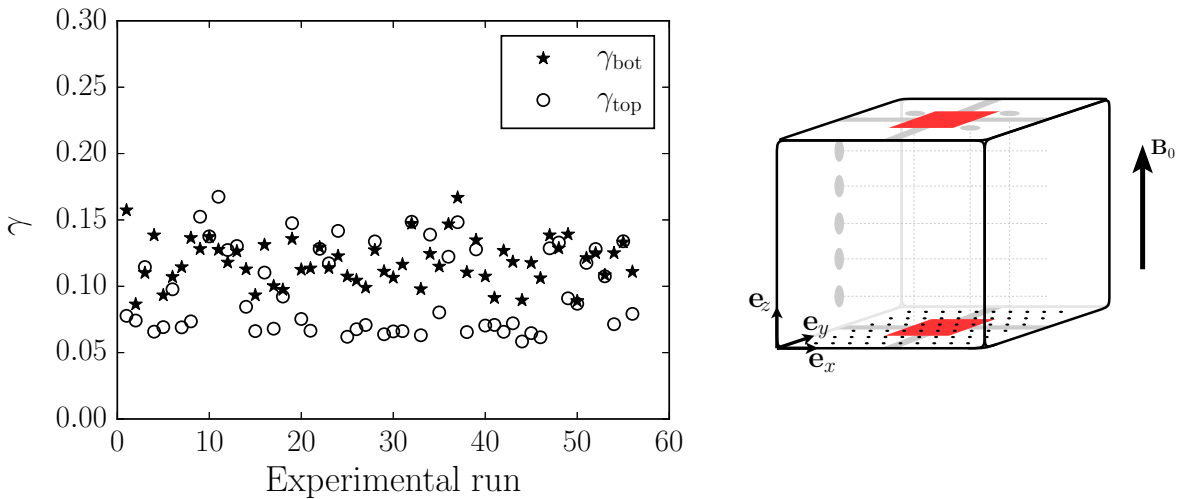


Figure 5.3. Left: horizontal homogeneity level γ computed from electric potential measurements along the top and bottom Hartmann walls. Each symbol represents a given set of operating parameters (l_i , Re^0 , Ha). On average, spatial inhomogeneities are of 10% near the top of the experiment, and 12% near the bottom. Right: the potential probes used to compute γ cover a $32.5 \times 32.5 \text{ mm}^2$ area located at the center of each Hartmann plate (highlighted in red).

allow for a sufficient level of turbulence to be generated). The level of inhomogeneity is relatively low, with an average over all experimental runs of 10% along the top plate, and 12% along the bottom one. The slightly worse level of homogeneity along the bottom wall most likely results from remaining traces of the inhomogeneous forcing at that location.

Comparing the top and bottom electric potential signals of figure 5.2 clearly indicates that the flow is unlikely to be homogeneous in the direction of the magnetic field. The exception to this statement of course, being when the flow is quasi-2D, that is to say when all horizontal planes are fully correlated to each other. Homogeneity (or lack thereof) in the direction of the magnetic field is best showcased by studying vertical profiles. Figure 5.4.left displays vertical profiles of vertical kinetic energy $E_{\parallel}(z) = \langle u_{\parallel}^2(z, t) \rangle_t$, normalized by the mean vertical kinetic energy averaged over the entire height of the experiment $\bar{E}_{\parallel} = \langle E_{\parallel}(z) \rangle_z$. These vertical profiles were acquired using a vertical ultrasound probe (figure 5.4.right). The argument is illustrated here by focusing on flows driven by the 8×8 injection pattern ($N_e = 64$), with a spacing between injection electrodes $l_i = 15$ mm (cf. figure 3.8.right). The intensity of the electric forcing is fixed to $Re^0 = 32000$, which corresponds to the strongest forcing available in Flowcube. The imposed magnetic field is set between $Ha = 900$ and 15000 ($B_0 = 0.25$ and 4 T, respectively). For low magnetic fields (i.e. for 3D turbulent flows), the profile of vertical kinetic energy is highly asymmetric and vertical kinetic energy is concentrated in the bottom portion of the experiment. From figure 5.4.left, it is evident that in such cases, the spatial

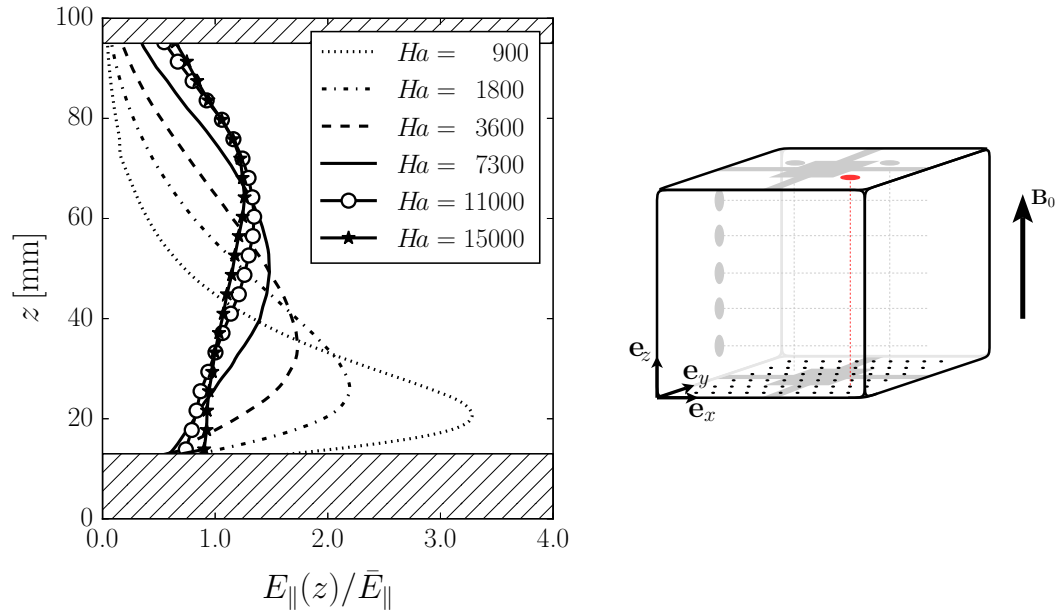


Figure 5.4. Left: vertical profile of vertical turbulent kinetic energy. Forcing conditions are the 8×8 injection pattern with $l_i = 15$ mm and $Re^0 = 32000$. Hatched areas along the top and bottom walls refer to blind zones for which ultrasound readings are unavailable due to strong echoes. Right: ultrasound probe used to measure these profiles (highlighted in red).

distribution of vertical kinetic energy highly depends on the height where it is evaluated at. As the magnetic field is increased however, the Lorentz force smooths out velocity gradients in the bulk, hence flattening out the profile of vertical kinetic energy. Ultimately, the vertical distribution of vertical kinetic energy tends to be more evenly distributed throughout the channel, thus more homogeneous.

To summarize, the turbulence driven in Flowcube is homogeneous to a good level in planes perpendicular to the magnetic field. From the results presented here, the flow is generally inhomogeneous in the direction of the magnetic field, except perhaps in the quasi-2D limit where all horizontal planes are correlated to each other.

5.1.3 Turbulence isotropy

In the general case of 3D turbulence, isotropy is understood as insensitivity of the turbulence statistics to rotations in any random direction. In the continuity of our previous discussion on homogeneity, observing isotropy in the full 3D sense is very unlikely. Looking for isotropy in the 2D sense (i.e. insensitivity of the statistics to random rotations contained within horizontal planes) seems however more reasonable. This property is tested in figure 5.6, which shows the total correlation function associated to the fluctuations of perpendicular velocity $R_{\perp} = \langle \mathbf{u}'_{\perp}(\mathbf{x}) \cdot \mathbf{u}'_{\perp}(\mathbf{x} + \mathbf{r}) \rangle_t$. This correlation function was evaluated in four distinct directions along the top and bottom walls. More specifically, we considered $\mathbf{r} = \rho \mathbf{e}_{\rho}$, where the angle $\theta = (\mathbf{e}_x, \mathbf{e}_{\rho})$ was respectively given by $\theta = 0^\circ, 45^\circ, 90^\circ$ and 135° (cf. figure 5.5). In this section, we focus on the results stemming from the 8×8 injection pattern with the $l_i = 15$ mm injection scale. The electric forcing is the same for all cases presented here and is set to $Re^0 = 32000$.

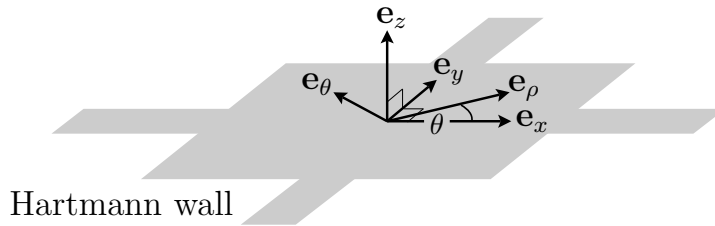


Figure 5.5. Testing rotational symmetry along a Hartmann wall. $\theta = (\mathbf{e}_x, \mathbf{e}_{\rho})$ is the traditionally defined azimuthal angle.

Figure 5.6.left represents the perpendicular correlation function along the bottom wall (i.e. closest to where the forcing takes place) for three different values of the magnetic field: $Ha = 3600, 11000$ and 36000 ($B_0 = 1, 3, 10$ T respectively). For a given magnetic field, figure 5.6.left indicates that R_{\perp}^{bot} is relatively insensitive to θ at small separations. Indeed, data points obtained along different directions reasonably collapse in the range $0 \text{ mm} < \rho < 10 \text{ mm}$. For $\rho > 10 \text{ mm}$ however, data points are more scattered, indicating some level of anisotropy along the bottom wall at large separations. As a matter of fact,

anisotropy appears at separations whose size is of the order, or larger than the injection scale $l_i = 15$ mm. This indicates that the square and Cartesian periodic forcing array does influence the statistics of turbulent fluctuations to some extent, which is hardly surprising.

This behavior contrasts with that of the perpendicular correlation function evaluated along the top wall R_{\perp}^{top} , which is shown in figure 5.6.right. Indeed, at lower magnetic fields ($Ha = 3600$ and 11000 for instance), all the data points evaluated in different directions collapse onto a single curve throughout the range of observable separations. In other words, the velocity fluctuations along the top wall are indeed 2D isotropic. However, the isotropy at large separations slightly degrades as the magnetic field is increased, which most likely results from the forcing scales becoming quasi-2D. Ultimately, the effects of the square forcing patch become apparent along the top wall at high magnetic fields. The influence of the operating conditions on the statistics of turbulence will be analyzed in much greater detail in sections 5.2 and 5.3.

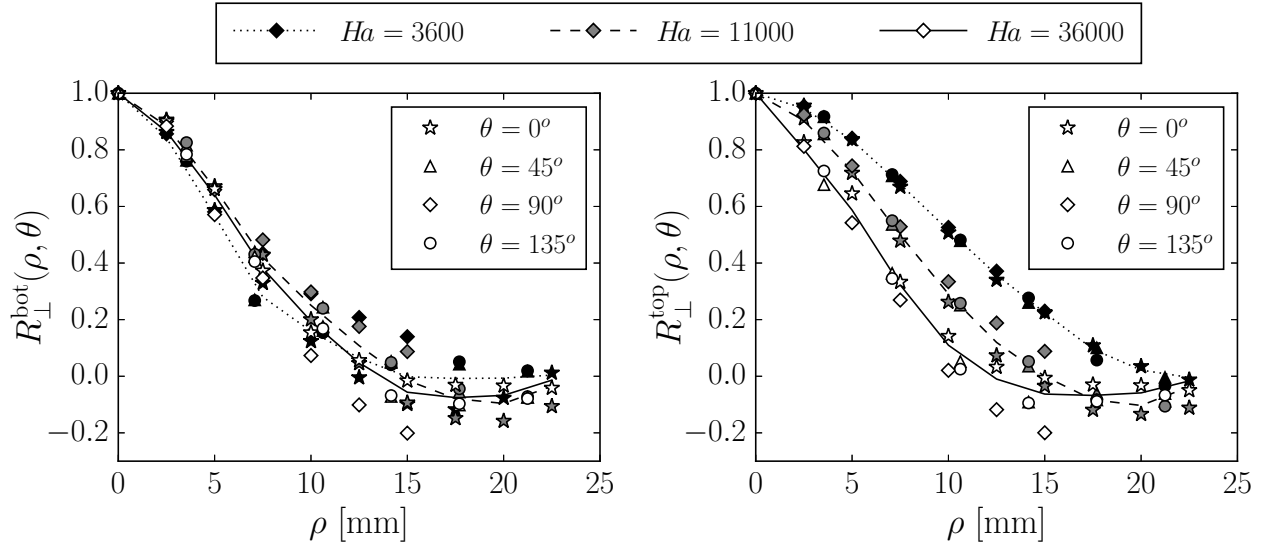


Figure 5.6. Correlation function associated to the perpendicular turbulent velocity $R_{\perp} = \langle \mathbf{u}'_{\perp}(\mathbf{x}) \cdot \mathbf{u}'_{\perp}(\mathbf{x} + \mathbf{r}) \rangle_t$, with $\mathbf{r} = \rho \mathbf{e}_{\rho}$ pointing in four different directions: $\theta = 0^\circ, 45^\circ, 90^\circ$ and 135° respectively. Left: R_{\perp}^{bot} computed from potential probes located along the bottom wall (i.e. closest from the injection area). Right: R_{\perp}^{top} computed from potential probes located along the top wall. Forcing conditions consist of the 8×8 injection pattern, with $l_i = 15$ mm and $Re^0 = 32000$ ($I_0 = 224$ A). Three distinct magnetic fields are represented: $Ha = 3600, 11000$ and 36000 ($B_0 = 1, 3$ and 10 T respectively). Filled symbols indicate the actual values of $R_{\perp}(\rho, \theta)$, while the lines represent $\bar{R}_{\perp}(\rho)$ for each value of the magnetic field.

Although planar isotropy appears to depend on the radial separation ρ , we may still quantify it, as we did in section 5.1.2 through the mean standard deviation

$$\vartheta = \frac{\sqrt{\left\langle [R_{\perp}(\rho, \theta) - \bar{R}_{\perp}(\rho)]^2 \right\rangle_{\theta, \rho}}}{\langle \bar{R}_{\perp}(\rho) \rangle_{\rho}}. \quad (5.4)$$

In the above, $\bar{R}_{\perp}(\rho) = \langle R_{\perp} \rangle_{\theta}$ is the perpendicular correlation function averaged over all directions θ . $\bar{R}_{\perp}(\rho)$ is reported on figure 5.6 by lines of different styles, each corresponding to a given magnetic field. Averaging over all our different experimental cases, we find that the mean anisotropy level along the bottom wall is of the order $\vartheta^{\text{bot}} = 33\%$, while it is $\vartheta^{\text{top}} = 9\%$ along the top wall. It is clear from these results that the forcing does influence the perpendicular statistics, although surprisingly less than what could be anticipated at first given the geometry of the forcing.

These observations, combined with horizontal homogeneity, suggest that describing the turbulence driven in Flowcube through the prism of homogeneous and axisymmetric turbulence is legitimate. As a result, we will now indistinctly refer to directions in the horizontal plane as $\mathbf{e}_{\perp} = \mathbf{e}_{\rho}$, while the direction along the magnetic field will be taken as $\mathbf{e}_{\parallel} = \mathbf{e}_z$. We shall thus adopt the usual cylindrical system of coordinates $(\mathbf{e}_{\perp}, \mathbf{e}_{\theta}, \mathbf{e}_{\parallel})$. Any position vector $\mathbf{r} = r_x \mathbf{e}_x + r_y \mathbf{e}_y + r_z \mathbf{e}_z$ in Cartesian coordinates will thus be preferentially decomposed as $\mathbf{r} = r_{\perp} \mathbf{e}_{\perp} + r_{\parallel} \mathbf{e}_{\parallel}$, with $r_{\perp} = \sqrt{r_x^2 + r_y^2}$ and $r_{\parallel} = r_z$. Owing to axisymmetry, we will assume that the statistics of the turbulent flow are independent of θ . Practically speaking, we will compute these statistics along \mathbf{e}_x (for which measurements span a greater range), and we will assume they are rigorously the same as if they had been computed in any random horizontal direction.

5.1.4 Turbulence intensity

The magnitude of turbulence is customarily measured through the Reynolds number Re based on a typical velocity of the flow, and a large scale imposed by the geometry of the system. In section 3.2.6, we have seen that Re is of the order of 10^4 in our experiments, which indicates that inertia is much more influential than viscous friction, and that we indeed observe turbulence in our setup. The intensity of turbulence may alternately be quantified by the Reynolds number $Re_{\lambda} = u' \lambda / \nu$, where λ is the Taylor microscale (first introduced by Taylor (1935)), and u' is the rms of the velocity fluctuations. In 3D homogeneous and isotropic turbulence, λ is an intermediate scale laying between the Kolmogorov scale and the integral scale. In particular, λ marks the end of the inertial range in the sense that any turbulent structure of size $r < \lambda$ will start experiencing the effects of viscosity (Pope, 2000). In the following, we define the Taylor microscale from measurements in the perpendicular plane according to

$$\lambda = \left[-\frac{1}{2} \frac{\partial^2 \bar{R}_{\perp}(\rho)}{\partial \rho^2} \right]^{-1/2}, \quad (5.5)$$

where $\bar{R}_{\perp}(\rho)$ is the perpendicular correlation function defined earlier. Equation (5.5) shows that λ is in fact a lengthscale purely based on the kinematics of the flow, hence Re_{λ} itself is

a measure of the turbulence which does not explicitly depend on the geometry of the system. As a result, calculating Re_λ appears to be a convenient way of comparing the intensity of various types of turbulence, originating from different systems and geometries.

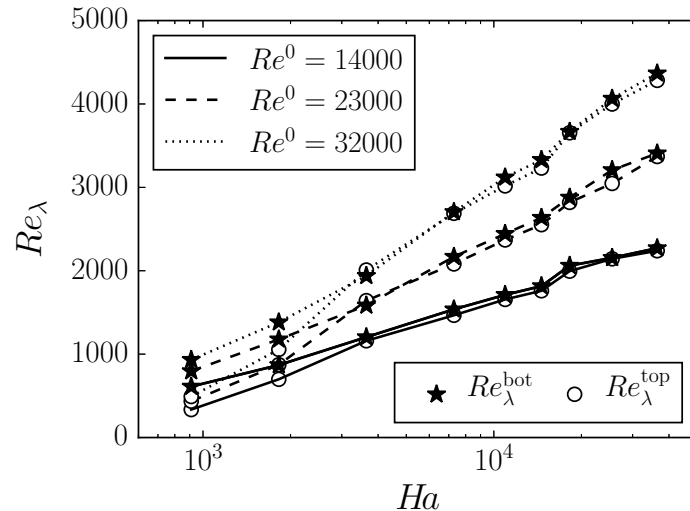


Figure 5.7. Taylor microscale based Reynolds number Re_λ as a function of the Hartmann number Ha . The operating settings consist of the 8×8 injection pattern with the injection scale $l_i = 15$ mm. Lines of different styles refer to three distinct values of the electric forcing: $Re^0 = 14000$, 23000 and 32000 ($I_0 = 96$, 160 and 224 A respectively).

Figure 5.7 shows the values of Re_λ evaluated along the top and bottom walls as a function of the magnetic field: $Ha = 900$ to 36000 ($B_0 = 0.25$ to 10 T respectively). The forcing pattern showcased here is the 8×8 array with the injection scale $l_i = 15$ mm. Three values of the electric forcing are represented: $Re^0 = 14000$, 23000 and 32000 ($I_0 = 96$, 160 and 224 A respectively). From this figure, it appears that the turbulence forced in the direction perpendicular to the magnetic field is substantial, regardless of the operating settings. Indeed, even for the lowest magnetic field and forcing presented here, Re_λ is still of the order of 300, both along the top and bottom walls. To get an idea, Gomes-Fernandes *et al.* (2012) observed Re_λ of the order of 300 in grid turbulence generated in a wind tunnel, while Rousset *et al.* (2014) reported values of Re_λ up to 10000 in their experimental study of the Von-Kármán flow of Helium. From this perspective, the turbulence driven in Flowcube can be expected to be very well developed, regardless of the operating conditions.

5.1.5 Componentality vs. dimensionality

Let us now investigate the relationship between componentality and dimensionality in our experiment. In the spirit of chapter 2, we define the dimensionality of the flow through the magnitude of the velocity gradients in the direction of the magnetic field estimated by the ratio l_z^u/h . Here l_z^u represents the diffusion length associated to a turbulent structure

of width l_\perp and velocity $u'(l_\perp)$. Assuming this structure lies in the inertial range, the main competing processes acting upon it are: On the one hand the diffusion of momentum by the Lorentz force characterized by $\tau_{2D} = (\rho/\sigma B_0^2)(l_z^u/l_\perp)^2$; On the other hand, energy transfers characterized by the eddy turnover time $\tau_u = l_\perp/u'(l_\perp)$. Equating both effects eventually yields

$$\frac{l_z^u}{h} = \sqrt{N} \frac{l_\perp}{h}, \quad (5.6)$$

where $N = \sigma B_0^2 l_\perp / \rho u'(l_\perp)$ is the local interaction parameter (in scale space) based on the width of the structure in question and its velocity. Here, we use the superscript u in l_z^u to stress that the velocity gradients in the bulk result from a competition between the Lorentz force and inertia. By contrast, we considered in chapter 2 that the dimensionality of the bulk resulted from the competition between the Lorentz force and viscous friction, noted as l_z^ν with the superscript ν . The interpretation we gave in chapter 2 for the ratio l_z^ν/h is readily adapted to the ratio l_z^u/h , namely: $l_z^u/h \ll 1$ implies that the turbulent structure in question is topologically 3D, as the Lorentz force is not quick enough to diffuse its momentum all the way to the top wall before the structure yields its energy to the energy cascade process; $l_z^u/h \gg 1$ means that the turbulent structure in question is quasi-2D, as the inertial transfers take place over a much longer time scale than the time required for the Lorentz force to diffuse its momentum all the way to the top wall. A global estimate of l_z^u is computed in our experiment based on the injection scale l_i and the rms of the turbulent fluctuations measured along the bottom plate $u'_{\text{bot}} = \sqrt{\bar{E}_\perp^{\text{bot}}}$, with $\bar{E}_\perp^{\text{bot}} = \langle \mathbf{u}'^2 \rangle_{t, \mathbf{x}_\perp^{\text{bot}}}$. In that respect our experimental assessment of l_z^u/h may be interpreted as the dimensionality of the forcing

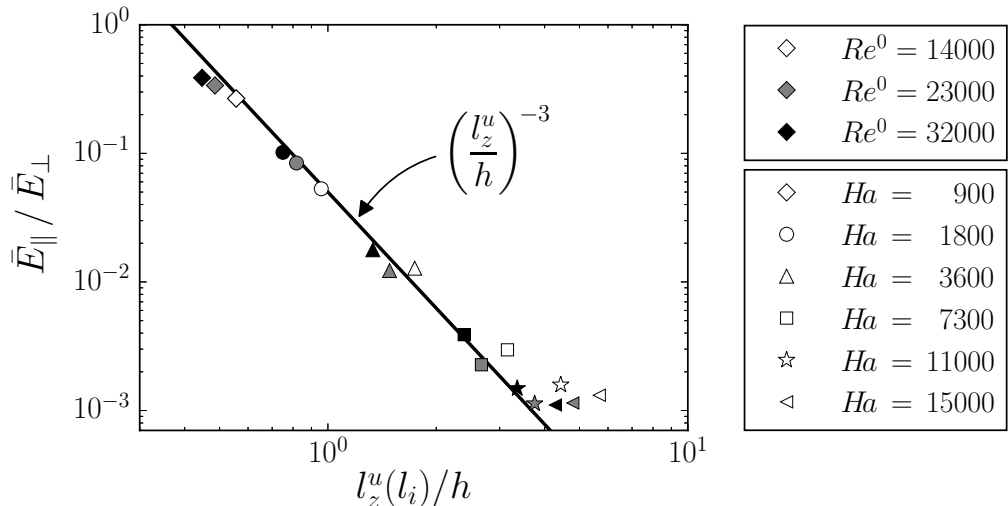


Figure 5.8. Componentality as a function of dimensionality. The ratio of vertical to horizontal kinetic energy is computed for different sets of magnetic fields Ha and electric forcing Re^0 , for the fixed forcing pattern consisting of the 8×8 injection array with the injection scale $l_i = 15$ mm.

scale. We shall therefore note it $l_z^u(l_i)/h$ from now on to keep in mind that this ratio is in fact a parameter based on global properties of the flow.

Figure 5.8 shows the ratio of parallel to perpendicular turbulent kinetic energy computed from ultrasound transducers. In the following, the vertical turbulent kinetic energy \bar{E}_\parallel is defined through a time and spatial average over the beam of a vertical ultrasound transducer $\bar{E}_\parallel = \langle u_z'^2 \rangle_{t,z}/2$. Owing to axisymmetry, the perpendicular turbulent kinetic energy \bar{E}_\perp is assimilated to $\langle u_x'^2 \rangle_{t,x}$, that is to say twice the x -component of the kinetic energy, time and spatially averaged along the beam of the horizontal ultrasound transducer located mid height of the channel (see for instance figure 5.13.right for a sketch of the ultrasound probes in use).

Three-dimensional flows are characterized by values of $l_z^u(l_i)/h$ lower than unity. In particular, one can see from figure 5.8 that for $l_z^u(l_i)/h \simeq 0.4$, the vertical to horizontal energy ratio $\bar{E}_\parallel/\bar{E}_\perp$ is close to 0.5. This result sounds very familiar, and is in fact what would be expected for fully homogeneous and isotropic 3D turbulence. Note however that despite this particular value of $\bar{E}_\parallel/\bar{E}_\perp$, we may not conclude that we are observing 3D homogeneous and isotropic turbulence, since the flow is inhomogeneous in the direction of the magnetic field (cf. our previous discussion backed by figure 5.4). Nevertheless, this shows that when the bulk presents strong velocity gradients in the direction of the field, the vertical and horizontal velocity components are of the same order of magnitude, and we are thus in presence of a three component velocity field. As the bulk becomes more and more two-dimensional (that is to say as $l_z^u(l_i)/h$ extends beyond unity), one can see that the amount of kinetic energy found in the vertical component becomes negligible compared to the horizontal one, and their ratio plummets according to a steep $[l_z^u(l_i)/h]^{-3}$ law. The explanation for such a clear power law is unknown yet. It however suggests that there is indeed a link between dimensionality and componentality in our experiment, since points obtained using different operating conditions collapse onto the same curve. In the light of what we have seen in chapter 2, a plausible explanation for this relationship between dimensionality and componentality could be that a gradual shift between pumping mechanisms occur, as velocity gradients are smoothed out in the bulk. This however needs confirmation.

Note that this behavior is not the sole consequence of the two-dimensionalization of the bulk by the Lorentz force, on the contrary. Recalling Moffatt (1967)'s discussion, he showed that the two-dimensionalization of an unbounded flow by a magnetic field was in fact accompanied by the *promotion* of the vertical velocity component. In our case, one must see here the concurrent influence of the boundary conditions imposed by the impermeable horizontal walls, which forbidden a vertical component in their vicinity (regardless of the dimensionality of the bulk). As a matter of fact, Pothérat & Kornet (2015) showed numerically, within the context of decaying MHD turbulence between Hartmann walls, that the presence of the latter indeed suppressed the velocity component aligned with the magnetic field. Interestingly, the vertical to horizontal ratio seems to level off and saturate around 10^{-3} for the highest values of $l_z^u(l_i)/h$. It is unclear whether this leveling off results from a lack of resolution of the ultrasound transducers, or a concomitant saturation of both the horizontal and vertical kinetic energies towards a constant value.

5.2 Transition between 3D and 2D kinematics

5.2.1 Turbulent kinetic energy density

We may now quantify in greater details the emergence of two-dimensionality, which can be achieved experimentally by comparing the electric potential signals measured along the top and bottom walls. This method was first introduced by Klein & Pothérat (2010) on instantaneous time series for two overhanging potential probes. We propose to take this method one step further by stepping into scale space, and comparing energy densities directly (this is only possible thanks to the Hartmann plates built during this thesis, which feature a high density of potential probes). The rationale is the following: a 2D flow is by definition invariant with respect to the coordinate in the direction of the magnetic field. In such a case, turbulent structures fully extend across the experiment, and the signals measured along the top and bottom walls must be identical. The scale by scale statistics of the flow should therefore also match. Conversely, any departure from a top/bottom mirror symmetry may be interpreted as a sign of three-dimensionality in the bulk. Although quite intuitive, the results stemming from this reasoning must still be interpreted with caution. Indeed, by time and spatially averaging the top and bottom plates independently from each other, we indirectly lose information on the flow occurring in the bulk. Consequently, this method does not rigorously allow to distinguish between genuinely quasi-2D turbulent structures, and those presenting the same level of energy at both their extremities, despite being 3D in the bulk. We will however partially circumvent this limitation in section 5.3.1 by introducing the second order structure function (at the cost however of losing the interpretation of the results in terms of energy density per se).

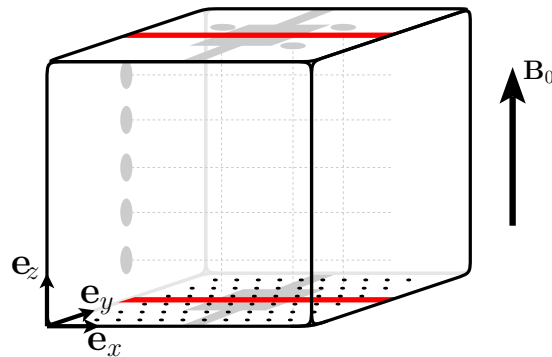


Figure 5.9. Assessing the energy density along strips of potential probes aligned with \mathbf{e}_x , and located on the top and bottom Hartmann plates.

Figure 5.10 gives the distribution of perpendicular turbulent kinetic energy among perpendicular scales, as quantified by the signature function presented in section 4.3.3. In the following, $V_{\text{bot}}(r_\perp)$ and $V_{\text{top}}(r_\perp)$ were computed using two strips of potential probes spanning the whole width of the bottom and top Hartmann plates respectively (sketched in figure 5.9

above). $\bar{E}_\perp^{\text{top}} = \langle \mathbf{u}'_\perp^2 \rangle_{t, \mathbf{x}_\perp^{\text{top}}}$ refers to the time and spatially averaged perpendicular kinetic energy along the top plate. As previously, we restrict ourselves to the case $l_i = 15 \text{ mm}$ and $Re^0 = 32000$ to illustrate our argument, as it is representative of the global behavior found with other operating settings. The derivatives involved in (4.49) were computed from a spline interpolation of the longitudinal velocity increment $\delta u'_l(r_\perp)$.

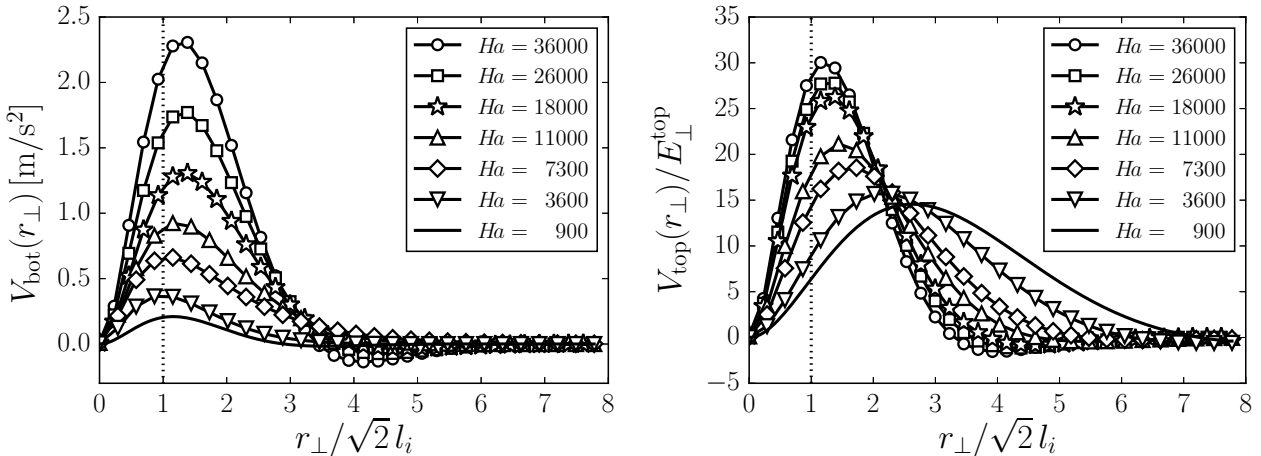


Figure 5.10. Mean turbulent kinetic energy densities as measured by the signature function $V(r_\perp)$. Left: energy density measured along the bottom plate (i.e. where the forcing takes place); Right: energy density measured along the top plate. The dotted line locates the injection scale. Operating settings shown here consist of the 8×8 injection pattern with $l_i = 15 \text{ mm}$ and $Re^0 = 32000$.

Figure 5.10.left yields some first valuable information on the driving mechanism taking place along the bottom Hartmann wall. To begin with, the turbulent kinetic energy injected into the experiment appears to increase with the magnetic field (for a given electric forcing). This argument is of course readily read from the area under each curve of figure 5.10.left, since $V(r_\perp)$ physically represents the density of turbulent kinetic energy. This observation may be understood by recalling that the electromagnetic stirring $\mathbf{j} \times \mathbf{B}_0$ of the turbulence in Flowcube occurs for a large part in the bottom Hartmann layer. As we have seen in section 1.3.2, the thickness of the bottom Hartmann layer δ is inversely proportional to B_0 . As a result, increasing the magnetic field ultimately diminishes the volume of the current sheet forming in the Hartmann layer, thereby increasing the current density of the latter according to $j \sim I_0/(\delta \mathcal{L}_\perp^2)$ (\mathcal{L}_\perp is a typical lengthscale in the direction perpendicular to the field, which is imposed by the geometry). Figure 5.10.left also shows that although the total amount of kinetic energy injected into the bulk depends on the magnitude of the magnetic field, its distribution among scales appears to be roughly the same regardless of the operating conditions. In particular, V_{bot} always peaks around the same value, which is quite close to the injection scale l_i . This observation confirms that most of the energy injected into the flow is in fact located in turbulent structures whose size is given by the distance separating two adjacent injection electrodes.

The overall shape of V_{top} contrasts quite strikingly with that of V_{bot} . The former is represented in figure 5.10.right. The position of the peak and the breadth of the energy distributions along the top wall appear to drastically depend on the operating conditions. To be more specific, weak magnetic fields imply a broad energy spectrum, whose most energetic scale is rather large. As a matter of fact, for $Ha = 900$, the most energetic scale at the top is found to be almost 3 times larger than the injection scale at the bottom. As the magnetic field is increased however, the energy spectrum narrows down and focuses energy into scales around the injection scale. In effect, as the magnetic field increases, V_{top} tends to become the same as V_{bot} both in shape and magnitude (the latter property is not shown here). These observations are in fact elements hinting at the two-dimensionalization of the flow both kinematically and dynamically. Indeed, given an injection scale l_i and an electric forcing Re^0 , applying a strong magnetic field makes the Lorentz force quicker to diffuse smaller and smaller turbulent scales. In that sense, the Lorentz force may be seen as a filtering process, which segregates between kinematically 2D and 3D scales over the height of the box. Consequently, it is only the 2D turbulent structures which can be observed along the top wall. The fact that the peak of the top spectrum tends towards an asymptotic value corresponding to the injection scale, suggests that the smallest scale observable in the experiment is indeed the injection scale, which in turn suggests that kinetic energy preferentially flows upscale following an inverse cascade.

Interestingly, one may think at first that a strong magnetic field would promote large energetic turbulent structures, via the inverse energy cascade. Looking at figure 5.10 however, it appears that the higher Ha , the narrower the range of energy containing scales. This behavior may have two explanations. First, as the strongly inertial injection scales are two-dimensionalized, they become more capable of breaking larger structures through inertial instabilities (Tabeling, 2002). Second, it should not be forgotten that an important energy sink exists for 2D turbulent scales confined between electrically insulating and no-slip walls. From (4.26), we know that the range of scales experiencing Hartmann braking is all the greater, as the magnetic field is high.

5.2.2 Experimental confirmation of the threshold for a kinematically 2D inertial range

Let us now adopt a more systematic approach to the observations made from figure 5.10. First, we recall Sommeria & Moreau (1982)'s argument developed in section 4.1.5, according to which there exists a critical lengthscale given by

$$\frac{l_{\perp}^c}{h} = \left(\frac{\sigma B_0^2 h}{\rho u'_{\perp}} \right)^{-1/3}, \quad (5.7)$$

above which turbulent structures are kinematically quasi-2D and under which they are kinematically 3D. From (5.7), one can see that l_{\perp}^c depends on the magnetic field and the electric forcing via B_0 and u'_{\perp} . This implies that changing the operating conditions in fact enables

us to directly alter the critical lengthscale, thus the overall dimensionality of the turbulence. We intend in this section to verify this assertion by evaluating experimentally the scaling law proposed by Sommeria & Moreau (1982), which governs the emergence of 2D turbulent structures confined between two insulating and no-slip walls. To do so, we first need to define a critical lengthscale and associate a critical velocity to it. In the light of our discussion on energy density, we suggest to experimentally define l_{\perp}^c as the value of r_{\perp} corresponding to the peak of $V_{\text{top}}(r_{\perp})$. This choice is guided by our physical intuition that the peak of energy density along the top plate should reasonably coincide with the smallest 2D scale. Indeed, the Lorentz force segregates between topologically quasi-2D and 3D scales, where the scales visible at the top are necessarily quasi-2D. This view is backed by the observation that the peak of $V_{\text{top}}(r_{\perp})$ is found at lengths which are all the larger, as the bulk is 3D. In addition, the location of the peak tends towards the injection scale in the limit of high magnetic fields, which in our experiment appears to be the smallest turbulent scale containing kinetic energy. Accepting this definition for the critical lengthscale, its corresponding velocity is merely deduced from the value of the top signature function for $r_{\perp} = l_{\perp}^c$ according to $u'_{\perp} = \sqrt{2 l_{\perp}^c V_{\text{top}}(l_{\perp}^c)}$.

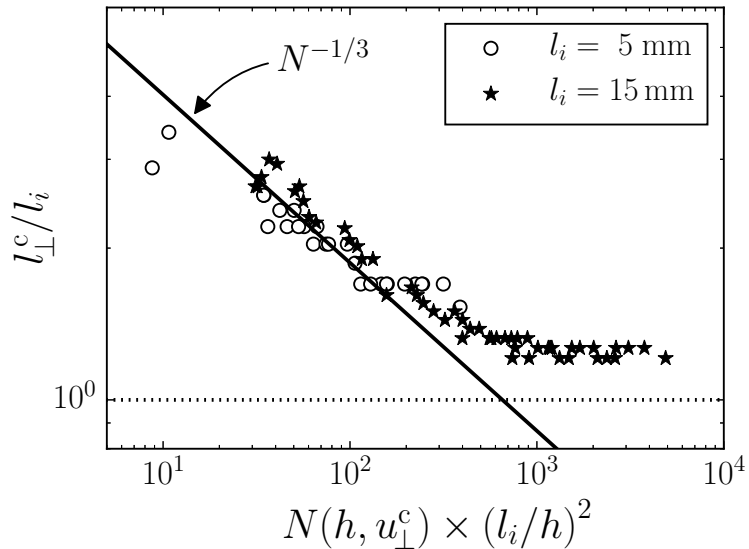


Figure 5.11. Normalized cutoff lengthscale l_{\perp}^c / l_i as a function of the interaction parameter $N(h, u_{\perp}^c)$ based on the height of the channel. The latter is normalized by the square of the aspect ratio of the injection scale l_i/h , in order to account for the geometry of the forcing (the two different injection patterns $l_i = 5$ and 15 mm are displayed). The $N^{-1/3}$ region of the plot confirms that the kinematics of the flow are indeed fixed by the competition between the solenoidal component of the Lorentz force and inertia. The flat region of the plot corresponds to a flow which is kinematically quasi-2D, in the sense that even the smallest existing scale has been two-dimensionalized.

Figure 5.11 shows the overall results obtained from determining l_\perp^c experimentally. Note that we are in fact plotting $l_\perp^c/l_i = (l_\perp^c/h)/(l_i/h)$ as a function of $N(h, u_\perp^c) \times (l_i/h)^2$. Introducing this normalization makes sets of data obtained with different injection scales collapse onto the same curve. The meaning of this collapse is that the dimensionality of the turbulence driven in Flowcube in fact follows a homothetic relationships with respect to the current injection pattern.

The curve presented in figure 5.11 features two different regimes. The first regime corresponds to the range $N \times (l_i/h)^2 < 10^3$, and displays a clear $N^{-1/3}$ power law, which spans a decade and a half. This scaling law agrees with the prediction put forward by Sommeria & Moreau (1982), and confirms that in this range, we are indeed observing an inertial range in which the competing processes are two-dimensionalization by the solenoidal component of the Lorentz force and inertia. In that respect, figure 5.11 is the first direct confirmation of this law, as previous work was only able to characterize a cutoff frequency in time domain (Klein & Pothérat, 2010). The second regime corresponds to the range $N \times (l_i/h)^2 > 10^3$, in which the curve levels off to an asymptotic value close to the injection scale (i.e. $l_\perp^c/l_i \sim 1$). This saturation was in fact already visible in figure 5.10.right, which showed that the smallest energetic structure visible along the top wall tended towards the injection scale, however not falling behind it. In other words, this leveling off corresponds to a state of the turbulence, where even the smallest existing scale has already been two-dimensionalized. That is to say, a state in which the bulk is *fully* quasi-2D. The saturation around the injection scale also suggests that turbulent structures laying beneath it do not receive a relevant amount of kinetic energy, which is an indirect visualization of the inverse energy cascade expected at least in the quasi-2D limit.

5.3 Statistical analysis in scale space

5.3.1 Kinematics

It is now time for us to step into scale space, and start investigating some statistical properties of the turbulent velocity increment $\delta\mathbf{u}'$. The second order structure function $\langle \delta\mathbf{u}'^2 \rangle_{t,\mathbf{x}}$ gives information on the energy distribution among turbulent scales. In particular, the angular integral

$$\mathcal{E}(r) = \int_0^{2\pi} \int_0^\pi \langle \delta\mathbf{u}'^2 \rangle_{t,\mathbf{x}}(r, \theta, \varphi) \sin \theta d\theta d\varphi, \quad (5.8)$$

is related to the cumulative turbulent kinetic energy found at scale of size $r = \|\mathbf{r}\|$ and less (Davidson, 2015). Invoking axisymmetry, $\delta\mathbf{u}'$ may legitimately be decomposed into a component parallel and perpendicular to the magnetic field $\delta\mathbf{u}'_{||}$ and $\delta\mathbf{u}'_\perp$ respectively, where $\delta\mathbf{u}'_{||} = (\delta\mathbf{u}' \cdot \mathbf{e}_z) \mathbf{e}_z$ and $\delta\mathbf{u}'_\perp = \delta\mathbf{u}' - \delta\mathbf{u}'_{||}$. Following sections 4.3.1 and 5.1.5, the second order structure function associated to the perpendicular component of the turbulent velocity increment $\langle \delta\mathbf{u}'_\perp^2 \rangle_{t,\mathbf{x}}$ (the only component experimentally accessible) is expected to

be a relatively good estimate for $\langle \delta \mathbf{u}'^2 \rangle_{t,\mathbf{x}}$, at least when the level of three componentality in the bulk remains low. Figure 5.12.left depicts the second order structure function normalized by $\bar{E}_\perp = \langle \mathbf{u}'_\perp^2(A) + \mathbf{u}'_\perp^2(B) \rangle_{t,\mathbf{x}} / 4$, the mean horizontal turbulent kinetic energy averaged over points A and B.

In this section, the increment vector is physically defined in the experiment as $\mathbf{r} = r_x \mathbf{e}_x + h \mathbf{e}_z$, which is assumed to be representative of $\mathbf{r} = r_\perp \mathbf{e}_\perp + r_\parallel \mathbf{e}_\parallel$ owing to axisymmetry. Practically speaking, \mathbf{r} is built by imposing the base and the tip of the increment vector to be contained within the bottom and top planes respectively, as sketched in figure 5.12.right. By defining \mathbf{r} this way, we allow for a vertical component of \mathbf{r} . Ultimately, this enables us to investigate the dependence of the energy distribution among turbulent scales, with respect to their alignment with the magnetic field. Accessing this information is crucial, since we know the magnetic field has an anisotropic effect on the organization of the turbulence in scale space (recall for instance the discussion of section 4.1.5). The only way for us to introduce a vertical component to the separation vector \mathbf{r} is by correlating the top and bottom walls, whose separation is unfortunately fixed at h . It is therefore impossible for us to actually change the vertical separation between two overhanging potential probes. We however argue that, much like in chapter 2, the second order statistics are likely to scale

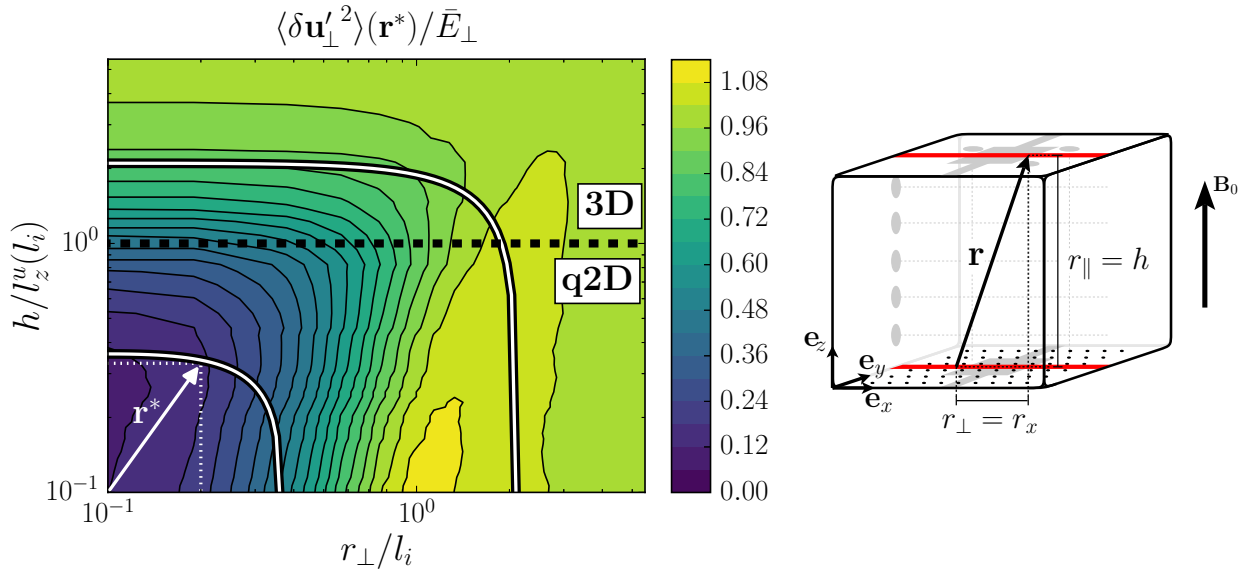


Figure 5.12. Left: iso-contours of the second order structure function $\langle \delta \mathbf{u}'_\perp^2 \rangle$ normalized by \bar{E}_\perp , the mean turbulent kinetic energy averaged over points A and B. \mathbf{r}^* is the reduced vector increment, which describes turbulent scales of different directions in the $(\mathbf{e}_\perp, \mathbf{e}_\parallel)$ plane. The two white paths are circles in logspace, which symbolize turbulent structures of constant reduced size $\|\mathbf{r}^*\| = 0.25$ and 2 respectively. Right: geometrical definition of the increment vector in our experiment, which correlates the signals measured along the bottom and top walls.

with the dimensionality of the forcing scale. As previously, the latter is associated to the dimensionality parameter $l_z^u(l_i)/h$ based on the injection scale l_i and the intensity of the turbulent fluctuations along the bottom plate u'_{bot} . As such, the second order structure function is depicted as a function of the reduced variables $r_{\perp}^* = r_{\perp}/l_i$ and $r_{\parallel}^* = h/l_z^u(l_i)$.

Figure 5.12.left results from the collapse of *all* available data onto the same plot (cf. table 3.1). That is to say, all combinations of injection patterns ($l_i = 5$ and 15 mm), magnetic fields ($Ha = 900$ to 36000) and electric forcing ($Re^0 = 4800$ to 32000) investigated throughout our various experimental campaigns are reported in figure 5.12. This first result is quite remarkable, and shows that only two global lengthscales are required to fully describe (hence predict) the distribution of kinetic energy in the $(\mathbf{e}_{\perp}, \mathbf{e}_{\parallel})$ meridional plane. First of all, the injection scale l_i , which is the distance separating two adjacent injection electrodes is fixed by the geometry. Second of all, the diffusion length $l_z^u(l_i)$ associated to the two-dimensionalization of the turbulence by the Lorentz force. This parameter of course depends on l_i , but is actually adjusted by tuning the magnetic field and the electric forcing. l_i and $l_z^u(l_i)$ are therefore global parameters which are fully imposed by the operating conditions, and may be set independently from each other. In other words, figure 5.12 proves that the integral lengthscales (i.e. the distance over which the flow is correlated) in the direction perpendicular to the field is given by the injection scale, while the integral scale in the direction of the field is given by the diffusion length $l_z^u(l_i)$. This seems reasonable given that the latter represents by definition, the distance over which the Lorentz force is capable of diffusing the momentum of the injection scale. The first strong conclusion stemming from this observation is that the turbulence driven in the Flowcube can in fact be considered homogeneous over the distance $l_z^u(l_i)$ in the direction of the magnetic field.

Figure 5.12.left may be interpreted as a map relating the energy content of a turbulent structure to its alignment with respect to the magnetic field. As a matter of fact, Lamriben *et al.* (2011) and Campagne *et al.* (2014) showed experimentally within the context of rotating turbulence, that turbulence anisotropy clearly transpired in the second order structure function. In particular, they showed that for 3D homogeneous and isotropic turbulence, the second order structure function displayed circular iso-contours in the meridional plane. Conversely, they also found that for 2D homogeneous and axisymmetric turbulence, the second order structure function yielded vertical iso-contours. We propose here to illustrate these effects in the context of MHD turbulence in the light of what we have seen so far. To this end, let us first notice that figure 5.12.left also relates the energy content of a scale to its kinematic dimensionality. Indeed, the transition between kinematically 2D and 3D scales is easily located, and is given by the threshold $h/l_z^u(l_i) = 1$. Note that because of the normalization by $l_z^u(l_i)$, quasi-2D turbulent scales are found in the lower part of the plot (i.e. for $h/l_z^u(l_i) < 1$), while 3D turbulent structures are located in the upper region (i.e. for $h/l_z^u(l_i) > 1$).

Next, two white paths are drawn on figure 5.12.left, which define circles (in logspace) of radius $r^* = 0.25$ and 2 respectively. These paths embody turbulent scales of constant size $\|\mathbf{r}^*\| = cte$ but oriented differently in scale space. Let us start by focusing on the

smaller path, for which $\|\mathbf{r}^*\| = 0.25$. By construction, $\|\mathbf{r}^*\| < 1$, thus all the turbulent scales symbolized by this smaller loop are necessarily quasi-2D (i.e. they always remain below the $h/l_z^u(l_i) = 1$ threshold). Strong anisotropy in the energy distribution is experienced by traveling along this smaller path. In particular, a turbulent scale of size $r^* = 0.25$ aligned with the magnetic field (i.e. for which $r_\perp^* = 0$) possesses virtually no energy, as evidenced by the value of the normalized second order structure function. Yet, a turbulent scale of the same size $r^* = 0.25$, this time laying in the plane perpendicular to the magnetic field possesses much more kinetic energy. Indeed, owing to figure 5.12, the normalized second order structure function associated to such a horizontal scale approximates 0.5. In addition, the iso-contours found in the lower half of the plot are almost vertical, which translates the invariance of the statistics in the direction of the magnetic field. Incidentally, this anisotropy has also been observed by Caperan & Alemany (1985) in the context of MHD grid turbulence, who found that the presence of a magnetic field flattened the 2D energy spectrum in Fourier space along the parallel direction.

The behavior of the statistics drastically changes however, as soon as the $h/l_z^u(l_i) = 1$ threshold is crossed. Let us now focus on the larger loop, for which $\|\mathbf{r}^*\| = 2$. It appears that the energy content of the scales described by this larger loop is much less sensitive to scale orientation with respect to the magnetic field. As a matter of fact, there is a range of perpendicular component $0 < r_\perp^* < 0.5$ for which the iso-contours of the second order structure function are circular, and run parallel to the path $\|\mathbf{r}^*\| = 2$. In other words, the statistics of turbulent structures belonging to the upper part of the plot are similar to those of 3D isotropic structures. Traveling from the vertical to horizontal directions along the path $\|\mathbf{r}^*\| = 2$, we are however bound to cross the 3D/quasi-2D threshold again, therefore reintroducing anisotropy to the statistics of structures laying close enough to the horizontal plane. This behavior is inherent to the existence of a magnetic field, hence of Lorentz forces. As a result, no matter how 3D the injection scale is, there always exists a large enough turbulent structure, which will be successfully two-dimensionalized by the Lorentz force. Unless of course the size of this particular horizontal structure extends beyond the lateral size of the experiment, or this structure is effectively dissipated by Hartmann friction.

5.3.2 Energy transfers

We are now in a position to unravel the energy transfers taking place in our experiment, and study the actual direction of the energy cascade. According to equation (4.48), the scale-wise fluxes of turbulent kinetic energy (i.e. what is referred to as the energy cascade) is buried within the term

$$\Pi(\mathbf{r}) = \nabla_{\mathbf{r}} \cdot \langle \delta \mathbf{u}'^2 \delta \mathbf{u}' \rangle_{t,\mathbf{x}}, \quad (5.9)$$

where $\langle \delta \mathbf{u}'^2 \delta \mathbf{u}' \rangle_{t,\mathbf{x}}$ is the third order structure function, which is a vector quantity. Similarly to the second order structure function, the angular integral of (5.9)

$$\mathcal{T}(r) = \int_0^{2\pi} \int_0^\pi \Pi(r, \theta, \phi) \sin \theta d\theta d\varphi, \quad (5.10)$$

can be physically interpreted as the cumulative flux of turbulent kinetic energy exchanged between scales of size $r = \|\mathbf{r}\|$ and less, with those of size r and greater. In particular, the sign of $\mathcal{T}(r)$ directly informs on the direction of the energy cascade: $\mathcal{T}(r) > 0$ implies that, on average, energy flows towards scales larger than r , i.e. following an inverse energy cascade; $\mathcal{T}(r) < 0$ implies that, on average, turbulent kinetic energy flows towards scales smaller than r , i.e. following a direct energy cascade. Invoking axisymmetry, $\Pi(\mathbf{r}) = \Pi(r_\perp, r_\parallel)$, and (5.9) can be rigorously decomposed as the sum of the four following distinct contributions:

$$\Pi_\perp^\perp = \nabla_\perp \cdot \langle \delta \mathbf{u}'_\perp^2 \delta \mathbf{u}'_\perp \rangle_{t,\mathbf{x}}, \quad (5.11)$$

$$\Pi_\perp^\parallel = \nabla_\perp \cdot \langle \delta \mathbf{u}'_\parallel^2 \delta \mathbf{u}'_\perp \rangle_{t,\mathbf{x}}, \quad (5.12)$$

$$\Pi_\parallel^\perp = \nabla_\parallel \cdot \langle \delta \mathbf{u}'_\perp^2 \delta \mathbf{u}'_\parallel \rangle_{t,\mathbf{x}}, \quad (5.13)$$

$$\Pi_\parallel^\parallel = \nabla_\parallel \cdot \langle \delta \mathbf{u}'_\parallel^2 \delta \mathbf{u}'_\parallel \rangle_{t,\mathbf{x}}, \quad (5.14)$$

where $\delta \mathbf{u}'_\parallel = (\delta \mathbf{u}' \cdot \mathbf{e}_z) \mathbf{e}_z = \delta u_z \mathbf{e}_z$ and $\delta \mathbf{u}'_\perp = \delta \mathbf{u}' - \delta \mathbf{u}'_\parallel = \delta u'_\rho \mathbf{e}_\perp + \delta u'_\theta \mathbf{e}_\theta$ are the respective parallel and perpendicular components of $\delta \mathbf{u}'$ with respect to the magnetic field. Additionally, $\nabla_\perp \cdot$ is the classically defined divergence operator in 2D polar coordinates, while $\nabla_\parallel \cdot = \partial/\partial r_\parallel \cdot \mathbf{e}_z$. Physically speaking, Π_\perp^\perp represents the horizontal flux of horizontal energy, Π_\perp^\parallel represents the horizontal flux of vertical energy, Π_\parallel^\perp represents the vertical flux of horizontal energy and finally Π_\parallel^\parallel represents the vertical flux of vertical energy. Although only Π_\perp^\perp is experimentally accessible from potential measurements along the top and bottom walls (and even then, Π_\perp^\perp may only be computed for purely horizontal increments), it is still possible to compute rough estimates for the different contributions to Π from ultrasound measurements. More specifically, we will assume $\langle \|\delta \mathbf{u}'_\alpha\|^2 \|\delta \mathbf{u}'_\beta\| \rangle_{\mathbf{x},E} \sim \langle \|\mathbf{u}'_\alpha\| \rangle_{\mathbf{x},E}^2 \langle \|\mathbf{u}'_\beta\| \rangle_{\mathbf{x},E}$ (where α and β indistinctly represent the \parallel or \perp direction), $\nabla_\perp \cdot \sim 1/l_i$ (where $l_i = 15$ mm is the fixed injection scale in the case at hand) and $\nabla_\parallel \cdot \sim 1/l_z^u(l_i)$ (where $l_z^u(l_i)$ is the diffusion length as defined in section 5.1.5). Estimates for the different contributions to Π (referred to as $\widehat{\Pi}_\alpha^\beta$) are plotted against the dimensionality parameter $l_z^u(l_i)/h$ in figure 5.13.left. The curves shown here were obtained from ultrasound signals, using the transducers highlighted in figure 5.13.right.

According to figure 5.13.left, it appears that the only contribution to the energy transfers, which does not vanish as the flow becomes quasi-2D is $\widehat{\Pi}_\perp^\perp$. There are two reasons for this, which we have already witnessed in section 5.1.5. On the one hand, we have seen that the vertical velocity component becomes very small compared to the horizontal one, as the flow becomes quasi-2D. As such, all contributions to Π involving $\delta \mathbf{u}'_\parallel$ are expected to dwindle with $l_z^u(l_i)$. On the other hand, the velocity field becomes independent of the spatial

coordinate parallel to the magnetic field, as a result of two-dimensionalization. Consequently, the parallel transfers of turbulent kinetic energy Π_{\parallel}^{\perp} and $\Pi_{\parallel}^{\parallel}$ given by vertical derivatives must also vanish in the quasi-2D limit. In the quasi-2D limit, measuring Π_{\perp}^{\perp} gives us in fact a very good picture of the actual transfers taking place in the experiment, and may legitimately be associated to the total energy transfer Π . This reasoning becomes however dicey anytime three-dimensionality and/or three-componentality exists in the bulk. All the more so in MHD turbulence, as three-dimensionality and three-componentality actually drive angular transfers from small to large latitude structures. In any event, figure 5.13 shows that the dominance of $\hat{\Pi}_{\perp}^{\perp}$ on the energy transfers coincides with the injection scale becoming quasi-2D. Indeed, $\hat{\Pi}_{\perp}^{\perp}$ is at least one order of magnitude larger than any other contribution when $l_z^u(l_i)/h > 1$.

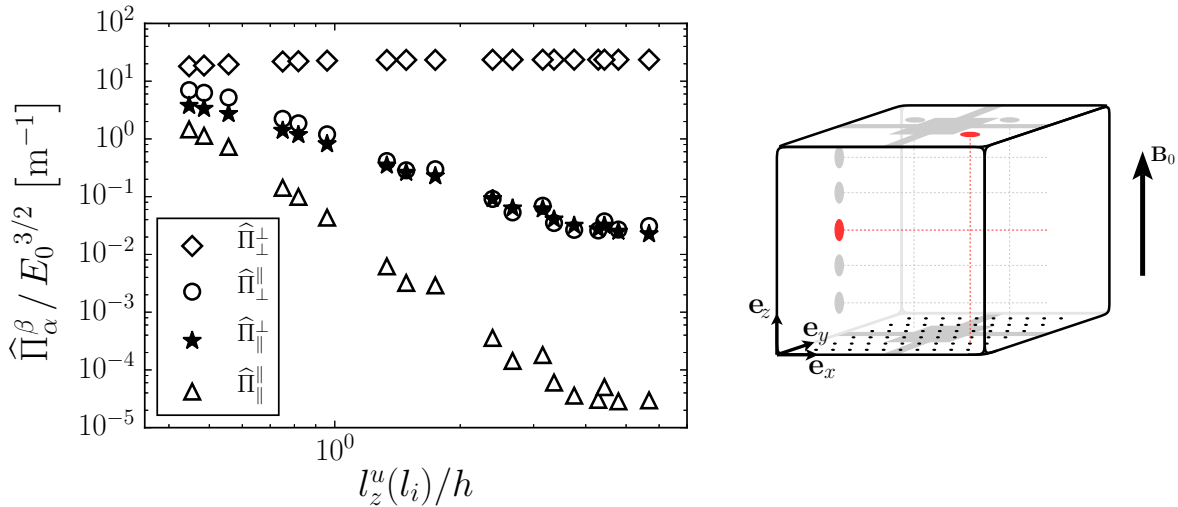


Figure 5.13. Estimation of the different contributions to energy fluxes as a function of the dimensionality, parametrized by $l_z^u(l_i)/h$: $l_z^u(l_i)/h \ll 1$ implies a 3D bulk, while $l_z^u(l_i)/h \gg 1$ implies a quasi-2D bulk. The normalization involves the total mean turbulent kinetic energy $\bar{E}_0 = [\langle \mathbf{u}'^2 \rangle_{t,z} + \langle \mathbf{u}'^2 \rangle_{t,x}] / 2$.

With these words of caution, we may finally look at $\Pi_{\perp}^{\perp}(r_{\perp})$, computed along the bottom and top Hartmann walls. Since there is no confusion as to which contribution to Π we are actually plotting, they will now be referred to as Π_{\perp}^{bot} and Π_{\perp}^{top} respectively. The operating settings used in this section consist of the 8×8 injection pattern with the injection scale $l_i = 15$ mm and a total electric forcing $Re^0 = 32000$ ($I_0 = 224$ A). The magnetic field is varied between $Ha = 1800$ and 15000 ($B_0 = 0.5$ and 4 T respectively). Figure 5.14 shows the energy transfers occurring along the bottom wall, where the electric forcing takes place. According to this figure, the energy flux experienced by structures of size $r_{\perp}/l_i > 2$ is positive. This indicates that on average, energy flows towards larger scales, that is to say following an inverse cascade. In addition, there exists a range of scales between $2 \leq r_{\perp}/l_i \leq 6$ for which the energy flux is constant (indicated by a plateau), which suggests the presence of

a small inertial range in our experiment. Comparing figure 5.10.left with figure 5.14.left, it appears that large structures (for instance $r_\perp/l_i > 3$) may possess very little energy, despite experiencing an incoming energy flux from adjacent scales. This may be an indication that there exists one or several mechanisms at large scale, which are responsible for the redistribution of this incoming flux of kinetic energy. Interestingly, an inverse cascade of horizontal energy seems to always exist, even at low magnetic fields, where the bulk is 3D. This result is consistent with the findings of Campagne *et al.* (2014), who found that in rotating turbulence, Π_\perp^\perp was mainly associated to an inverse flux of energy, while most of the direct flux was in fact borne by $\Pi_\perp^{\parallel\parallel}$. This is also consistent with figure 5.13.left, according to which the most important contribution to Π after Π_\perp^\perp is indeed $\Pi_\perp^{\parallel\parallel}$, when the bulk is 3D.

The global shape of the horizontal energy transfers occurring along the top wall (displayed in figure 5.14.right) are quite similar to those occurring at the bottom. Their actual magnitude depends however on the amount of turbulent kinetic energy found along the top wall, which is all the more important, as the flow is 2D (the flow at the top is most energetic when the injection scale spans across the box). In particular, figure 5.14.right features the establishment of a steady inertial range for scales in the range $2 \leq r_\perp/l_i \leq 6$, as the bulk becomes quasi-2D (visible for instance when $Ha \geq 7300$).

The behavior of the energy fluxes observed at scales $6 l_i$ and above, both at the bottom or the top of the container is still unclear. In particular, the peak occurring at $7 l_i = 105$ mm

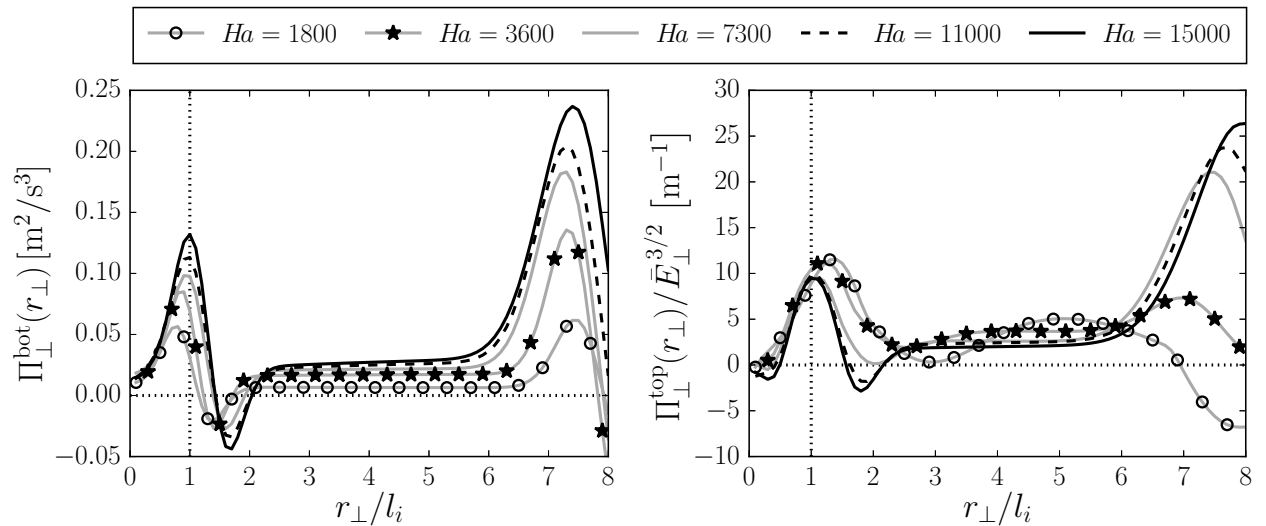


Figure 5.14. Horizontal transfers of horizontal turbulent kinetic energy. Left: along the bottom Hartmann wall (i.e. where the electric forcing takes place). Right: along the top wall (where observable scales are kinematically quasi-2D). The horizontal dotted line distinguishes between direct and inverse cascade domains ($\Pi_\perp > 0$ implies a flux of kinetic energy towards larger scales). The vertical dotted line locates the injection scale. The operating conditions are the 8×8 injection pattern with $l_i = 15$ mm and $Re^0 = 32000$ ($I_0 = 224$ A).

corresponds to turbulent structures of the size of the forcing patch. The homogeneity and isotropy level of these very large scales is perhaps questionable since they are likely to feel the presence of the vertical walls, and/or the periodic forcing. In any case, the positive peak at $r_\perp = 7l_i$ suggests that turbulent kinetic energy is injected at the scale of the forcing pattern in the quasi-2D limit. The mechanism for such a phenomenon is still to be clarified.

5.4 How to evaluate Joule dissipation in scale space?

We close this chapter by presenting an original contribution, which aims at introducing a way to experimentally evaluate the Joule dissipation induced by the Lorentz force. The work presented in this section is still ongoing; We deem it nonetheless worthwhile to present the ideas that have been investigated thus far. The main difficulties arising when trying to evaluate the Lorentz force come from its non local nature. As a result, evaluating the Lorentz force at a given point in space and time requires the knowledge of the whole flow. Unfortunately, such an amount of data is far from being available in Flowcube, where measurements of the horizontal velocity field are only available along the top and bottom walls. The procedure we report here takes advantage of the experimental observation of section 5.3.1, that although the turbulence driven in Flowcube is generally inhomogeneous over the whole height of our experiment h , it is nonetheless homogeneous over the diffusion length $l_z^u(l_i)$. This remarkable property was observed with the second order structure function $\langle \delta \mathbf{u}'_\perp^2 \rangle_{t,\mathbf{x}}$, and translated as a collapse of all experimental data on a single curve, when plotted against the reduced variables $(r_\perp/l_i, h/l_z)$. Owing to relationship (4.42), this universal property must also hold for the correlation function $\langle \mathbf{u}'_\perp(\mathbf{x}) \cdot \mathbf{u}'_\perp(\mathbf{x} + \mathbf{r}) \rangle_{t,\mathbf{x}}$.

Let us now write explicitly the term $\langle \delta \mathbf{f}'_S \cdot \delta \mathbf{u}' \rangle_{t,\mathbf{x}}$ found in the Kármán-Howarth equation (4.48) derived earlier. By definition, $\delta \mathbf{f}'_S \cdot \delta \mathbf{u}'$ is given by

$$\delta \mathbf{f}'_S \cdot \delta \mathbf{u}' = \mathbf{f}'_S(B) \cdot \mathbf{u}'_B - \mathbf{f}'_S(B) \cdot \mathbf{u}'_A - \mathbf{f}'_S(A) \cdot \mathbf{u}'_B + \mathbf{f}'_S(A) \cdot \mathbf{u}'_A, \quad (5.15)$$

where $\mathbf{r} = \mathbf{x}_B - \mathbf{x}_A$, and $\mathbf{f}'_S(P)$ is the fluctuation of the solenoidal component of the Lorentz force given at point $P = A$ or B . According to section 1.2.2, \mathbf{f}'_S satisfies the following Poisson equation

$$\Delta \mathbf{f}'_S = -\frac{1}{\tau_J} \frac{\partial^2 \mathbf{u}'}{\partial z^2}, \quad (5.16)$$

where $\tau_J = \rho/\sigma B_0^2$ is the classically defined Joule time. Equations such as (5.16) may be solved by seeking for the associated Green's function. In the case of the Laplacian operator (cf. Appendix B for the details of the derivation), the solution is given in the form of the Biot-Savart integral

$$\begin{aligned} \mathbf{f}'_S(P) = & -\frac{1}{4\pi\tau_J} \int_V \frac{\partial^2 \mathbf{u}'(\boldsymbol{\xi})}{\partial \xi_z^2} \frac{d^3 \boldsymbol{\xi}}{\|\mathbf{x}_P - \boldsymbol{\xi}\|} \\ & -\frac{1}{4\pi\tau_J} \int_{\partial V} \left[\mathbf{f}'_S(\boldsymbol{\xi}) \frac{\partial \|\mathbf{x}_P - \boldsymbol{\xi}\|^{-1}}{\partial \mathbf{n}} - \|\mathbf{x}_P - \boldsymbol{\xi}\|^{-1} \frac{\partial \mathbf{f}'_S(\boldsymbol{\xi})}{\partial \mathbf{n}} \right] d^2 \boldsymbol{\xi}. \end{aligned} \quad (5.17)$$

In the above, \mathcal{V} represents the control volume (i.e. the experiment's container) and $\partial\mathcal{V}$ its boundaries. Furthermore, $\mathbf{x}_P = (x_P, y_P, z_P)$ are the Cartesian coordinates of point P, while $d^3\xi$ and $d^2\xi$ represent an infinitesimal volume and surface in Cartesian space respectively. With words, (5.17) translates the fact that the Lorentz force has a non local influence on the bulk. This behavior stems from the presence of electric currents traveling throughout the fluid, thus connecting regions of space which are far apart. This behavior is quite similar to the effect of the pressure field in hydrodynamics, which connects distant regions of the flow through pressure waves. The surface integrals appearing in (5.17) transcribe nothing else than the boundary conditions required to fully solve the Poisson problem. These integrals certainly bear some crucial physics. As a matter of fact, we suspect that Hartmann braking hides within them since they involve, among other things, gradients of current density along the perpendicular walls. Their explicit solving is however far beyond the scope of this section, as they would require a thorough investigation of their own. We propose to focus on the contribution resulting from the volume integral, which we will denote with a superscript \mathcal{V} .

The single point quantities found in (5.15) are of form $\mathbf{f}'_S(P) \cdot \mathbf{u}'_P$. Noticing that $\mathbf{u}'_S(P) = \mathbf{u}'(\mathbf{x}_P)$ is a constant with respect to the integration variable ξ , and that time averages commute with spatial integrals, one can write $\langle \mathbf{f}'_S(P) \cdot \mathbf{u}'_P \rangle_t^\mathcal{V}$ as

$$\langle \mathbf{f}'_S(P) \cdot \mathbf{u}'_P \rangle_t^\mathcal{V} = -\frac{1}{4\pi\tau_J} \int_{\mathcal{V}} \frac{\partial^2 \langle \mathbf{u}'(\xi) \cdot \mathbf{u}'(\mathbf{x}_P) \rangle_t}{\partial \xi_z^2} \frac{d^3\xi}{\|\mathbf{x}_P - \xi\|}. \quad (5.18)$$

At this stage, $\langle \mathbf{f}'_S(P) \cdot \mathbf{u}'_P \rangle_t^\mathcal{V}$ remains very much a function of the location \mathbf{x}_P where it is evaluated at. Introducing the change of variable $\xi = \mathbf{x}_P + \zeta$, and multiplying the integrand by $1 = 4E_0/4E_0$ with $4E_0 = \langle \mathbf{u}'_B^2 \rangle_t + \langle \mathbf{u}'_A^2 \rangle_t$, yields

$$\langle \mathbf{f}'_S(P) \cdot \mathbf{u}'_P \rangle_t^\mathcal{V} = -\frac{E_0}{\pi\tau_J} \int_{\mathcal{V}'} \frac{\partial^2}{\partial \zeta_z^2} \left[\frac{\langle \mathbf{u}'(\mathbf{x}_P + \zeta) \cdot \mathbf{u}'(\mathbf{x}_P) \rangle_t}{4E_0} \right] \frac{d^3\zeta}{\|\zeta\|}, \quad (5.19)$$

where \mathcal{V}' is the translated control volume resulting from the space shift induced by the linear change of variable. Equation (5.19) introduces $R(\mathbf{x}_P, \zeta) = \langle \mathbf{u}'(\mathbf{x}_P + \zeta) \cdot \mathbf{u}'(\mathbf{x}_P) \rangle_t / 4E_0$ the correlation function of vector separation ζ , with respect to point P. Invoking homogeneity in the perpendicular plane, R is expected not to depend on the lateral positioning of point P. Spatial averaging over all points of fixed altitude z_P may thus be performed, which we shall write $\langle \cdot \rangle_{\mathbf{x}_\perp}$. In addition, invoking axisymmetry, R can also be expected to depend only on two spatial coordinates ζ_\perp and ζ_\parallel , which represent the radial and vertical distance from point P respectively. In other words, we take the correlation function to be a function satisfying $R(\mathbf{x}_P, \zeta) = R(z_P; \zeta_\perp, \zeta_\parallel)$.

Figure 5.15 shows the correlation functions $R(0; r_\perp/l_i, h/l_z^u)$ and $R(h; r_\perp/l_i, -h/l_z^u)$ computed with respect to the bottom wall ($z_P = 0$) and top wall ($z_P = h$) respectively. As for the second order structure function, the correlation functions plotted against the reduced variables $r_\perp^* = r_\perp/l_i$ and $r_\parallel^* = h/l_z^u(l_i)$ collapse onto the same curve. It can also be noticed from

this plot that $R(h; r_\perp/l_i, -h/l_z^u) = R(0; r_\perp/l_i, h/l_z^u)$. This reflexive symmetry implies that despite the turbulence being inhomogeneous along the direction of the field, the statistics relative to turbulent fluctuations are independent of the vertical orientation of the vertical increment over the distance $l_z^u(l_i)$.

Figure 5.15 also shows that R decays radially over the perpendicular integral lengthscale $\mathcal{L}_\perp \sim l_i$. We can thus expect R to have a negligible contribution to the integral as soon as the perpendicular component of the separation vector is much greater than \mathcal{L}_\perp . As a result, integrating radially over a few \mathcal{L}_\perp should account for most of the non-local lateral effects of the Lorentz force. This argument of course only holds as long as the point of reference P lays sufficiently far from any source of radial anisotropy, such as the lateral boundary of the forcing patch or vertical walls. Note that such a reasoning does not apply in the parallel direction, since two-dimensionalization induces long distance correlations in the direction of the magnetic field.

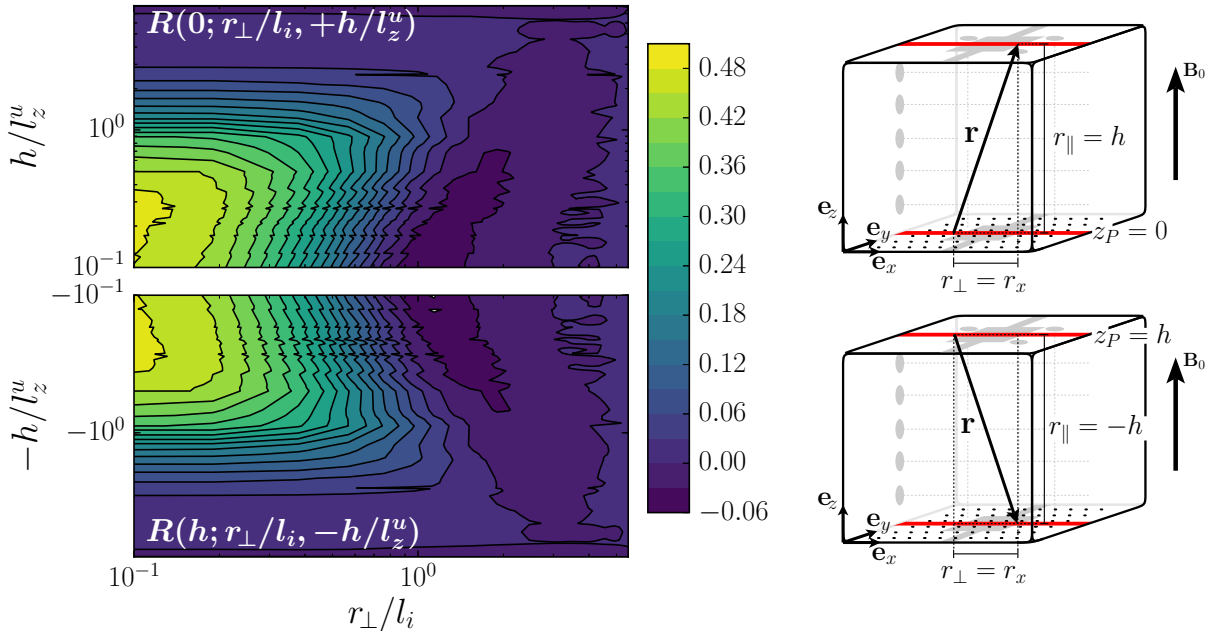


Figure 5.15. Flowcubes's universal correlation function $R(z_P; r_\perp/l_i, h/l_z^u)$ plotted using all our experimental data points. Top: $R(0; r_\perp/l_i, h/l_z^u)$ measured with respect to \mathbf{x}_P laying within the bottom plate ($z_P = 0$). Bottom: $R(h; r_\perp/l_i, -h/l_z^u)$ measured with respect to \mathbf{x}_P laying within the top plate ($z_P = h$).

Thanks to the universal shape of $R(r_\perp/l_i, h/l_z^u)$, the vertical integral in (5.19) may be numerically computed a posteriori of all experiments, without the need to measure the correlation function in the bulk. In practice, equation (5.19) may thus be approximated by integrating over a cylinder of radius \mathcal{L}_\perp and any given height l_z^u . We therefore introduce the cylindrical change of variables $\zeta_x = \zeta_\perp \cos \theta$, $\zeta_y = \zeta_\perp \sin \theta$, $\zeta_z = \zeta_\parallel$, and (5.19) becomes

5.4. How to evaluate Joule dissipation in scale space?

equivalent to

$$\langle \mathbf{f}'_S(P) \cdot \mathbf{u}'_P \rangle_{t,\mathbf{x}_\perp}^{\mathcal{V}} \simeq -\frac{2E_0}{\tau_J} \int_{-z_P}^{h-z_P} \int_0^{\mathcal{L}_\perp} \frac{\partial^2 R(z_P, \zeta_\perp, \zeta_\parallel)}{\partial \zeta_\parallel^2} \frac{\zeta_\perp d\zeta_\perp d\zeta_\parallel}{\sqrt{\zeta_\perp^2 + \zeta_\parallel^2}}. \quad (5.20)$$

Practically speaking, we take points A and B along the bottom and top walls respectively, i.e. $z_A = 0$ and $z_B = h$. According to (5.20), we therefore have

$$\langle \mathbf{f}'_S(B) \cdot \mathbf{u}'_B \rangle_{t,\mathbf{x}_\perp}^{\mathcal{V}} \simeq -\frac{2E_0}{\tau_J} \int_{-h}^0 \int_0^{\mathcal{L}_\perp} \frac{\partial^2 R(h, \zeta_\perp, \zeta_\parallel)}{\partial \zeta_\parallel^2} \frac{\zeta_\perp d\zeta_\perp d\zeta_\parallel}{\sqrt{\zeta_\perp^2 + \zeta_\parallel^2}}, \quad (5.21)$$

and

$$\langle \mathbf{f}'_S(A) \cdot \mathbf{u}'_A \rangle_{t,\mathbf{x}_\perp}^{\mathcal{V}} \simeq -\frac{2E_0}{\tau_J} \int_0^h \int_0^{\mathcal{L}_\perp} \frac{\partial^2 R(0, \zeta_\perp, \zeta_\parallel)}{\partial \zeta_\parallel^2} \frac{\zeta_\perp d\zeta_\perp d\zeta_\parallel}{\sqrt{\zeta_\perp^2 + \zeta_\parallel^2}}. \quad (5.22)$$

Let us now proceed with the evaluation of the two point terms $\mathbf{f}'_S(B) \cdot \mathbf{u}'_A$ and $\mathbf{f}'_S(A) \cdot \mathbf{u}'_B$. We recall that the separation vector between A and B is by definition $\mathbf{r} = \mathbf{x}_B - \mathbf{x}_A$. In the spirit of the previous paragraph, we manipulate the corresponding integrals to make the correlation function appear. Posing the change of variable $\boldsymbol{\xi} = \mathbf{x}_A + \boldsymbol{\zeta}$ in the integral related to $\mathbf{f}'_S(B) \cdot \mathbf{u}'_A$ yields

$$\langle \mathbf{f}'_S(B) \cdot \mathbf{u}'_A \rangle_t^{\mathcal{V}} = -\frac{E_0}{\pi \tau_J} \int_{V'} \frac{\partial^2}{\partial \zeta_z^2} \left[\frac{\langle \mathbf{u}'(\mathbf{x}_A + \boldsymbol{\zeta}) \cdot \mathbf{u}'(\mathbf{x}_A) \rangle_t}{4E_0} \right] \frac{d^3 \boldsymbol{\zeta}}{\|\boldsymbol{\zeta} - \mathbf{r}\|}, \quad (5.23)$$

while posing the change of variable $\boldsymbol{\xi} = \mathbf{x}_B + \boldsymbol{\zeta}$ in the integral related to $\mathbf{f}'_S(A) \cdot \mathbf{u}'_B$ reads

$$\langle \mathbf{f}'_S(A) \cdot \mathbf{u}'_B \rangle_t^{\mathcal{V}} = -\frac{E_0}{\pi \tau_J} \int_{V'} \frac{\partial^2}{\partial \zeta_z^2} \left[\frac{\langle \mathbf{u}'(\mathbf{x}_B + \boldsymbol{\zeta}) \cdot \mathbf{u}'(\mathbf{x}_B) \rangle_t}{4E_0} \right] \frac{d^3 \boldsymbol{\zeta}}{\|\boldsymbol{\zeta} + \mathbf{r}\|}. \quad (5.24)$$

Invoking the same arguments as earlier and introducing cylindrical coordinates give

$$\begin{aligned} \langle \mathbf{f}_B \cdot \mathbf{u}_A \rangle_{t,\mathbf{x}_\perp}^{\mathcal{V}} &\simeq \\ -\frac{E_0}{\pi \tau_J} \int_0^{2\pi} \int_0^h \int_0^{\mathcal{L}_\perp} &\frac{\partial^2 R(0, \zeta_\perp, \zeta_\parallel)}{\partial \zeta_\parallel^2} \frac{\zeta_\perp d\zeta_\perp d\zeta_\parallel d\theta}{\sqrt{(r_\perp - \zeta_\perp)^2 + 2r_\perp \zeta_\perp (1 - \cos \theta) + (r_\parallel - \zeta_\parallel)^2}}, \end{aligned} \quad (5.25)$$

and

$$\begin{aligned} \langle \mathbf{f}_A \cdot \mathbf{u}_B \rangle_{t,\mathbf{x}_\perp}^{\mathcal{V}} &\simeq \\ -\frac{E_0}{\pi \tau_J} \int_0^{2\pi} \int_{-h}^0 \int_0^{\mathcal{L}_\perp} &\frac{\partial^2 R(h, \zeta_\perp, \zeta_\parallel)}{\partial \zeta_\parallel^2} \frac{\zeta_\perp d\zeta_\perp d\zeta_\parallel d\theta}{\sqrt{(r_\perp + \zeta_\perp)^2 - 2r_\perp \zeta_\perp (1 - \cos \theta) + (r_\parallel + \zeta_\parallel)^2}}. \end{aligned} \quad (5.26)$$

In the two previous integrals, \mathbf{r} was assumed, without loss of generality, to be laying in the $(\mathbf{e}_x, \mathbf{e}_z)$ plane. As such, θ represents the angle between \mathbf{r} and ζ in cylindrical coordinates.

Adding up integrals (5.21), (5.22), (5.25) and (5.26) yields the overall scale by scale Joule dissipation stemming from three-dimensionality *in the bulk* (as opposed to Joule dissipation induced by Hartmann braking in the boundary layers). As of now, the actual numerical evaluation of these integrals is not hindered by the lack of information, but rather by their singular nature. In particular, (5.21) and (5.22) are singular at $r_{\perp}^* = r_{\parallel}^* = 0$, which owing to our method, coincides with the asymptotic state $l_z^u(l_i) \rightarrow \infty$ (which in turn corresponds to infinite magnetic fields). Figure 5.16 shows one-dimensional profiles of the correlation function at different fixed radii. This plot suggests that an asymptotic behavior may perhaps be extrapolated from our experimental data to solve the singularities found in the aforementioned integrals. Removing the singularity in the integral (5.25) requires performing an asymptotic expansion around $\zeta = \mathbf{r}$.

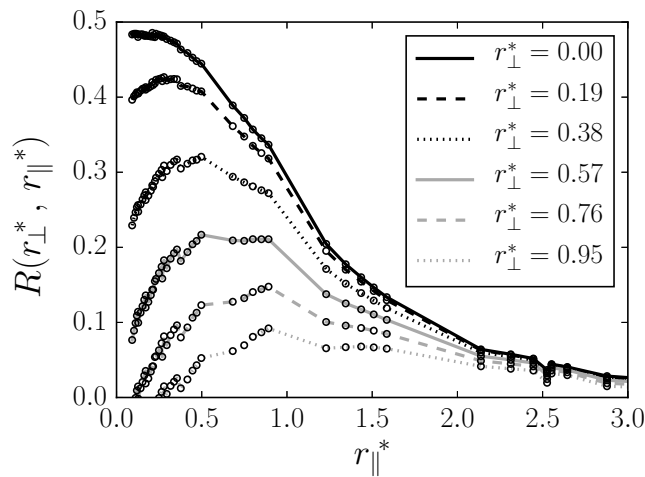


Figure 5.16. One dimensional profiles of the universal correlation function R , as a function of r_{\parallel}^* , given at different radial positions r_{\perp}^* .

5.5 Summary of the main findings and prospects

We started this chapter with an extensive inspection of the properties in physical space of electrically driven MHD turbulence at low- Rm in a wall bounded-vessel. We showed in particular that despite an inhomogeneous and anisotropic forcing taking place along the bottom wall, the turbulent fluctuations presented an acceptable level of homogeneity and horizontal isotropy both along the top and bottom walls. These observations confirmed that the turbulence driven in our experiment could legitimately be described through the prism of homogeneous and axisymmetric turbulence, which made its description simpler.

Secondly, we investigated the emergence of two-dimensionality on a scale-wise basis by comparing the turbulent kinetic energy densities computed along the top and bottom Hartmann walls. By defining the smallest quasi-2D structure as the most energetic structure observable along the top wall, we were able to recover Sommeria & Moreau (1982)'s prediction for a cutoff lengthscale above which all turbulent scales are kinematically quasi-2D and under which they are kinematically 3D. As such, we gave the very first experimental validation that the prominent physical mechanisms occurring in the 3D inertial range of wall-bounded MHD turbulence at low- Rm are indeed the two-dimensionalization by the solenoidal component of the Lorentz force on the one hand, and inertial energy transfers on the other.

Thirdly, we inspected the distribution of turbulent kinetic energy in scale space, as measured by the second order structure function. It turns out that this function follows a universal shape in our experimental setup and is fully defined by two lengthscales only. On the one hand, the injection scale l_i , which controls the size of the vortices sustained by the forcing mechanism. On the other hand, the diffusion length $l_z^u(l_i)$ associated to the dimensionality of the forcing scale. We interpreted the collapse of the statistics with $l_z^u(l_i)$ as evidence that the turbulence forced in our experiment is in fact vertically homogeneous over this very distance $l_z^u(l_i)$. We further observed in scale space the anisotropy introduced by the Lorentz force along the magnetic field, and we demonstrated that the threshold for this anisotropy to appear coincided exactly with turbulent structures becoming quasi-2D.

Fourthly, we evaluated experimentally the scale by scale flux of perpendicular turbulent kinetic energy along perpendicular scales. We found in particular that regardless of the dimensionality of the bulk, there always existed a range of scales larger than the injection scale, which experienced an upscale flux of kinetic energy. This observation suggests that perpendicular kinetic energy always follows an inverse energy cascade, despite the scales supporting it being kinematically 3D.

Last but not least, we introduced a method aimed at evaluating experimentally Joule dissipation in scale space. This method relies on the experimental observation that the kinematics of the turbulence driven in Flowcube follows a universal curve, which makes it possible to deduce the statistics of the flow in the bulk from measurements along the boundaries only. Although some technical and numerical obstacles still need to be overcome, the recent developments are quite encouraging.

From here on, a possible promising prospect would be to explore in greater details the different phenomena taking part in the dynamics of wall-bounded MHD turbulence, which appear in the Kármán-Howarth equation presented in chapter 4. Without a doubt, the next points requiring full attention are energy dissipation via Hartmann braking, and the forcing mechanism taking place in the Flowcube.

General conclusion

Throughout this thesis, we clarified the role of the solenoidal component of the Lorentz force in imposing the topological dimensionality of a low- Rm MHD flow confined between electrically insulating and no-slip walls, laying perpendicularly to a static and uniform magnetic field. More specifically, we followed Sommeria & Moreau (1982)'s argument according to which the solenoidal component of the Lorentz force acts as a pseudo-diffusive process of momentum, whose diffusivity is scale dependent.

We showed in chapter 2 that the topology of a single electrically driven vortex confined between two perpendicular walls resulted, in the weakly inertial limit, from a competition between the solenoidal component of the Lorentz force and viscous friction. Within this context, it was shown that the dimensionality of the vortex could be fully described using the single parameter l_z^ν/h , which compares the range of action of the Lorentz force in the direction of the magnetic field, compared to the height of the channel. In other words, l_z^ν/h succinctly quantifies the magnitude of the gradients along the magnetic field. This neat parameter introduces a very simple and intuitive criterion to describe the dimensionality of a steady single vortex: $l_z^\nu/h \ll 1$ implies that the vortex is three-dimensional, while $l_z^\nu/h \gg 1$ means that the vortex is quasi-2D. The model put forward in chapter 2 has also highlighted two inertial mechanisms able to introduce a third velocity component by means of first order meridional recirculations. More specifically, 3D base flows at leading order induced inverse Ekman pumping driven by an axial pressure gradient along the axis of the vortex, while quasi-2D base flows favored direct Ekman pumping originating from radial pressure gradients inside the Hartmann layers.

We confirmed in chapter 5 that the ideas put forward in the weakly inertial limit also applied to the statistics of fully developed turbulent flows in scale space. In particular, it was shown experimentally that the kinematics of turbulence were fully described by two lengthscales. On the one hand the forcing scale l_i , which characterizes the kinematics of the turbulence in the direction perpendicular to the magnetic field. On the other hand $l_z^u(l_i)$, which describes the correlation of the flow in the direction of the field resulting from the Lorentz force. In that sense, the ratio $l_z^u(l_i)/h$ physically represents the dimensionality of turbulent structures whose size coincides with the forcing scale l_i . By comparing the energy densities measured along the top and bottom walls, we gave the first experimental validation of Sommeria & Moreau (1982)'s scaling law, which confirms that the kinematics of low- Rm MHD turbulence confined between Hartmann walls indeed results from a competition

GENERAL CONCLUSION

between the solenoidal component of the Lorentz force and inertia. Furthermore, we were able to establish an authoritative link between energy distribution and dimensionality in scale space. To be more specific, the second order structure function associated to quasi-2D structures presented very strong anisotropy and invariance along the magnetic field. This anisotropy vanished for 3D turbulent structures. Finally, we showed by computing the actual flux of perpendicular turbulent kinetic energy along perpendicular scales, that an inertial range existed, which always followed an inverse energy cascade (i.e. 2D dynamics), despite the scales experiencing these 2D dynamics being topologically 3D.

The experimental study presented in this thesis was carried out using an improved and enlarged version of the Flowcube. In particular, we have designed and built new Hartmann plates, which enabled us to capture the scale-wise dynamics of MHD turbulence at low- Rm . Thanks to the high probe density introduced in these new Hartmann plates, it was possible for us to capture the inertial range with a good resolution in scale space. Thanks to the wide range of magnetic fields available (and especially the very high fields provided by the LNCMI), we were able to continuously set the dimensionality of the bulk at will, from 3D to fully quasi-2D.

Many exciting aspects of low- Rm MHD turbulence confined between insulating walls may be investigated from here on. The first point that deserves to be addressed, is of course to fully clarify Joule dissipation in scale space both resulting from three-dimensionality in the bulk and in the Hartmann layers. The groundwork for such an investigation has been laid out at the end of chapter 5. In addition, owing to the large amount of experimental data gathered throughout this project, it is also worth considering the actual assessment of terms appearing in the Kármán-Howarth equation. Doing so would undoubtedly help understand how the different physical processes compete with each other in setting the dynamics of wall-bounded MHD turbulence. In particular, it would be quite interesting to evaluate the energy dissipation due to viscosity, and see how it compares against Joule dissipation. Furthermore, examining the forcing terms may help understand and perhaps model the mechanisms involved in injecting turbulent kinetic energy into electrically forced MHD turbulence at low- Rm .

Appendix A: Derivation of the Kármán-Howarth equation

The purpose of this section is to specify the steps leading to the inhomogeneous and anisotropic version of the Kármán-Howarth equation given by Hill (2002) in section 4.3.2, which is reproduced below

$$\begin{aligned} \frac{\partial \delta \mathbf{u}^2}{\partial t} + \nabla_{\mathbf{r}} \cdot [\delta \mathbf{u}^2 \delta \mathbf{u}] + \nabla_{\mathbf{x}} \cdot [\delta \mathbf{u}^2 \mathbf{u}_m] &= 2 \delta \mathbf{f}_S \cdot \delta \mathbf{u} - 4 \epsilon_m \\ &+ 2 \nu \nabla_{\mathbf{r}} \cdot [\nabla_{\mathbf{r}} \delta \mathbf{u}^2] + 2 \nabla_{\mathbf{x}} \cdot \left[-\frac{\delta p^* \delta \mathbf{u}}{\rho} + \frac{\nu}{4} \nabla_{\mathbf{x}} (\delta \mathbf{u}^2 - 8 p_m) \right]. \end{aligned} \quad (5.27)$$

In the above, subscript m refers to the mid point quantity evaluated between A and B, i.e. $\mathbf{u}_m = (\mathbf{u}_A + \mathbf{u}_B)/2$, $p_m = (p_A + p_B)/2$ and $\epsilon_m = (\epsilon_A + \epsilon_B)/2$, with $\epsilon_P = 2\nu \mathbb{S}_P : \mathbb{S}_P$. In addition, $\delta \mathbf{u}^2$ is a shorthand for $\|\delta \mathbf{u}\|^2$. This equation is derived by subtracting the Navier-Stokes equation evaluated at point A to the Navier-Stokes equation evaluated at point B

$$\frac{\partial \mathbf{u}_A}{\partial t} + \nabla_A \cdot (\mathbf{u}_A \otimes \mathbf{u}_A) = \nabla_A \cdot \left[-\frac{p_A^*}{\rho} \mathbb{I} + 2\nu \mathbb{S}_A \right] + \mathbf{f}_S^A \quad (5.28)$$

and

$$\frac{\partial \mathbf{u}_B}{\partial t} + \nabla_B \cdot (\mathbf{u}_B \otimes \mathbf{u}_B) = \nabla_B \cdot \left[-\frac{p_B^*}{\rho} \mathbb{I} + 2\nu \mathbb{S}_B \right] + \mathbf{f}_S^B \quad (5.29)$$

respectively, and by taking the dot product of the result with $\delta \mathbf{u} = \mathbf{u}_B - \mathbf{u}_A$. Writing \mathbf{x}_A and \mathbf{x}_B the coordinates of points A and B respectively, the following change of variables is then introduced

$$\mathbf{X} = (\mathbf{x}_A + \mathbf{x}_B)/2 \quad \text{and} \quad \mathbf{r} = \mathbf{x}_B - \mathbf{x}_A,$$

with the differentiation rules

$$\nabla_A = -\nabla_{\mathbf{r}} + \frac{1}{2} \nabla_{\mathbf{x}} \quad \text{and} \quad \nabla_B = \nabla_{\mathbf{r}} + \frac{1}{2} \nabla_{\mathbf{x}}.$$

Let us now proceed with the derivation of every term found in (5.27).

Temporal term

The temporal terms are readily integrated to yield

$$\left[\frac{\partial \mathbf{u}_B}{\partial t} - \frac{\partial \mathbf{u}_A}{\partial t} \right] \cdot \delta \mathbf{u} = \frac{1}{2} \frac{\partial \delta \mathbf{u}^2}{\partial t}$$

Inertial terms

Keeping in mind that \mathbf{u}_A and \mathbf{u}_B do not depend on \mathbf{x}_B and \mathbf{x}_A respectively, the following equality holds: $\nabla_A \cdot (\mathbf{u}_B \otimes \mathbf{u}_A) = -\nabla_B \cdot (\mathbf{u}_A \otimes \mathbf{u}_B) = 0$. The inertial terms may therefore be re-written in the following form by adding zero

$$\begin{aligned} & [\nabla_B \cdot (\mathbf{u}_B \otimes \mathbf{u}_B) - \nabla_A \cdot (\mathbf{u}_A \otimes \mathbf{u}_A)] \cdot \delta \mathbf{u} \\ &= [\nabla_B \cdot (\mathbf{u}_B \otimes \mathbf{u}_B) - \nabla_B \cdot (\mathbf{u}_A \otimes \mathbf{u}_B) + \nabla_A \cdot (\mathbf{u}_B \otimes \mathbf{u}_A) - \nabla_A \cdot (\mathbf{u}_A \otimes \mathbf{u}_A)] \cdot \delta \mathbf{u} \\ &= [\nabla_B \cdot (\delta \mathbf{u} \otimes \mathbf{u}_B) + \nabla_A \cdot (\delta \mathbf{u} \otimes \mathbf{u}_A)] \cdot \delta \mathbf{u} \end{aligned}$$

Now performing the change of variables $\nabla_A = -\nabla_{\mathbf{r}} + 1/2 \nabla_{\mathbf{X}}$ and $\nabla_B = \nabla_{\mathbf{r}} + 1/2 \nabla_{\mathbf{X}}$, and calling $\mathbf{u}_m = (\mathbf{u}_A + \mathbf{u}_B)/2$ leads to

$$\begin{aligned} & [\nabla_B \cdot (\delta \mathbf{u} \otimes \mathbf{u}_B) + \nabla_A \cdot (\delta \mathbf{u} \otimes \mathbf{u}_A)] \cdot \delta \mathbf{u} \\ &= [\nabla_{\mathbf{r}} \cdot (\delta \mathbf{u} \otimes \delta \mathbf{u})] \cdot \delta \mathbf{u} + [\nabla_{\mathbf{X}} \cdot (\delta \mathbf{u} \otimes \mathbf{u}_m)] \cdot \delta \mathbf{u} \\ &= \frac{1}{2} \nabla_{\mathbf{r}} \cdot [(\delta \mathbf{u})^2 \delta \mathbf{u}] + \frac{1}{2} \nabla_{\mathbf{X}} \cdot [(\delta \mathbf{u})^2 \mathbf{u}_m]. \end{aligned}$$

The final expression is a consequence of the incompressibility assumption according to which $\nabla_{\mathbf{r}} \cdot \delta \mathbf{u} = \nabla_{\mathbf{X}} \cdot \mathbf{u}_m = 0$. This representation shows that in the general (inhomogeneous) case, the inertial terms split into two different energy transfer terms: first a transfer of turbulent kinetic energy which takes place exclusively in scale space (represented by $\nabla_{\mathbf{r}} \cdot$), but also a transfer of energy in the physical space, resulting from the advection of turbulent kinetic energy by the mean local velocity \mathbf{u}_m .

Pressure term

Noting that p_A^* and p_B^* do not depend on \mathbf{x}_B and \mathbf{x}_A respectively, zero is added under the form $\nabla_B \cdot [p_A^*/\rho \mathbb{I}] - \nabla_A \cdot [p_B^*/\rho \mathbb{I}]$, which yields

$$\begin{aligned} & \left[-\nabla_B \cdot \left(\frac{p_B^*}{\rho} \mathbb{I} \right) + \nabla_A \cdot \left(\frac{p_A^*}{\rho} \mathbb{I} \right) \right] \cdot \delta \mathbf{u} \\ &= \left[-\nabla_B \cdot \left(\frac{p_B^*}{\rho} \mathbb{I} \right) + \nabla_B \cdot \left(\frac{p_A^*}{\rho} \mathbb{I} \right) + \nabla_A \cdot \left(\frac{p_A^*}{\rho} \mathbb{I} \right) - \nabla_A \cdot \left(\frac{p_B^*}{\rho} \mathbb{I} \right) \right] \cdot \delta \mathbf{u} \\ &= \left[-\nabla_B \cdot \left(\frac{\delta p^*}{\rho} \mathbb{I} \right) - \nabla_A \cdot \left(\frac{\delta p^*}{\rho} \mathbb{I} \right) \right] \cdot \delta \mathbf{u}, \end{aligned}$$

Substituting the operators $\nabla_A = -\nabla_{\mathbf{r}} + 1/2 \nabla_{\mathbf{X}}$ and $\nabla_B = \nabla_{\mathbf{r}} + 1/2 \nabla_{\mathbf{X}}$ yields

$$\left[-\nabla_B \cdot \left(\frac{\delta p^*}{\rho} \mathbb{I} \right) - \nabla_A \cdot \left(\frac{\delta p^*}{\rho} \mathbb{I} \right) \right] \cdot \delta \mathbf{u} = \left[\nabla_{\mathbf{X}} \cdot \left(-\frac{\delta p^*}{\rho} \mathbb{I} \right) \right] \cdot \delta \mathbf{u}$$

which eventually simplifies to

$$\nabla_{\mathbf{X}} \cdot \left[-\frac{\delta p^*}{\rho} \delta \mathbf{u} \right],$$

thanks to incompressibility. Interestingly, one can see that pressure forces do not work in scale space.

Viscous terms

Thanks to incompressibility, viscous terms may be written as

$$\begin{aligned} & \left[\nabla_B \cdot (2\nu \mathbb{S}_B) - \nabla_A \cdot (2\nu \mathbb{S}_A) \right] \cdot \delta \mathbf{u} \\ &= 2\nu \left[\nabla_B \cdot (\mathbb{S}_B \cdot \delta \mathbf{u}) - \nabla_A \cdot (\mathbb{S}_A \cdot \delta \mathbf{u}) \right] - 2\nu \mathbb{S}_B : \nabla_B \delta \mathbf{u} + 2\nu \mathbb{S}_A : \nabla_A \delta \mathbf{u} \\ &= 2\nu \left[\nabla_B \cdot (\mathbb{S}_B \cdot \delta \mathbf{u}) - \nabla_A \cdot (\mathbb{S}_A \cdot \delta \mathbf{u}) \right] - 2\epsilon_m, \end{aligned}$$

where $2\epsilon_m = \epsilon_B + \epsilon_A$, is twice the mean viscous energy dissipation rate evaluated between points A and B, with $\epsilon_B = 2\nu \mathbb{S}_B : \mathbb{S}_B$ and $\epsilon_A = 2\nu \mathbb{S}_A : \mathbb{S}_A$ respectively. Replacing \mathbb{S}_B and \mathbb{S}_A by their respective definitions yields

$$\begin{aligned} & 2\nu \nabla_B \cdot (\mathbb{S}_B \cdot \delta \mathbf{u}) - 2\nu \nabla_A \cdot (\mathbb{S}_A \cdot \delta \mathbf{u}) - 2\epsilon_m \\ &= \nu \nabla_B \cdot \left[\left(\nabla_B \mathbf{u}_B + (\nabla_B \mathbf{u}_B)^T \right) \cdot \delta \mathbf{u} \right] - \nu \nabla_A \cdot \left[\left(\nabla_A \mathbf{u}_A + (\nabla_A \mathbf{u}_A)^T \right) \cdot \delta \mathbf{u} \right] - 2\epsilon_m \\ &= \frac{\nu}{2} \nabla_B \cdot (\nabla_B \delta \mathbf{u}^2) + \nu (\nabla_B \mathbf{u}_B)^T : \nabla_B \mathbf{u}_B + \frac{\nu}{2} \nabla_A \cdot (\nabla_A \delta \mathbf{u}^2) + \nu (\nabla_A \mathbf{u}_A)^T : \nabla_A \mathbf{u}_A - 2\epsilon_m. \end{aligned}$$

Using the Laplace equation for the pressure according to which $(\nabla_B \mathbf{u}_B)^T : \nabla_B \mathbf{u}_B = -\Delta_B p_B^*$ and $(\nabla_A \mathbf{u}_A)^T : \nabla_A \mathbf{u}_A = -\Delta_A p_A^*$ respectively, as well as substituting for the new variables $\nabla_A = -\nabla_{\mathbf{r}} + 1/2 \nabla_{\mathbf{X}}$ and $\nabla_B = \nabla_{\mathbf{r}} + 1/2 \nabla_{\mathbf{X}}$ and keeping in mind $2\nabla_{\mathbf{r}} = \nabla_B - \nabla_A$ and $\nabla_{\mathbf{X}} = \nabla_B + \nabla_A$ yields

$$\begin{aligned} & 2\nu \nabla_B \cdot (\mathbb{S}_B \cdot \delta \mathbf{u}) - 2\nu \nabla_A \cdot (\mathbb{S}_A \cdot \delta \mathbf{u}) - 2\epsilon_m \\ &= \frac{\nu}{2} \nabla_B \cdot \left(\nabla_{\mathbf{r}} \delta \mathbf{u}^2 + \frac{1}{2} \nabla_{\mathbf{X}} \delta \mathbf{u}^2 \right) + \frac{\nu}{2} \nabla_A \cdot \left(-\nabla_{\mathbf{r}} \delta \mathbf{u}^2 + \frac{1}{2} \nabla_{\mathbf{X}} \delta \mathbf{u}^2 \right) - \nu [\Delta_B p_B^* + \Delta_A p_A^*] - 2\epsilon_m \\ &= \nu \nabla_{\mathbf{r}} \cdot (\nabla_{\mathbf{r}} \delta \mathbf{u}^2) + \frac{\nu}{4} \nabla_{\mathbf{X}} \cdot (\nabla_{\mathbf{X}} \delta \mathbf{u}^2) + \nu [\Delta_B p_B^* + \Delta_A p_A^*] - 2\epsilon_m \end{aligned}$$

APPENDIX A: DERIVATION OF THE KÁRMÁN-HOWARTH EQUATION

We finally notice that $\Delta_B p_B^* = 2 \nabla_B \cdot [\nabla_B p_m^*]$ and $\Delta_A p_A^* = 2 \nabla_A \cdot [\nabla_A p_m^*]$, with $p_m^* = (p_A^* + p_B^*)/2$. The pressure terms appearing in the equation above thus become

$$\begin{aligned} \Delta_B p_B^* + \Delta_A p_A^* &= 2 \nabla_B \cdot \left(\nabla_{\mathbf{r}} p_m^* + \frac{1}{2} \nabla_{\mathbf{x}} p_m^* \right) + 2 \nabla_A \cdot \left(-\nabla_{\mathbf{r}} p_m^* + \frac{1}{2} \nabla_{\mathbf{x}} p_m^* \right) \\ &= 2 [\nabla_B \cdot - \nabla_A \cdot] (\nabla_{\mathbf{r}} p_m^*) + [\nabla_B \cdot + \nabla_A \cdot] (\nabla_{\mathbf{x}} p_m^*) \\ &= 4 \nabla_{\mathbf{r}} \cdot (\nabla_{\mathbf{r}} p_m^*) + \nabla_{\mathbf{x}} \cdot (\nabla_{\mathbf{x}} p_m^*) \end{aligned}$$

Appendix B: Green's function for the Laplacian operator

In this appendix, we will derive the complete solution to the Poisson equation using Green's functions. To be more specific, we wish to determine the function Ψ , which satisfies the equation

$$\Delta\Psi = f(\mathbf{x}), \quad (5.30)$$

in the domain \mathcal{V} of boundary $\partial\mathcal{V}$. In the above, Δ is the 3D Laplacian operator and $f(\mathbf{x})$ is a source function which is a priori known throughout the control volume. We also assume that the value of Ψ is known along the boundary $\partial\mathcal{V}$.

Green's function in free space

This problem is solved by seeking beforehand an elementary solution $G(\mathbf{x}, \mathbf{x}')$ satisfying

$$\Delta G = \delta(\mathbf{x} - \boldsymbol{\xi}), \quad (5.31)$$

where δ is the Dirac distribution. The function $G(\mathbf{x}, \boldsymbol{\xi})$ (also known as Green's function) may be interpreted as an elementary response evaluated at location $\boldsymbol{\xi}$ to a process resulting from a point source located at position \mathbf{x} . The rationale is the following: noticing that the Laplacian operator is linear, the solution to the general problem (5.30) may be found by summing all the elementary responses to point sources distributed across space. In this paragraph, we focus on solutions $G(\mathbf{x}, \boldsymbol{\xi})$, which vanish at infinity (we will handle boundary conditions in the following section). We shall consider the configuration sketched in figure 5.17, where a point source is located at position \mathbf{x} , in an otherwise unbounded domain. Space is decomposed into two spherical sub-domains each centered on \mathbf{x} : \mathcal{V}_e and \mathcal{V}_o , which are delimited by the surfaces \mathcal{S}_e and \mathcal{S}_o respectively. The Green's function is sought in the form $G(\mathbf{x}, \boldsymbol{\xi}) = G(\|\mathbf{x} - \boldsymbol{\xi}\|)$, that is to say as a function of the distance separating \mathbf{x} and $\boldsymbol{\xi}$ exclusively.

We start by considering the elementary response inside the outer volume \mathcal{V}_o . Since this sub-domain excludes the point source, $\delta(\mathbf{x} - \boldsymbol{\xi}) = 0$ for all $\boldsymbol{\xi} \in \mathcal{V}_o$. Integrating (5.31) over \mathcal{V}_o thus yields

$$\int_{\mathcal{V}_o} \Delta G d^3\boldsymbol{\xi} = 0. \quad (5.32)$$

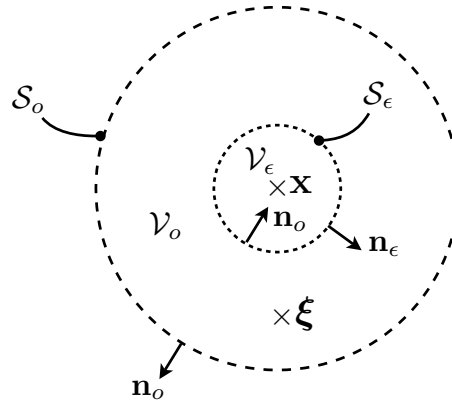


Figure 5.17. Control volume centered on a point source located at \mathbf{x} .

According to the divergence theorem (owing to $\Delta G = \nabla \cdot (\nabla G)$), the previous integral is equivalent to

$$\int_{V_o} \Delta G d^3\xi = \oint_{S_o \cup S_\epsilon} \frac{\partial G}{\partial \mathbf{n}_o} d^2\xi = 0, \quad (5.33)$$

where $\partial G / \partial \mathbf{n}_o = \mathbf{n}_o \cdot \nabla G$ is the directional derivative along the normal to V_o . In other words, $\partial G / \partial \mathbf{n}_o = \partial G / \partial s$ on S_o , while $\partial G / \partial \mathbf{n}_o = -\partial G / \partial s$ on S_ϵ , with $s = \|\mathbf{x} - \xi\|$. Equation (5.33) therefore yields

$$\oint_{S_o} \frac{\partial G}{\partial s} d^2\xi = \oint_{S_\epsilon} \frac{\partial G}{\partial s} d^2\xi = K1, \quad (5.34)$$

where $K1$ must be a constant. Equation (5.34) in fact holds over any sphere of fixed radius s larger than V_ϵ . Since G is a function of s only, integrating (5.34) over such a sphere yields

$$4\pi s^2 \frac{dG}{ds} = K1, \quad (5.35)$$

hence noting $K2$ an integration constant

$$G(s) = -\frac{K1}{4\pi s} + K2. \quad (5.36)$$

Next, we consider the elementary response inside the inner volume V_ϵ . Within this sub-domain, G satisfies $\Delta G = \delta(\mathbf{x} - \xi)$, hence by definition of the Dirac distribution

$$\int_{V_\epsilon} \Delta G d^3\xi = \int_{V_\epsilon} \delta(\mathbf{x} - \xi) d^3\xi = 1. \quad (5.37)$$

As before, the divergence theorem applied to (5.37) also reads

$$\oint_{S_\epsilon} \mathbf{n}_\epsilon \cdot \nabla G d^2\xi = \oint_{S_\epsilon} \frac{\partial G}{\partial s} d^2\xi = K1, \quad (5.38)$$

by virtue of equation (5.34). Combining (5.37) and (5.38) eventually proves that $K1 = 1$. Ultimately, the Green's function satisfying (5.31) in the entire volume and vanishing at infinity is the function

$$G(\|\mathbf{x} - \boldsymbol{\xi}\|) = -\frac{\|\mathbf{x} - \boldsymbol{\xi}\|^{-1}}{4\pi} \quad (5.39)$$

Solution to the Poisson equation in a bounded domain

We start by recalling Green's second identity, which is found by integrating the following vector identity over a domain \mathcal{V} delimited by the boundary $\partial\mathcal{V}$ of normal \mathbf{n} :

$$\nabla \cdot [\Psi \nabla G - G \nabla \Psi] = \Psi \Delta G - G \Delta \Psi. \quad (5.40)$$

Integrating the left hand side of (5.40) yields, thanks to the divergence theorem

$$\int_{\mathcal{V}} \nabla \cdot [\Psi \nabla G - G \nabla \Psi] d^3\xi = \oint_{\partial\mathcal{V}} \left[\Psi \frac{\partial G}{\partial \mathbf{n}} - G \frac{\partial \Psi}{\partial \mathbf{n}} \right] d^2\xi, \quad (5.41)$$

where again $\partial/\partial\mathbf{n} = \mathbf{n} \cdot \nabla$ is the directional derivative along \mathbf{n} . Integrating the right hand side of (5.40), in which $\Delta G = \delta(\mathbf{x} - \boldsymbol{\xi})$ and $\Delta \Psi = f(\mathbf{x})$ have been substituted yields

$$\int_{\mathcal{V}} [\Psi \Delta G - G \Delta \Psi] d^3\xi = \int_{\mathcal{V}} \Psi(\boldsymbol{\xi}) \delta(\mathbf{x} - \boldsymbol{\xi}) d^3\xi - \int_{\mathcal{V}} G(\|\mathbf{x} - \boldsymbol{\xi}\|) f(\boldsymbol{\xi}), d^3\xi \quad (5.42)$$

which eventually simplifies to

$$\int_{\mathcal{V}} [\Psi \Delta G - G \Delta \Psi] d^3\xi = \Psi(\mathbf{x}) + \frac{1}{4\pi} \int_{\mathcal{V}} \frac{f(\boldsymbol{\xi})}{\|\mathbf{x} - \boldsymbol{\xi}\|} d^3\xi. \quad (5.43)$$

Combining (5.41) and (5.43) eventually yields

$$\Psi = -\frac{1}{4\pi} \int_{\mathcal{V}} \frac{f(\boldsymbol{\xi})}{\|\mathbf{x} - \boldsymbol{\xi}\|} d^3\xi - \frac{1}{4\pi} \oint_{\partial\mathcal{V}} \left[\Psi \frac{\partial \|\mathbf{x} - \boldsymbol{\xi}\|}{\partial \mathbf{n}} - \|\mathbf{x} - \boldsymbol{\xi}\|^{-1} \frac{\partial \Psi}{\partial \mathbf{n}} \right] d^2\xi, \quad (5.44)$$

which is the complete solution to the Poisson equation. In particular, (5.44) shows that Ψ results from a source $f(\mathbf{x})$ integrated over the entire volume. In addition, the boundary conditions transpire through the surface integral which imposes the value of Ψ and its derivative at the boundary of the domain.

Bibliography

- AKKERMANS, R.A.D., CIESLIK, A.R., KAMP, L.P.J., TRIELING, R.R., CLERCX, H.J.H. & VAN HEIJST, G.J.F. 2008 Three-dimensional structure of an electromagnetically generated dipolar vortex in a shallow fluid layer. *Phys. Fluids* **20**, 116601.
- ALBOUSSIÈRE, T. & LINGWOOD, R.J. 2000 A model for the turbulent hartmann layer. *Phys. Fluids* **12** (6), 1535–1543.
- ALEMANY, A., MOREAU, R., SULEM, P.L. & FRISCH, U. 1979 Influence of an external magnetic field on homogeneous MHD turbulence. *J. Méc.* **18**, 277–313.
- BAKER, N.T., POTHERAT, A. & DAVOUST, L. 2015 Dimensionality, secondary flows and helicity in low- Rm MHD vortices. *J. Fluid Mech.* **779**, 325–350.
- BELMONTE, A., GOLDBURG, W.I., KELLAY, H., RUTGERS, M.A., MARTIN, B. & WU, X.L. 1999 Velocity fluctuations in a turbulent soap film: The third moment in two dimensions. *Phys. Fluids* **11** (5).
- BOFFETTA, G. & ECKE, R. E. 2012 Two-dimensional turbulence. *An. Rev. Fluid Mech.* **44**, 427–451.
- BRITO, D., NATAF, H.-C., CARDIN, P., AUBERT, J. & MASSON, J.-P. 2001 Ultrasonic doppler velocimetry in liquid gallium. *Exp. Fluids* **31** (6), 653–663.
- CAMPAGNE, A., GALLET, B., MOISY, F. & CORTET, P.-P. 2014 Direct and inverse energy cascades in a forced rotating turbulence experiment. *Phys. Fluids* **26** (12).
- CAPERAN, P. & ALEMANY, A. 1985 Turbulence homogène MHD à faible nombre de Reynolds magnétique. Etude de la transition vers la phase quasi-bidimensionnelle et caractérisation de son anisotropie. *J. Méc. Th. App.* **4** (2), 175–200.
- CELANI, A., MUSACCHIO, S. & VINCENZI, D. 2010 Turbulence in more than two and less than three dimensions. *Phys. Rev. Let.* **104** (18), 184506.
- DAVIDSON, P.A. 1995 Magnetic damping of jets and vortices. *J. Fluid Mech.* **299**, 153–186.
- DAVIDSON, P.A. 2001 *An Introduction to Magnetohydrodynamics*. Cambridge University Press.

BIBLIOGRAPHY

- DAVIDSON, P.A. 2014 The dynamics and scaling laws of planetary dynamos driven by inertial waves. *Geophys. J. Int.* **198** (3), 1832–1847.
- DAVIDSON, P.A. 2015 *Turbulence: an introduction for scientists and engineers*. Oxford University Press.
- DAVIDSON, P.A. & KROGSTAD, P.-Å. 2008 On the deficiency of even-order structure functions as inertial-range diagnostics. *J. Fluid Mech.* **602**, 287–302.
- DAVIDSON, P.A. & PEARSON, B.R. 2005 Identifying turbulent energy distributions in real, rather than fourier, space. *Phys. Rev. Lett.* **95** (21), 214501.
- DAVOUST, L., ACHARD, J.-L. & DRAZEK, L. 2015 Low to moderate Reynolds number swirling flow in an annular channel with a rotating end wall. *Phys. Rev. E* **91**, 023019.
- DOERING, C.R. & GIBBON, J.D. 1995 *Applied analysis of the Navier-Stokes equations*. Cambridge University Press.
- EKMAN, V.W. 1905 On the influence of the earth's rotation on ocean currents. *Ark. Mat. Astron. Fys.* **2**, 1–53.
- FRISCH, U. 1995 *Turbulence: the legacy of A.N. Kolmogorov*. Cambridge University Press.
- GOMES-FERNANDES, R., GANAPATHISUBRAMANI, B. & VASSILICOS, J.C. 2012 Particle image velocimetry study of fractal-generated turbulence. *J. Fluid Mech.* **711**, 306–336.
- HAMBA, F. 2015 Turbulent energy density and its transport equation in scale space. *Phys. Fluids* **27** (8), 085108.
- HARTMANN, J. 1937 Theory of the laminar flow of an electrically conductive liquid in a homogeneous magnetic field. *K. Dan. Vidensk. Selsk. Mat. Fys. Medd* **15(6)**, 1–28.
- HEISER, W.H. & SHERCLIFF, J.A. 1965 A simple demonstration of the hartmann layer. *J. Fluid Mech.* **22**, 701–707.
- HILL, R.J. 2002 Exact second-order structure-function relationships. *J. Fluid Mech.* **468**, 317–326.
- KALIS, KH. E. & KOLESNIKOV, YU. B. 1980 Numerical study of a single vortex of a viscous incompressible electrically conducting fluid in a homogeneous axial magnetic field. *Magnetohydrodynamics* **16**, 155–158.
- KÁRMÁN, T. & HOWARTH, L. 1938 On the statistical theory of isotropic turbulence. *Proc. Royal Soc. London* **164** (917), 192–215.
- KIT, L.G. & TSINOBER, A.B. 1971 Possibility of generating and investigating two-dimensional turbulence in a strong magnetic field. *Magnitn. Gidrodinam.* **3**, 27–34.

- KLEIN, R. 2010 MHD experiments on quasi two-dimensional and three-dimensional liquid metal flows. PhD thesis, Coventry University.
- KLEIN, R. & POTHÉRAT, A. 2010 Appearance of three-dimensionality in wall bounded MHD flows. *Phys. Rev. Lett.* **104** (3).
- KLJUKIN, A. & THESS, A. 1998 Direct measurement of the stream-function in a quasi-two-dimensional liquid metal flow. *Exp. Fluids* **25** (4), 298–304.
- KOLESNIKOV, YU. B. & TSINOBER, A.B. 1972 Two-dimensional turbulent flow behind a circular cylinder. *Magnitn. Gidrodinam.* **8**, 23–31.
- KOLMOGOROV, A.N. 1941a Dissipation of Energy in Locally Isotropic Turbulence. *Dokl. Akad. Nauk SSSR* **32**, 16.
- KOLMOGOROV, A.N. 1941b The local structure of turbulence in incompressible viscous fluid for very large reynolds numbers. *Dokl. Akad. Nauk SSSR* **30**, 301–305.
- KORNÉT, K. & POTHÉRAT, A. 2015 A method for spectral DNS of low- Rm channel flows based on the least dissipative modes. *J. Comp. Phys.* .
- KRAICHNAN, R.H. 1967 Inertial ranges in two-dimensional turbulence. *Phys. Fluids* **10**, 1417–1423.
- LAMRIBEN, C., CORTEL, P.-P. & MOISY, F. 2011 Direct measurements of anisotropic energy transfers in a rotating turbulence experiment. *Phys. Rev. Lett.* **107** (2), 024503.
- LINDBORG, E. 1999 Can the atmospheric kinetic energy spectrum be explained by two-dimensional turbulence? *J. Fluid Mech.* **388**, 259–288.
- MESSADEK, K. & MOREAU, R. 2002 An experimental investigation of MHD quasi-two-dimensional turbulent shear flows. *J. Fluid Mech.* **456**, 137–159.
- MOFFATT, H.K. 1967 On the suppression of turbulence by a uniform magnetic field. *J. Fluid Mech.* **28** (03), 571–592.
- MORESCO, P. & ALBOUSSIÈRE, T. 2004 Experimental study of the instability of the hartmann layer. *J. Fluid Mech.* **504**, 167–181.
- OKAMOTO, N., DAVIDSON, P.A. & KANEDA, Y. 2010 On the decay of low-magnetic-reynolds-number turbulence in an imposed magnetic field. *J. Fluid Mech.* **651**, 295–318.
- PARET, J. & TABELING, P. 1998 Intermittency in the two-dimensional inverse cascade of energy: Experimental observations. *Phys. Fluids* **10** (12), 3126–3136.
- PODESTA, J.J., FORMAN, M.A., SMITH, C.W., ELTON, D.C., MALÉCOT, Y. & GAGNE, Y. 2009 Accurate estimation of third-order moments from turbulence measurements. *Nonlin. Proc. Geophys.* **16** (1), 99–110.

BIBLIOGRAPHY

- POPE, S.B. 2000 *Turbulent flows*. Cambridge University Press.
- POTHÉRAT, A. & KLEIN, R. 2014 Why, how and when MHD turbulence at low- Rm becomes three-dimensional. *J. Fluid Mech.* **761**, 168–205.
- POTHÉRAT, A. & KORNET, K. 2015 The decay of wall-bounded MHD turbulence at low- Rm . *J. Fluid Mech.* **783**, 605–636.
- POTHÉRAT, A., RUBICONI, F., CHARLES, Y. & DOUSSET, V. 2013 Direct and inverse pumping in flows with homogeneous and non-homogeneous swirl. *Eur. Phys. J. E* **36** (8).
- POTHÉRAT, A., SOMMERIA, J. & MOREAU, R. 2000 An effective two-dimensional model for MHD flows with transverse magnetic field. *J. Fluid Mech.* **424**, 75–100.
- POTHÉRAT, A., SOMMERIA, J. & MOREAU, R. 2002 Effective boundary conditions for magnetohydrodynamic flows with thin Hartmann layers. *Phys. Fluids* **14** (1), 403–410.
- REYNOLDS, O. 1883 An experimental investigation of the circumstances which determine whether the motion of water shall be direct or sinuous, and of the law of resistance in parallel channels. *Proc. Royal Soc. London* **35** (224-226), 84–99.
- ROBERTS, P.H. 1967 *Introduction to Magnetohydrodynamics*. Longmans.
- ROUSSET, B., BONNAY, P., DIRIBARNE, P., GIRARD, A., PONCET, J.-M., HERBERT, E., SALORT, J., BAUDET, C., CASTAING, B., CHEVILLARD, L. *et al.* 2014 Superfluid high Reynolds Von-Kármán experiment. *Rev. Sci. Inst.* **85** (10), 103908.
- RUTGERS, M.A. 1998 Forced 2D turbulence: experimental evidence of simultaneous inverse energy and forward enstrophy cascades. *Phys. Rev. Lett.* **81** (11), 2244.
- SATIJN, M. P., CENSE, A. W., VERZICCO, H., CLERCX, H. J. H. & VAN HEIJST, G. J. F. 2001 Three-dimensional structure and decay properties of vortices in shallow fluid layers. *Phys. Fluids* **13** (7), 1932–1945.
- SCHLICHTING, H. 1979 *Boundary-Layer Theory*. McGraw-Hill.
- SMITH, D.M. 1991 Algorithm 693: A FORTRAN package for floating-point multiple-precision arithmetic. *ACM Trans. Math. Softw.* **17** (2), 273–283.
- SOMMERIA, J. 1986 Experimental study of the two-dimensional inverse energy cascade in a square box. *J. Fluid Mech.* **170**, 139–168.
- SOMMERIA, J. 1988 Electrically driven vortices in a strong magnetic field. *J. Fluid Mech.* **189**, 553–569.
- SOMMERIA, J. & MOREAU, R. 1982 Why, how and when MHD turbulence becomes two-dimensional. *J. Fluid Mech.* **118**, 507–518.

- SREENIVASAN, B. & ALBOUSSIÈRE, T. 2002 Experimental study of a vortex in a magnetic field. *J. Fluid Mech.* **464**, 287–309.
- TABELING, P. 2002 Two-dimensional turbulence: a physicist approach. *Phys. Rep.* **362** (1), 1–62.
- TAYLOR, G.I. 1935 Statistical theory of turbulence. *Proc. Royal Soc. London A.* **151** (873), 421–444.
- TSINOBER, A. 1998 Is concentrated vorticity that important? *Eur. J. Mech. B/Fluids* **17** (4), 421–449.
- VAN HEIJST, G.J.F., CLERCX, H.J.H. & MOLENAAR, D. 2006 The effects of solid boundaries on confined two-dimensional turbulence. *J. Fluid Mech.* **554**, 411–431.
- WILLEMETZ, J.-C. 1990 Etude quantitative de l'hémodynamique de vaisseaux sanguins profonds par échographie doppler ultrasonore. PhD thesis, Ecole polytechnique fédérale de Lausanne.
- XIA, H., BYRNE, D., FALKOVICH, G. & SHATS, M. 2011 Upscale energy transfer in thick turbulent fluid layers. *Nature Phys.* **7**, 321–324.

Personal publications

- [1] N. T. Baker, A. Pothérat, L. Davoust, and F. Debray. Inverse cascade in 3D MHD turbulence at low- Rm . *Considered for Phys. Rev. Lett.*, (In preparation).
- [2] N. T. Baker, A. Pothérat, L. Davoust, and F. Debray. Controlling the dimensionality of low- Rm MHD turbulence experimentally. *Accepted for publication in Exp. Fluids*, 2017.
- [3] N. T. Baker, A. Pothérat, and L. Davoust. Dimensionality, secondary flows and helicity in low- Rm MHD vortices. *J. Fluid Mech.*, 779:325–350, 2015.

Conference presentations

- [1] N. T. Baker, A. Pothérat, L. Davoust, and F. Debray. The dynamics of 2D/3D turbulence: an experimental study in the low- Rm MHD framework. In *Europ. Fluid Mech. Conf. 11, Seville*, Sept. 2016.
- [2] N. T. Baker, A. Pothérat, and L. Davoust. Dimensionality and secondary flows in electrically driven MHD vortices. In *Europ. Fluid Mech. Conf. 11, Seville*, Sept. 2016.
- [3] N. T. Baker, A. Pothérat, L. Davoust, and F. Debray. The dynamics of 2D/3D turbulence: an experimental study in the low- Rm MHD framework. In *10th PAMIR Int. Conf.: Fund. and App. MHD, Cagliari*, June 2016.
- [4] N. T. Baker, A. Pothérat, L. Davoust, and F. Debray. The 2D/3D dynamics of wall-bounded MHD turbulence at low- Rm . In *Europ. Turb. Conf. 15, Delft*, Aug. 2015.
- [5] N. T. Baker, A. Pothérat, L. Davoust, and F. Debray. The 2D/3D dynamics of wall-bounded MHD turbulence at low- Rm . In *Europ. Fluid Mech. Conf. 10, Copenhagen*, Sept. 2014.
- [6] N. T. Baker, A. Pothérat, L. Davoust, and F. Debray. Experimental study of forced and freely decaying wall bounded MHD turbulence at low- Rm . In *9th PAMIR Int. Conf.: Fund. and App. MHD, Riga*, June 2014.